Budker Institute of Nuclear Physics

Siberian Branch of Russian Academy of Sciences

The 53th ICFA Advanced Beam Dynamics Workshop on Energy Recovery Linacs "ERL-2013"

9 -13 September, 2013

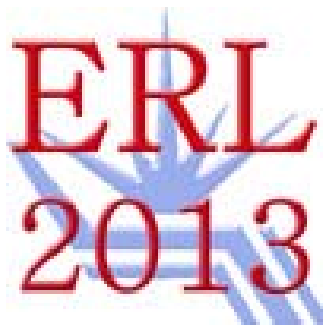

PROCEEDINGS

Novosibirsk 2013

Dear Colleagues,

ERL 2013 will take place at Budker Institute of Nuclear Physics (Novosibirsk, Russia). Particle accelerators have become one of the main fields of activity of our Institute. In particular, we have an ERL with one-, two- and four-orbit operation modes and a high-power terahertz free electron laser user facility on it. Still, prospective applications of ERLs require far more advanced and challenging installations. Such applications comprise short-duration high-brightness x-ray sources, high-power free electron lasers, nuclear physics facilities with internal target, etc. The new ERL projects for these applications necessitates further development of beam dynamics, electron guns, RF systems and other technological issues. The previous ERL workshops made a significant contribution to this progress. We hope that ERL 2013 will also provide great possibilities for fruitful discussions and important personal contacts of leading scientists in our field.

Sincerely,
Gennady N. Kulipanov, Academician,
International Organizing Committee Chair,
Budker INP, Novosibirsk

Contents

International Organizing Committee

G. N. Kulipanov, BINP (Chairman)
– S. Benson, TJNAF
– I. Ben-Zvi, BNL
– R. Hajima JAEA
– G. Hoffstaetter, Cornell
– H. Kawata KEK
– K-J. Kim, ANL and the U. of Chicago
– J. Knobloch, HZB
– S. Smith , STFC/DL/ASTeC
– Yu. Shatunov, BINP

Workshop Scientific Secretary

Ya. Getmanov, BINP

International Program Committee

O. Shevchenko, BINP (Chairman)
– R. Hajima, JAEA
– D. Angal-Kalinin, STFC/DL/ASTeC
– I. Bazarov, Cornell U.
– S. Belomestnykh, BNL
– B. Dunham, Cornell U.
– P. Evtushenko, JLAB
– T. Furuya, KEK
– C. Hernandez-Garcia, JLAB
– G. Hoffstaetter, Cornell U.
– A. Jankowiak, HZB
– T. Kamps, HZB
– D. Kayran, BNL
– K-J. Kim, ANL and the Univ. of Chicago
– E-S. Kim, Kyungpook Natl. U.
– J. Knobloch, HZB
– Y. Kobayashi, KEK
– M. Liepe, Cornell U.
– V.N. Litvinenko, BNL
– K. Liu, Peking U.
– P. McIntosh, STFC/DL/ASTeC
– L. Merminga, TRIUMF
– J. M. Klopf, Jefferson Lab
– L. Militsyn, STFC Daresbury Laboratory
– S. Sakanaka, KEK
– T. Smith, Stanford U.
– J. Teichert, HZDR
– A. Tribendis, BINP
– N. Vinokurov BINP
– J. Wang, IHEP
– N. Nakamuro, KEK


ERL 2013
Workshop on Energy Recovery Linacs
ИНСТИТУТ ЯДЕРНОЙ ФИЗИКИ

STATUS OF THE MESA ACCELERATOR *

K. Aulenbacher, J. Diefenbach, R. Heine, F. Schlander
Institut für Kernphysik, Johannes Gutenberg-Universität Mainz, Germany

Abstract

MESA will be operated as a superconducting multi-turn energy recovery linac (ERL), with the option to perform experiments with a windowless target with beam current of 1 mA which is to be increased towards 10 mA in a later stage of the project. Alternatively the machine can be used as a conventional c.w. accelerator with spin-polarized external beam at 150 MeV. We present the status of the design work.

INTRODUCTION

Figure 1 shows the underground areas which are available at our institution in Mainz. The existing accelerator cascade "MAMI-C" is foreseen to drive hadron physics experiments at the areas A1 and A2 for many years to come. On the other hand, the halt of the A4-experiments in autumn 2012 allows to make use of this space (see fig 1) in order to build a small "stand alone" machine, the **M**ainz **E**nergy recovering **S**uperconducting **A**ccelerator, MESA. In June 2012 the project received considerable funding by the German university excellence initiative within the cluster of excellence "PRISMA" (**PR**ecision experiments, fundamental **I**nteractions and **S** tructure of **MA**tter).

The feasibility of the ERL-concept was demonstrated at JLAB [1]. Such machines are widely known as possible drivers for future light sources of "fourth generation". We, however, try to use the ERL for electron scattering experiments, which relieves several of the requirements that plague the designers for light sources, such as operation in excess of 10 pC bunch charge. In this paper we describe the status of the accelerator design.

MESA LAYOUT

MESA will be installed in Hall 3 and in a part of the former MAMI-beamline tunnel (see fig. 1). Hall 4 will be employed for experiments, which gives the advantage that a high power beamdump is already available. The complex will be separated from the MAMI-accelerator and its remaining experiments (A1 and A2) by a 2 m thick heavy-concrete wall, for reasons of radiation protection. In the plane of the MAMI accelerator this shielding is increased additionally with at least 30 radiation length of material to protect against forward directed gamma-showers which could be created due to beam losses in MAMI-operation. MAMI experiments and the construction of MESA can therefore be performed independently. During the time of the conference the area of the beamline tunnel is about to be cleared, we expect the wall to be completed until summer 2014. The wall is a prerequisite to obtain permission from the authorities to work within the MESA Halls during MAMI operation. The main modification of infrastructure will be enlarging of the breakthrough between the beamline tunnel and hall 3.

Figure 2 demonstrates how the machine could be integrated into the existing building. Due to reasons which will be discussed below it is planned to erect the machine in two stages, the parameters for the stages can be found in table 1. If not mentioned otherwise, the discussion in this paper refers to stage-1 parameters.

The R.f.-operating frequency of MESA has still to be defined. A possible choice is 1300 MHz since a great number of superconducting accelerators around the world (e.g. E-XFEL, ALICE, ELBE, C-ERL) use this frequency. Advantages and disadvantages for a lower frequency are discussed below.

The superconducting main linac will allow for an energy gain of 50 MeV. Two recirculations are foreseen in conventional beam mode (external beam, EB-mode), leading to an output energy of the external beam of 150 MeV. This is presently considered as an optimum energy for the 'P2' experiment measuring the weak mixing angle [2]. The current foreseen for P2 is 150 μA with a polarization P$\geq$0.85. The beam power of 30 kW will be released in the beam dump system which was in use for MAMI-C with similar beam powers.

In ERL operation the current is increased to 1 mA (unpolarized), corresponding to a bunch charge of 0.77 pC in c.w. operation. In the second recirculation at 105 MeV the beam orbit is directed towards the experimental hall 4 and passes a windowless target. In contrast to storage ring operation with an internal target the beam particles pass this "pseudo-internal target" (PIT) only once. This allows to achieve stationary beam conditions with minimized multiple and wall-scattering. The high beam power at the target (0.1 MW) allows for a luminosity in excess of $10^{35} cm^{-2} s^{-1}$ in spite of the low target density. Since energy straggling and Coulomb scattering are minimized in this set-up, emittance deterioration is negligible as far as RMS values are concerned. Of course long tails of the distribution exist which have to be collimated before the beam is redirected towards the accelerator. The long recirculation through hall-4 offers enough space for this. After passing the PIT the beam is redirected towards the MESA set-up where it re-enters the recirculation system.

The length of the (second) recirculation in ERL-mode - with PIT - is adjusted to a half integer number of wavelengths so that the electrons get decelerated in the main

* This work was supported by the excellence cluster PRISMA within the German university excellence initiative.

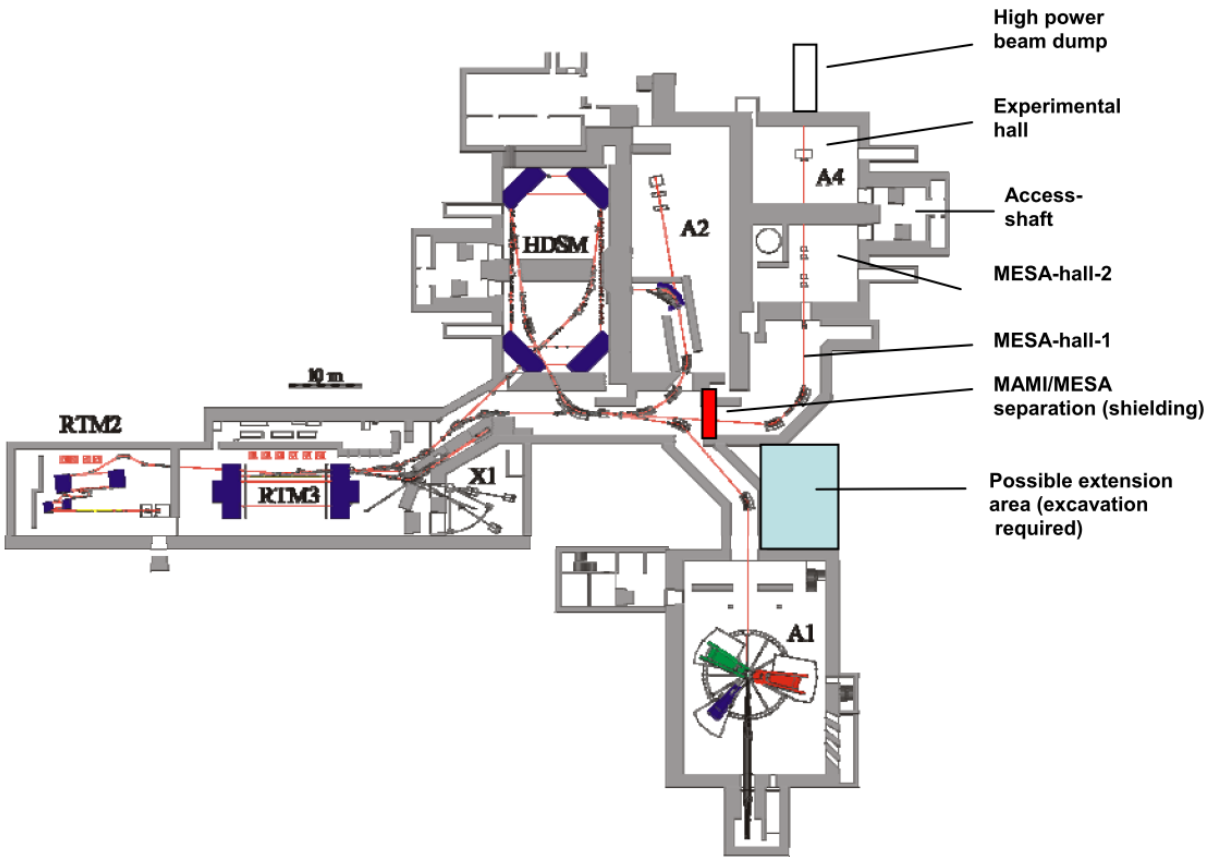

Figure 1: MAMI-C floor plan with experimental halls. The former beamline tunnel (Mesa-Hall-1) and the former Halls 3 (MESA-Hall-2) and Hall 4 (A4) will be available for the installation of MESA and its experiments.

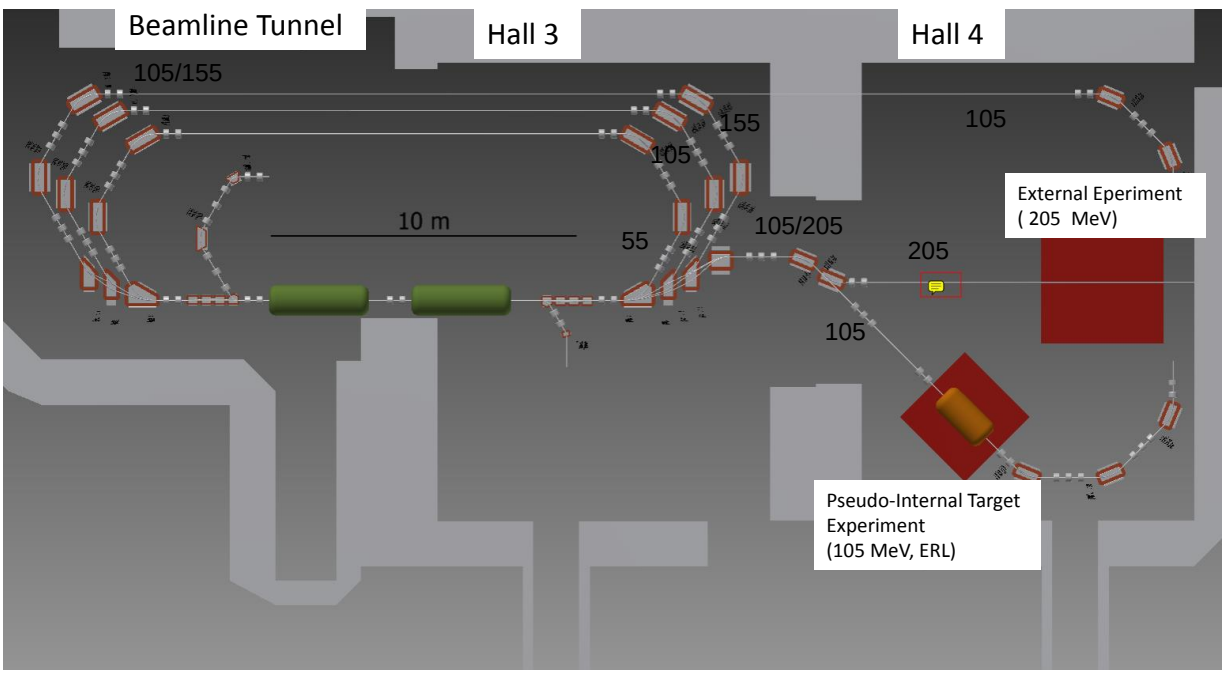

Figure 2: Integration of MESA inside the existing building. Shown is a three fold recirculating flat lattice (stage-2) which would allow for 205 MeV in EB mode. In ERL-mode the beam is deflected in the second recirculation into a loop through experimental hall 4. Numbers are beam energies in MeV on the orbits in ERL or EB mode.

linac. After this the beam propagates into the first recirculation orbit which has an integer number of wavelengths, so that the arrival phase is not changed at the next passage, leading to another deceleration of the beam. Then, the beam leaves the main linac at the injection energy (5 MeV). MESA would represent the first superconducting multi-turn ERL - a normal conducting system exists at the NOVOFEL facility at Budker institute in Novosibirsk [3].

CRYOMODULES

Parameter	stage-1 (EB/ERL)	stage-2 (EB/ERL)
Beam energy, MeV	155/105	205/105
Bunch charge, pC	0.15/0.77	0.15/7.7
norm. emittance, μm	0.2 / <1	0.2/< 1
Beam polarization, %	>0.85/n.a.	>0.85/n.a.
Recirculations	2	3
Beam power at exp., kW	22.5/100	31/1000

Table 1: Parameter set for MESA in stages 1 and 2.

Cryoplant

Our institute already possesses a cryoplant with a liquefaction capacity of 140 l/h. This capacity can be doubled by using liquid Nitrogen precooling. We estimate that about 40% of the enthalpy of evaporation of the liquified Helium will be available for cooling the main linac, corresponding to a cooling power of ≈ 90 Watt at 2 K.

Main linac

Losses in the superconducting cavities are $\propto U_{acc}^2/Q_0$, where eU_{acc} is the energy gain of the linac and Q_0 is the quality factor of the accelerating cavity. We assume to have an active cavity-length of about 4 meters. Then, in order to achieve the objective of $U_{acc} = 50\,MV$ with the given cryoplant it is necessary to have $Q_0 > 10^{10}$. Values of $Q_0 > 1.5 \cdot 10^{10}$ at 1.8 K have been reported for 9 cell cavities of the TESLA type [4] even at accelerating fields of more than 25 MV/m. At the ELBE facility, TESLA cavities have been installed in cryomodules that have been modified for c.w. operation. These "ELBE"-cryomodules comprise two TESLA cavities. At a not too ambitious c.w. field of $13MV/m$ two cryomodules would allow to achieve the envisaged energy gain of 50 MeV. The ELBE modules are commercially available.

However, TESLA cavities have not been intended for high current c.w. operation, especially not for recirculating operation. The chain of 9 coupled superconducting cavities can be exited in different, so called higher order modes (HOM's). HOM's with deflection properties (similar to TM_{110}-modes) may be excited by the beam. Such modes deflect particles with deviations from the axis. In particular, in recirculating systems a positive feedback can occur since a small misalignment of the beam excites the deflecting mode which in turn increases the misalignment. The excitation is proportional to the bunch charge or, equivalently, the beam current. Under simplifying assumptions a compact formula may be given which defines the threshold current for this, so-called beam blow up (BBU) instability [5].

$$I_{th} = \frac{2c^2}{e(R/Q)_{HOM}Q_{HOM}\omega_{HOM}} \frac{1}{T_{ij}sin(\omega_{HOM}t_r)} \quad (1)$$

T_{ij} stands for the transfer of deviations through the recirculations for the longitudinal and transverse coordinates, especially in the transverse plane this means the transfer of an angular deviation into a position deviation after the recirculation. These matrix elements can be varied by a suitable design of the recirculating lattice.

In this formula $(R/Q)_{HOM}$ and Q_{HOM} are separated for the following reason: R/Q is a geometry factor which is fixed by the shape of the cavity. Q_{HOM} is the actual (external) quality factor of the HOM which may be reduced for instance by extracting the power to the outside world by suitable antennas. Such antennas, so-called higher order mode couplers (or dampers) must not change Q_0 of the fundamental mode. Though two HOM couplers are foreseen in the TESLA cavity they are very probably not sufficient to allow for reasonably high threshold for MESA stage-2 parameters. Ongoing investigations must reveal if – or if not – TESLA cavities are suitable at least for MESA stage-1 parameters.

The time window for the decision which type of cryomudule should serve for MESA is still open, we guess that a 2 year period from ordering a module until delivery is not unrealistic. This sets the latest date for ordering to the end of 2014, if timely completion of MESA (before end of 2017) shall prevail.

802 MHZ AS ALTERNATIVE FREQUENCY

The choice of TESLA cavities with its limited HOM damping properties implies that, in order to achieve stage-2 parameters, new cryomodules would have to be acquired. Since the modules are one of the most expensive parts of the accelerator, this is not an attractive perspective. We are thinking of alternative schemes. This means finding suitable new cryomodules with improved HOM damping.

Optimized HOM damping is foreseen in many ongoing ERL projects. Usually the number of resonators is reduced (typically 5 or 7) and stronger damping (with adequate cooling of absorbers) is foreseen . It is evident that cryomodules with optimized cavities are potentially better suited for MESA but tests of such advanced cryomodules have only just begun in places such as BNL or SFTC [6], [7]. The fabrication and operation of such advanced modules is even more demanding than ELBE/TESLA, which will increase the costs and make the timeline longer. Since our institution does not have the resources to perform the necessary design work for an adaptation to our needs we cannot embark into such a project without additional part-

ners. The absence of such a collaboration at the time of the funding proposal was the main argument why the project objectives were reduced towards stage-1 parameters.

Since spring 2013 we consider designing a 802 MHz cryomodule together with the RF group of CERN. CERN accelerator scientists discuss the LHeC collider project. This linac-ring collider [8] will enable high luminosity collisions of polarized electrons with protons from LHC. The so-far unresolved issues of multi-turn ERL operation at the multi-10 GeV range require the construction of a test-facility, which is foreseen to be build on the same timescale as MESA. The beam current foreseen for LHeC is also similar to the one needed for MESA, creating the same needs regarding the module design, in particular HOM damping. 802 MHz is a harmonic of the LHC frequency and offers considerable technical advantages as far as high power Rf-sources are considered. The collaboration with CERN would compensate for our own limitation in resources. Furthermore, we envisage to double the active length of the modules with respect to the stage-1 plan. This will not only reduce the power loss at 2 K but also the reduced gradient will lead to more reliable operation and to a larger tolerance of the system in case of a cavity which is not performing according to the specifications. A further advantage would be that the increased active length would allow to increase the energy gain per turn towards 100 MeV, hence doubling the available output energies. We will decide if we join a collaboration with CERN with the objective to design and build such cryomodules before end of 2013.

OPTIONS FOR RECIRCULATING LATTICES

A first priority for MESA is to provide beam for particle and nuclear physics experiments, the P2 experiment being of particular importance. P2 requires a beam energy of 150 MeV and a very good control of the beam parameters. A necessary condition for this is very high stability of the accelerator. Multi turn acceleration is necessary due to the restrictions in space and budget. There exist several options how to realize the multi-turn recirculation. Though a flat recirculation with independent orbits is shown in figure 2 we presently favor a CEBAF-style lattice with two axis acceleration, i.e. the two cryomodules would be placed parallel to each other. The orbits are vertically separated and good compensation of vertical dispersion can be achieved. Such an approach needs twice the number of spreaders if compared with the single axis recirculation shown in fig 2. This additional effort can be tolerated. We have already achieved a reasonable solution for the lattice functions in both ERL and EB mode in this double axis set-up [9].

An independent orbit recirculator offers high flexibility especially if one is concerned with the dependence of eq. 1 on the matrix elements T_{ij}. However, if sufficient HOM-damping could be provided, we can also investigate a polytron approach which would allow to increase the number of recirculations in order to save costs. Such a polytron lattice consist of 2*N segment magnets, where N is the order of the polytron. We presently investigate a polytron of second order. The device would have an energy gain 25 MeV per turn by a single cryomodule. The single axis acceleration is a difference to the canonical "double sided microtron", we therefore call the lattice an 'asymmetric polytron of second order (AP-2)'. Such a lattice has the following advantages if compared to the independent orbit recirculator:

- Considerably reduced investment for cryomodules, cavities and cryogenic infrastructure
- Strong longitudinal focusing allows inherently for very stable beam conditions and also comparatively long bunches.
- sufficient transverse focusing is possible due to techniques which were applied during the design of MAMI-C [10].
- The number of components (bending magnets, quadrupoles) is much smaller if compared to an independent orbit recirculator.
- considerably reduced size is a very important feature for our given space restrictions

These advantages make the AP2 a very tempting alternative to conventional lattices. However there also disadvantages:

- In a polytron the matrix elements are not very varianble. Fixed parameters T_{ij} may imply low threshold currents, especially since the stored currents in the module are doubled for a given current.
- In order to obtain sufficient transverse focusing inhomogeneous fields are applied in the bending magnets. These lead to large phase slips during the recirculations. In order to maintain the synchronous phase, chicanes are needed to compensate for these shifts.

CONCLUSION

MESA is an interesting accelerator project that offers unique conditions for several experiments in particle and hadron physics and especially parity violating electron scattering. The compact size and favorable conditions regarding infrastructure and staff make the realization of MESA within the given constraints of budget and infrastructure conceivable. Future work will concentrate on detailed design studies to be completed within the next two years. We believe that the MESA accelerator could start to operate by the end of 2017.

ACKNOWLEDGEMENT

I thank Daniel Simon and Karl-Heinz Kaiser for productive discussions concerning the MESA lattice.

REFERENCES

[1] L. Merminga, D.R. Douglas and G.A. Krafft: *Annu. Rev. Part. Sci.* **53** 387-429 (2003)

[2] D. Becker, S. Baunack and F.E. Maas: *Hyperfine Interact.* **213** 141-148 (2013)

[3] V.P. Bolotin et al.: *Nucl. Instrum. Meth.* **A 557** 23-27 (2006)

[4] B. Aune et al.: *Phys. Rev. ST/AB* **3** 092001 (2000)

[5] G.H. Hoffstaetter and I.V. Bazarov: *Phys. Rev. ST/AB* **7** 054401 (2004)

[6] P. A. McIntosh et al.: Proceedings IPAC2012, New Orleans, http://accelconf.web.cern.ch/ AccelConf/IPAC2012/papers/weppc031.pdf

[7] W. Xu et al.: Proceedings IPAC2012, New Orleans, http://accelconf.web.cern.ch/ AccelConf/IPAC2012/papers/weppc113.pdf

[8] F. Zimmermann et al. proceedings IPAC 2010 http://accelconf.web.cern.ch/ AccelConf/IPAC10/papers/tupeb039.pdf

[9] D. Simon, Diploma Thesis, Institut für Kernphysik, Universität Mainz (2013)

[10] K.H. Kaiser et al.: *Nucl. Instrum. Meth.* **A 593** 159-170 (2008)

COMMISSIONING STATUS AND FURTHER DEVELOPMENT OF THE NOVOSIBIRSK MULTITURN ERL*

O.A.Shevchenko#, V.S.Arbuzov, E.N.Dementyev, B.A.Dovzhenko, Ya.V.Getmanov, E.I.Gorniker, B.A.Knyazev, E.I.Kolobanov, A.A.Kondakov, V.R.Kozak, E.V.Kozyrev, S.A.Krutikhin, V.V.Kubarev, G.N.Kulipanov, E.A.Kuper, I.V.Kuptsov, G.Ya.Kurkin, L.E.Medvedev, L.A.Mironenko, V.K.Ovchar, V.M.Petrov, A.M.Pilan, V.M.Popik, V.V.Repkov, T.V.Salikova, M.A.Scheglov, I.K.Sedlyarov, S.S.Serednyakov, A.N.Skrinsky, S.V.Tararyshkin, V.G.Tcheskidov, A.G.Tribendis, N.A.Vinokurov, M.G.Vlasenko, P.D.Vobly, V.N.Volkov, BINP, Novosibirsk, Russia

Abstract

The Novosibirsk ERL is used as a source of electron beams for the powerful Free Electron Laser. It is based on the normal conducting RF structure which operates in CW mode. The third stage of this facility which is the first in the world four-turn ERL has been commissioned recently. More than 90% of electrons were transported to the beam dump, which allowed to increase the average beam current up to 5 mA. The obtained parameters are sufficient to get lasing at the third stage FEL which will be installed at fourth track in the nearest future. In this paper we report the commissioning status and talk about further development of the Novosibirsk ERL and FEL facility.

ACCELERATOR DESIGN

The Novosibirsk FEL facility is based on the multiturn energy recovery linac (ERL) which scheme is shown in Fig. 1. In this scheme the beam goes through the linac several times before it enters undulator. As the result one can increase the final electron energy.

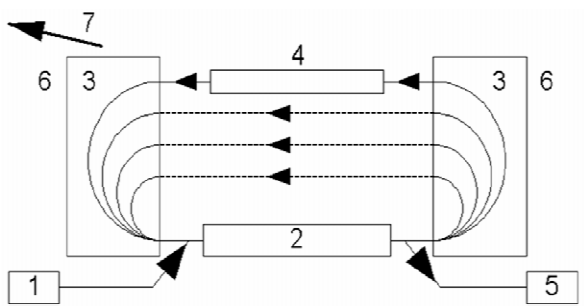

Figure 1: Simplest multiturn ERL scheme: 1 – injector, 2 – linac, 3 – bending magnets, 4 – undulator, 5 – dump.

Multiturn ERLs look very promising for making ERLs less expensive and more flexible, but they have some serious intrinsic problems. Particularly in the simplest scheme shown in Fig.1 one has to use the same tracks for accelerating and decelerating beams which essentially complicates adjustment of the magnetic system. This problem can be solved by using more sophisticated scheme based on two linacs [1].

At present the Novosibirsk ERL is the only one multiturn ERL in the world. It has rather complicated lattice as it can be seen from Fig. 2. The ERL can operate in three modes providing electron beam for three different FELs. The whole facility can be treated as three different ERLs (one-turn, two-turn and four-turn) which use the same injector and the same linac. The one-turn ERL is placed in vertical plane. It works for the THz FEL which undulators are installed at the floor. This part of the facility is called the first stage. It was commissioned in 2003 [2].

The other two ERL orbits are placed in horizontal plane at the ceiling. At the common track there are two round magnets. By switching these magnets on and off one can direct the beam either to horizontal or to vertical beamlines. The 180-degree bending arcs also include small bending magnets with parallel edges and quadrupoles. To reduce sensitivity to the power supply ripples, all magnets on each side are connected in series. The quadrupole gradients are chosen so that all bends are achromatic. The vacuum chambers are made from aluminium. They have water-cooling channels inside.

The second horizontal track has bypass with the second FEL undulator. The bypass provides about 0.7 m lengthening of the second orbit. Therefore when the beam goes through the bypass it returns back to the linac in decelerating phase and after two decelerations it finaly comes to the dump. This part (the second stage) was commissioned in 2009. The final third stage will include full-scale four-turn ERL and FEL installed on the last track.

The basic beam and linac parameters common for all three ERLs are listed in Table 1.

*Work supported by the Ministry of Education and Science of the Russian Federation; RFBR grant 11-02-91320
#O.A.Shevchenko@inp.nsk.su

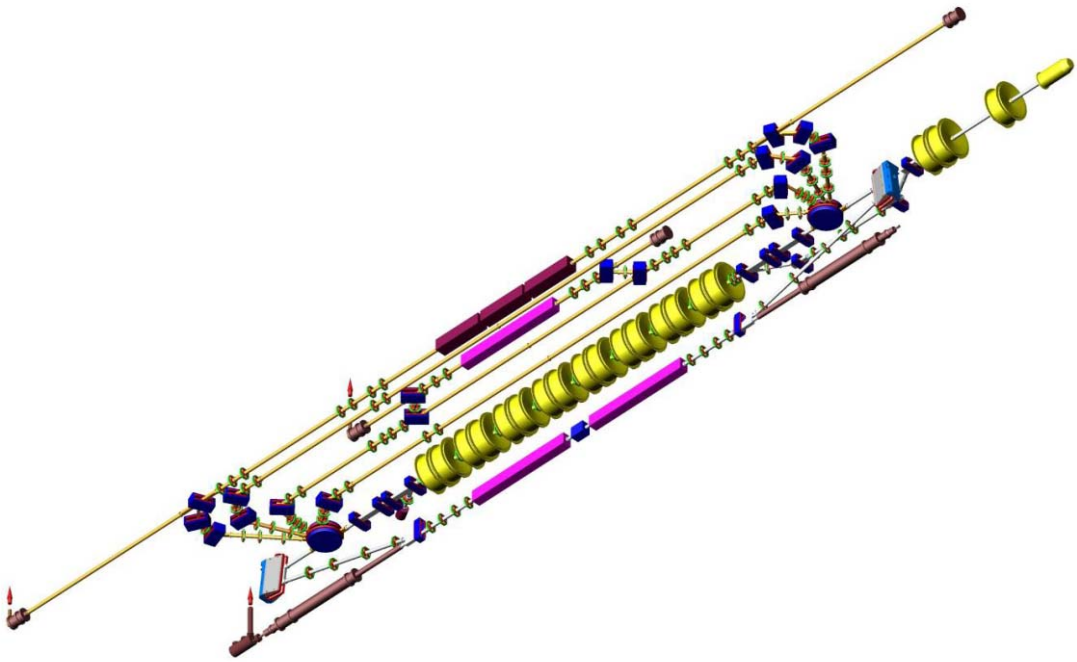

Figure 2: The Novosibirsk ERL with three FELs (bottom view).

Table 1: Basic ERL parameters

Injection energy, MeV	2
Main linac energy gain, MeV	10
Charge per bunch, nC	1.5
Normalized emittance, mm·mrad	30
RF frequency, MHz	180.4
Maximum repetition rate, MHz	90.2

Depending on the number of turns the maximum final electron energy can be 12, 22 or 42 MeV. The bunch length in one-turn ERL is about 100 ps. In two and four-turn ERLs the beam is compressed longitudinally up to 10-20 ps. The maximum average current achieved at one-turn ERL is 30 mA which is still the world record.

One essential difference of the Novosibirsk ERL compared to other facilities [3,4] is using of the low frequency non-superconducting RF cavities. On one hand it leads to increasing of the linac size but on the other hand it also allows to increase transversal and longitudinal acceptances which allows to tolerate longer electron bunches with large transversal and longitudinal emittances.

The location of different parts of the facility in the accelerator hall is shown in Fig. 3.

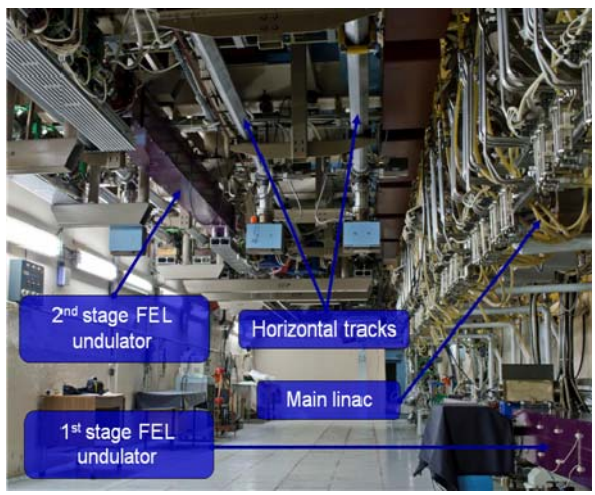

Figure 3: Accelerator hall (bottom view).

THE FIRST STAGE FEL

Design and Basic Parameters

The first stage FEL includes two electromagnetic undulators with period 12 cm, phase shifter and optical cavity. Undulator pole shape is chosen to provide equal electron beam focusing in vertical and horizontal directions. The matched beta-function is about 1 m. The phase shifter is installed between undulators and it is used to adjust the slippage. The optical cavity is composed of two copper mirrors covered by gold. The distance between mirrors is 26.6 m which corresponds to the round-trip frequency (and the resonance electron repetition rate) 5.64 MHz. Radiation is outcoupled

through the hole made in the mirror center. The optical beamline is separated from the vacuum chamber by diamond window. The beamline pipe is filled with dry nitrogen.

The FEL generates coherent radiation tunable in the range 120-240 micron as a continuous train of 40-100 ps pulses at the repetition rate of 5.6 - 22.4 MHz. Maximum average output power is 500 W, the peak power is more than 1 MW [5,6]. The minimum measured linewidth is 0.3%, which is close to the Fourier-transform limit.

Operation Experience

For the last two years about 30 experiments were carried out at the Novosibirsk THz FEL. They include: pioneering works on THz ablation; study of micro- and nanoparticles, vaccines, polymers, metamaterials; production of nanotubes and nanostructures; composite diagnostics; terahertz radioscopy, imaging, detection of concealed objects; interferomety, holography & tomography; speckle and Talbot metrology; ellipsometry; fast water vapor detection; flame and gas detonation study; impact of THz radiation on genetic materials; impact of THz radiation on cells; study of integrated proteomic response; coherent effects in gases; ultrafast time-domain spectroscopy; interaction of atoms with strong THz EM-field.

Five user stations are in operation now. Two other are in progress. The new spectrometer has been installed recently. It allows to measure continuously radiation spectrum not interrupting user experiments (Fig. 4). Other radiation diagnostics include Fourier spectrometer, thermograph, microbolometer matrix, Shottky diode together with wideband oscilloscope. The last one is used for time-resolved measurements. It allows to detect longitudinal power distribution of radiation pulses.

Figure 4: Spectrum measurement diagnostic control (white line - the measured FEL radiation spectrum, blue line - water absorption spectrum).

Recently the third harmonics lasing was obtained. It was achieved by suppression of the first harmonics lasing using aperture-decreasing scrapers installed inside the optical cavity and proper adjustment of the phase shifter. The measured detuning curves for the first and third harmonics lasing are shown in Fig. 5.

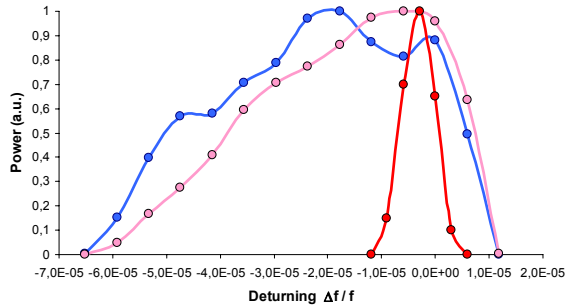

Figure 5. Normalized detuning curves for the lasing at the first (blue) and third (red) harmonics and the detuning curve for the amplified spontaneous emission at the third harmonic (pink).

THE SECOND STAGE FEL

The second stage FEL includes one electromagnetic undulator with period 12 cm and optical cavity. The undulator is installed on the bypass where the electron energy is about 22 MeV. Therefore the FEL radiation wavelength range is 40 - 80 micron. The undulator design is identical to the first stage one but it has smaller aperture and higher maximum magnetic field amplitude. The optical cavity length is 20 m (12 RF wavelengths). Therefore the bunch repetition rate for initial operation is 7.5 MHz.

The first lasing of this FEL was achieved in 2009. The maximum gain was about 40% which allowed to get lasing at 1/8 of the fundamental frequency (at bunch repetition rate ~1 MHz).

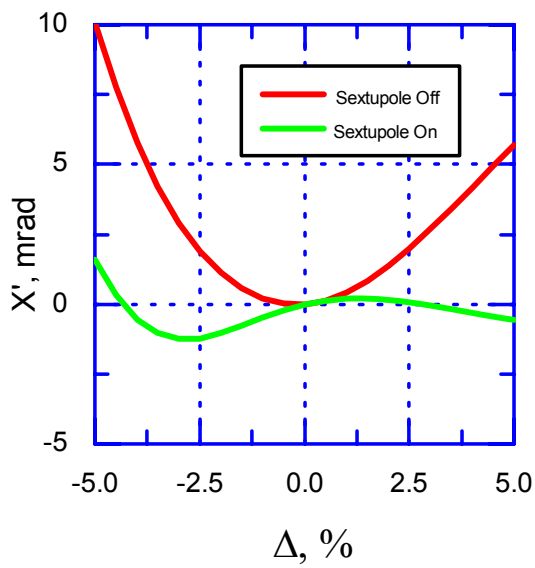

Figure 6: Compensation of quadratic dependence of the bending angle on energy by sextupoles in the first orbit bending arcs.

The significant (percents) increase of beam losses took place during first lasing runs. Therefore sextupole corrections were installed into some of quadrupoles to make the 180-degree bends second-order achromatic. It increased the energy acceptance for used electron beam (Fig. 6).

The optical beamline (Fig. 7) which delivers radiation from new FEL to existing user stations is assembled and commissioned. The output power is about 0.5 kW at the 9 mA ERL average current. Thus, the first in the world multiturn ERL operates for the far infrared FEL.

Figure 7: Optical beamlines for the first and the second stage FELs. Radiation of both FELs is delivered to the same user stations. Switching between FELs is done by retractable mirror.

THIRD STAGE ERL AND FEL

The scheme of the third stage ERL with FEL undulators is shown in Fig. 8. Electron beam in the third stage ERL is accelerated four times. The third FEL undulators are already installed on the last track (Fig. 9) where the beam energy is 42 MeV. In this FEL three permanent magnet undulators with period 6 cm and variable gap will be used. The wavelength range will be 5-30 microns. The electron outcoupling is planned to be used here [7].

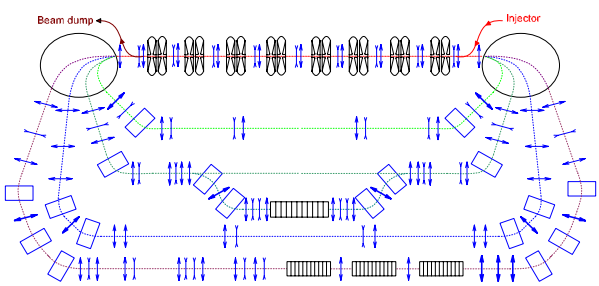

Figure 8: The third stage ERL with FEL undulators.

All magnetic system elements and vacuum chambers of the third stage ERL are assembled and installed. The first shifts for lattice adjustment took place and 95% of the injector beam current has been dumped already.

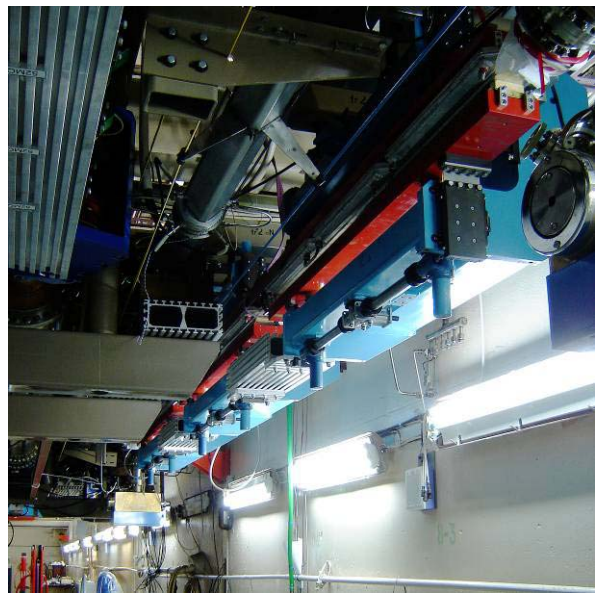

Figure 9: Three permanent magnet undulators with variable gap installed on the last track.

The signal from the BPM installed in the accelerating structure near the dump is shown in Fig. 10. All eight peaks here correspond to the same beam at different stages – the first four are in accelerating phase and the last four - in decelerating phase. One can see that the first and the last peak amplitudes do not differ significantly. It means that the beam losses mostly take place near the dump.

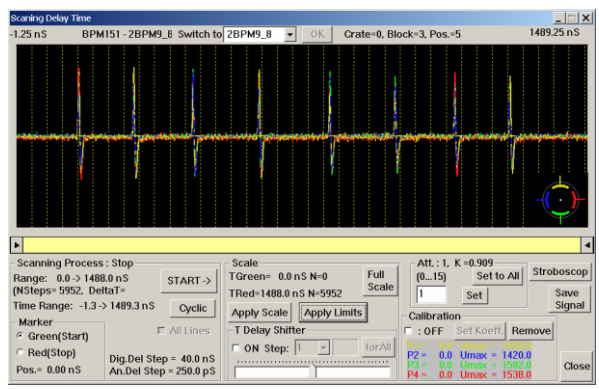

Figure 10: Signal from the BPM installed in the accelerating structure.

The obtained level of beam losses allowed to increase the average current up to 5 mA. The minimal repetition rate required to get lasing has been demonstrated.

FUTURE PROSPECTS

In the nearest future we plan to continue the third stage ERL commissioning. The third FEL optical cavity will be assembled and the lasing of this FEL will be obtained shortly. After that the main problem will be optimization of the longitudinal acceptance for recuperation of the beam with large energy spread. To solve this problem we

are planning to optimize the lattice and to install additional sextupole correctors.

The other important issue which we are working on now is the operation stability and improvement of the existing FEL parameters. We plan to make some improvements of the RF system. We also plan to increase accelerating voltage amplitude and stability of the DC gun. For this purpose the new power supply is being commissioned now. In distant prospect we consider an option to replace DC gun by new RF gun which is being developed in our institute. The test setup for this gun is in operation already (Fig. 11).

Figure 11: RF gun test setup.

By now one has achieved the following beam parameters from this gun: bunch charge – 1.5 nQ, pulse duration – 1 ns, average beam current – 25 mA.

More serious modernization e.g. using the new type of undulators with variable period [8] is also considered.

REFERENCES

[1] D. Douglas, A Generic Energy-Recovering Bisected Asymmetric Linac (GERBAL), ICFA BD-Nl 26, 2001, P. 40-45.
[2] A E. A. Antokhin et al. NIM A528 (2004) p.15.
[3] G.R. Neil et al. Phys. Rev. Lett. 84 (2000), p. 662.
[4] E.J. Minehara. NIM A483 (2002) p. 8.
[5] V.P. Bolotin et al. NIM A 557 (2006) p.23.
[6] E.A.Antokhin et al., Problems of Atomic Science and Technology, p.3, №1, 2004.
[7] A.N. Matveenko et al., Proc. of FEL2007, p. 204.
[8] N.A. Vinokurov et al., Proc. of FEL2010, p. 696.

PROGRESS OF SRF GUN DEVELOPMENT AND OPERATION AT THE ELBE ACCELERATOR

J. Teichert#, A. Arnold, P. Murcek, R. Xiang, HZDR, Dresden, Germany
P. Lu, H. Vennekate, HZDR & Technische Universität, Dresden, Germany
T. Kamps, J. Rudolph, HZB, Berlin, Germany,
P. Kneisel, TJNL, Newport News, USA,
I. Will, MBI, Berlin, Germany

Abstract

Superconducting RF photo guns are suitable candidates for electron injectors in future free-electron lasers and energy recovery linacs. For the radiation source ELBE an SRF gun was build and put into operation. During long-term tests, the operation of normal-conducting photocathodes in the superconducting cavity has been successfully demonstrated. At moderate average currents of some hundreds of μA the Cs_2Te photocathodes possess long lifetime. The acceleration gradient is the key parameters for emittance and the maximum achievable bunch charge of the gun. Therefore two new cavities with higher performance were developed, built and treated. The final tests of these cavities are ongoing. An upgraded cryomodule with an integrated superconducting solenoid was built.

ELBE SRF PHOTO GUN

The superconducting radio-frequency photoelectron gun (SRF gun) has been developed for the injection of a high-brightness, medium average current (about 1 mA), and continuous wave (CW) beam into the ELBE linac. Due to its potential advantages, consisting in the combination of high-brightness and CW operation, this electron gun type is suitable for future use in energy recovery linacs and next-generation light sources. At ELBE the SRF gun will deliver beam in two operation modes: (a) the FEL mode with 13 MHz repetition rate and up to 80 pC bunch charge, and (b) the high-charge mode with 500 kHz repetition rate and up to 1 nC bunch charge.

The superconducting cavity, the main part of the SRF gun, consists of three TESLA cells and one optimized half-cell. The gun uses normal-conducting Cs_2Te photo cathodes with high quantum efficiency, illuminated with a picosecond ultraviolet laser. The cathode is placed in the cavity half-cell isolated by a 1 mm vacuum gap and cooled with liquid nitrogen. Additionally, a resonant superconducting choke filter surrounds the cathode and serves to prevent RF leakage through the coaxial vacuum gap. Details of the SRF gun design have been published earlier [1].

At ELBE the SRF gun is installed in parallel to the thermionic injector, which is used as injector for user operation most of the time. An extra diagnostic beamline connected to the SRF gun serves for characterization of the electron beam. Furthermore a dogleg-like beamline section with two 45°-bending magnets allows for injection of the SRF gun beam into ELBE (see Fig. 1).

SRF GUN OPERATION

With the present niobium cavity, produced by the company ACCEL (now RI) and surface-treated at DESY, the SRF gun has been in operation since 2007. It turned out that the usual cleaning procedures applied for TESLA cells are hampered for the SRF gun cavity, mainly due to the narrow cathode channel and the presence of the choke filter cell. For that reason, the processing attempts were not as successful as expected. The achieved peak field in the vertical test was limited by field emission to peak field of 23 MV/m at a $Q_0 = 1\times10^{10}$. Details are published in [2]. After commissioning the Q_0 inside the cryomodule revealed an intrinsic quality factor one order of magnitude lower. The achievable peak field is again limited by strong field emission and He consumption. In the following period, various measurements, done under different conditions, have shown that the performance keeps unchanged independent of whether the cathode is inserted or not. The gradient could be improved by applying high power pulsed RF processing To this day, a stable CW operation up to peak field of 18 MV/m is routinely established.

In order to reach higher gradients with the present cavity and simultaneously keep the low load to the liquid helium system, the input RF power can be pulsed. The typical repetition rate varies from 1 Hz to 10 Hz, and the pulse length can be adjusted from 5 to 20 ms. Recently, operation with 22 MV/m peak field was performed in the RF-pulsed mode. Compared with the CW mode, the beam energy reaches higher values up to 4 MeV and the beam emittance becomes also better.

The intrinsic quality factor versus gradient has been regularly measured in the past. Fig. 2 shows the curves measured from the years 2007 until 2013. The practical limitation for the peak field value of the acceleration field in the present cavity is the Q0 decrease and the corresponding increase of the RF heat loss in the cavity surface. For higher fields the source is the strong field emission. The acceptable heat loss is about 30 W.

#j.teichert@hzdr.de

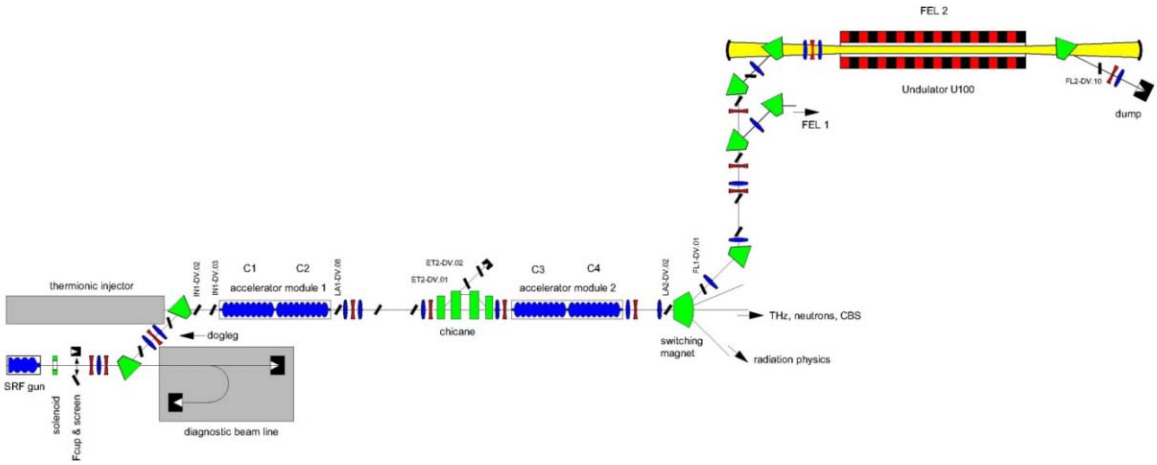

Figure 1: Layout of the ELBE linear accelerator with SRF gun and diagnostic beam line. In detail the figure shows the beam path from the SRF gun to the infrared free-electron laser FEL2: SRF gun, dogleg section, accelerator module 1, chicane section, accelerator module 2, S-shaped beamline section, FEL2. The beamlines to the other user stations are not shown in this figure.

From 2007 until 2011 the values for the peak fields were 16 M/m in CW and 21.5 MV/m for pulsed RF. (3 MeV and 4 MeV kinetic energy, respectively.) A temporary increase was obtained by high power processing (HPP) of the cavity. In autumn 2011 a number of photocathodes where exchanged within a short time for testing new designs and materials, as well as vacuum repair work was carried out at the beamline near the SRF gun. The measurement carried out afterwards (December 2011) showed a performance decrease of 12 %. But no further deterioration has been observed up to the present. Our experience is that the photocathode operation does not lower the gun cavity performance, but the cathode exchange is a critical issue.

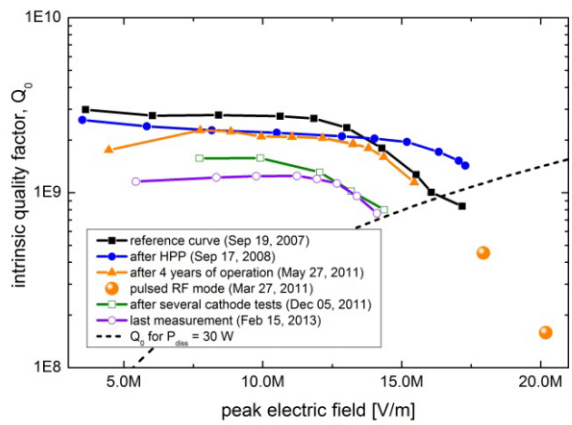

Figure 2: Summary of the SRF gun cavity performance measurements from 2007 to 2011.

Another problem for the high gradient is the dark current which increases rapidly to µA level in the macro pulse. Moreover, the dark current beam has nearly the same energy as the photocurrent. The main source of the dark current is believed to be the field emission from the rear wall of the cavity half-cell.

LASER

In 2012 a new UV driver laser for the SRF gun was delivered and commissioned. The laser had been developed by the Max-Born-Institut in Berlin and is called a two-channel laser system because it can deliver both laser pulses at 13 MHz with 3 ps FWHM and at 500 kHz (optionally 250 or 100 kHz) with 14 ps FWHM. These two channels support the two planned operation modes of the SRF gun. Both channels produce temporally Gaussian shaped pulses, and the average power at 258 nm is about 1 W. The laser consists of a Nd:glass oscillator at 52 MHz, a pulse picker generating the 13 MHz with an electro-optical modulator, a fiber-laser preamplifier for the 13-MHz-channel, a regenerative preamplifier for the 500-kHz-channel, a multipass final amplifier for both channels, and a frequency conversion stage with lithium triborate (LBO) and beta-barium borate (BBO) crystals.

PHOTOCATHODES

Because of its good quantum efficiency (QE) and robustness in RF fields Cs_2Te has been chosen as the standard photocathode for the SRF gun. From 2007 on, eleven Cs_2Te photocathodes have served for the SRF gun beam production. The photocathodes are prepared in a separate photocathode lab and then transported to the gun. The QE of the fresh photocathodes is between 8-15%. The cathodes are stored and transported in the chamber with vacuum in the order of 1×10-9 mbar. But the cathode QEs drop down quickly to 1-2% because of the material degradation and also the vacuum variation during transportation. Once the cathode is installed in the gun cavity, no obvious QE degradation has been found during the beam production. For example, cathode #170412Mo worked in SRF gun for more than one year, providing totally beam time of over 600 hours and 265 C charge.

Operating the SRF gun in CW with 13 MHz repetition rate, the typical electron current was 0.3 mA and maximum average current achieved was 0.5 mA up to now.

ELBE INJECTION

Beam Characterization

In the past years the electron beam injected into ELBE was mainly used to perform beam characterization studies. The combination of the first acceleration module in ELBE and the Browne Buechner (BB) spectrometer allow for measurements of the longitudinal phase space [3] and of the bunch slice emittance [4].

The method for determination of the longitudinal beam parameters is the measurement of the energy spread after the first accelerator module as a function of the cavity phase. The electrons from the gun are guided through the achromatic dogleg into the first accelerator module. Then the RF phase of one cavity is varied and energy and energy spread are measured. The rms bunch length is presented in Fig. 3. The bunch length is between 3 and 4 ps, shorter than the rms laser pulse length of 6.2 ps. The minimum bunch length appears at the gun laser phase of 5°-10°. The results are closer to the ASTRA simulation results than the measurement with Cherenkov radiation and a streak camera performed in former times.

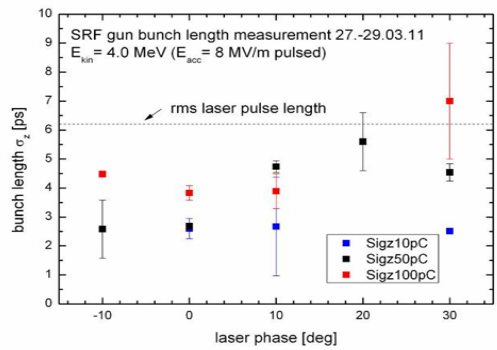

Figure 3: Results of bunch length measurements.

The method delivers the longitudinal phase space ellipse, as it is shown in Fig. 4. In this measurement the phase of cavity C2 was varied and therefore the picture shows the phase space after cavity C1. The phase space correlation is positive, i.e. the bunch head has higher energy. The energy width as well as the longitudinal emittance increase with laser phase.

For the slice emittance measurement the zero-phasing technique is applied which in a similar way converts the longitudinal distribution into a transverse distribution. The phase of cavity C2 is set to a value far from crest to produce a suitable energy chirp. Thus the horizontal position on the screen after the BB spectrometer characterizes the position in the bunch and a split in slices is possible. For these slices a quad-scan is carried out to obtain the vertical transverse emittances of the bunch slices using one of the quadrupoles between cavity C2 and BB spectrometer.

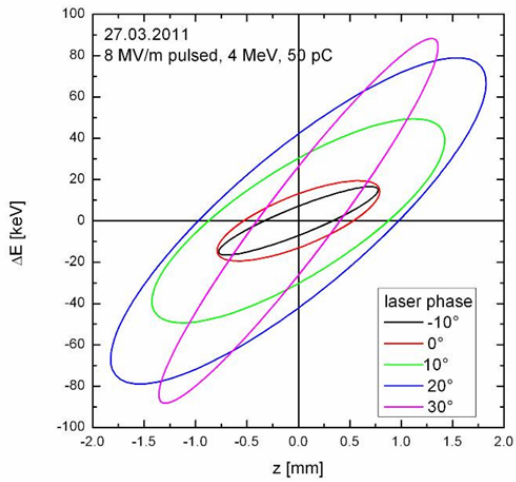

Figure 4: Longitudinal phase space measurement results for different laser phases.

In the measurement the bunch has been split into five slices. The transverse phase space ellipses measured for the five slices are shown in Fig. 5. For this measurement the beam of the gun had a kinetic energy of 3 MeV, bunch charge was 10 pC and the laser phase was 0°. The corresponding normalized emittances and the intensity distribution along the bunch are shown in Fig. 6. The slice emittance is an important quantity for characterization and optimization of the emittance compensation in RF photo guns. The present results confirm that the zero-phasing technique is applicable for further studies on this topic.

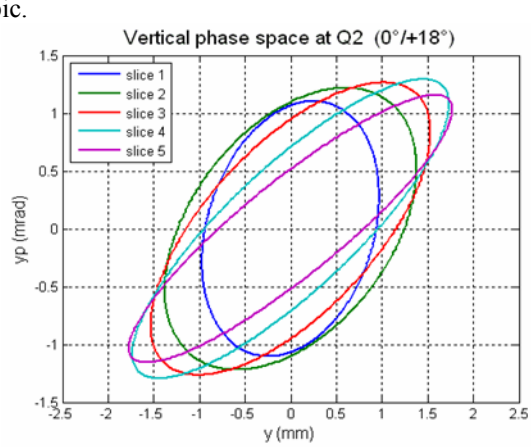

Figure 5: Measured transverse phase space ellipses of the five bunch slices.

Recently, another sophisticated beam diagnostics was tested. This method is described in Ref. [5] and allows a direct measurement of the longitudinal electron bunch profile. In principle, the longitudinal phase space is rotated by 90° so that the momentum distribution, measured finally with a spectrometer, delivers a one-to-one image of the initial longitudinal of the electron bunch.

The method uses a magnetic chicane and following zero-phasing RF acceleration. At ELBE both components, chicane and accelerator module 2, are available and the following dipole was used as spectrometer (see Fig. 1).

One result is presented in Fig. 7 which shows in the lower part the temporal bunch distribution with an rms bunch length of 1.6 ps.

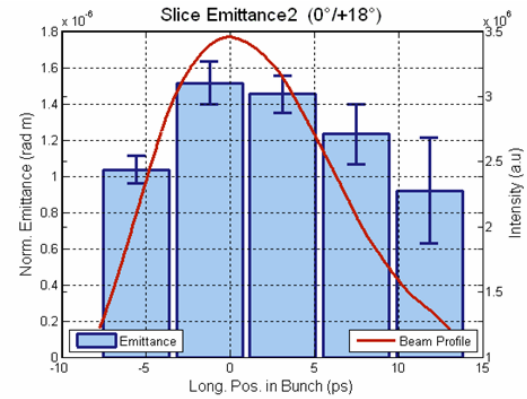

Figure 6: Measured normalized slice emittance values and bunch charge distribution.

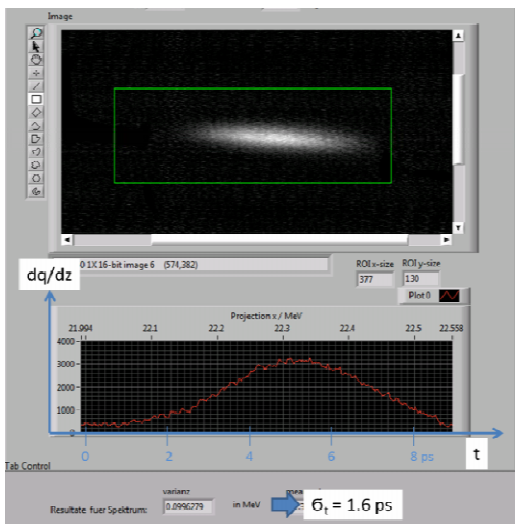

Figure 7: Bunch profile measurement with the method proposed by Crosson [5] for 13 MHz and 2 µA beam. The initial longitudinal laser distribution is a Gaussian with 2 ps rms.

Compton Backscattering

A first sophisticated experiment towards user application of the SRF gun was carried out in collaboration with the high-power laser group at HZDR in fall 2011. The electron beam was transported through the dogleg, accelerated in the two ELBE modules to 24 MeV and then guided to an interaction chamber with a permanent magnet quadrupole triplet to form the final focus. The pulse repetition rate was reduced to 10 Hz in order to adopt it to the DRACO laser. In a head-on collision with the 150 TW laser pulse, Compton-backscattered x-rays of 13 keV were produced and detected with an x-ray camera. The experiment confirmed the synchronization and electron beam stability of the SRF gun. Troublesome for the background and the beam alignment was the dark current from the SRF gun.

Far-infrared FEL

With the new UV laser system the SRF gun is able to produce beam with 13 MHz pulse repetition rate. That allows driving the free-electron lasers of ELBE with the SRF gun. A first successful attempt was carried out in spring 2013 using the far-infrared FEL 2. The beamline layout is shown in Fig. 1. For this first lasing the SRF gun was operated in pulsed mode. The acceleration gradient was 6.6 MV/m which corresponds to a peak field of 18 MV/m and yields 3.3 MeV kinetic energy. The beam current was 260 µA (20 pC bunch charge) within the macro pulse. After passing the dogleg section, the electrons were accelerated to 16 MeV in the first ELBE module (cavities C1 and C2) and up to the final energy of 27.9 MeV in the second ELBE module (cavities C3 and C4). A loss-free and achromatic beam transport in the dogleg section was essential for the success. After achieving that, the phases of the linac cavities were matched and the final energy adjusted. Finally, the steering and focusing in the S-bend and undulator section were carried out.

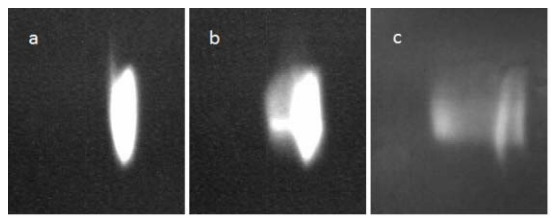

Figure 8: Screenshots with the electron beam in the dispersive section behind the FEL: (a) before lasing, (b) first lasing, (c) lasing with optimized beam transport in the undulator.

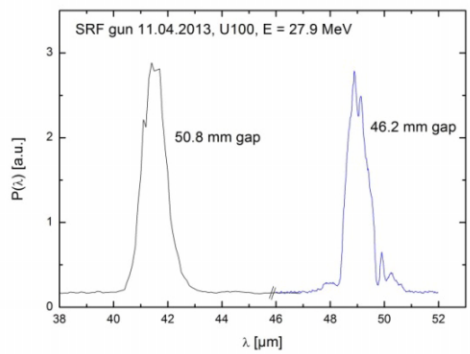

Figure 9: First measured FEL infrared spectra for undulator gaps of 50.8 and 46.2 mm.

An indicator for successful lasing is the increased energy spread behind the FEL which has been observed on an OTR screen behind the dipole (see Fig. 1). The images are presented in Fig. 8. The infrared radiation produced by the FEL was guided into a diagnostic room. As a measurement example, the spectra of the radiation for two undulator gaps are shown in Fig. 9.

The operation of a FEL requires a comparably high level of beam quality with respect to all kinds of stabilities like beam energy, bunch charge, transverse position, phase jitter etc. Thus, successful lasing with the SRF gun represents an important milestone and confirms the design concept for this gun and the applicability in accelerator facilities.

FUTURE PLANS

To overcome the low-gradient problem with the existing SRF gun at ELBE, in a collaboration with JLab two new 1.3-GHz, 3.5-cell photo-injector cavities (one made of polycrystalline niobium, and one of large grain niobium) were fabricated. The design of the new cavities is slightly different in order to make the half-cell more rigid and simplify assembly in the clean-room. After time-consuming surface treatment and cleaning, for the small-grain cavity a very good performance has been obtained. After welding the cavity into the He tank, a peak field of 43 MV/m and a Q_0 of 2×10^{10} were obtained. Fig. 10 shows a photograph of the cavity prepared for the vertical test at Jlab.

Figure 10: Photograph of the small-grain SRF gun cavity within the He tank at Jlab.

The cavity will be installed in a new cryomodule with an upgraded design. The main difference to the existing one is the integration of a superconducting solenoid. The solenoid was designed and built by Niowave Inc. and has a similar design as the NPS SRF gun solenoid [6]. In our cryomodule the solenoid is positioned on a remote-controlled x-y table. A design drawing is shown in Fig. 8. The x-y table allows beam based alignment of the horizontal and vertical solenoid position with respect to the cavity´s electrical axis. The solenoid is directly cooled with liquid He via tubes connected to the He vessel of the cavity. The two step-motors are cooled with liquid nitrogen in order to hold the heat input into the He bath low.

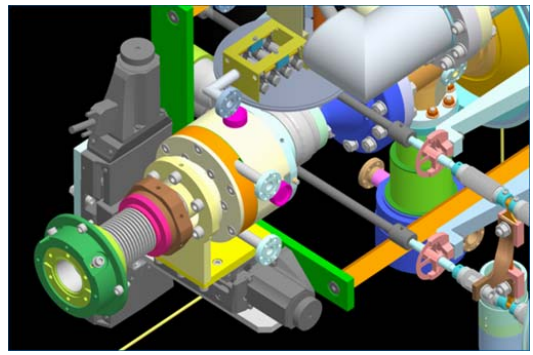

Figure 11: Design of the SC solenoid with x-y table in the new SRF gun cryomodule.

SUMMARY

Here, we have reported the operational status of the 3½-cell SRF gun at the ELBE accelerator of HZDR. Although the design value of the acceleration gradient could not be achieved, the gun is in operation as a unique test bench. Furthermore, the electron beam has been injected into the ELBE accelerator for beam parameter measurements and in order to check future user operation.

The low Q-value of the present gun cavity limits the beam quality. In cooperation with JLab two new cavities have been fabricated and tested. One of them, made of polycrystalline niobium, has shown a very promising performance in the vertical test bench. This cavity will be installed in a new improved cryomodule with a SC solenoid and will replace the present SRF gun at ELBE.

ACKNOWLEDGEMENT

We would like to thank the whole ELBE team for their help and assistance. The work is supported by the European Community under the FP7 programme (EuCARD-2, contract number 312453, and LA3NET, contract number 289191), and by the German Federal Ministry of Education and Research grant 05K12CR1.

REFERENCES

[1] A. Arnold, et al., Nucl. Instr. and Meth. A577 (2007) 440.

[2] A. Arnold, et al., “First RF-Measurements at the 3.5-Cell SRF-Photo-Gun Cavity in Rossendorf”, FEL 2006, Berlin, Germany, p. 567.

[3] J. Teichert, et al., “Pulsed Mode Operation and longitudinal Parameter measurement of the Rossendorf SRF Gun”, IPAC 2011, San Sebastian, Spain, p. 262.

[4] J. Rudolph, M. Abo-Bakr, T. Kamps, J. Teichert, “Slice-Emittance Measurements at ELBE/SRF-Injector”, DIPAC 2011, Hamburg, Germany, p. 416.

[5] K.N. Ricci, E.R. Crosson, and T.I. Smith, Nucl. Instr. Meth. A 445 (2000) 333.

[6] J. R. Harris, et al., Phys. Rev. Spec. Top. AB 14 (2011) 053501.

CONSTRUCTION AND COMMISSIONING OF COMPACT-ERL INJECTOR AT KEK

S. Sakanaka, M. Adachi, S. Adachi, M. Akemoto, D. Arakawa, S. Asaoka, K. Enami, K. Endo, S. Fukuda, T. Furuya, K. Haga, K. Hara, K. Harada, T. Honda, Y. Honda, H. Honma, T. Honma, K. Hosoyama, K. Hozumi, A. Ishii, E. Kako, Y. Kamiya, H. Katagiri, H. Kawata, Y. Kobayashi, Y. Kojima, Y. Kondo, O. A. Konstantinova, T. Kume, T. Matsumoto, H. Matsumura, H. Matsushita, S. Michizono, T. Miura, T. Miyajima, H. Miyauchi, S. Nagahashi, H. Nakai, H. Nakajima, N. Nakamura, K. Nakanishi, K. Nakao, K. Nigorikawa, T. Nogami, S. Noguchi, S. Nozawa, T. Obina, T. Ozaki, F. Qiu, H. Sagehashi, H. Sakai, S. Sasaki, K. Satoh, M. Satoh, Y. Seimiya, T. Shidara, M. Shimada, K. Shinoe, T. Shioya, T. Shishido, M. Tadano, T. Tahara, T. Takahashi, R. Takai, T. Takenaka, Y. Tanimoto, M. Tobiyama, K. Tsuchiya, T. Uchiyama, A. Ueda, K. Umemori, K. Watanabe, M. Yamamoto, Y. Yamamoto, Y. Yano, M. Yoshida,
High Energy Accelerator Research Organization (KEK), Tsukuba, Ibaraki 305-0801, Japan
E.Cenni, the Graduate University of Advanced Studies (Sokendai), Tsukuba, Ibaraki 305-0801, Japan
R. Hajima, S. Matsuba, R. Nagai, N. Nishimori, M. Sawamura, T. Shizuma,
Japan Atomic Energy Agency (JAEA), Tokai, Naka, Ibaraki 319-1195, Japan
H. Takaki, Institute for Solid State Physics, University of Tokyo, Kashiwa, Chiba 277-8581, Japan
M. Kuriki, H. Iijima, Hiroshima University, Higashihiroshima, Hiroshima 739-8530, Japan
J.-G. Hwang, Kyungpook National University, Daehakro, Bukgu, Daegu 702-701, Korea

Abstract

The Compact Energy-Recovery Linac (cERL) is under construction at KEK in order to demonstrate the technologies that are needed for the future 3-GeV ERL project. In April 2013, the 5-MeV injector of the cERL was completed and commissioned. During April to June in 2013, we tuned up the injector and evaluated its beam performance. From July to November in 2013, we are constructing the entire cERL including its return loop.

INTRODUCTION

In KEK, we aim to construct a 3-GeV energy recovery linac (ERL) [1,2] that will be used as a super-brilliant and ultra-short-pulse synchrotron light source as well as a driver for an X-ray free-electron-laser oscillator (XFEL-O). This project was recently named the PEARL (Photon Factory Advanced Research Laboratory). To demonstrate the production, acceleration, and recirculation of low-emittance and high-current beams that are need to the 3-GeV ERL, we are constructing the Compact ERL at KEK.

A planned layout of the cERL is shown in Fig. 1. The cERL consists of a 5-MeV injector, a main linac, and a return loop. Low-emittance electron beams are produced in a 500-kV photocathode DC gun, and they are boosted to a beam energy of about 5 MeV in a superconducting (SC) injector cryomodule. The beams are merged to the superconducting main linac where the beams are accelerated to a kinetic energy of 35 MeV, and they are transported through the return loop. The beams are then decelerated through the main linac, and are dumped. The beams from the injector can also be transported to an injector dump through an injector-diagnostic beamline. This allows us to evaluate the various beam properties of the injector. Design parameters of the cERL are given in Table 1.

The cERL injector was completed in April 2013. From 22 April to 28 June in 2013, we commissioned the injector and measured beam properties such as the beam emittance, the bunch length, the momentum spread, and the momentum jitter. During July to November in 2013, we are constructing the return loop [3].

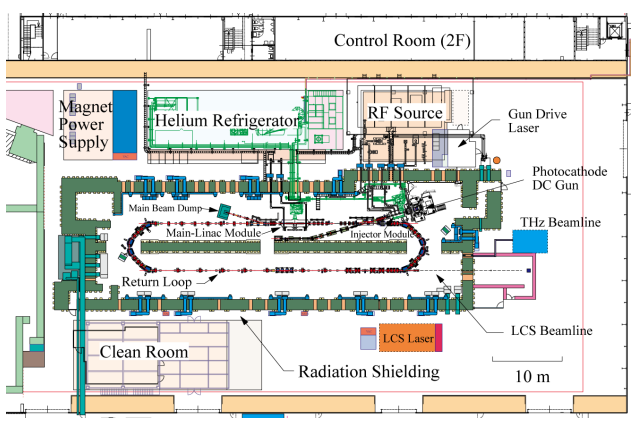

Figure 1: Planned layout of the cERL.

Table 1: Design Parameters of the cERL

Beam kinetic energy (injector) (return loop)	5 MeV 35 MeV
Beam current (initial goal) (future goal)	10 mA 100 mA
Normalized beam emittance	< 1 mm·mrad
Repetition frequency of bunches	1.3 GHz (CW)

CONSTRUCTION OF THE INJECTOR

From March to September in 2012, we constructed a radiation-shielding room which consists of reinforced concrete blocks in the ERL development building of KEK. The shielding room covers an area of about 60 m × 20 m. The thicknesses of side walls and a roof are 1.5 m and 1 m, respectively. After its construction, we installed air conditioners, a ventilator, electric lights, and a drainer system for the cERL.

The first 500-kV photocathode DC gun [4,5] was developed at JAEA. In October 2012, we successfully demonstrated [4] the beam production at high voltages up to 500 kV at JAEA. Then, the gun was disassembled and was transported to KEK. From October 2012 to March 2013, we reassembled the gun, and carried out high-voltage tests on the gun assembly. During the test, we found a slight problem in two of the ten pieces of ceramic insulators of the gun. For this reason, we chose a modest voltage of 390 kV as an applied voltage to the cathode during the injector commissioning. Figure 2 shows an injector section of the cERL including the 500-kV photocathode DC gun.

Figure 2: The injector of the cERL at KEK. The 500 kV photocathode DC electron gun and a superconducting cryomodule for the injector are shown.

Following the first gun, the second 500-kV photocathode DC gun is under development at KEK [6]. In this gun, several measures to achieve extremely-high vacuum have been employed. At present (September 2013), we could apply high voltage of 500 kV to the gun assembly.

To excite the photocathode (Gallium Arsenide) of the gun, a drive laser system [7] was developed. The laser system consists of a 1.3-GHz Nd:YVO_4 oscillator, both pre- and main-amplifiers using Yb photonic-crystal fibers (at a wavelength of 1064 nm), a second-harmonic generator (wavelength: 532 nm), a gating system, and a pulse shaping system.

A cryomodule for the injector, which houses three two-cell cavities, was assembled from April to June 2012. The injector module was installed in the cERL in June 2012, as shown in Fig. 2. We carried out cool-down test, low-power measurements, and high-power test during September 2012 to April 2013. During the high-power test [8], we could operate the injector cavities up to an accelerating gradient of 15 MV/m in pulsed operations (duty factor of 10%). We could also demonstrate stable operations of the injector cavities at an accelerating gradient of 8 MV/m in CW operation. We found that heating up of HOM couplers limited the maximum gradient in CW operations. Although an advanced design [9] was employed for these HOM couplers which are suitable for CW operations, the cooling of the HOM couplers was still insufficient because these HOM couplers were placed out of the helium jackets. In a future design, we will reinforce the cooling of the HOM couplers.

In a short (1.12 m) section between the gun and the injector module, we installed a laser-input chamber, a 1.3-GHz buncher cavity, and a screen chamber. To keep the lifetime of the photocathode, extremely-high vacuum is required in this section. We pre-assembled this section in a clean room, and installed it in a local clean hut. After the bake out, we achieved ultrahigh vacuum of about 2×10^{-9} Pa in the laser input chamber.

In order to evaluate the beam properties from the injector, we constructed an injector diagnostic beamline [10], as shown in Fig. 3.

Figure 3: The injector diagnostic beamline.

An rf system [11] for the injector consists of rf sources, a digital low-level rf system, and an rf distribution system. For the rf sources of the injector, we employed a 20-kW IOT, a 25-kW klystron, and a 300-kW klystron, to drive the buncher cavity and three SC cavities of the injector. Using the digital low-level system, we could precisely stabilize the amplitudes and the phases of cavity voltages. We have so far achieved amplitude and phase stabilities within 0.1% (rms) and 0.1 degrees (rms), respectively.

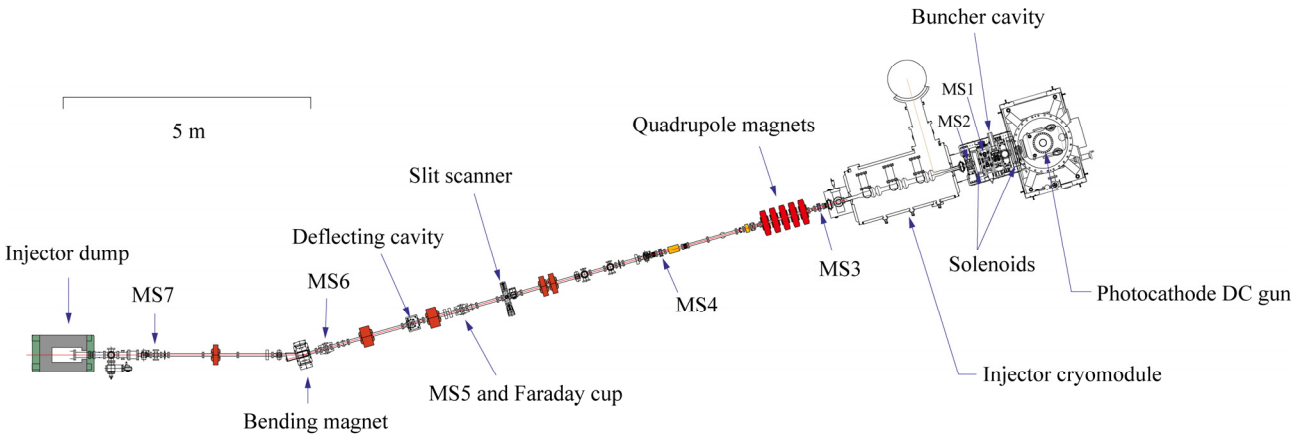

Figure 4: Plane layout of the cERL injector and its diagnostic beamline. The symbols "MS" indicate screen monitors.

A cryogenic system for the cERL consists of a TCF200 liquid-helium refrigerator, a 3000-liter Dewar, two 2K cold boxes, and a pumping system. The system has a cooling capacity of about 600 W at a temperature of 4.5 K, and that of about 80 W at 2 K using eight sets of evacuating pumps for helium gases.

Each component of the cERL is controlled through the Experimental Physics and Industrial Control System (EPICS). For safety management, we also constructed a personnel protection system (PPS) and a machine mode system (MMS).

A cryomodule for the main linac, which houses two 9-cell cavities, was assembled from August to October 2012, and it was installed in the cERL. We cooled it down to 2 K in November 2012, and carried out cryogenic test, low-power test, and high-power test in December 2012. In the cool down test, we confirmed that the components such as input couplers, frequency tuners, and HOM absorbers, worked well as expected. In the high-power test, we achieved accelerating voltages of 16 MV (accelerating gradient of 15.4 MV/m) in both cavities [12]. Unfortunately, field emissions started at an accelerating voltage of about 8 MV in both cavities. We are preparing to use this cryomodule to the main linac of the cERL. In future, we will continue R&D effort on the module assembly technique to reduce the field emissions.

COMMISSIONING OF THE INJECTOR

Setup of Injector Beamline

Figure 4 shows a plane layout of the injector beamline which was used for the commissioning during April to June, 2013. Electron beams were produced at the photocathode DC gun with a cathode voltage of 390 kV. The beams passed through the buncher cavity which produced energy chirp needed to compress the electron bunches. The beams were transported to the injector cavities while being focused by two solenoid magnets. The beams were then accelerated by the three injector cavities up to kinetic energies of about 5-6 MeV. The beams were then transported to the injector dump through the diagnostic beamline.

The positions and profiles of the beams were observed using seven screen monitors (indicated by MS1 to MS7 in Fig. 4). We employed Ce:YAG scintillator having a thickness of 0.1 mm for these screen monitors. The screens were placed at an angle of 45 degrees to the beam direction while the scintillation lights were observed at a right angle to the beam. To measure the beam emittances [10], we installed a slit scanner, having both horizontal and vertical slits, in the diagnostic beamline. We also installed a 2.6-GHz transverse deflecting cavity for bunch-length measurement [10]. The beam current was monitored using a faraday cup at the location of the screen monitor "MS5" as well as using the injector dump as a faraday cup. The beam current was also measured at a power supply of the DC gun by subtracting offset currents due to divide resistors of the insulators.

Initial Commissioning

To observe the beams using screen monitors at low average currents, we produced macropulse beams from the gun by gating the drive-laser pulses. Typical parameters of the macropulse operation are given in Table 2. Under the macropulse operations of the beams, the gun high-voltage and the injector cavities were operated in DC or CW modes.

On 22 April in 2013, we started commissioning of the injector. First, we adjusted the position of the laser spot to the center of the cathode, and positioned the beams to the centers of two solenoids. Then, we adjusted the phase of each injector cavity to that of on-crest acceleration; the buncher cavity was tentatively turned off. While adjusting the phases, the beam momentum was monitored by using a steering magnet and a screen monitor. In the first five days, we could accelerate the beams up to the kinetic energy of about 5.6 MeV, and could transport the beams to the injector dump. Typical machine parameters during the initial commissioning are shown in Table 3 (see columns labeled by "At low charges").

By elongating the length of macropulses to 1.6 ms, we demonstrated the (temporary) maximum average beam current of 300 nA at a beam energy of 5.6 MeV. We confirmed that the radiation levels were background ones at the outside the shielding room at the maximum current.

After the initial commissioning, we adjusted the parameters of the injector step by step. At the same time, we measured the beam properties such as the beam emittances at very-low bunch charges of 10-20 fC/bunch. Then, we increased the bunch charges up to 7.7 pC/bunch, and measured the beam properties at these charges.

Table 2: Typical parameters of the beam pulses during the commissioning

Parameter	Value
Repetition frequency of bunches	1.3 GHz
Charge/bunch	0.01 - 7.7 pC
Temporal length of macropulses	1 μs (typically)
Repetition frequency of macropulses	5 Hz (typically)
Rise/fall times of macropulses	10 ns
Number of bunches/macropulse	1300
Average beam current	65 pA - 50 nA

Table 3: Typical parameters of the cERL injector during the commissioning operations

Parameter	At low charges	At modest charge
Charge/bunch	~ 10 fC	7.7 pC
Gun DC voltage	390 kV	390 kV
Laser spot diameter	1.2 mm	1.2 mm
Laser pulse length	3.3 ps rms (Gaussian)	15.7 ps FWHM (semi-flat)
Magnetic fields of solenoids No. 1, 2	(0.0248, 0.0103) T	(0.0286, 0.0172) T
Voltage and phase of buncher cavity	0 kV or (40 kV, -90 deg.)	(50 kV, -90 deg.)
E_{acc} of three injector cavities	(6.2, 6.7, 6.2) MV/m	(6.2, 6.7, 6.2) MV/m
Phases of injector cavities	0 degree (on crest)	0 degree (on crest)
Beam kinetic energy	5.6 MeV (typ.)	5.6 MeV (typ.)

Emittance of Beams from the Gun

We measured the emittances of 390-keV beams from the gun at low bunch charges of 10-20 fC/bunch under the macropulse operation (shown in Table 2). A setup for the measurement is shown in Fig. 5. While changing the fields of solenoids, we measured the beam sizes using screen monitors. An example of the wait scan is shown in Fig. 6, where the solenoid "SL2" shown in Fig. 5 was scanned while the beam sizes were measured using the screen monitor "MS3" in Fig. 4; the injector cavities were turned off and detuned. From three sets of such measurements, we estimated the normalized beam emittance of $\varepsilon_n \approx 0.070$ mm·mrad at the exit of the gun.

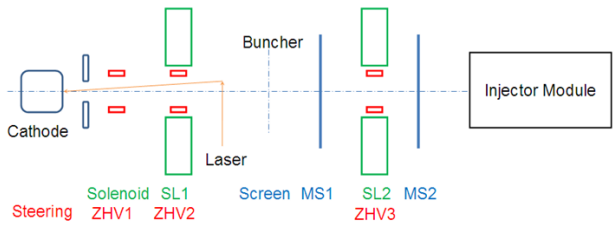

Figure 5: Setup of the emittance measurement of the beam from the photocathode DC gun.

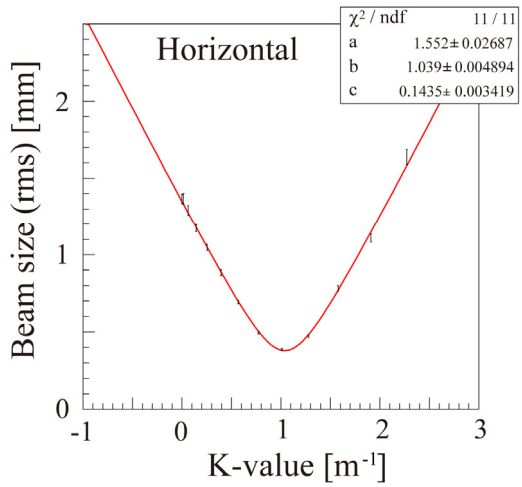

Figure 6: An example of the waist scan. Measured horizontal beam sizes at "MS3" are shown as a function of the focusing strength of the solenoid "SL2".

Emittance of Accelerated Beams at Low Charges

We measured the emittances of accelerated beams using a slit-scan method under the macropulse operation. The method of the measurement is schematically shown in Fig. 7. We scanned the position of a beam slit having a width of 100 μm; the slit was cut in a tungsten plate having a thickness of 1 mm. At each position of the slit, we measured the beam profile with a screen monitor. From these data, we deduced a distribution of particles in phase space. Both horizontal and vertical slits were installed in the silt scanner, and these slits were apart from the screen monitor "MS6", where the beam profile was measured, by 3.79 m and 3.94 m, respectively.

An example of the emittance measurement is shown in Fig. 8. In this example, the bunch charge was approximately 20 fC; a short (3 ps rms) laser pulse was used; the buncher cavity was turned off. The kinetic energy of the beam was approximately 5.6 MeV. From the measurement, we estimated the normalized emittance to be $\varepsilon_n \approx 0.17$ mm·mrad (at 20 fC/bunch). At a higher charge of 0.77 pC/bunch, we obtained a normalized emittance of $\varepsilon_n \approx 0.3$ mm·mrad.

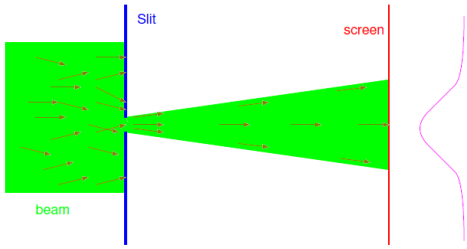

Figure 7: Schematic drawing of the slit-scan method.

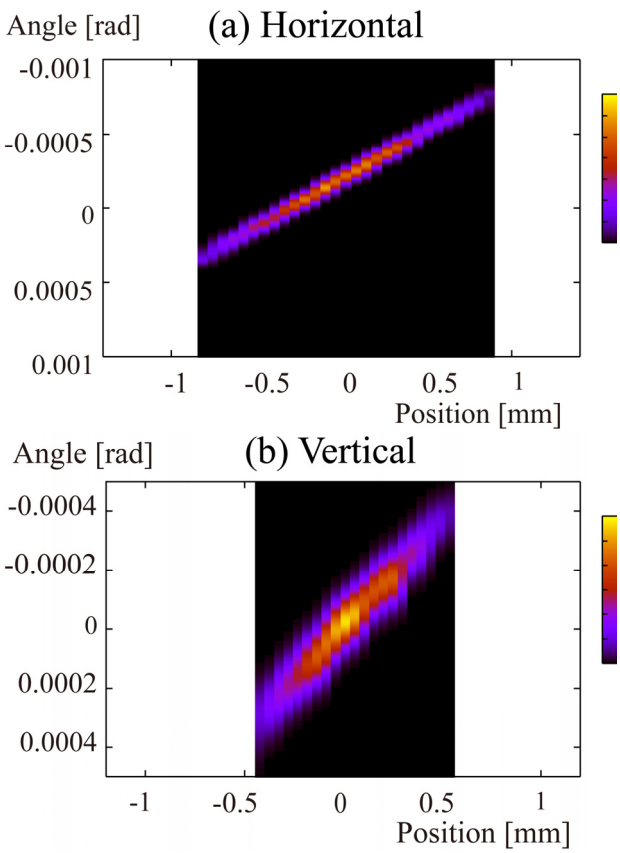

Figure 8: Example of the emittance measurement at a bunch charge of about 20 fC. The figures (a) and (b) indicate the measured distributions of particles in the horizontal and the vertical phase spaces, respectively.

Beam Emittance at Higher Charges

At higher bunch charges, we needed to optimize the machine parameters so that the space charge effects could be compensated. We expect that the space charge effect in the low-energy section can be mitigated by using longer laser pulses. For this reason, we prepared two laser pulses: (1) Gaussian shape having an rms length of 3 ps, and (2) semi-flat shape having an FWHM length of approximately 15.7 ps. Typical rf voltages (for particle of v/c=1) of the buncher cavity were set to 40-50 kV in both cases. Typical parameters of operation at a bunch charge of 7.7 pC are given in Table 3.

At higher charges, we observed that the beam profiles were not axially symmetric after the acceleration, as shown in Fig. 9. We measured the beam emittances using the slit-scan method at bunch charges of up to 7.7 pC. The measurements were carried out using both short and long laser pulses. The results of the emittance measurements are shown in Fig. 10. Typical normalized emittances at 7.7 pC/bunch were 0.90 mm·mrad in horizontal, and 0.49 mm·mrad in vertical, respectively, after the acceleration (~ 5.6 MeV) using the long (15.7 ps) laser pulse. Note that due to limited time, the above measurements were carried out before sufficient optimization of the injector. Contrary to our expectation, the beam emittance did not improve much by elongating the laser pulses under the present parameters.

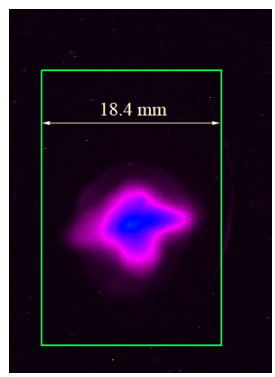

Figure 9: An example of the beam profile at a bunch charge of 7.7 pC, which was observed at a screen monitor "MS6" (after acceleration to about 5.6 MeV).

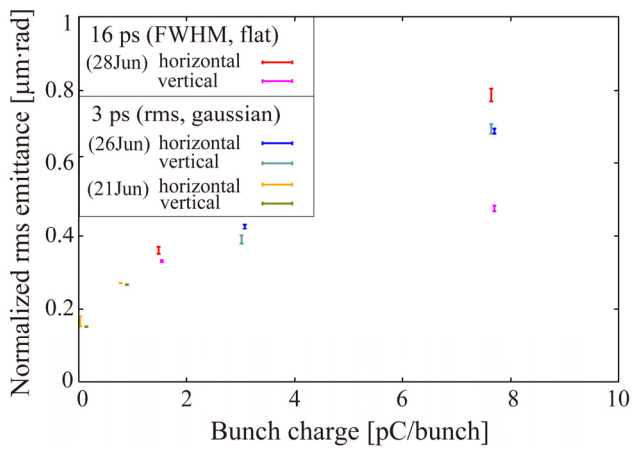

Figure 10: Measured beam emittances (at the kinetic energy of about 5.6 MeV) as a function of the bunch charge. Results with the short (3 ps rms) and the long (16 ps semi-flat) laser pulses are shown.

Bunch Length and Momentum Spread

To measure the bunch length, we applied transverse (vertical) kicks to the bunches using the 2.6-GHz deflecting cavity (in Fig. 4). The longitudinal distribution of particles was then projected to the vertical plane at a downstream screen monitor "MS6". To improve the resolution of the measurement, we adjusted the beam optics between the deflecting cavity and the screen monitor so that small beam sizes were obtained at the

monitor while the deflections due to rf kicks became large. We estimated typical time resolution of the measurement to be 0.7 ps.

Figure 11 shows the measured bunch lengths as a function of the bunch charge; the measurements were carried out using both short and long laser pulses. The bunch length elongated as the bunch charge. Note that the optimization of the machine parameters was insufficient at high charges. At present, we did not understand the reason why the bunch length did not change much by changing the laser pulse lengths.

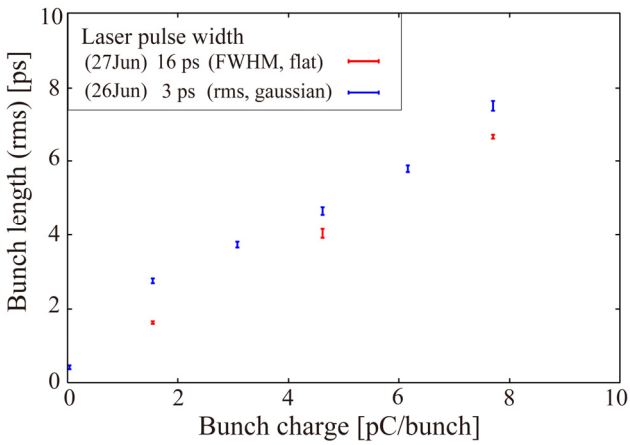

Figure 11: Measured bunch lengths as a function of the bunch charge. Results with the short (3 ps rms) and the long (16 ps semi-flat) laser pulses are shown.

The momentum spread of the accelerated beams was measured using a screen monitor "MS7" where the dispersion function was approximately 0.825 m. Figure 12 shows the measured momentum spreads as a function of the bunch charge. The momentum spread increased as the bunch charge. At a bunch charge of 7.7 pC, we obtained a typical rms momentum spread of 1.5×10^{-3}.

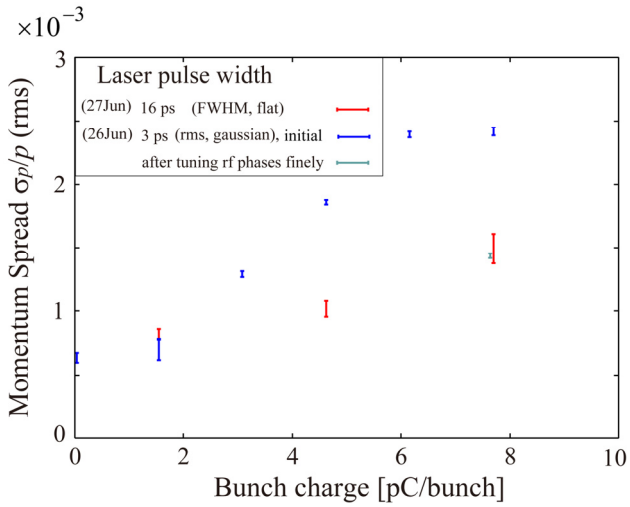

Figure 12: Measured momentum spreads as a function of the bunch charge. Results with the short (3 ps rms) and the long (16 ps semi-flat) laser pulses are shown.

CONCLUSION

The 5-MeV injector of the cERL was completed and commissioned. We measured beam properties such as the beam emittance, the bunch length, and the momentum spread, at bunch charges of up to 7.7 pC. At very low charges of 10-20 fC/bunch, we obtained a typical normalized emittance of 0.07 mm·mrad at the exit of the gun (voltage: 390 kV), and that of 0.17 mm·mrad after acceleration to about 5.6 MeV. We are on the way to optimize the parameters at higher charges, and at present, we have obtained typical normalized emittances of 0.49 - 0.90 mm·mrad at 7.7 pC/bunch.

During April to June 2013, we carried out the beam operation of the injector for about 202 hours. During this period, we demonstrated stable operations of the injector including the photocathode DC gun (at a cathode voltage of 390 kV) and the injector SC cavities (at an accelerating gradient of approximately 7 MV/m). From July 2013, we are constructing the return loop of the cERL. From these R&D results, we are approaching to obtain the technology needed to construct the PEARL project.

ACKNOWLEDGMENT

We would like to thank the people of the Cornell University, Argonne National Laboratory, Jefferson Lab., TRIUMF, HZDR, HZB, ASTeC, and the other institutes, for useful discussions and/or collaboration.

REFERENCES

[1] KEK Roadmap, May 23, 2013 http://www.kek.jp/ja/About/OrganizationOverview/Assessment/Roadmap/roadmap2013-E.pdf
[2] "Energy Recovery Linac Conceptual Design Report", KEK Report 2012-4, KEK, October, 2013 http://ccdb5fs.kek.jp/tiff/2012/1224/1224004.pdf
[3] M. Shimada, talk at the ERL-2013, WG205.
[4] N. Nishimori, R. Nagai, S. Matsuba, R. Hajima, M. Yamamoto, T. Miyajima, Y. Honda, H. Iijima, M. Kuriki, M. Kuwahara, "Generation of a 500-keV electron beam from a high voltage photoemission gun," Appl. Phys. Lett. 102 (2013) 234103.
[5] N. Nishimori, talk at the ERL-2013, WG109.
[6] M. Yamamoto et al., in these proceedings, WG108.
[7] Y. Honda et al., "Photo Cathode Laser System for Compact-ERL Injector," to be published in the Proceedings of the 10th Meeting of Particle Accelerator Society of Japan, August 2013 [in Japanese].
[8] E. Kako et al., "High Power Tests of Injector Cryomodule for Compact-ERL," IPAC2013, Shanghai, May 2013, WEPWO013, p. 2340.
[9] K. Watanabe, S. Noguchi, E. Kako, K. Umemori, T. Shishido, "Development of the superconducting rf 2-cell cavity for cERL injector at KEK," Nucl. Instrum. Methods Phys. Res. A 714 (2013) 67.
[10] Y. Honda, "Beam Performance Measurement at Compact-ERL Injector", poster presentation at ERL-2013, PS03.
[11] T. Miura et al., in these proceedings, WG306.
[12] K. Umemori et al., "Construction of Main Linac Cryomodule for Compact ERL Project," IPAC2013, Shanghai, May 2013, WEPWO016, p. 2349.

STUDIES OF NEA-PHOTOCATHODES

V.V. Bakin, D.V. Gorshkov, H.E. Scheibler, S.N. Kosolobov and A.S. Terekhov,
ISP SB RAS, Novosibirsk, Russia

Abstract

Domains of validity for dipole layer and heterojunction models of the (Cs,O) – activation layer for GaAs – photocathode are determined. Two – step photoelectron escape model from NEA-photocathode is proved. Dominated elastic and inelastic scattering processes, which are accompanied the photoelectron escape, are revealed.

INTRODUCTION

In the present work we studied (Cs,O) - activation procedure of p-GaAs/(Cs,O) – photocathode and identified domains of validity for the actual models for p-GaAs/(Cs,O)/vacuum interfaces with Negative Electron Affinity (NEA). To develop photoelectron escape model and to reveal dominated mechanisms of their scattering, we discuss energy distributions of photoelectrons which were measured previously at low temperatures.

EXPERIMENTEL DETAILS

Most of experiments were performed with transmission-mode p-GaAs/(Cs,O) and p-GaN/(Cs,O) photocathodes. Details of surface cleaning and activation procedures were described in [1,2]. To measure NEA – value (χ^*), the retarding field electron energy analyzer was installed within photocathode preparation chamber (PPC). Measurements of $N_e(\varepsilon_{lon})$ were performed during interruption of photocathode activation, when it was transferred to the measuring position below the mesh by rotation of carousel. Measurements of electron distributions $N_e(\varepsilon_{lon})$ and $N_e(\varepsilon,\theta)$ at low temperatures were performed by using of self - made parallel plate photodiodes with homogeneous electric field. Parallel plate image intensifier with microchannel plate (MCP) was used for measurements of $N_e(\varepsilon_{tr})$ at RT.

EXPERIMENTAL RESULTS AND DISCUSSIONS

Determination of Actual Activation Layer Models for p-GaAs / (Cs,O) – Photocathode

At the beginning of activation, when (Cs,O) – layer is thin enough, properties of p-GaAs/(Cs,O)/vacuum interface are obviously described by dipole layer model (DLM)[3], because at this stage of activation both absolute value of NEA and QE of photocathode are increasing along with activation due to the increasing of the dipole moment of the (Cs,O) – layer. Nevertheless, it was not undoubtedly demonstrated that DLM is dominated also at the point of activation, where the

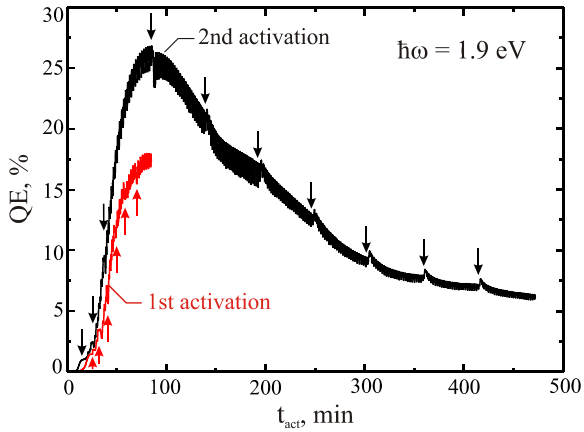

Figure 1: Time dependence of the QE during the activations.

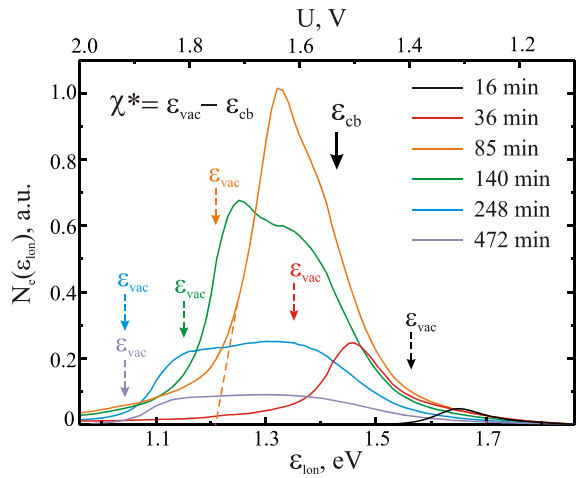

Figure 2: $N_e(\varepsilon_{lon})$ – distributions measured during the 2nd activation.

absolute maximum of QE for particular photocathode occurs. To clarify this topic, we performed prolonged activation of p-GaAs/(Cs,O) – photocathode, which continued far beyond the absolute maximum of the activation curve. In addition of QE, evolution of NEA-value was monitored along with activation by periodical measurements of $N_e(\varepsilon_{lon})$ – distributions. Shapes of the first (conventional) activation and the second (prolong) activations are shown on fig. 1. One can see that the second activation increase maximal QE from 18% up to 27%. One can see also, that when the absolute maximum of prolonged activation is passed, QE begins to drop down, but the rate of dropping become to be lower little by little. At the last stage of activation, at $t_{act} > 300$ min, QE drops down linearly with time. One should mention

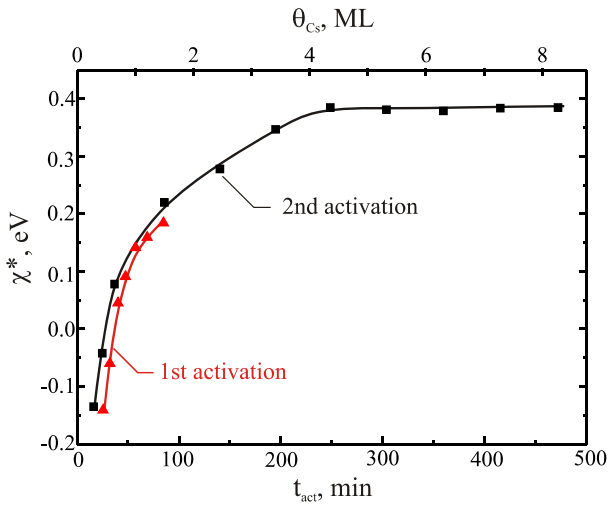

Figure 3: Time dependence of the negative electron affinity χ* during the activations.

also, that interruptions of activation, which are marked by vertical arrows, did not "disturb" considerably the shape of the activation curve.

Fig. 2 presents part of measured $N_e(\varepsilon_{lon})$ – curves, which are marked by thick arrows on fig.1. Vertical arrows on fig. 2 indicate specific energy points of $N_e(\varepsilon_{lon})$ – curves. Arrow, marked by ε_{cb}, indicates the position of conduction band minima ε_{cb} in the bulk of semiconductor. It have been shown [4], that ε_{cb} at RT coincides with the energy, were derivative of high energy tail of $N_e(\varepsilon_{lon})$ reaches its minimal value. Several dashed arrows, marked by ε_{vac}, indicate vacuum levels of photocathode at different points of prolonged activation. Resolution of energy analyzer within PPC was not good enough. Due to that we evaluated ε_{vac} by the linear approximation of the low energy tail of $N_e(\varepsilon_{lon})$, as it shown on fig.2 by dashed line. The energy on this figure is counted off top of the valence band. By using of this approach, we determined ε_{vac} for every measured $N_e(\varepsilon_{lon})$. Values of negative electron affinity (NEA) χ* were calculated as a differences between ε_{cb} and ε_{vac}. Resulted $\chi^*(t_{act})$ - curve is shown on fig. 3. One can see, that $\chi^*(t_{act})$ grows sub-linearly during first half of prolonged activation, but thereafter saturates at its maximal value, which is close to 0.4 eV. This kind of behaviour of $\chi^*(t_{act})$ can be explained easily: during first half of activation, the (Cs,O) – layer is thin enough and due to that value of $\chi^*(t_{act})$ is dominated by the dipole moment of (Cs,O) – layer. Therefore, one can conclude that properties of p-GaAs/(Cs,O) – vacuum interface along within considerable part of the first half of activation can be described by DLM. Before the end of the first half of prolonged activation, the thickness of (Cs,O) – layer d approaches to some critical value d_{cr}, which is enough for the formation of the thin layer of solid state material with some particular band structure. Since that point, value of χ* characterizes the band structure of this (Cs,O) – material and the constancy of χ* during the second half of prolonged activation means, that the band structure of this material and, consequently its composition, do not vary any more. Value of QE along the second half of activation decreases gradually with the near - linear slope. Both peculiarities of the second half of activation: constancy of χ* and linear decreasing of QE coincide with predictions of heterojunction model (HJM) [3]. To evaluate value of d_{cr}, we did the following. At first, we took into account that the first local Cs – maximum of QE(t) during activation occurs when Cs – coverage approaches to $\theta_{Cs} \approx 0.5$ ML [5]. Secondly, we assumed that in the presence of oxygen, the sticking coefficient of Cs should be close to 1. Under this assumption value of d, which correspond to the absolute maximum of QE, was estimated to be close to 1.5 ML of Cs and the beginning of the second half of prolonged activation corresponds to d ≈ 6 - 7 ML of Cs. Together with adsorbed oxygen, it is enough to form the band structure of thin solid state layer. Therefore, one may conclude that if thickness of (Cs,O) – layer exceeds 6-7 ML of Cs, properties of p-GaAs/(Cs,O) – vacuum interface follow predictions of HJM.

Photoelectron Escape Model

Phenomenological escape probability P_{esc} is defined as a ratio of external and internal photocurrents. External photocurrent can be measured in vacuum, while internal photocurrent should be calculated at the boundary between near-surface band bending region (BBR) and the bulk of semiconductor. To describe $N_e(\varepsilon_{tr})$ and $N_e(\varepsilon_{lon})$ of emitted photoelectrons from NEA – photocathode, one have to develop the microscopic description of escape process. To do that, one has to consider self-consistently the electron transport across BBR and semiconductor – vacuum interface. This description should include size quantization of electron spectra within BBR, because the width of BBR in p-GaAs with optimal concentration of charged acceptors is close to 10 nm [6]. Moreover, elastic and inelastic scattering of photoelectrons within BBR and during their escape should be included also. Bell [3] was probably the first, who put attention to the necessity of quantum description of electrons within BBR of photocathode. Mills [7] and Mills and Ibach [8] stressed, that inelastic scattering processes of low energy electrons during their escape coincide, with those, which dominated HREELS – spectra. For p-GaAs these processes consist of photoelectron interaction with Fuchs – Kliever surface optical phonons and with surface plasmons [9]. The importance of quantization of electron spectra within BBR of p-GaAs(Cs,O) - photocathode and the considerable contribution of Fuchs – Kliever surface optical phonons to the scattering of photoelectrons during their escape was revealed experimentally by measurements $N_e(\varepsilon_{lon})$ – distributions at low temperatures. To detect these phenomena in p-GaAs(Cs,O) – photocathode, we studied $N_e(\varepsilon_{lon})$ – distributions at T = 4.2 – 77 K range [6,10]. Fig. 3 reproduces $N_e(\varepsilon_{lon})$ from [6], which demonstrates the quantization of electron spectra within BBR and emission of Fuchs – Kliever

surface optical phonons during photoelectron's escape. One can see on fig. 4, that $N_e(\varepsilon_{lon})$ contains fine structure: the sharp peak I_0 in the vicinity of ε_{cb} together with weak peak I_1 and knee I_2 at lower energies. Value of ε_{cb} was calculated by use of energy diagram of GaAs, the known energy of exciting photons ($\hbar\omega = 1.7$ eV) and measured energy positions of two peculiarities, which were detected in the derivative of $N_e(\varepsilon_{lon})$ (dot line on fig. 3). These peculiarities are related to the photoemission of ballistic photoelectrons, which are excited from the heavy holes band (hh – c) and from the light holes band (lh – c). Comparison of ε_{cb} and with energy position of peak I_0 led us to the conclusion that this peak is positioned 20 – 30 meV below ε_{cb}. Electrostatic potential and 2D - electron spectrum within band bending region (BBR) were calculated by the self-consistent solution of Poisson and Schrödinger equations [6] as a function of both band banding V_b and acceptor concentration N_a. It was concluded, that for the actual value of N_a and for expected values of V_b, BBR in our photocathode contains two 2-D quantum electron bands. The bottom of the upper band is positioned slightly below ε_{cb}, while the lower 2-D band is positioned in the vicinity of ε_{vac}. Therefore, it was concluded, that peak I_0 corresponds to the elastic emission of photoelectrons from the bottom of the upper 2-D quantum band. Energy intervals $\Delta_{1,2}$ between positions of peak I_1 and knee I_2 and position of peak I_0 were found to be equal to: $\Delta_1 = \hbar\Omega_x$ and $\Delta_2 = 2\times\hbar\Omega_x$, were $\hbar\Omega_x = 38\pm3$ meV. Value of $\hbar\Omega_x$ coincides within experimental accuracy with the energy of Fuchs – Kliever surface optical phonons $\hbar\Omega_{FK} = 36$ meV [11], which was measured by use of high resolution electron energy loss spectroscopy (HREELS) in undoped GaAs. It was found also [12], that phonon – related losses are well pronounced in HREELS – spectrum of heavily doped p – doped GaAs. The presence of energy losses, related to Fuchs – Kliever phonons and the absence of energy losses, related to the interaction of electrons with surface plasmons, was explained in [12] by the repulsion of holes from the surface by the BBR – potential. The importance of this repulsion was confirmed in [9]. On the other side, it was demonstrated, that in the absence of band bending, electron energy losses in heavily doped p-GaAs, measured by HREELS, are dominated by the emission of surface plasmons [9]. Instead of sharp peaks of phonon-related losses [11], the shape of plasmon - related energy losses looks like a broad (but intensive!) shoulder [9,13], because surface plasmons in heavily doped p – GaAs are dumped considerably. The width of this shoulder for actual value of p is as high, as ~60 meV [9]. One should to mention also, that in p–GaAs/(Cs,O) - photocathode electron – surface plasmon scattering could be intensified because the maximum of the wave function of photoelectron at the upper quantum band within BBR of p-GaAs(Cs,O) - photocathode is located near the inner border of BBR [6]. Therefore, one can conclude, that plasmon – related energy losses of photoelectrons in p - GaAs(Cs,O) photocathodes could be considerable, but it

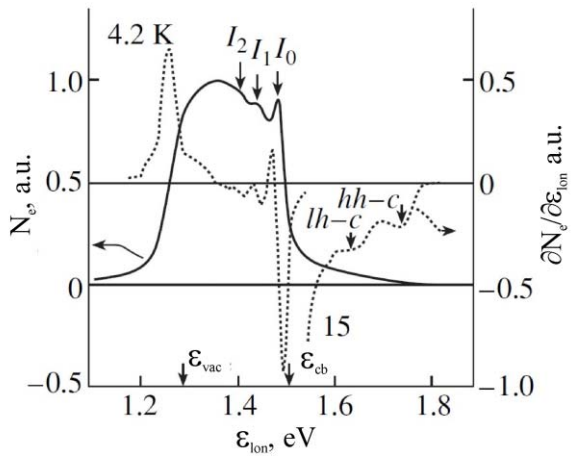

Figure 4: $N_e(\varepsilon_{lon})$ – distribution measured at 4.2 K (solid line) and derivative of the $N_e(\varepsilon_{lon})$ (dash line).

is not easy to reveal the intensity of these losses because they do not manifest itself by sharp structures in $N_e(\varepsilon_{lon})$.

We have found, that energy intervals Δ between ε_{cb} and energy positions of peaks I_0, which were measured at different photocathodes and at different temperatures 4.2 K and 77 K, are near the same. The universality of Δ means, that energy positions of upper 2-D quantum band within BBR at different photocathodes with different, concentrations of acceptors, different values of χ^*, different thicknesses of the activation layers are near the same. This finding led us to conclusion, that this specific value of Δ should have some physical sense. To find out this sense, the following model is proposed. It is known, that (Cs,O) – activated surface of p-GaAs – photocathode is highly reflective [14,15] for photoelectrons with kinetic energies, which exceed ε_{cb}, and due to that the probability of their escape after single collision with surface does not exceed ~ 1%. To explain the high value of escape probability of photoelectrons with kinetic energies below ε_{cb}, it was assumed [6,15] that before escape photoelectrons should be trapped to the electron states within BBR. When photoelectrons are trapped, they are collided with surface repeatedly and the probability of their escape increases [15]. To realize this scenario, value of Δ should have some compromise value. On the one hand, Δ should be low enough to "simplify" fast trapping of photoelectrons to the upper 2-D quantum band, because this probability is limited by the probability of the photoelectron energy loss. The most efficient mechanism of the photoelectron energy losses near the surface is the emission of surface optical phonons. Therefore, to provide effective trapping of photoelectrons, value of Δ should not exceed the energy of surface optical phonons. On the other hand, to prevent fast thermal "re-excitation" of trapped photoelectrons to the bulk of semiconductor, value of Δ should not be too low. It seems to us that measured value of Δ = 20 – 30 meV could be an appropriate compromise, which could provide the effective trapping of photoelectrons within BBR. Probability of "re-excitation" should be lower or be

compatible with probability of photoelectron escape to the vacuum and with probability of photoelectron surface recombination via defect – induced surface states with lower energies. Therefore, to provide maximal value of P_{esc}, Δ should be adjusted to the value within 20–30 meV. This adjustment is performed during activation of photocathode, when we maximize value of P_{esc} by varying both thickness and composition of (Cs,O) – layer. Our GaAs - surface cleaning procedure provides low density of charged defects at the surface and due to that, variations of parameters of (Cs,O) – layer is accompanied by the variation of V_b [16,17]. By-turn, variation of V_b causes variation of energy positions of 2-D quantum bands within BBR [6]. Therefore, during of activation of "defect–free" photocathode surface we are reaching highest P_{esc}, together with optimization of other essential parameters, Δ is also adjusted to its optimal value.

STUDY OF TRANSVERSE ENERGY DISTRIBUTIONS FROM NEA – PHOTOCATHODES

Experimental studies of energy and angular distributions of photoelectrons, emitted from NEA – photocathodes, enable one to understand better the physics of photoelectron escape. Data obtained have a practical meaning also, because they can be used for the calculation of the point spread function of position-sensitive photon detectors, for the calculation of mean transverse energy and for the calculation of the physical limit of "hallo" of electron beams. Experimental methods, which enable one to measure accurately both energy and angular distributions of photoelectrons, are well developed in for high photon energies, when kinetic energies of photoelectrons exceed 5 - 10 eV. Kinetic energies of photoelectrons, which are emitted from NEA - photocathodes are within 0.0 – 1.0 eV – interval. Due to low kinetic energies, trajectories of photoelectrons from NEA – photocathodes are extremely sensitive to the electric fields in the vicinity of photocathode, which are could vary in time due to adsorption and desorption processes. To overcome these problems we use parallel – plate photoelectron spectrometers, which are most suitable for measurements of $N_e(\varepsilon_{lon})$ – and $N_e(\varepsilon_{tr})$ – distributions. Different versions of these spectrometers operate in homogeneous electric and magnetic fields. To simplify the design of spectrometers, transmission – mode photocathodes are used. To provide homogeneity of electric field, diameters of photocathode and opposite electrode should be much more, than the distance between them. Actual homogeneities of work-functions of both electrodes can be measured. Time stability of work-functions is guaranteed by the use of XHV – conditions. We realized these spectrometers as a compact, vacuum-sealed XHV - devises, which do not contain any magnetic materials and can be cooled by direct immersion to the liquid nitrogen [10] or helium [6]. Some examples of these spectrometers are presented on fig. 5. Examples of their use are described below.

Figure 5: Photo of vacuum-sealed XHV - devises, which were used as a parallel-plate electron spectrometers.

Ballistic Photoemission from p-GaAs - (Cs,O) – Photocathode

Sharp peak I_0, which was observed in low temperature $N_e(\varepsilon_{lon})$ was interpreted as a elastic escape of photoelectrons, which were concentrated within ~ kT energy interval near the bottom of 2-D quantum band. The distribution of these electrons along with transverse energy or along with total energy (ε) and emission angle (θ), were not measured. To determine $N_e(\varepsilon,\theta)$, we developed electron spectrometer, which operates in homogeneous magnetic and retarding electric fields, which are perpendicular to each other. It have been shown theoretically [18], that if to measure photocurrent J_{ph} within parallel plate photodiode as function of retarding voltage U_{ret} and magnetic field strength H, the resulted function $J_{ph}(U_{ret},H)$ can be recalculated to $N_e(\varepsilon,\theta)$ - distribution. Experiments were performed at 77K. One can see (see fig. 6), that measured $N_e(\varepsilon_{lon})$ – distribution contains peak I_0 and one phonon replica. To determine angular distribution of photoelectrons within peak I_0 , the retarding voltage U_{ret}* cut off all electrons with ε_{lon}, which are lower than energy, which correspond to the maximum of I_0. Fig.7 presents $\partial J_{ph}/U_{ret}(U_{ret}*,H)$, while Fig.8 shows $N_e(\theta)$ – distribution, which was obtained from $\partial J_{ph}/U_{ret}(U_{ret}*,H)$. Details one can find in [10]. One can see on fig. 8, that $N_e(\theta)$ consist of narrow peak and broad halo. Narrow peak in the $N_e(\theta)$ – distribution contains electrons, which were escaped ballistically, without any momentum scattering. In contrary, electrons within halo were escaped along with diffusive scattering of their momentum. Our future studies should reveal the dominant mechanism of elastic diffusive momentum scattering of elastically emitted photoelectrons: is it surface roughness, disorder within (Cs,O) – layer, or the tangential component of the electric field, which occurs because of randomly distributed charged bulk acceptors and surface defects.

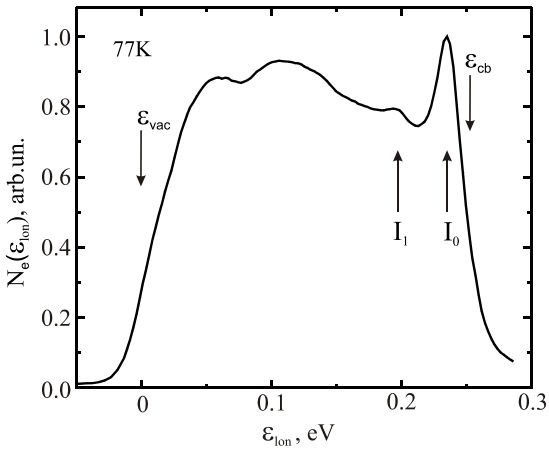

Figure 6: $N_e(\varepsilon_{lon})$ – distribution measured at 77 K

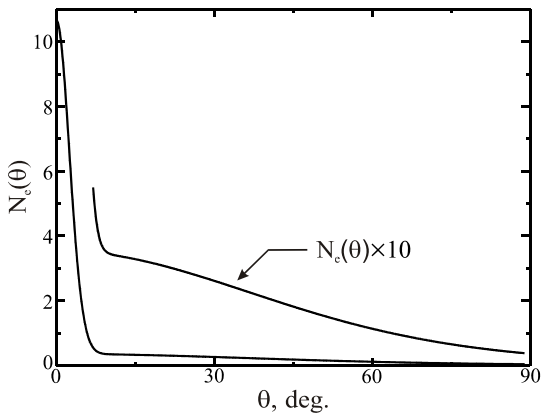

Figure 8: Photoelectron angular distribution.

Transverse Energy Distribution of Photoelectrons Emitted from p-GaN(Cs,) – Photocathode

To determine $N_e(\varepsilon_{tr})$, the spread of electron beam in the homogeneous accelerating electric field could be measured [19]. We utilized this principle by use of home-made parallel plate image intensifier with transmission – mode p- GaN(Cs,O) – photocathode, microchannel plate and luminescent screen with 18 mm working diameters. Light spot with ~ 25 μm FWHM - diameter and radial intensity distribution $N_{ph}^{i}(\rho)$ was formed at the centre of photocathode by the use of xenon arc lamp, grating monochromator with circular diaphragm at the exit slit and quartz lenses. Electrons moved within gap d ≈ 1mm between photocathode and MCP under the influence of accelerating voltage U_a. Simultaneously, they move along with ρ in accordance with $N_e(\varepsilon_{tr})$ and form broadened radial distribution of electrons $N_e(\rho)$ near MCP. After intensification by MCP, $N_e(\rho)$ was transferred to the screen. Optical replica $N_{ph}^{f}(\rho)$ of $N_e(\rho)$ was transferred to the digital cooled megapixel CCD-camera and then to PC. To account for the real shape of $N_{ph}^{i}(\rho)$ and for other

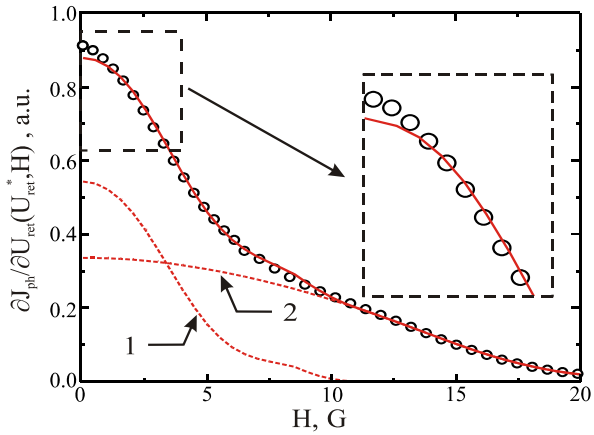

Figure 7: Measured (dots) and calculated (lines) magnetic field dependence $\partial J_{ph}/U_{ret}(U_{ret}^{*},H)$.

distortions of electron and light beams within experimental setup, we expressed the measured $N_{ph}^{f}(\rho)$ – distributions as a multiple integral convolution. After taking into account several reasonable simplifications it was transformed to the following form:

$$N_{ph}^{f}(\rho) = \int N_e\left(\varepsilon_{tr} = \frac{e \times U_a \times |\vec{\rho}|}{4 \times d^2}\right) \times \Psi(\vec{\rho} - \vec{\rho}_1)\, d\vec{\rho}_1 \quad (1)$$

were e is electron charge and ψ(ρ) is the instrument function of our set up. By substituting in (1) several $N_{ph}^{f}(\rho)$ – distributions, which were measured at different U_a, we obtained several integral equations for two unknown functions: ψ(ρ) and $N_e(\varepsilon_{tr})$. Equations (1) were solved for several U_a by using standard methods from [20]. More details will be given elsewhere. Measured $N_e(\varepsilon_{tr})$ – distribution is shown on fig. 9 together with $N_e(\varepsilon_{lon})$ - distribution. One can see, that $N_e(\varepsilon_{tr})$ contains three parts: (i) the pronounced peak at lowest ε_{tr} , (ii) the broad tail at "middle" energies and (iii) the high energy shoulder with near - exponential shape, which restrict the total width of $N_e(\varepsilon_{tr})$. This shape was interpreted as follows. Most of electrons with lowest ε_{tr} has high ε_{lon}. Due to that "fast" photoelectrons have higher probability to "run away" from the surface without excitation of surface phonons and without scattering by random electron field in the close vicinity of photocathode surface. One should mention here, that electron scattering by surface phonons near GaN – surface is much more intensive than near GaAs – surface [21]. The energy position of the high energy shoulder is determined by the value of χ* of p – GaN/(Cs,O) – photocathode while the near - exponential tail forms by electrons, which gained energy from surface phonons. It is seen also, that total widths of $N_e(\varepsilon_{tr})$ and $N_e(\varepsilon_{lon})$ are near the same, because both are limited by value of χ*.

To evaluate the accuracy of determined $N_e(\varepsilon_{tr})$ and ψ(ρ), we have solved the "inverse problem" and used these

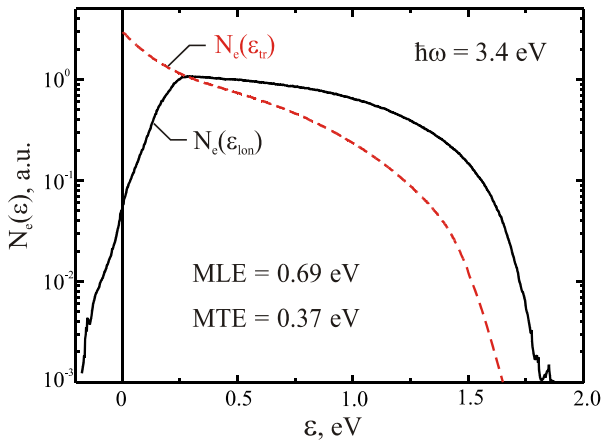

Figure 9: $N_e(\varepsilon_{tr})$ – distribution (red dash line) and $N_e(\varepsilon_{lon})$ – distribution (solid dark line) of electrons, emitted from p-GaN(Cs,O) -photocathode.

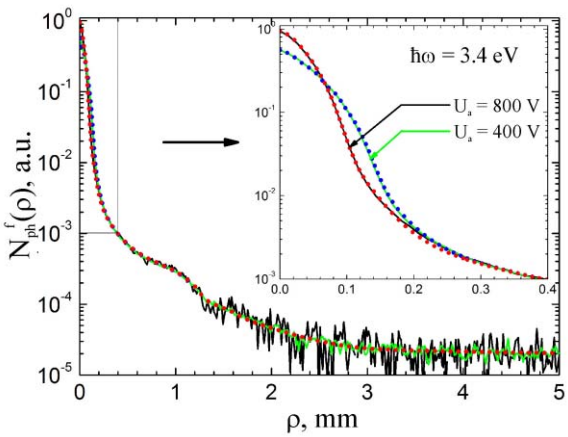

Figure 10: Measured (lines) and calculated (dots) radial intensity distributions $N_{ph}^f(\rho)$.

functions for the calculation of $N_{ph}^f(\rho)$ – distributions for different U_a. Results of these calculations, which are marked by dots on fig. 10, were compared with measured (continuous) $N_{ph}^f(\rho)$ – curves. One can see, that calculated points and measured curves coincide well.

SUMMARY AND CONCLUSIONS

The final conclusions are as follow. (i) NEA – state on p-GaAs(Cs,O) – surface can be prepared with different thicknesses of (Cs,O) – layer. Photocathodes with "thin" layers can be described by dipole layer model, while photocathodes with "thick" layers follow predictions of heterojunction model. (ii) Escape of photoelectron includes two basic steps: at the first step it is trapped by 2-D can quantum band near the surface while at the second step is escaped to the vacuum. Small part of electrons is escaped ballistically, while most of them is accompanied by various scattering processes: inelastic scattering of surface phonons and plasmons, elastic scattering by electric field of randomly distributed surface and bulk charged centres together with short range random potential of (Cs,O) layer. (iii) To study the actual energy diagram of GaAs(Cs,O)/vacuum – interface and photoelectron escape, parallel plate electron spectrometers with energy and angular resolutions are well effective at temperatures within 4.2 K – 300 K range.

REFERENCES

[1] O.E. Tereshchenko et al., J. Vac. Sci. Technol. A 17 (1999) 2655.
[2] V.V. Bakin et al., e-J. Surf. Sci. Nanotech. 5 (2007) 80.
[3] R.L. Bell, *Negative electron affinity devices*, (Oxford: Clarendon Press, 1973) 148.
[4] A.S. Terekhov, D.A. Orlov, JETP Letters 59 (1994) 864.
[5] O.E. Tereshchenko et al, JETP Letters 79 (2004) 163.
[6] D.A. Orlov et al, JETP Letters 71 (2000) 220.
[7] D.L. Mills, Surf. Sci. 48 (1975) 59.
[8] H. Ibach, D.L. Mills, Electron energy loss spectroscopy and surface vibrations, (Academic Press, 1982) 336.
[9] Y. Meng et al. Phys. Rev. B 44 (1991) 4040.
[10] V.V. Bakin et al, JETP Letters 77 (2003) 167.
[11] A. Degiovanni et. al, Surf.Sci. 251/252 (1991) 238.
[12] R.G. Egdell et al, J. Electron Spectrosc. Related Phen. 45 (1987) 177.
[13] Y. Meng et al. Phys. Rev. B 45 (1992) 1500.
[14] A.L. Musatov et. al, Izv. Akad.Nauk SSSR, Ser. Fiz 40 (1976) 2523 (in Russian).
[15] A.L. Musatov et. al, Izv. Akad.Nauk SSSR, Ser. Fiz 46 (1982) 1357 (in Russian).
[16] V.L. Alperovich et al., Phys. Rev. B 50 (1994) 5480.
[17] V.L. Alperovich et al., Appl. Phys. Lett. 66 (1995) 2122.
[18] V.E. Andreev, A.L, Bukhgeim, A.S. Terekhov, Journal of Inversed and Ill-Posed problems, 7 (1999) 427.
[19] G. Vergara et.al., J. Appl. Phys., 80 (1996) 1809.
[20] R.C. Gonsalez, R.E. Woods, *Digital Image Processing*, *2nd Edition*, (Prentice Hall, 2002) 780.
[21] S.P. Grabowski et.al., Appl. Surf. Sci., 123/124 (1998) 33.

CONSTRUCTION OF THE SECOND 500 KV PHOTOCATHODE DC-GUN AT KEK

M. Yamamoto#, T. Miyajima, Y. Honda, T. Uchiyama, M. Kobayashi,
KEK, 1-1 Oho, Tsukuba, Japan 304-0801
N. Nishimori, R. Nagai, S. Matsuba, R. Hajima,
JAEA, 2-4 Shirane Shirakata, Tokai, Naka-gun, Ibaraki, Japan 319-1195
M. Kuriki, Hiroshima Univ., 1-3-1 Kagamiyama, Higashihirosima, Hiroshima, Japan
M. Kuwahara, Nagoya Univ., Furo-cho, Chikusa-ku, Nagoya, Japan 4648603
H. Yoshida, AIST, 1-1-1 Umezono, Tsukuba, Ibaraki, Japan 305-8563
H. Kurisu, Yamaguchi Univ., Ube, Yamaguchi, Japan 755-8611

Abstract

A 500 kV photocathode DC-gun has been developed at KEK since 2009. The gun was almost completed and high voltage conditioning has been carried out up to 500 kV. In addition, we have designed a new quick cathode preparation system for a practical operation of the DC-gun without long interruption. The detail result and status are presented in this paper.

INTRODUCTION

A construction of compact-ERL (cERL) has been started in KEK and a 500 kV photocathode DC-gun (the first DC-gun) developed at JAEA has been installed in October 2012 [1-3]. The second 500 kV photocathode DC-gun has been developed at KEK since 2009 [4] not only for a substitution for the first DC-gun but also for a test machine for continuous R&D's on challenging issues because the second DC-gun can be operated independent of cERL.

Some main parts of the second gun system such as segmented insulator were designed to be compatible with the first gun. However, the second gun system has some new features. We have chosen TA010 (Kyocera) for the insulator, which is different from conventional Al_2O_3 material. Since TA010 is tolerant for surface discharge phenomenon in voltage condition higher than Al_2O_3, we expect the second gun would reach the higher voltage and the higher electric field. In order to investigate a dark current and find a sign of discharge between anode and cathode electrodes in high voltage (HV) conditioning, an isolated anode plate was installed. In addition, a new pump system to generate extreme high vacuum (XHV) will be tested to maintain a long cathode lifetime. A repeller electrode was employed to protect the cathode from ion back bombardment since the electrode can reflect low energy ions which generated at downstream of the gun exit.

A 600 kV oil-impregnation Cockcroft-Walton high voltage power supply (HVPS) was tested up to 580 kV independently. The HVPS and the DC-gun system were connected through a SF_6 vessel (Fig. 1.).

A new cathode preparation system was designed for a practical operation of the DC-gun to compensate short cathode lifetime in high-current electron beam generation. The preparation system can handle plural cathodes in parallel for cleaning, activation and storage.

Figure 1:A photograph of the second DC-gun. The HVPS (left) is connected to the gun chamber (right).

VACUUM SYSTEM

A DC-gun equipped with a photocathode of GaAs having an negative electron affinity (NEA) surface has advantages to generate a beam with low mean transverse energy and a high quantum efficiency. Therefore, a high voltage dc gun using an NEA-GaAs photocathode is one of the candidates for a high brightness electron source of ERL. However, the NEA-GaAs photocathode has disadvantage of a lifetime itself. The cathode QE degradation is dominated by back stream ions which are produced by collision between electron beams and residual molecules during high beam current operations. To improve the cathode lifetime, reduction of the residual molecules is essential. In order to achieve XHV better than 10^{-10} Pa, a chamber of the DC-gun system should have low outgassing property and vacuum pumps with a high effective pumping speed under XHV are indispensable. Generally, a combination of ion pump (IP) and non-evaporable getter (NEG) pumps is employed for

the main vacuum pump system of GaAs-based photocathode dc guns. Inert gases, which are not pumped by the NEG, are pumped by the IPs. However, the effective pumping speed of general IPs ordinarily decreases down to almost zero under XHV condition. Therefore, we employed a combination of bakeable cryopump [5] and NEGs for the main pump of the second DC-gun.

Outgassing Rate Measurement

Chemically polished titanium was chosen for a material of the main components of the gun vacuum chamber, guard rings, anode and cathode electrodes, because it achieves low outgassing rate [6].

A measurement of outgassing rate at the gun chamber was carried out in a situation that all vacuum components except the main vacuum pump system had been installed. Before the measurement, the system was baked at 150-200 °C for 100 hours. A total outgassing rate was measured by rate-of-rise (RoR) method using spinning rotor gauge (SRG) as shown in Fig. 2. The total outgassing rate of the system was estimated to be 8.1×10^{-11} Pa·m^3/s equivalent for hydrogen.

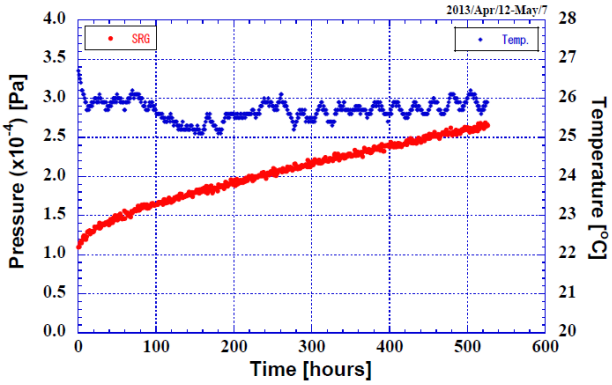

Figure 2: Result of rate-of-rise measurement of the second DC-gun system without the main vacuum pump system.

Pumping Speed of 4K Bakeable Cryopump

We employed a 4K bakeable cryopump, which has a G-M refrigerator spatially separated from a cryopump housing. This configuration enables one to bakeout the pump including cryopanels and adsorbent at a temperature above 150 °C, thus the pump has a potential to maintain high effective pumping speed even in the XHV. We measured a pumping speed of the bakeable cryopump using a standard conductance element for introducing test gas into a chamber accurately [7,8].

A result of the effective pumping speed measurement of the 4K bakeable cryopump is shown in Fig. 4, where the pumping speed was estimated from the pressure measured by extractor gauge. The pressure of each gas was converted using relative sensitivity factors that was calibrated at AIST. The pumping speed of CH_4, N_2, Ar, CO_2 were not significantly degraded under XHV condition below 1×10^{-9} Pa, however the pumping speed measurement of hydrogen was restricted for a pressure above 1×10^{-9} Pa because of adsorption equilibrium of the charcoal for hydrogen in this situation. To improve pumping speed of hydrogen, degassing of charcoal by high-temperature baking is required.

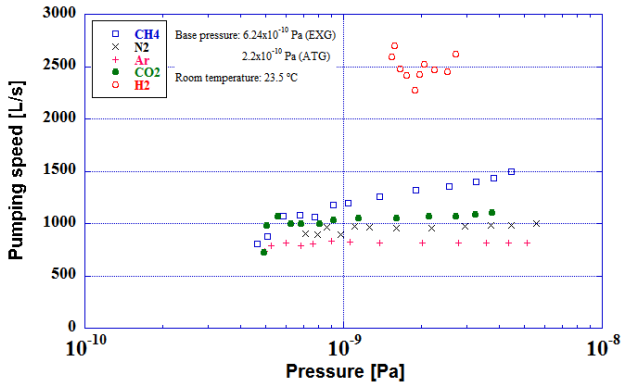

Figure 3: Result of pumping speed measurement at the 4K bakeable cryopump.

HV SETUP & CONDITIONING

High Voltage System Setup

After the measurement of outgassing rate, the gun chamber was evacuated again using a 1000 L/s turbo molecular pump (TMP) system for a high-voltage test. The main pump of the bakeable cryopump and NEGs was not installed at that time and a pressure in the gun chamber reached ~1×10^{-8} Pa in a few days.

To avoid discharge from the high voltage terminal and outside of segmented insulators, +0.2 MPa pressurized SF_6 gas was introduced to the vessel. In the HV conditioning mode, a resistor of 100 MΩ is connected between HVPS and the top of segmented insulator to avoid hard arcing inside the chamber. For the segmented insulators, 500 MΩ resistor is connected between each segment in series to obtain uniform electric field on the insulator surface.

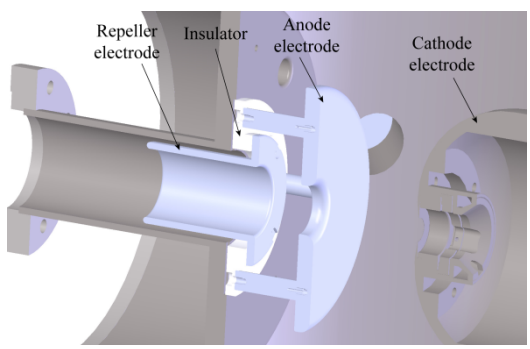

Figure 4: Cross-section view around the anode electrode.

In the gun chamber, anode and repeller electrodes were fixed with isolation from the ground level independently. (Fig. 4.) Since anode plate was fixed by four props, the anode-cathode gap can be tuneable (~110

mm at maximum) by exchanging the props. In this experiment, the gap was chosen at 70 mm.

2D cylindrical electric field around anode-cathode area was calculated by PISSON-SUPREFISH. The on-axis electric field $E_z(r=0,z)$ for a gun voltage of 500 kV is shown in Fig. 5. The field at the cathode center is 6.9 MV/m, and the maximum electric field on the cathode ball is around 11 MV/m.

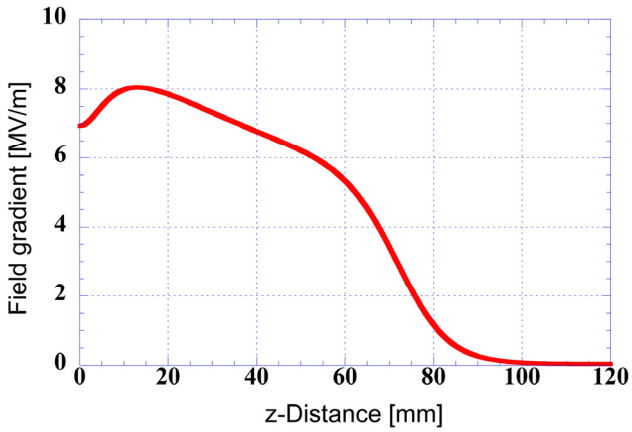

Figure 5: Calculate on-axis electric field in the second DC-gun for a gun voltage of 500 kV.

For the safety interlock of HVPS, we installed monitors: HVPS voltage, total supply current, a current of divide resistors, a dark current which flow between anode and cathode electrode and a load current which contain dark current from a cathode electrode and a high voltage terminal. Additionally, vacuum gauges of gun chamber and a radiation monitor were checked during the high-voltage test. These monitors help us to find troubles in the test. The interlock level were set to 500 nA for the anode current, $5x10^{-7}$ Pa for the vacuum, 20 μSv/h for the radiation. The HV output was turned off immediately when a value of monitors exceeded the interlock level.

High Voltage Conditioning

The result of HV conditioning is shown in Fig. 6. The chamber was evacuated by TMP during HV conditioning. The first HV trip to trigger the interlock happened at 300 kV, then HV trips happened over 350 times in 5 days conditioning. In this conditioning, all trips occurred in the vacuum side because the trips involved vacuum rising without any exception. From the interlock record, about 90% trips occurred between anode-cathode gap. In order to reduce X-ray dose during HV conditioning, the anode current monitor was useful since a response time of the anode current was faster than the other monitors.

After 350 times HV trips, a HV holding test at 480 kV was done for two hours. Some small vacuum trips and anode current trips were detected, however these levels were lower than the interlock level and no HV trip happened during the two-hour test.

A voltage stability of HVPS was monitored by using two methods independently in this HV test. One is a HVPS voltage monitor and the other is a current monitor of ceramic divide resistor. The HVPS system needs a warm-up period about 1.5 hours to stabilize the output voltage, then it shows a good voltage stability better than $2x10^{-4}$ for two monitors.

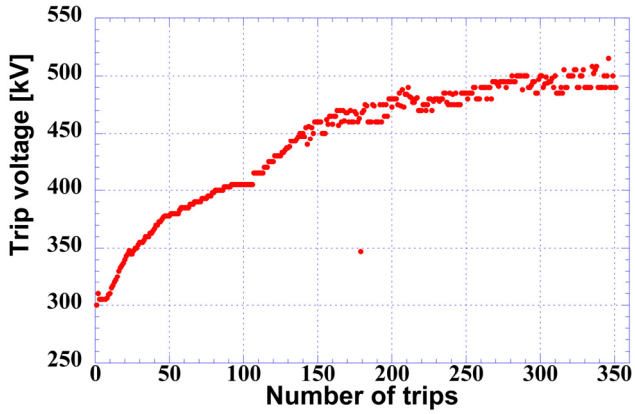

Figure 6: Result of HV conditioning.

CATHODE PREPARATION SYSTEM

An efficient cathode preparation system is important for a practical ERL electron gun, because a cathode lifetime becomes shorter for the higher beam current. Additionally, an NEA GaAs cathode is difficult to transferred by a vacuum suitcase, therefore a simultaneous three cathodes preparation system was designed as shown in Fig. 7.

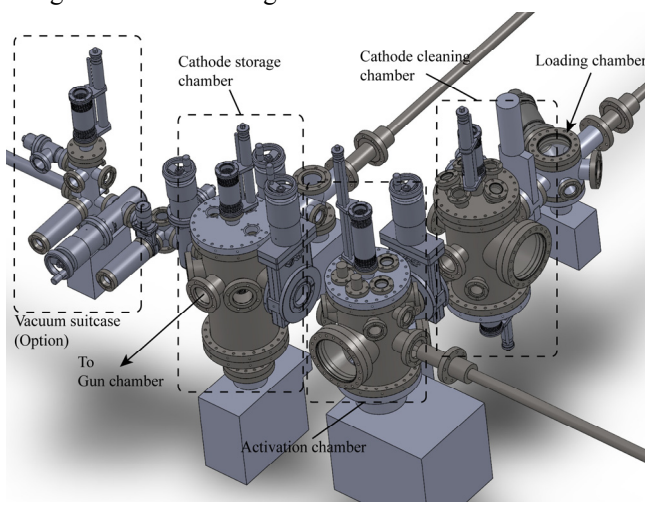

Figure 7: Schematic view of the cathode preparation system with simultaneous handling of plural cathodes for cleaning, activation and storage.

The preparation system consists of four sections: a loading chamber, cathode cleaning chamber, activation chamber and storage chamber. A cathode container that can mount three cathode is transferred between the loading chamber to the activation chamber. The system can treat three cathode containers, since 6~9 cathodes can be activated and stored in one day. Therefore, the system is effective to reduce a dead time to exchange cathodes during gun operation. Optionally, other type of cathode

such as a thin multi-alkali layer cathode can be installed to the storage chamber directly using a vacuum suitcase.

These vacuum chambers and components were almost fabricated and a vacuum test and motion check of cathode transfer system are in progress.

CONCLUTION

Construction of the second DC-gun at KEK was almost completed and HV conditioning was started. The outgassing rate of the DC-gun system was estimated at 8.1×10^{-11} Pa m^3/s and the effective pumping speed of 4 K cryopump was measured in XHV condition. From these results, the pressure in the gun chamber can certainly reach to vacuum below 10^{-10} Pa. For electrodes in the gun chamber, a narrow anode-cathode gap of 70mm was chosen. In order to monitor a dark current between anode-cathode gap, the isolated anode electrode was employed. HV conditioning was carried out in this situation. The HV trip voltage exceeded 500 kV after 5 days conditioning, and a holding test at 480 kV was carried out for 2 hours with no HV trip. According to these result, a high voltage of ~500 kV and high electric field of ~7 MV/m on the cathode are feasible in the DC-gun system.

A simultaneous three cathodes preparation system was designed for compensating a short cathode lifetime in actual high current DC-gun operation. The vacuum components were almost fabricated and construction of the preparation system is in progress. Demonstration of efficient preparation and quick cathode exchange process at the second DC-gun is the next step.

ACKNOWLEDGMENT

We thank Professor H. Kawata, K. Satoh, H. Satoh and Y. Kobayashi of KEK for continuous encouragement for this work. We are also grateful to Associate Professor T. Obina and Mr. S. Nagahashi for contributions to build the HVPS interlock system.

REFERENCES

[1] S. Sakanaka, et al., WG102, ERL2013.
[2] R. Nagai et al., Rev. Sci. Instrum. **81**, 033304 (2010) .
[3] N. Nishimori et al., Appl. Phys. Lett. **102**, 234103 (2013).
[4] T. Miyajima et al., FLS2010 presentation in WG5.
[5] H. Yamakawa, Vacuum **44**, (1993) 675.
[6] H. Kurisu et al., J. Vac. Sci. Technol. A **21**,(2003) L10.
[7] H. Yoshida et al., Vacuum **86**, (2012) 838.
[8] M. Yamamoto et al., TUODB02, IPAC2011 proceedings.

ANALYSIS OF INJECTION AND RECOVERY SCHEMES FOR A MULTI-TURN ERL BASED LIGHT SOURCE*

Y. Petenev#, T. Atkinson, A.V. Bondarenko, A.N. Matveenko
Helmholtz-Zentrum Berlin für Materialien und Energie GmbH, Germany

Abstract

A multi-turn energy recovery linac -based light source is under discussion. Using the superconducting Linac technology, the Femto-Science-Factory(FSF) will provide its users with ultra-bright photon beams of angstrom wavelength. The FSF is intended to be a multi-user facility and offer a variety of operation modes. The driver of the facility is a 6 GeV multiturn energy recovery linac with a split linac.

In this paper we discuss designs of the optic in the linac and compare different schemes of beam acceleration: a direct injection scheme with acceleration in a 6 GeV linac, a two-stage injection with acceleration in a 6 GeV linac, and a multi-turn (3-turn) scheme with a two-stage injection and two main 1 GeV linacs. The key characteristic of comparison is the beam breakup (BBU) instability threshold current.

INTRODUCTION

Our group at Helmholtz Zentrum Berlin is designing a new future multi-turn Energy Recovery Linac (ERL) based light source (LS) with 6 GeV maximum energy of electron beam. This future facility is named Femto-Science Factory (FSF) [1].

One potential weakness of the ERLs is transverse beam breakup (BBU) instability, which may severely limit a beam current. If an electron bunch passes through an accelerating cavity it interacts with dipole modes (e.g. TM_{110}) in the cavity. First, it exchanges energy with the mode; second, it is deflected by the electro-magnetic field of the mode. After recirculation the deflected bunch interacts with the same mode in the cavity again which constitutes the feedback. If net energy transfer from the beam to the mode is larger than energy loss due to the mode damping the beam becomes unstable.

The actuality of this problem was recognized in early experiments with the recirculating SRF accelerators at Stanford [2] and Illinois [3], where threshold current of this instability was occurring at few microamperes of the average beam current. In the works of Rand and Smith in [4] dipole high order modes were identified as a driver of this instability. In late of the 80's the detailed theoretical model and simulation programs had been developed [5, 6]. Nowadays the interest to this problem was renewed. The requirements for more detailed theory and simulation programs [7-9] are given by the needs of high current (~100 mA) ERLs.

* Work supported by German Bundesministerium für Bildung und Forschung, Land Berlin, and grants of Helmholtz Association VH-NG-636 and HRJRG-214.
#yuriy.petenev@helmholtz-berlin.de

In this document we compare different schemes of acceleration for FSF: a direct injection scheme with acceleration in a 6 GeV linac, a two-stage injection with acceleration in a 6 GeV linac, and a multi-turn (3-turn) scheme with a two-stage injection and two main linacs.

DIRECT INJECTION SCHEME

In this part we discuss the simplest scheme of an ERL based LS. In this scheme the beam after an injector section goes directly to the main linac (see Fig. 1), where it accelerated up to 6 GeV and used for the experiments, and after the recirculation turn it arrives to the linac and decelerated there. After the deceleration the beam goes to the dump.

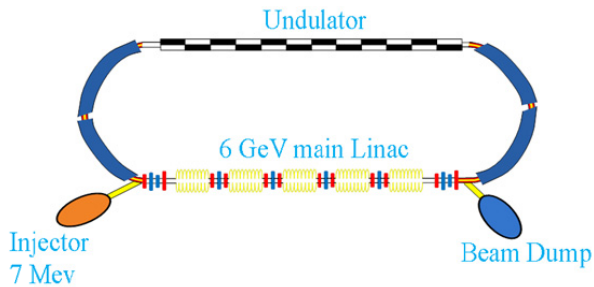

Figure 1: Direct injection scheme.

The linac is planned to be based on the BERLinPro[12] 7-cell cavities. To reach 6 GeV in the Linac we took 464 cavities with an accelerating gradient G about 16 MeV/m and distributed them over 58 cryomodules. The cryomodule is schematically presented in Fig. 2, where λ~0.231 m is the wavelength of the accelerating mode.

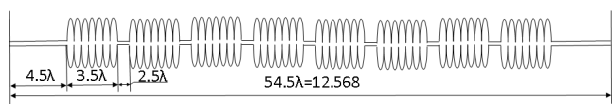

Figure 2: The scheme of FSF cryomodule.

Triplets of quadrupoles are planned to be in between the cryomodules in the linac and were optimized in such a way that the BBU instability will develop similarly for all the cavities in the linac. In this case the highest threshold current might be achieved. The threshold current for the transverse beam breakup may be estimated for the case of a single cavity and single mode for a multipass ERL in the form as [9]:

$$I_{th} \approx I_0 \frac{\lambda\!\!\!^{-2}}{Q_a L_{eff} \sqrt{\sum_{m=1}^{2N-1} \sum_{n=m+1}^{2N} \frac{\beta_m \beta_n}{\gamma_m \gamma_n}}}, \qquad (1)$$

where I_0- Alfven current, Q_a is the quality factor of HOM, $\lambda\!\!\!^{-} = \lambda/2\pi$, λ is the wavelength corresponding to the resonant frequency of the TM_{110} mode, γ_m is the Lorentz factor at the m-th pass through the cavity, β_m – is the Twiss parameter, L_{eff} – is the effective length of the cavity, N is the number of passes during acceleration.

One can see from (1) that the threshold current is higher when the square root in the denominator is minimized. We will use this eq. to find the best optic solution assuming the HOM nature is predictable. But however there could be some unique set of the HOMs parameters when there will exist a better optic solution. The most dangerous for the BBU stability are the cavities where the beam has the lower energies. Therefore the initial Twiss parameters before the linac were optimized to minimize the beta functions in the first cryomodule. In this cryomodule the energy is changed from 7 to 110 MeV. And an RF focusing, which was described in [10] still affect the beam in the first cavities.

To estimate the optimum values of the initial Twiss parameters we used the cavity model given by [10]:

$$\begin{pmatrix} \cos(\alpha)-\sqrt{2}\sin(\alpha) & \frac{\sqrt{8}\gamma_0 L\sin(\alpha)}{(\gamma_1-\gamma_0)} \\ -\frac{3}{\sqrt{8}}\frac{(\gamma_1-\gamma_0)\sin(\alpha)}{L\gamma_1} & \left(\cos(\alpha)+\sqrt{2}\sin(\alpha)\right)\frac{\gamma_0}{\gamma_1} \end{pmatrix}, \quad (2)$$

where $\alpha = \frac{1}{\sqrt{8}}\ln\left(\gamma_1/\gamma_0\right)$, $\gamma_{1(0)}$ is the final(initial) normalized energy of the particle, L – the length of the cavity (or cryomodule). Also we assume that there are symmetrical β-functions on acceleration and deceleration in the linac and that the cryomodule is one long cavity with an effective gradient given by:

$$G_{eff} = G\frac{8L_{cav}}{L_{cryo}}, \quad (3)$$

where L_{cav} is the length of the cavity and L_{cryo} the length of the cryomodule.

We can transfer the beta function through the 1st cryomodule as:

$$\beta_1 = \frac{\gamma_1}{\gamma_0}\left(\beta_0 m_{11}^2 - 2\alpha_0 m_{11}m_{12} + \frac{1+\alpha_0^2}{\beta_0}m_{12}^2\right), \quad (4)$$

where m_{11} and m_{12} - the coefficients of the transfer matrix of the cryomodule given by (2). Now we just have to minimize β_1 in (4) for the initial Twiss parameter α_0, what gives:

$$\alpha_0 = \frac{m_{11}}{m_{12}}\beta_0. \quad (5)$$

We also want to keep constant the value of β/γ:

$$\frac{\beta_0}{\gamma_0} = \frac{\beta_1}{\gamma_1}. \quad (6)$$

The solution is given by:

$$\begin{cases} \beta_0 = m_{12} \sim 2\,m \\ \alpha_0 = m_{11} \sim -0.61 \\ \beta_1 = \frac{\gamma_1}{\gamma_0}m_{12} \sim 31\,m \end{cases}. \quad (7)$$

Modelling in the Elegant [11] program shows similar results but of course our model is not ideal. Because we assumed one long cavity instead of 8 short with drifts in between. Therefore the initial Twiss parameters of the beam were adjusted to get the smaller value of the β_1. In Fig. 3 we show the difference in optic given by the theoretic results from (7) and after an optimization in Elegant. The black curve (β_x) shows the dependence of the beta-function for the theoretical and the blue (β_y) one for the initial parameters optimized by elegant.

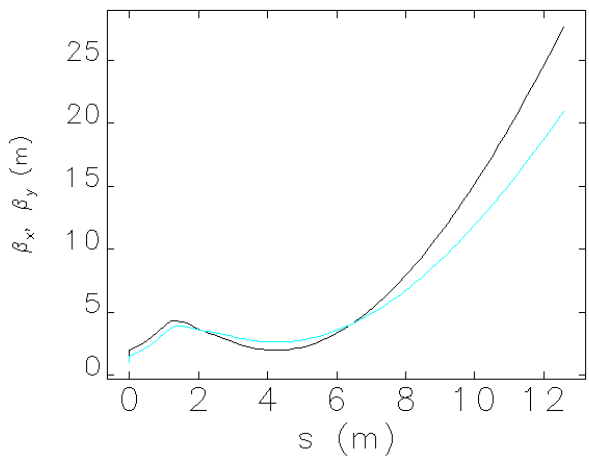

Figure 3: Beta-functions in the first cryomodule.

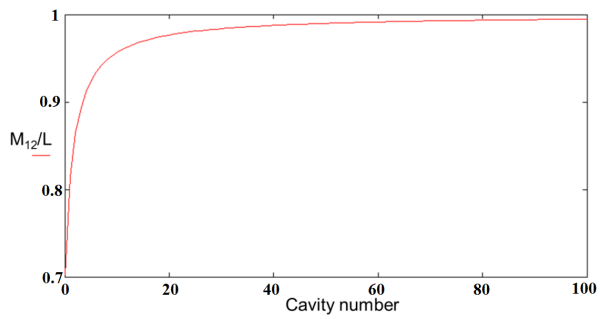

Figure 4: Difference of M_{12} matrix element from the length of the cavity for different cavities.

Later on the higher energies the RF focusing can be neglected. Therefore, we can use the model of cavity as a free drift but with acceleration. In Fig. 4 we show the dependence of (M_{12}/L) for different cavities. On the x axis the number of the cavity is shown and on the y axis one can see how the matrix element which is responsible for RF focusing differs from the length of the cavity L. And the results show that they quite fast reach each other and for the last cavity of the first cryomodule this coefficient is about 0.95.

So our goal is to keep constant the values of β/γ, the preferable theoretically for the BBU stability optics should look then like it is shown in Fig. 5.

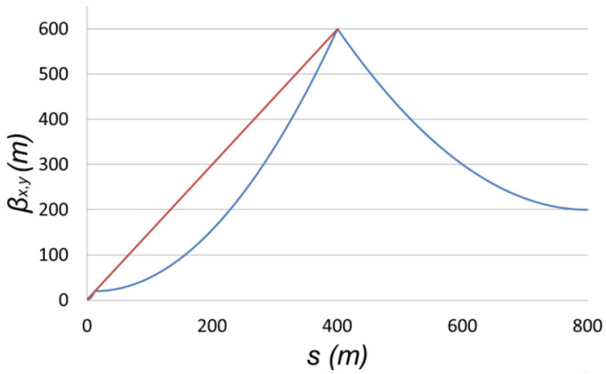

Figure 5: Theoretical optic design of the beta-functions in the main linac for the direct injection scheme.

The red line shows the values with a constant $\beta/\gamma \sim 0.1$ *m*, and the values below this line will give a higher threshold current. Optics calculated in Elegant using this pattern is presented in Fig. 6.

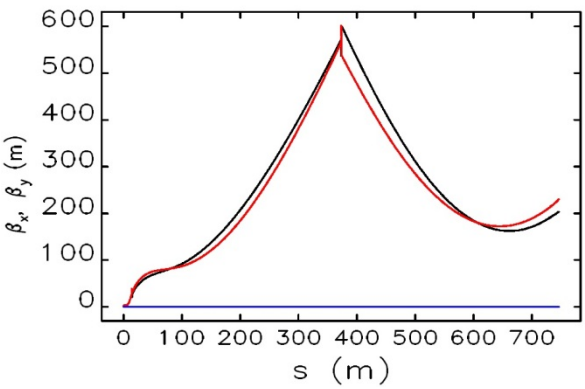

Figure 6: Optic for the main linac 6 GeV linac for the direct injection scheme.

It should be noted that we used only 5 triplets (between first and second, between 8th and 9th cryomodules and in the middle of the linac, and as we said optics has a mirror symmetry therefore there are two more triplets one the second half of the linac) and the length of the linac is then about 750 m.

The main disadvantage of this scheme is the high ratio between the injection energy E_{in}=7 MeV and the final energy E_{fin}=6 GeV: $E_{in}/E_{fin} \sim 850$. What complicates the transverse focusing in the main linac, because the triplets which focus a beam at the beginning of the linac will not affect the beam at the same position on the deceleration phase. For a given optics in Fig. 6 one can estimate the value of the threshold current using: $I_{th} = \frac{10^{-6}}{4\pi}\frac{E}{\beta} \sim 400\ mA$ for the middle point of the linac. For the estimations we took a mode with $(R/Q)_d \cdot Q_d = 6 \cdot 10^5$ Ω, $\omega = 2\pi \cdot 2 \cdot 10^9$ Hz.

TWO STAGE INJECTION SCHEME

In this part we discuss an improved scheme of ERL based light source, which is presented in Fig. 7.

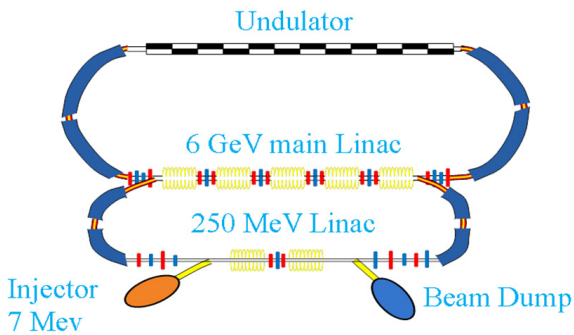

Figure 7: Two stage injection scheme.

The main improvement is that now a beam after an injector goes to a short linac, where it is accelerated up to 250 MeV, then it passes the first arc and comes to the main linac where it accelerated up to 6 GeV. After that it might be used as a light source. And after the beam was used it goes back on the deceleration phase. Our goal again will be to find the optimum optic solution for the beam break up stability in the both linacs. But first let us discuss the stability in the preinjection linac.

Preinjector

For the preinjection linac we suggest to use two cryomodules with a triplet of quadrupole magnets in between. To find the optimum initial twiss conditions we will use the same approach as in the chapter about direct injection scheme. The role of the triplet is to change the sign of the Twiss parameter α of the beam. Let us find the initial injection Twiss parameters to have the equal threshold currents for the entrance and for the middle of the linac.

The beta-function through the 1st cryomodule transferred again by (4).

As we already said the role of the triplet is to change the sign of alpha, therefore we assume that at the entrance to the second cryomodule a beam will have β_1 and $-\alpha_1$. So the beta function at the end of the linac might be found as:

$$\beta_2 = \frac{\gamma_2}{\gamma_1}\left(\beta_1 t_{11}^2 + 2\alpha_1 t_{11} t_{12} + \frac{1+\alpha_1^2}{\beta_1} t_{12}^2\right). \qquad (8)$$

where t_{11} and t_{12} are the transport elements of the second cryomodule. The minimum of the β_2 is given, when

$$\alpha_1 = -\frac{\beta_1}{t_{12}} t_{11}, \quad (9)$$

which gives

$$\beta_2 = \frac{\gamma_2}{\gamma_1} \frac{t_{12}^2}{\beta_1}. \quad (10)$$

Now we can proceed with an equation which gives the same threshold currents for the middle and the beginning (end) of the linac using (1):

$$\sqrt{\frac{\beta_0 \beta_2}{\gamma_0 \gamma_2}} = \frac{\beta_1}{\gamma_1}. \quad (11)$$

Now we can find the initial beta-function:

$$\beta_0 = \frac{\gamma_0}{\gamma_1} \frac{\beta_1^3}{t_{12}^2}. \quad (12)$$

And from Eq. 4 we get:

$$\beta_1 = \frac{m_{11}^2 \beta_1^3}{t_{12}^2} - 2\frac{\alpha_0 m_{11} m_{12} \gamma_1}{\gamma_0} + \frac{1+\alpha_0^2}{\beta_1^3} t_{12}^2 m_{12}^2. \quad (13)$$

After the minimization over α_0 one can find the initial Twiss parameters:

$$\beta_0 = \sqrt{\frac{\gamma_1}{\gamma_0} \frac{m_{12}^3}{t_{12}}}, \quad \alpha_0 = m_{11}\sqrt{\frac{\gamma_1}{\gamma_0} \frac{m_{12}}{t_{12}}}. \quad (14)$$

Using Elegant program we can find the matrix elements of the cryomodules: m_{11}= -0.835, m_{12}= 1.62 m. and t_{12}= 7.261 m. And finally we get the initial parameters: α_0 = -1.421 and β_0= 2.757 m. As we already said the role of the triplet of quadrupole magnets is to change the sign of the alpha-function. It should be noted that the initial parameters we found there are located at the entrance to the cavity but not to the cryomodule (where it is about 1 m of a free drift Fig. 2), therefore we should send it back. The final optic is presented in Fig. 8.

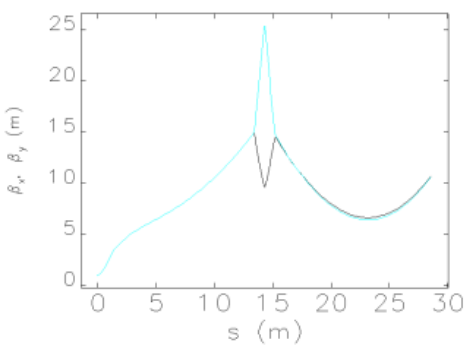

Figure 8: Optics design of the preinjection linac.

The value of the threshold current for the same mode as in the part about direct injection scheme is I_{th} = 1.64 A. As we said before our goal was to have the same values of the threshold currents for all cavities in the linac. But in our model we assumed the same values for the first and the last cavity of the cryomodule in fact we got it the same but the value in the middle of cryomodule is higher (one can see this already from the Fig. 8) - about 2.5 A. In the next part we discuss the optics in the main Linac.

Main Linac

The main difference for the optic design between two schemes with direct injection and with a preinjector is that in the scheme with two stage injection the initial energy in the main linac is 250 MeV instead of 7 in the scheme with a direct injection. Therefore this strongly improves the optics. Because the quadrupole magnets which focus the beam on the low energies (>250 MeV) will also focus the beam on the high energies (<6 GeV).

On such high energies an RF focusing can be neglected and the cavity is like a free drift with acceleration. Therefore we calculate the optic in the following way: for the first half of the linac we adjust the triplets between the cryomodules in such a way that the beam will go like in a free drift with initial/final beta-functions about the length of the cryomodule (Fig. 9). The second part we assume to be symmetrical with the same optics on the deceleration, which is given from right to left in Fig. 9.

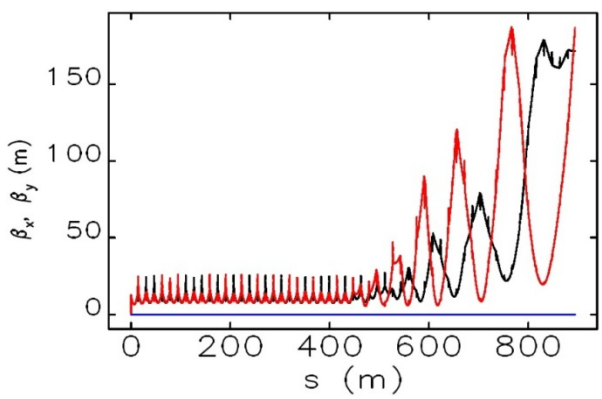

Figure 9: Two stage injection scheme.

For the first/last cavities estimations give the threshold current about 4 A and about 35 A for the middle of the linac for the same mode parameters as we used before.

Scalable scheme of FSF

In this part we present an upgrade of the acceleration scheme of FSF which was presented in [13]. In this scheme the acceleration in the preinjection linac and in two main linacs is assumed to be scalable. The injection energy is assumed to be E_0 = 10 MeV. The final energy of

a beam E_{fin} = 6 GeV, and E_{linac} = 960 MeV and E_{preinj} = 230 MeV are the energy gains in the main linacs and in the preinjection linac correspondingly. So our main scheme of FSF is now looks like it presented in Fig. 10.

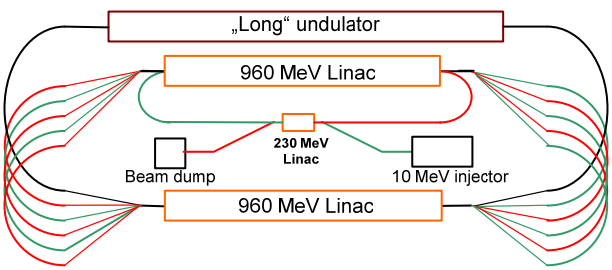

Figure 10: New scheme of a scalable FSF.

This change for the scalable facility was made because of the spreader design. A design of the spreader for 6 arcs is quite complicated and if the energy is changed somewhere due to unforeseen circumstances we could change field gradients of cavities in a proportional way to use the same spreader, therefore we would like to keep constant the deviations of the energies on different passes through the spreader. But it should be noted that accelerating gradients are different in the preinjector and in the main linacs.

Optic in the preinjection linac was optimized in the same way as it was described earlier in the preinjector subsection and it is similar to the Fig. 8.

The strengths of the quadrupoles were optimized to have the minimum of the beta functions on the 1-st pass. Optic for the 3 passes through the first and the second main linacs is presented in Figs. 11, 12.

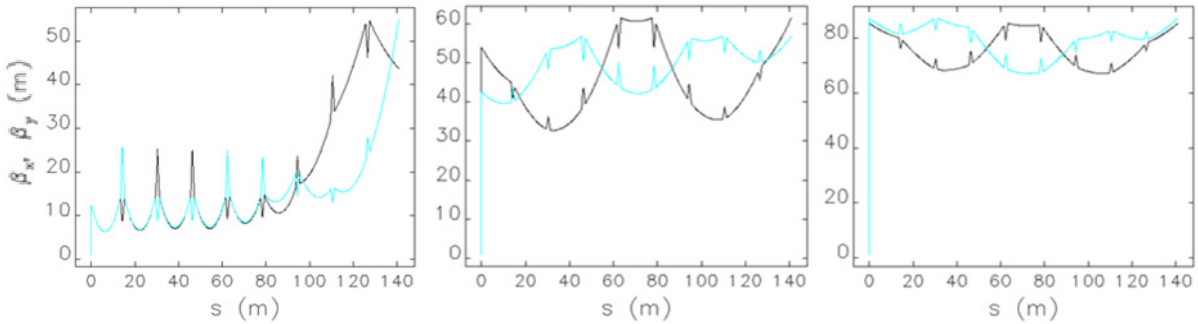

Figure 11: Optics design of the first 0.96 GeV linac. 3 passes on acceleration are presented from left to right correspondingly.

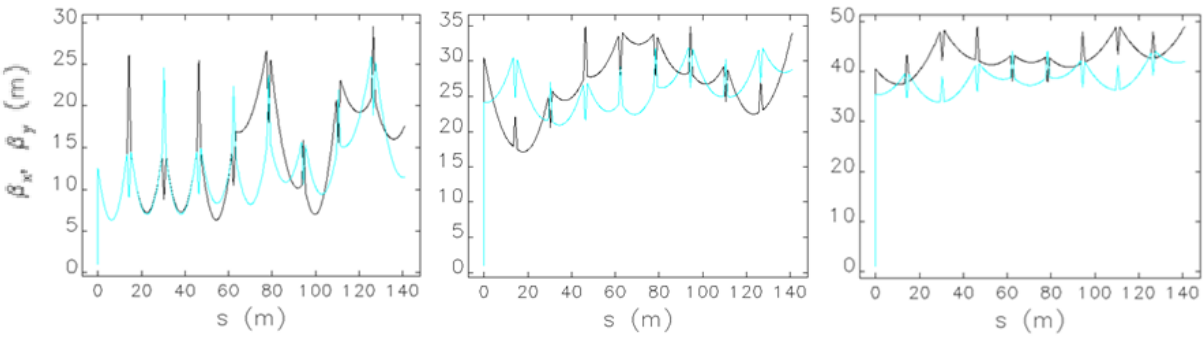

Figure 12: Optics design of the second 0.96 GeV linac. 3 passes on acceleration are presented from left to right correspondingly.

In both linacs the optic is assumed to have mirror symmetry at the middle of the 5-th cryomodule. Optic for deceleration is then shown from right to left in Figs. 11, 12.

The threshold currents for this optic solution can be estimated using the following equation (which is a combination of Eq. 1 and [8]):

$$I_{th} = \frac{2mc^3}{e\omega\left(\frac{R}{Q}\right)_d Q_d} \frac{1}{\sqrt{\sum_{m=1}^{5}\sum_{n=m+1}^{6}\frac{\beta_m\beta_n}{\gamma_m\gamma_n}}} \qquad (15)$$

and for a mode which we always used before one could get for the beginning of the first linac I_{th} = 0.73 A and for the second I_{th} = 2.34 A, when for the preinjector it is about 1.14 A. What means the instability should develop in the first main linac.

CONCLUSION

We summarize the results of the threshold currents for different schemes in Table 1.

Table 1: Estimations of the threshold currents

Scheme	I_{th}, A
Direct injection	~0.4
Two stage injection	~1.64
Scalable FSF	~0.73

As one can see from the Table 1 from all 3 schemes the highest threshold current is given for the scheme with two stage injection and one turn. For the scheme of FSF the threshold current is about factor of 2 lower but it has a 3 times shorter main linac what makes it cheaper and smaller.

It should be noted that the values in table 1 are just the estimations of the threshold currents. These estimations were made assuming that it is only one mode in a cavity. In principle this is the comparison of the square roots in the denominator of Eq. 1 for the different cavities and different injection schemes. Therefore such problems like coupling and overlapping of the different modes are not taken into account. These problems will decrease the threshold current and, therefore, should be taken into account later.

REFERENCES

[1] Y. Petenev et al., "Feasibility Study of an ERL-Based GeV scale Multi-turn Light Source", IPAC2012, New Orleans, USA.

[2] Claude M. Lyneis, Michael S. McAshan, Roy E. Rand, H. Alan Schwettman, Todd I. Smith and John P. Turneaure, The Stanford Superconducting Recyclotron, IEEE Transactions on Nuclear Science, Vol. NS-26, No. 3, June 1979.

[3] P.Axel, L.S.Cardman, H.D.Graef, A.O.Hanson, R.A.Hoffswell, D.Jamnik, D.C.Sutton, R.H.Taylor, and L.M.Young, Operating Experience with MUSL-2, IEEE Transactions on Nuclear Science, Vol. NS-26, No. 3, June 1979.

[4] R.E. Rand and T.I. Smith, Beam optical control of beam breakup in a recirculating electron accelerator, Particle accelerators, Vol. 11, pp. 1-13 (1980).

[5] J.J. Bisognano, R.L. Gluckstern, in Proceedings of the 1987 Particle Accelerator Conference, Washington, DC (IEEE Catalog No. 87CH2387-9), pp. 1078-1080.

[6] G.A. Krafft, J.J. Bisognano, in Proceedings of the 1987 Particle Accelerator Conference, Washington, DC (IEEE Catalog No. 87CH2387-9), pp. 1356-1358.

[7] G.H. Hoffstaetter, I.V. Bazarov, „Beam-breakup instability theory for the energy recovery linacs", Phys. Rev. ST AB 7, 054401 (2004).

[8] E. Pozdeyev, et al., "Multipass beam breakup in energy recovery linacs", NIM A 557 (2006) 176-188.

[9] N.A. Vinokurov et al., Proc. of SPIE Vol. 2988, p. 221 (1997).

[10] J. Rosenzweig, L. Serafini. "Transverse particle motion in radio-frequency linear accelerators". Phys. Rev., E49 (1994), p. 1601.

[11] M. Borland, "Elegant: A Flexible SDDS-Compliant Code for Accelerator Simulation," APS LS-287, 2000.

[12] A.N. Matveenko, et al., "Status of the B*ERL*inPro optics design", Proc. of IPAC'11, pp.1500-1502.

[13] Y. Petenev et al., "Linac optics design for multi-turn ERL light source", LINAC2012, Tel Aviv, Israel.

START-TO-END BEAM DYNAMIC SIMULATIONS FOR FEMTO-SCIENCE-FACTORY FEASIBILITY STUDY*

T. Atkinson†, A. Bondarenko, A. Matveenko, Y. Petenev,
Helmholtz-Zentrum Berlin für Materialien und Energie GmbH (HZB), Germany.

Abstract

Design studies for a future multi-turn ERL based light source at HZB are being investigated. The Femto-Science-Factory will provide its users with ultra-bright photons of angstrom wavelength at 6 GeV. The FSF is intended to be a multi-user facility and offer a wide variety of operation modes. A low emittance $\sim 0.1\,\mu$m rad mode will operate in conjunction with a short-pulse $\sim$10 fs mode. This paper reports on the first results of the start-to-end beam dynamic simulations for both modes. Higher order geometric and chromatic aberration terms have been suppressed using both multipole magnets and biased off-crest acceleration. The influence of the collective effects (coherent synchrotron radiation) on the transversal emittance is minimised by adjusting the horizontal phase advance.

INTRODUCTION

This paper continues on from a recent Analysis of Injection and Recovery study[1] for Multi-turn ERL based light sources and highlights the physical limitations when trying to offer interchangeable modes and preserve beam quality.

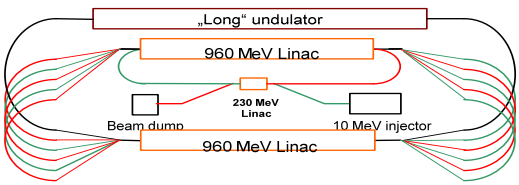

Figure 1: Schematic of the FSF Multi-Turn ERL.

The main design parameters of the FSF are listed in Table 1 and Fig. 1 shows the layout of the light source. In this scheme the acceleration of the whole FSF is constrained to be scalable. This modification relaxes the design of the vertical spreaders, so that if the energy is changed, due to possible upgrades or unforeseen circumstances one would simply adjust the field gradient in the cavity rather than redesign the spreader. Using the scaling formula $E_f = (1+2kN)(E_i+E_{pre})$, an SRF injector based on the design parameters of BERLinPro[2], injects the $E_i = 10\,MeV$ electron beam into a $E_{pre} = 230\,MeV$ preinjector accelerator. From here onwards two equally long linacs are continually traversed each with $N = 3$ passes until the $E_f = 6\,GeV$ final beam energy is reached. Choosing a suitable value $k = 4$ sets the main linacs to both $960\,MeV$.

Table 1: Main design parameters of FSF

Parameter	Low Emittance Mode	Short Pulse Mode
Preinjector (MeV)	230	
Main Linacs (MeV)	960	
Final Energy (GeV)	6	
Charge (pC)	15	4
Emittance (mm mrad)	0.1	0.4
Bunch Length (fs)	2000	10

Each Arc contains straight sections for undulators and in the final energy Arc 3000 period long of 40 mm period length undulators are foreseen.

The higher energy injection into the independent orbit ERL recirculator has naturally modified the beam dynamics from previous studies[3]. The new optic in the linacs has been optimised for the highest Beam Break Up threshold[1]. In this paper the remaining optic with regards to transversal and longitudinal emittance growth are discussed.

TRANSVERSAL EMITTANCE PRESERVATION

The difference in the two modes with regards to the lattice design occurs in the low energy section of the machine. For the Low Emittance Mode (LEM) a beam of higher charge is accelerated on crest in all of the linacs and circulates round isochronous Arcs. The Short Pulse Mode (SPM) however relies on achromatic arcs for the telescopic compression technique[3] removing the correlated energy spread due to the off-crest acceleration. The modes share common high energy arcs where radiation effects play an important role in emittance growth and will be firstly addressed.

High Energy Arcs

Consider the geometrical parameters of Coherent Synchrotron Radiation (CSR) as described in [4]. Taking the

*Work supported by German Bundesministerium für Bildung und Forschung, Land Berlin, and grants of Helmholtz Association VH NG 636 and HRJRG-214.

† terry.atkinson@helmholtz-berlin.de

FSF beam properties, the characteristic radiation length a, is smaller than the deviation of the tangent from the circulating beam at the overtaking distance L_t, and with it the vacuum chamber diameter D, $a < L_t < D$, hence a 1D model without shielding will suffice [5]. The transversal CSR shift $(\delta x, \delta x')$ depends only on the longitudinal bunch profile and the slice coordinate.

For two consecutive identical isochronous bends, the longitudinal bunch shape does not change and the bunch dynamics are identical if the additional relative energy spread δ_{CSR} due to CSR produced in the first bend is small enough in the chosen dispersive section, hence $\delta_{CSR} R_{56} << \sigma_z$. Let the bends have a horizontal transformation matrix M_x. In the first bend, particles experience shifts δx and $\delta x'$ due to CSR. In the second bend these deviations undergo betratron oscillations and exactly the same shifts δx and $\delta x'$ are simply added Eq. 1 to them once more.

$$\begin{aligned}\begin{pmatrix}\delta x\\ \delta x'\end{pmatrix}_2 &= \begin{pmatrix}\delta x\\ \delta x'\end{pmatrix}_0 + M_x \begin{pmatrix}\delta x\\ \delta x'\end{pmatrix}_0 \\ &= \left(I(1+cos\mu_x) + Jsin\mu_x)\right) \begin{pmatrix}\delta x\\ \delta x'\end{pmatrix}_0\end{aligned} \tag{1}$$

If the betatron phase $\mu_x = \pi$ the impact of CSR on the transversal emittance is null[6]. The same effect can be achieved for a system of N identical isochronous bends. The CSR shift is then given by Eq. 2.

$$\begin{aligned}\begin{pmatrix}\delta x\\ \delta x'\end{pmatrix}_N &= \sum_{n=0}^{N} M_x^n \begin{pmatrix}\delta x\\ \delta x'\end{pmatrix}_0 \\ &= \left(I\sum_{n=0}^{N} cos(n\mu_x) + J\sum_{n=0}^{N} sin(n\mu_x)\right) \begin{pmatrix}\delta x\\ \delta x'\end{pmatrix}_0\end{aligned} \tag{2}$$

Now if $\mu_x = 2\pi \cdot k/N$ where k is an integer, the impact of CSR on the transversal emittance is again nullified.

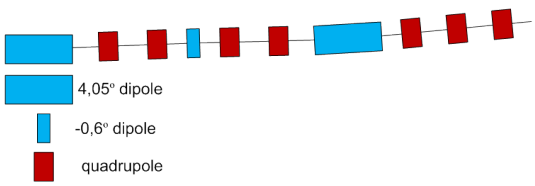

Figure 2: Schematic of a cell with anti-magnet.

Consider a 7.05 ° cell of a 30 ° bend as shown in Fig. 2. Here long dipoles (blue) of bending angle 4.05 ° are separated by quadrupoles (red) and a short -0.6 ° bend anti-magnet dipole (also blue) that keeps the quadrupole strength low (no need to actively change the sign of the dispersion to ensure $R_{56} = 0$). Fig. 3 shows the beta-functions for a 30 ° bend of horizontal phase advance $\mu_x = 2\pi \cdot 3/4$. There are four quadrupoles at each end to match the twiss parameters to those needed for the undulator sections between the Arcs.

When simulating a 15 pC, 10 fs input bunch using CSRtrack[7] the relative energy spread δ_{CSR} produced in

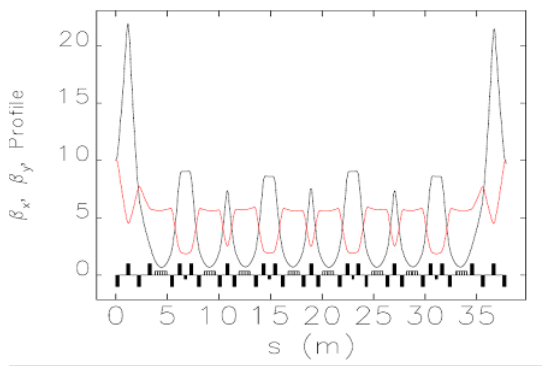

Figure 3: Beta functions in the 30 ° bend.

one cell can be estimated[8] as $\delta_{CSR} \sim q/\sigma_z^{4/3} \sim 10^{-4}$ and is depicted in Fig. 4. The emittance growth from each 7.5 ° bending cell is almost fully compensated Fig. 5 for a 30 ° Arc.

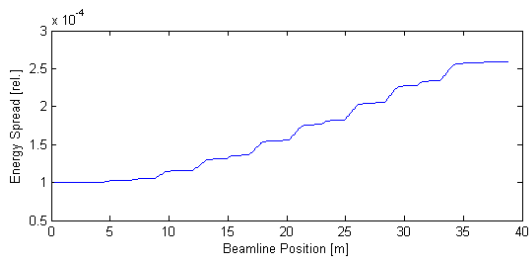

Figure 4: Relative energy spread along the 30 ° bend.

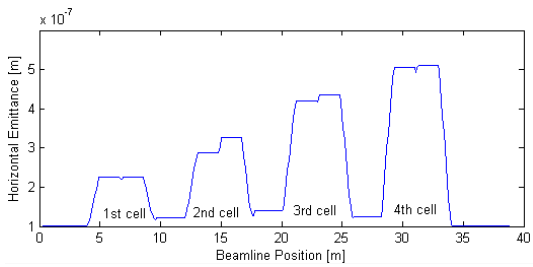

Figure 5: Normalised transversal emittance along the 30 ° bend.

The bends described have been implemented into the FSF optic of the 180 ° High Energy Arcs. It has been found however that especially for the short pulse mode, the second order aberrations also play a significant role in the causes of emittance growth, the next section describes the suppression techniques currently being investigated.

2nd Order Aberrations

Rather than using multipoles to manipulate "all" the higher matrix terms in order to optimise the chromatic dependence of the phase advance; $\xi = \Delta\xi/(\Delta p/p)$ the transfer line chromaticity, a simpler approach has been undertaken to find the key 2nd order terms which stimulate

traversal emittance growth. Consider the chromatic aberrations in the horizontal plane given by Eq. 3.

$$\begin{aligned} x_1 &= T_{161}\delta_0 x_0 + T_{162}\delta_0 x_0' + ... \\ x_1' &= T_{261}\delta_0 x_0 + T_{262}\delta_0 x_0' + ... \end{aligned} \quad (3)$$

Using these linear terms of the chromatic aberration, one can approximate the emittance change as Eq. 4.

$$\begin{aligned} \varepsilon_x^2 &= < x_1^2 >< x_1'^2 > - < x_1 x_1' >^2 \quad (4) \\ &= < (T_{161}\delta x + T_{162}\delta x')^2 >< (T_{261}\delta x + T_{262}\delta x')^2 > \\ &- < (T_{161}\delta x + T_{162}\delta x')(T_{261}\delta x + T_{262}\delta x') >^2 \end{aligned}$$

many like terms simply cancel out

$$\begin{aligned} \varepsilon_x^2 = \Big\{ & (T_{161}^2 T_{261}^2 + T_{162}^2 T_{261}^2) < \delta^2 x^2 >< \delta^2 x'^2 > \\ & + 4T_{161}T_{162}T_{261}T_{262} < \delta^2 x x' >^2 \\ & - \\ & + 2T_{161}T_{162}T_{261}T_{262} < \delta^2 x^2 >< \delta^2 x'^2 > \\ & + (T_{161}T_{262} + T_{162}T_{261})^2 < \delta^2 x x' >^2 \Big\} \end{aligned}$$

$$\begin{aligned} \varepsilon_x^2 = & (T_{161}T_{262} - T_{162}T_{261})^2 * \\ & \{ < \delta_0^2 x_0^2 >< \delta_0^2 x_0'^2 > - < \delta_0^2 x_0 x_0' >^2 \} \end{aligned} \quad (5)$$

One can interpret Eq. 5 as a useful tool to suppress the transverse emittance growth. By implementing two families of sextupoles so that for the horizontal plane $T_{161}T_{262} = T_{162}T_{261}$ and likewise for the vertical plane $T_{363}T_{464} = T_{364}T_{463}$ the magnitude of the chromatic emittance growth is dramatically reduced.

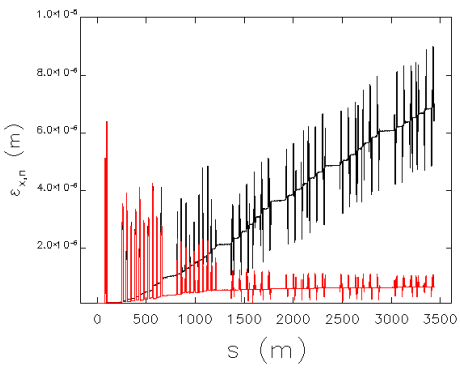

Figure 6: Correction of the 2nd order aberrations.

Fig. 6 demonstrates this concept over the complete 3.5 km long acceleration stage of the FSF to the long undulator section, with a chromatic perturbation in the preinjector Arc. The curves shown are both for the horizontal plane, the wavering effect due to the dispersion show the six Arcs and between them the linac sections. The Arcs containing sextupoles (red) using Eq. 5 reduce the emittance growth due to 2nd order aberrations in this example for the short pulse mode by almost a magnitude.

This new approach gives comparable results to standard chromaticity optimisation techniques but more importantly relaxes the restrictions on other essential 2nd order terms such as T_{566} which are additionally optimised to aid the longitudinal dynamics during bunch compression.

LONGITUDINAL EMITTANCE PRESERVATION

The longitudinal emittance compensation scheme first described in [3] uses the higher order magnetic terms created in the Arc and the off-crest acceleration Eq. 8 to recover the longitudinal emittance of the injector. Using the linacs relative energy Eq. 6 and the Arcs bunch length Eq. 7 variations respectively one can calculate the emittance variation across the two stages as follows.

$$\begin{aligned} & LINAC \\ & \delta_1 = \delta_0 + R_{65}c\Delta t_0 + T_{655}(c\Delta t_0)^2 \quad (6) \\ & c\Delta t_1 = c\Delta t_0 \end{aligned}$$

$$\begin{aligned} & +ARC \\ & \delta_2 = \delta_1 \\ & c\Delta t_2 = c\Delta t_1 + R_{56}\delta_1 + T_{566}\delta_1^2 \quad (7) \end{aligned}$$

Keeping only second order terms, assuming $\delta_0 = 0$ and substituting Eq. 6 and Eq. 7 the emittance can be approximated as Eq. 8

$$\begin{aligned} \epsilon_z^2 &= < (c\Delta t_2)^2 >< \delta_2^2 > - < (c\Delta t_2 \delta_2) >^2 \quad (8) \\ \epsilon_z^2 &= \left(T_{566}R_{65}^3 - T_{655}\right)^2 < (c\Delta t_0)^4 >< (c\Delta t_0)^2 > \end{aligned}$$

The accelerating phase ϕ determines both the R_{65} and T_{655} terms and sextupoles in the Arc can adjust T_{566} to compensate longitudinal emittance growth. Fig. 7 shows the recovery of normalised longitudinal emittance (black) using sextupoles in the first two Arcs with the optimum T_{566} for the given linac phase.

The emittance then slowly starts to increase (between s=1→6 km) due to radiation effects producing the unwanted energy spread. Shown also is the bunch length (red) along the whole machine. The logarithmic plot (where 15→1 fs), shows an optic producing a bunch length of less then 10 fs at the long undulator section at the half way point along the machine.

The optimum T_{566} setting is extremely sensitive to the linac phase setting Eq. 9 and only technical feasible values for T_{566} are produced for off crest acceleration, hence the main linacs in the SPM are +10 ° and -20 ° respectively.

$$T_{566} = \frac{T_{655}}{R_{65}^3} \sim \frac{c}{2\omega}\left(\frac{E}{\Delta E}\right)^2 \frac{1}{\phi^3} \quad (9)$$

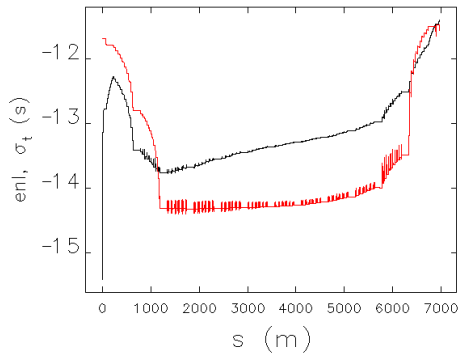

Figure 7: Log plot of the longitudinal bunch properties.

Each off-crest acceleration is followed by achromatic Arcs of positive R_{56} values constitute the telescopic compression scheme in the lower energy acceleration sections.

AT THE LONG UNDULATOR

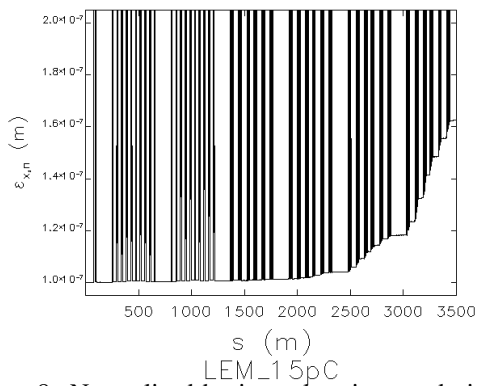

Figure 8: Normalised horizontal emittance during the acceleration stage for the LEM.

Table 2: Simulation results at long undulator entrance

Type	ε_{nx} (mm mrad)	ε_{ny} (mm mrad)	St (fs)	$\Delta E/E$ (10^{-4})	Charge (pC)
Input	0.10	0.10	2000	0.10	Gaussian
SPM	0.22	0.11	6	10.2	1
SPM	0.21	0.10	20	7.01	5
LEM	0.16	0.10	2000	1.96	15

The machine optic was optimised independent of input bunch parameters. The first results from tracking a low emittance Gaussian input bunch to the long undulator are given in Table 2 and compare well with the expectations Table 1 of a high brilliance light source.

For the low emittance mode Fig. 8, with all the suppression techniques previously described in place, the transversal emittance mainly grows due to classical radiation effects and can be analytically estimated using the integral Eq. 10 of the 6 GeV Arc. One can then cross reference the emittance growth by simply using Eq. 11.

$$I_5 = \int \frac{H}{|\rho|^3} ds \sim 2 \cdot 10^{-5} \tag{10}$$

$$\Delta(\gamma\varepsilon) \simeq 4 \cdot 10^{-8} E^6 I_5 = 0.04\,\text{mm mrad} \tag{11}$$

START-TO-END

Injection

Producing a 6D ultra low emittance bunch to match the FSF parameter expectations remains an essential part of this and many other future projects. ASTRA[9] simulations from the photo-injector, through the Booster and Merger to the preinjector linac remain ongoing.

Table 3: Injector ASTRA simulations

Pos.	ε_{nx} (mm mrad)	ε_{ny} (mm mrad)	ε_z (keV mm)	Ss (mm)	$\Delta E/E$ (10^{-4})	Energy (MeV)
Gun	0.15	0.15	0.40	0.65	2.10	2.80
Booster	0.16	0.16	1.20	0.67	3.10	10.0
Merger	0.28	0.18	1.17	0.70	3.79	10.0

Table 3 shows a subtle beam transformation through the space charge dominated injection process to produce a low emittance beam in all dimensions.

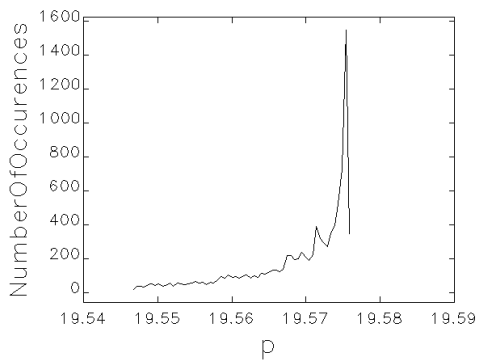

Figure 9: Energy distribution of input beam at 10 MeV.

Fig. 9 reiterates the very low rms energy spread for this input file. These beam distributions are then converted, matched and tracked onwards using Elegant[10].

A possible scenario to make good use of each 50 m long transfer line between the 230 MeV preinjector and Arcs is

to envisage optic that may be used at a future date to aid the non-linear beam dynamics. For instance on the acceleration side, green in Fig. 1, a series of Laser Heater undulators could be implemented and used to suppress the micro-bunching instability at the expense of the longitudinal emittance. Such a scheme could based on [11] where a TiSa laser is used to overlap and interact with the electron beam.

$$\lambda = \frac{d}{2\gamma^2}(1 + \frac{K^2}{2}) \tag{12}$$

Considering Eq. 12, a laser wavelength of $\lambda = 800\,nm$ and common undulator parameters are suitable for interaction at this relatively low energy stage ($\gamma = 480$).

On the deceleration side, an optic based on a pseudo-reflector[12] (rotator) could be included to interchange the x-y motion. Such a rotation in bunch coordinates has been theoretically shown to suppress beam breakup and increase the threshold current in the preinjector linac.

Energy Loss Considerations

It is envisaged that the total energy loss due to radiation in the Arcs alone will exceed the 10 MeV injection energy of the FSF. Considering the contribution from ISR using Eq. 13 in each Arc of bending radius R.

$$U\,[MeV] = 0.088E^4\,[GeV]/R\,[m] \tag{13}$$

The total energy loss due to ISR alone is 15 MeV. In a similar manner, the total energy loss due to ISR in the abundance of undulators can be calculated using Eq. 14.

$$U\,[keV] = 0.633E^2\,[GeV]B^2[T]L[m] \tag{14}$$

Given the present undulator parameters, this amounts to an energy loss of 6.4 MeV during acceleration. These values coupled with the addition of energy loss due to CSR ΔE_{CSR} far exceeds an injection energy of 10 MeV. Using the rectangular bunch[13] model the ΔE_{CSR} per turn can be approximated as Eq. 15.

$$\Delta E_{CSR} \simeq -\left(\frac{3^{\frac{2}{3}}e^2N^2}{l_b^{\frac{4}{3}}R^{\frac{2}{3}}}\right)(R\phi_m)* \left(1 + \frac{3^{\frac{1}{3}}4}{9}\frac{l_b^{\frac{1}{3}}}{R^{\frac{1}{3}}\phi_m}\left[\ln\left(\frac{l_b\gamma^3}{R}\right) - 4\right]\right) \tag{15}$$

The contribution in the LEM is negligible compared to that of the SPM which is given in Table 4 for different bunch charge.

Table 4: Energy loss due to radiation, acceleration stage

SPM	ISR		CSR	
	Arc	Und.	1 pC	5 pC
Energy loss (MeV)	15.5	6.4	3.3	16.4

Booster modules were implemented in the simulations to compensate for this energy loss due to radiation. These modules operate without energy recovery and require approximately 300 kW and 200 kW of power for the LEM and SPM respectively.

Low Emittance Mode

The transverse emittance growth is kept to a minimum throughout the whole 7 km machine, Fig. 10 to utilize the undulator radiation in all acceleration and deceleration sections in order to maximize user potential. Plotted is both the horizontal (black) and vertical (red) normalised emittance.

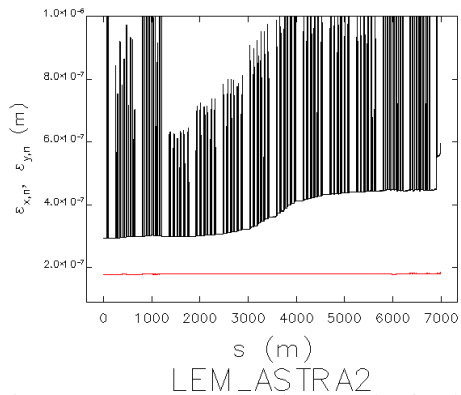

Figure 10: Start-to-end emittance plot for the LEM.

The horizontal plane follows the same fate as previously discussed, with the emittance growth mainly due to incoherent radiation, whereas the vertical values relatively remain constant until the small wavering in the final stages due to the increase in energy spread Fig. 11 during deceleration. Neglecting the correlated content the energy spread increase factor is approximately given by the ratio of the energy on deceleration $E_{in}/E_{out} = 24$.

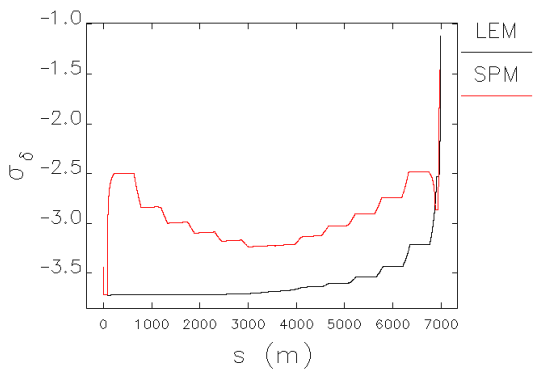

Figure 11: Log plot of the energy spread for both modes.

Short Pulse Mode Recovery Scheme

The complicated SPM relies on off-crest acceleration and deceleration, achromatic Arcs with telescopic $\mp R_{56}$ (de)compression and the charge dependent, bunch length limiting effects from coherent radiation is discussed here.

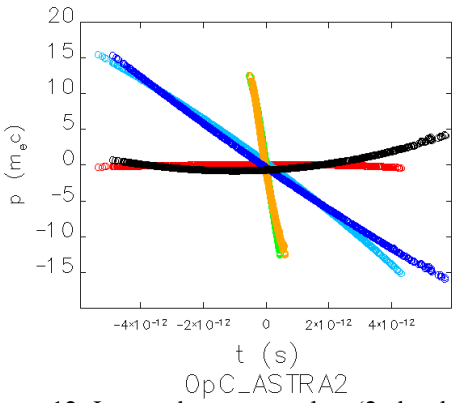

Figure 12: Long. phase space plots (2nd order theory).

Fig. 12 shows the theory of the telescopic compression without radiation effects during acceleration (red, light blue, green) in the first two Arcs up to a beam energy of 2 GeV using off-crest acceleration $\phi_1 = +10\,^\circ$, $\phi_2 = -20\,^\circ$ and positive R_{56} values in both Arcs. Also shown is the symmetric deceleration (orange, dark blue, black) from 2 GeV back to the preinjector for an ASTRA input bunch. On recovery the phase space plots are made to overlap and follow the trend used during acceleration by setting $\phi_{1,2} \rightarrow \pi^c$ so that $\phi_1 = 190\,^\circ$, $\phi_2 = 160\,^\circ$ and creating optic with negative R_{56} values.

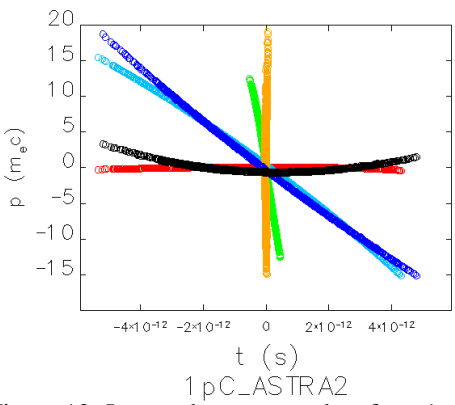

Figure 13: Long. phase space plots for a 1 pC beam.

However in reality, when radiation effects are taken into account, the recovery is not perfect. The increase in energy spread, Fig. 13 (orange compared to green) during the high energy passes requires a slightly modified optic to match the final beam properties during decompression. It is also envisaged that multipoles can once again be used in the deceleration stages to correct the 2nd order effects or enhance the chromaticity[14] to suppress beam breakup. The suitability of this optic is still under investigation.

Table 5: Simulation results at the Beam Dump entrance

Type	ε_{nx} (mm mrad)	ε_{ny} (mm mrad)	St (ps)	$\Delta E/E$ (%)	Charge (pC)
SPM	0.48	0.20	2.24	3.76	1
LEM	0.36	0.18	4.02	7.60	15

Simulation results of the recovery of the beam to the dump are given in Table 5. Although the energy spread of the beam in both modes at the entrance to the dump line is approximately 5%, the beam could be safely transported to the dump using a low dispersive optic.

REFERENCES

[1] Y. Petenev et al., "Multi-Turn ERL Based Light Source: Analysis of Injection and Recovery Schemes", IPAC2013, China.

[2] J. Knobloch et al., Status of the BERLinPro Energy Recovery Linac Project, IPAC 2012, New Orleans, July 2012.

[3] T. Atkinson et al., "Feasibility Study of Short Pulse Mode Operation for Multi-Turn ERL light source", Linac12, Israel.

[4] Ya.S. Derbenev et al., "Transerve Effects of Microbunch Radiative Interaction", SLAC Report 7181, 1996.

[5] R.D. Ryne et al., "Large Scale Simulation of Synchrotron Radiation Using a Lienard-Wiechert Approach", IPAC 2012, New Orleans.

[6] J. Wu et al., PAC 2001, p.2866-2868.

[7] CSRtrack, http://www.desy.de/fel-beam/csrtrack/index.html.

[8] S.Di Mitri et al., "Cancellation of Coherent Synchrotron Radiation Kicks with Optic Balance", Physical Review Letters 110,014801,2013

[9] ASTRA code, A Space Charge Tracking Algorithm, http://tesla.desy.de/ meykopff/ 2012.

[10] M. Borland, "elegant: A Flexible SDDS-Compliant Code for Accelerator Simulation", Advanced Photon Source LS-287, September 2000.

[11] Z. Huang et al, "Measurement of the LCLS laser Heater and its impact on the x-ray FEL performance", SLAC-PUB-13854

[12] E. Pozdeyev, "Regenerative multipass beam breakup in two dimensions", Phys. Rev. ST AB 8, 054401

[13] E.L. Saldin et al, "On the Coherent Radiation of an Electron Bunch Moving in an Arc of a Circle", TESLA FEL 1996.

[14] V. N. Litvinenko, "Chromaticity of the lattice and beam stability in energy recovery linacs", Phys. Rev. ST AB 15, 074401 (2012)

LONGITUDINAL STABILITY OF MULTITURN ERL WITH SPLIT ACCELERATING STRUCTURE

Ya. V. Getmanov#, O. A. Shevchenko, Budker INP, Novosibirsk, Russia
N. A. Vinokurov, Budker INP, Novosibirsk, Russia and KAERI, Daejon, Korea

Abstract

Some modern projects of the new generation light sources use the conception of multipass energy recovery linac with split (CEBAF-like) accelerating structures [1 - 5]. One of the advantages of these light sources is the possibility to obtain a small bunch length. To help reduce it, the longitudinal dispersion should be non-zero in some arcs of the accelerator. However small deviations in voltages of the accelerating structures can be enhanced by induced fields from circulating bunches due to the dependence of the flight time on the energy deviation and the high quality factor of the superconducting radio-frequency cavities. Therefore, instabilities caused by interaction of electron bunches and fundamental modes of the cavities can take place. The corresponding stability conditions are discussed in this paper. Numerical simulations were performed for project MARS [4].

INTRODUCTION

The scheme of an ERL with two accelerating structures is shown in Fig. 1.

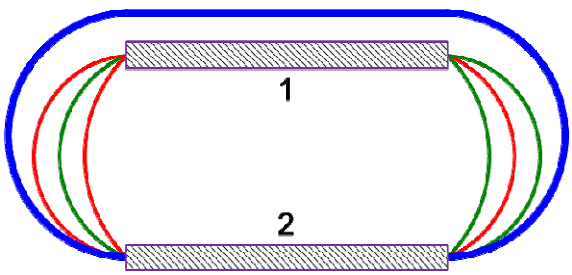

Figure 1: Scheme of ERL with two linacs.

Electrons are injected to the linac 1. After two passes through linac 1 and linac 2 they are used, for example, in undulators. After that electrons are decelerated.

There are four electron beams in each linac simultaneously. Each beam induced large voltage in the linac, but the sum is not so large. If the phases of the beams vary, the sum voltage also varies, and initially small phase deviation may increase due to the dependence of flight times through arcs on the particle energy. This longitudinal instability is considered in our paper.

THEORY

The Voltage Equations

To simplify the picture, consider each linac as one RF cavity. Its equivalent circuit is shown in Fig. 2.

The gap voltage expression $U = L\,d\left(I_b + I_g - C\,dU/dt - U/R\right)/dt$, I_b and I_g are the currents of the beam and of the RF generator, leads to the standard equation

$$\frac{d^2U}{dt^2} + \frac{1}{RC}\frac{dU}{dt} + \frac{1}{LC}U = \frac{1}{C}\frac{d}{dt}\left(I_b + I_g\right) \qquad (1)$$

Taking the effective voltage on the linac with number α in the form $\mathrm{Re}(U_\alpha e^{-i\omega t})$ (ω is the frequency of the RF generator), one obtains:

$$\frac{2}{\omega}\frac{dU_\alpha}{dt} = \frac{i\xi_\alpha - 1}{Q_\alpha}U_\alpha + \rho_\alpha(I_{b\alpha} + I_{g\alpha}), \qquad (2)$$

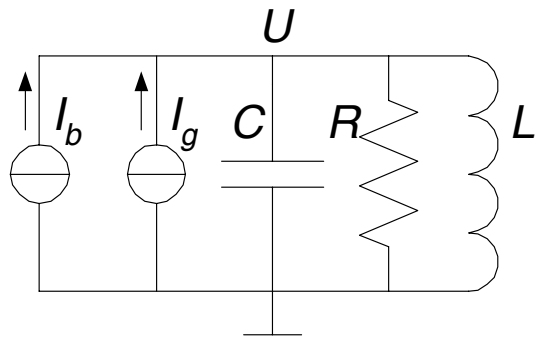

Figure 2: Equivalent circuit of the RF cavity.

where $\omega_\alpha = 1/\sqrt{L_\alpha C_\alpha} = (1 - \xi_\alpha/2Q_\alpha)\omega$ is the resonant frequency, $Q_\alpha = R_\alpha/\sqrt{L_\alpha/C_\alpha} >> 1$ is the loaded quality of the cavity, $\rho_\alpha = R_\alpha/Q_\alpha = \sqrt{L/C}$ and R_α are the characteristic and the loaded shunt impedances for the fundamental (TM_{010}) mode, and $I_{b\alpha}$ and $I_{g\alpha}$ are the complex amplitudes of the beam and (reduced to the gap) generator currents correspondingly. We are interested in the case of constant $I_{g\alpha}$. The beam currents $I_{b\alpha}$ depend on all U_α due to phase motion. Linearization of Eq. (2) near the stationary solution

$$U_{0\alpha} = \frac{R_\alpha}{1 - i\xi_\alpha}\left[I_{b\alpha}(\mathbf{U}_0) + I_{g\alpha}\right] \qquad (3)$$

gives:

$$\frac{2}{\omega}\frac{d\delta U_\alpha}{dt} = \frac{i\xi_\alpha - 1}{Q_\alpha}\delta U_\alpha + \qquad (4)$$

$$+\rho_\alpha\sum_\beta\left(\frac{\partial I_{b\alpha}}{\partial\,\mathrm{Re}\,U_\beta}\,\mathrm{Re}\,\delta U_\beta+\frac{\partial I_{b\alpha}}{\partial\,\mathrm{Im}\,U_\beta}\,\mathrm{Im}\,\delta U_\beta\right)$$

Strictly speaking, I_b depends on the values of U at previous moments of time, so Eq. (4) is valid only if the damping times Q_α/ω are much longer than the time of flight through the ERL.

The Stability Conditions

Considering the exponential solutions $\exp(\omega\lambda t/2)$ of system of linear differential equations Eq. (4), one can find the stability conditions. Indeed, the system Eq. (4) corresponds to the system of the linear homogeneous equations $\lambda\delta\mathbf{U}=\mathbf{M}\delta\mathbf{U}$ with the consistency condition $|\mathbf{M}-\lambda\mathbf{E}|=0$. Re($\lambda$) < 0 for all roots of this equation (i. e., eigenvalues of the matrix **M**) is the stability condition.

The stability condition for ERL with one linac was derived in paper [2]. In this case

$$\mathbf{M}=\begin{pmatrix}-\frac{1}{Q}+\rho\frac{\partial\,\mathrm{Re}\,I_b}{\partial\,\mathrm{Re}\,U} & -\frac{\xi}{Q}+\rho\frac{\partial\,\mathrm{Re}\,I_b}{\partial\,\mathrm{Im}\,U}\\ \frac{\xi}{Q}+\rho\frac{\partial\,\mathrm{Im}\,I_b}{\partial\,\mathrm{Re}\,U} & -\frac{1}{Q}+\rho\frac{\partial\,\mathrm{Im}\,I_b}{\partial\,\mathrm{Im}\,U}\end{pmatrix} \qquad (5)$$

and the characteristic equation is

$$\lambda^2-\lambda Tr(\mathbf{M})+|\mathbf{M}|=0 \qquad (6)$$

According to Eq. (5) the stability condition is

$$Tr(\mathbf{M})=\rho\left(\frac{\partial\,\mathrm{Re}\,I_b}{\partial\,\mathrm{Re}\,U}+\frac{\partial\,\mathrm{Im}\,I_b}{\partial\,\mathrm{Im}\,U}\right)-\frac{2}{Q}<0\,. \qquad (7)$$

One can say, that the beam "active conductivity" $\left(\partial\,\mathrm{Re}\,I_b/\partial\,\mathrm{Re}\,U+\partial\,\mathrm{Im}\,I_b/\partial\,\mathrm{Im}\,U\right)/2$ has not to exceed the linac active conductivity $(\rho Q)^{-1}$.

For the ERL with two linacs

$$\mathbf{M}=\begin{pmatrix}\rho_1\frac{\partial\,\mathrm{Re}\,I_{b1}}{\partial\,\mathrm{Re}\,U_1}-\frac{1}{Q_1} & \rho_1\frac{\partial\,\mathrm{Re}\,I_{b1}}{\partial\,\mathrm{Im}\,U_1}-\frac{\xi_1}{Q_1} & \rho_1\frac{\partial\,\mathrm{Re}\,I_{b1}}{\partial\,\mathrm{Re}\,U_2} & \rho_1\frac{\partial\,\mathrm{Re}\,I_{b1}}{\partial\,\mathrm{Im}\,U_2}\\ \rho_1\frac{\partial\,\mathrm{Im}\,I_{b1}}{\partial\,\mathrm{Re}\,U_1}+\frac{\xi_1}{Q_1} & \rho_1\frac{\partial\,\mathrm{Im}\,I_{b1}}{\partial\,\mathrm{Im}\,U_1}-\frac{1}{Q_1} & \rho_1\frac{\partial\,\mathrm{Im}\,I_{b1}}{\partial\,\mathrm{Re}\,U_2} & \rho_1\frac{\partial\,\mathrm{Im}\,I_{b1}}{\partial\,\mathrm{Im}\,U_2}\\ \rho_2\frac{\partial\,\mathrm{Re}\,I_{b2}}{\partial\,\mathrm{Re}\,U_1} & \rho_2\frac{\partial\,\mathrm{Re}\,I_{b2}}{\partial\,\mathrm{Im}\,U_1} & \rho_2\frac{\partial\,\mathrm{Re}\,I_{b2}}{\partial\,\mathrm{Re}\,U_2}-\frac{1}{Q_2} & \rho_2\frac{\partial\,\mathrm{Re}\,I_{b2}}{\partial\,\mathrm{Im}\,U_2}-\frac{\xi_2}{Q_2}\\ \rho_2\frac{\partial\,\mathrm{Im}\,I_{b2}}{\partial\,\mathrm{Re}\,U_1} & \rho_2\frac{\partial\,\mathrm{Im}\,I_{b2}}{\partial\,\mathrm{Im}\,U_1} & \rho_2\frac{\partial\,\mathrm{Im}\,I_{b2}}{\partial\,\mathrm{Re}\,U_2}+\frac{\xi_2}{Q_2} & \rho_2\frac{\partial\,\mathrm{Im}\,I_{b2}}{\partial\,\mathrm{Im}\,U_2}-\frac{1}{Q_2}\end{pmatrix} \qquad (8)$$

and the characteristic equation is (see, e. g., [6])

$$\lambda^4-S_1\lambda^3+S_2\lambda^2-S_3\lambda+S_4=0\,, \qquad (9)$$

where $S_1=\sum_{1\le k\le 4}A\begin{pmatrix}k\\k\end{pmatrix}=\sum_{1\le k\le 4}M_{kk}=Tr(\mathbf{M})$,

$$S_2=\sum_{1\le k<l\le 4}A\begin{pmatrix}k & l\\ k & l\end{pmatrix},\ S_3=\sum_{1\le k<l<m\le 4}A\begin{pmatrix}k & l & m\\ k & l & m\end{pmatrix},$$

and $S_4=A\begin{pmatrix}1&2&3&4\\1&2&3&4\end{pmatrix}=|\mathbf{M}|$ are the sums of main minors of the matrix **M**. The necessary conditions for stability (Re(λ) < 0 for all four roots of Eq. (9)) is positivity of all the coefficients of the polynomial Eq. (9). In particular, the only independent on detunings ξ_1 and ξ_2 condition $S_1 < 0$ gives

$$\rho_1\left(\frac{\partial\,\mathrm{Re}\,I_{b1}}{\partial\,\mathrm{Re}\,U_1}+\frac{\partial\,\mathrm{Im}\,I_{b1}}{\partial\,\mathrm{Im}\,U_1}\right)+\rho_2\left(\frac{\partial\,\mathrm{Re}\,I_{b2}}{\partial\,\mathrm{Re}\,U_2}+\frac{\partial\,\mathrm{Im}\,I_{b2}}{\partial\,\mathrm{Im}\,U_2}\right)<\frac{2}{Q_1}+\frac{2}{Q_2} \qquad (10)$$

The sufficient conditions are given by the Liénard-Chipart criterion [6]. It requires the positivity of of all the coefficients of the polynomial Eq. (9) and the third Hurwitz minor

$$S_1<0,\ S_2>0,\ S_4>0,\ \Delta_3=S_1\left(S_2S_3-S_1S_4\right)-S_3^2>0 \qquad (11)$$

In the simplest case of the isochronous ERL arcs the conductivity matrix is zero. Then it is easy to proof, that all stability conditions are satisfied.

As the qualities of the superconducting cavities are very large, it is interesting to consider the opposite limiting case, neglecting small terms $1/Q_{1,2}$ in the matrix Eq. (8). Then all stability conditions do not depend on the beam current. They depend only on the ratio ρ_1/ρ_2 and the beam conductivity matrix, which is fully defined by the ERL magnetic system.

The Conductivity Matrix

To proceed further, we have to specify the elements of the beam conductivity matrix in the stability conditions. The complex amplitude of the beam current I_b may be written in the form

$$I_{b\alpha}=-2I\sum_{n=0}^{N-1}\left(e^{i\varphi_{2n+\alpha-1}+i\psi_{2n+\alpha-1}}+e^{i\varphi_{4N-2n-\alpha}+i\psi_{4N-2n-\alpha}}\right)\approx$$
$$\approx I_{b\alpha}(\mathbf{U}_0)-2iI\sum_{n=0}^{N-1}\left(e^{i\varphi_{2n+\alpha-1}}\psi_{2n+\alpha-1}+e^{i\varphi_{4N-2n-\alpha}}\psi_{4N-2n-\alpha}\right) \qquad (12)$$

where I is the average beam current, $\varphi_{2n+\alpha-1}$ is the equilibrium phase for the n-th pass through the resonator with the number α (α = 1, 2), and N is the number of orbits for acceleration. The small energy and phase deviations ε_n and ψ_n obey the linear equations:

$$\varepsilon_{n+1}=\varepsilon_n+e\,\mathrm{Im}\left[U_{0\alpha(n)}e^{-i\varphi_n}\right]\psi_n+e\,\mathrm{Re}\left[\delta U_{\alpha(n)}e^{-i\varphi_n}\right], \qquad (13)$$

$$\psi_{n+1}=\psi_n+\omega\left(\frac{dt}{dE}\right)_{n+1}\varepsilon_{n+1}\,, \qquad (14)$$

where

$\alpha(2n)=1,\ \alpha(2n+1)=2$ *for* $0\le n\le N-1$ and

$\alpha(2n)=2,\ \alpha(2n+1)=1$ *for* $N\le n\le 2N-1$.

$(dt/dE)_n$ is the longitudinal dispersion of the n-th 180-degree bend. The initial conditions for the system of Eqs. (13) and (14) are, certainly, ε_0=0 and ψ_0=0, if we have no special devices to control them for the sake of the beam

stabilization, or other purposes. The solution of Eq. (13) and Eq. (14) may be written using the longitudinal sine-like trajectory S_{nk} and its "derivative" S'_{nk} (elements 56 and 66 of the transport matrix). These functions are the solutions of the homogenous system

$$S'_{n+1,k} = S'_{n,k} + e\,\mathrm{Im}\left[U_{0\alpha(n)}e^{-i\varphi_n}\right]S_{n,k}, \quad (15)$$

$$S_{n+1,k} = S_{n,k} + \omega\left(\frac{dt}{dE}\right)_{n+1} S'_{n+1,k}, \quad (16)$$

with the initial conditions $S_{k,k} = 0$, $S'_{k,k} = 1$. Then

$$\psi_n = e\sum_{k=0}^{n-1} S_{nk}\,\mathrm{Re}\left[\delta U_{\alpha(k)}e^{-i\varphi_k}\right], \quad (17)$$

$$\varepsilon_n = e\sum_{k=0}^{n-1} S'_{nk}\,\mathrm{Re}\left[\delta U_{\alpha(k)}e^{-i\varphi_k}\right]. \quad (18)$$

Substitution of Eq. (20) to Eq. (15) gives

$$\delta I_{b\alpha} = -2ieI\sum_{n=0}^{N-1}\{e^{i\varphi_{2n+\alpha-1}}\sum_{k=0}^{2n+\alpha-2} S_{2n+\alpha-1,k}\,\mathrm{Re}\left[\delta U_{\alpha(k)}e^{-i\varphi_k}\right] + e^{i\varphi_{4N-2n-\alpha}}\sum_{k=0}^{4N-2n-\alpha-1} S_{4N-2n-\alpha,k}\,\mathrm{Re}\left[\delta U_{\alpha(k)}e^{-i\varphi_k}\right]\} \quad (19)$$

For an ERL it needs to satisfy (at least approximately) the recuperation condition

$$\mathrm{Re}\left[U_{01}\sum_{n=0}^{N-1}\left(e^{-i\varphi_{2n}} + e^{-i\varphi_{4N-2n-1}}\right)\right] = 0$$
$$\mathrm{Re}\left[U_{02}\sum_{n=0}^{N-1}\left(e^{-i\varphi_{2n+1}} + e^{-i\varphi_{4N-2n-2}}\right)\right] = 0 \quad (20)$$

For the longitudinal stability it also needs to have longitudinal focusing for most of passes through the linac (see Eq. (12, 13)):

$$e\,\mathrm{Im}\left[U_{0\alpha(n)}e^{-\varphi_n}\right] < 0 \quad (21)$$

if all $(dt/dE)_n > 0$). Conditions Eq. (20) and Eq. (21) may be satisfied simultaneously, if ($0 \le n \le 2N-1$)

$$\arg(eU_{0\alpha(n)}e^{-i\varphi_n}) + \arg(eU_{0\alpha(4N-n-1)}e^{-i\varphi_{4N-n-1}}) = -\pi, \quad (22)$$

which leads to

$$\varphi_{4N-n-1} = \pi - \varphi_n + 2\arg\left(eU_{0\alpha(n)}\right) \quad (23)$$

Conditions Eq. (23) affords equality of beam energies after n-th and ($4N$-n)-th passes through a linac.

The Threshold Current

To make the stability condition Eq. (10) more explicit, consider a simple example. Assume that equilibrium phases are equal during acceleration. In this simplest case $\varphi_{2n} - \arg(eU_{01}) = \Phi_1$, $\varphi_{2n+1} - \arg(eU_{02}) = \Phi_2$ for $0 \le n \le N-1$. Eq. (20) defines the equilibrium phases for deceleration. Then Eq. (19) gives

$$e\rho_1 I\sin(2\Phi_1)\sum_{n=0}^{N-1}\sum_{k=0}^{N-1} S_{4N-2n-1,2k} + e\rho_2 I\sin(2\Phi_2)\sum_{n=0}^{N-1}\sum_{k=0}^{N-1} S_{4N-2n-2,2k+1} < \frac{1}{Q_1} + \frac{1}{Q_2} \quad (24)$$

SIMULATIONS

The Induced Voltage

To simulate the instability evolution one can use the turn-by-turn calculations of the voltage induced by each bunch. Passing through the cavity the electron excites the voltage oscillations on the cavity resonance frequency ω_r. Considering the bunch as the point with charge q one can calculate it induced voltage [9]

$$V_{\parallel}(t) = q\frac{\omega_r R_s}{Q}\cos(\omega_r t)\exp(-\frac{\omega_r}{2Q}t)H(t) \quad (25)$$

where R_s is the shunt impedance, Q is the loaded quality factor, $H(t)$ is Heaviside's step-function. As the recirculating frequency of the generator is close to resonance, but not equal, electrons will see the phase of induced voltage by previous bunch slightly changed. Let's consider two electron bunches pass the cavity from the same magnet arc. The distance difference between them is cT_g (considering the equal frequencies of the cavity and gun), the reference phases are the same and its deviations are $\delta\phi_1$, $\delta\phi_2$ respectively:

$$\omega_g t_{1,2} = 2\pi n + \phi_{ref} + \delta\phi_{1,2}, n \in N$$

Therefore the 2-nd bunch will see the induced voltage by 1-st bunch with phase

$$\omega_r(t_1 - t_2) = \frac{\omega_r}{\omega_g}\omega_g(t_1 - t_2) = \frac{\omega_r}{\omega_g}\left[2\pi + (\delta\phi_1 - \delta\phi_2)\right] \quad (26)$$

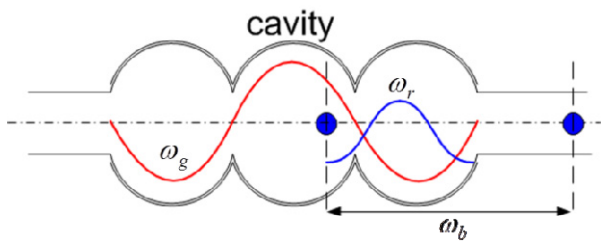

Figure 3. Frequencies in the bunch-cavity system

In case of bunches from different arcs, i.e. with different reference phases, the voltage phase is

$$\phi = \frac{\omega_r}{\omega_b}\left[2\pi(N_1 - N_2) + (\phi_{1ref} - \phi_{2ref}) + (\delta\phi_{1N_1} - \delta\phi_{2N_2})\right]$$

where N_1, N_2 – the numbers of RF-buckets.
Induced voltage by Nb bunches at the times $(t_1,\ldots,t_{Nb})$ in complex form $V_{\parallel}(t) = \mathrm{Re}\,W_{\parallel}(t)$ is

$$V_{\parallel}(t) = \mathrm{Re}\, W_{\parallel}(t - t_n) =$$

$$\mathrm{Re}\exp(i\omega_r t) q \frac{\omega_r R_s}{2Q} \exp(-i\omega_r t_n) \exp\left(-\frac{\omega_r}{2Q}(t - t_n)\right)$$

This formula can be transformed in phasors representation as the production bunch complex current $i(t)$ and complex voltage, induced by previous bunches with saturation and phase shift

$$\Delta W_{n+1} = -\mathrm{Re}\, W(t_{n+1}) i^*(t_{n+1}) T =$$

$$-\mathrm{Re}\, i^*(t_{n+1}) W(t_n) \exp\left(-\frac{\omega_r}{2Qc}\Delta L\right) \exp\left(i\frac{\omega_r}{\omega_b} 2\pi\right) T_g \quad (27)$$

where $\Delta L = cT_g$ is the distance between bunches.

The time dependence of current and voltage transforms to phases as

$$i(\phi_1) = \frac{e}{T_g} \exp\left(-i\frac{\omega_r}{\omega_b}\left(\phi_{1ref} + \delta\phi_1\right)\right),$$

$$W(\phi_2) = q\frac{\omega_r R_s}{Q} \exp\left(-i\frac{\omega_r}{\omega_b}\left(\phi_{2ref} + \delta\phi_2\right)\right).$$

Since the time of the saturation of the excited oscillations is much longer than gun period bunches can be united in groups by recuperation parameter (Fig. 4), where the total gain and induced voltages are close to zero

$$W_g(t_n) = \sum_{n=1}^{2Na} W_n(t_n) = q\frac{\omega_r R_s}{Q} \sum_{n=1}^{2Na} \exp(-i\frac{\omega_r}{\omega_g}\phi_n) \quad (28)$$

Accordingly the bunch will see the total voltage induced by previous N groups as

$$W(t_{N+1}) = W_g(t_N) + W(t_{N-1}) \exp(-\frac{\omega_r}{2cQ}\Delta L) \exp(i\frac{\omega_r}{\omega_g}\phi_{N+1}) \quad (29)$$

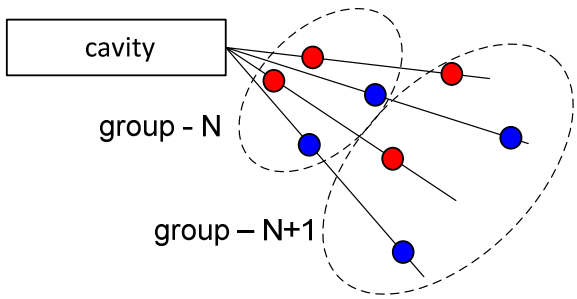

Figure 4. Recuperation groups of bunches: red – accelerating, blue - decelerating

For each point-like bunch the energy phase system is

$$\Delta E_n = \Delta E_{n-1} + e\Delta U(\delta\phi_n) + \Delta W_{n-1}(\delta\phi_n)$$

$$\delta\phi_n = \delta\phi_{n-1} + \frac{\omega_g}{c}(R_{56})_n \frac{\Delta E_n}{E_n} \quad (30)$$

where $\Delta U(\delta\phi_n)$ is additional energy received by electron with phase deviation $\delta\phi_n$, $\Delta W_{n-1}(\delta\phi_n)$ - additional energy due to the induced voltage by previous *n-1* turns (30).

The MARS Structure

Numerical calculations were made for proposed structure of MARS [7,8] (Multipass Accelerator-Recuperator Source) (the scheme is shown in Fig. 5).

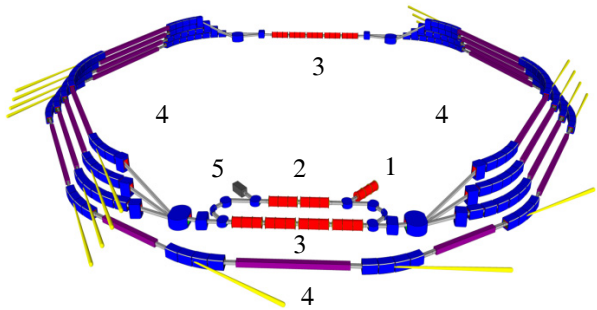

Figure 5: Scheme of MARS - ERL with two linacs: 1 – injector, 2 – preinjection linac, 3 – main linacs, 4 – bending arcs with undulators, 5 – dump.

Parameters of the main accelerating structures are: $Q_1 = Q_2 = 10^6$, $\rho_1 = 40K\Omega$, $\rho_2 = 90\mathrm{K}\Omega$, $\omega = 2\pi \cdot 1.3 \cdot 10^9$ Hz, $U_1 = 0.8$ GV, $U_2 = 1.8$ GV. The transport matrix elements $R_{56} \sim 1$m at all arcs. The dependence of the threshold currents calculated by stability condition (24) and by numerical simulation on accelerating phases $\Phi_1 = \Phi_2$.

Simulations: without Preinjection Accelerating Structure

To compare the theoretical limit of the beam current given by (24) and by wakes simulations it's necessary to calculate system without preinjection.

Simulations start with filling the accelerator trajectory by array of bunches without initial deviation. Bunches with appropriate numbers interact with cavities. After that, the unperturbed bunch is injected in the facility and the last one goes to the dump. The examples of the phase to time dependence are shown in Fig. 6 and Fig. 7. The deviation of the bunch phase is decreasing and increasing exponentially defining the stable and unstable operations.

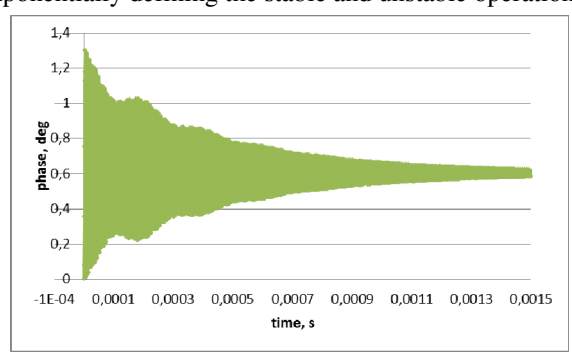

Figure 6: Example of the relaxation of the bunch's phase after the last deceleration to the equilibrium value.

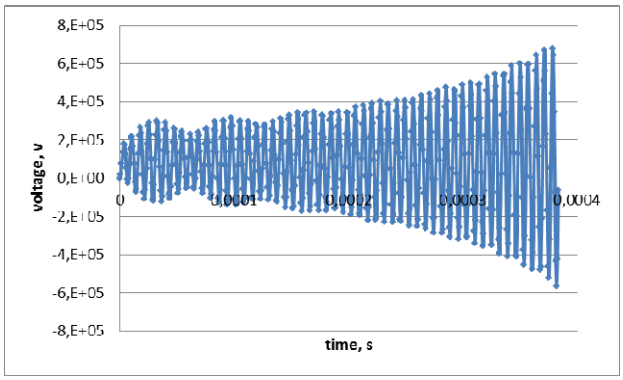

Figure 7: Example of the unstable operation.

Theoretical formulas (24) define the area of beam phases with extremely high threshold current. The comparison between simulated and theoretically calculated threshold currents is shown on Fig. 8. The numerical calculated current is much lower than that given by theory, but the areas of the maximum threshold parameters are correlated. The difference in the current values can be explained by second and high order terms: theory formulas use the linearization of the voltage-phase dependence (see (12), (13)), and near the zero reference phase the influence of the second order perturbations can be significant.

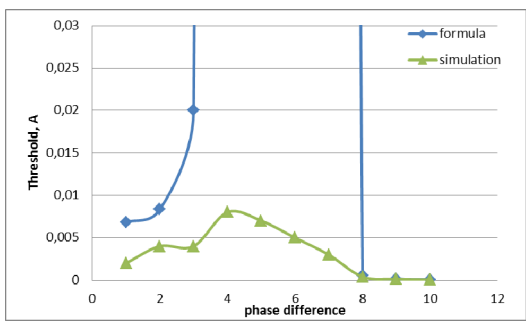

Figure 8: Threshold current: blue – formula (24), green – wakefields simulations ($\xi_{1,2} = 100$).

The Fig. 9 shows the comparison between the theory and simulations with high values of the reference phases.

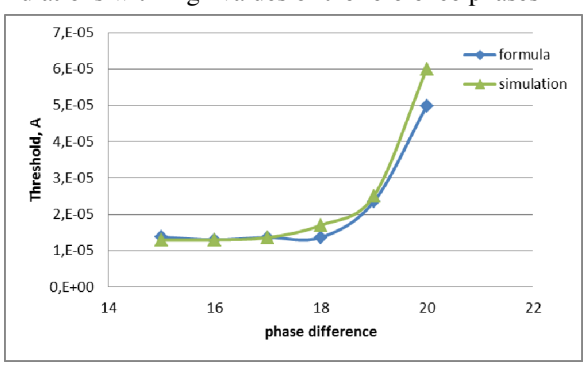

Figure 9: Threshold current: blue – formula (24), green – wakefields simulations ($\xi_{1,2} = 100$).

The maximum values of the threshold currents should be at the highest detunings of the cavities (all conditions of the Lienard-Chipard criterion (9, 10) are satisfied, excepts the last one (24), which does not depends on detunings). Fig. 10 shows the thresholds currents at the highest detunings.

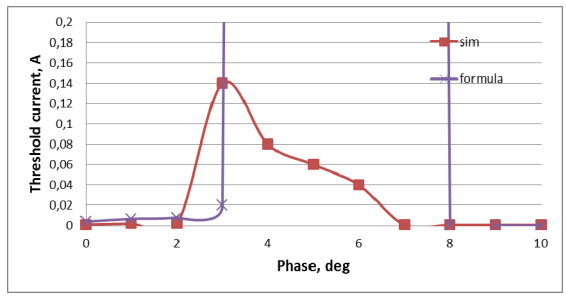

Figure 10: Threshold current: violet – formula (24), red – wakefields simulations ($\xi_{1,2} = 1000$).

Simulations: with Preinjection Accelerating Structure

The proposed scheme of the multiturn ERL (Fig. 5) has also the preliminary acceleration/deceleration system to reduce beam induced radiation and RF power consumption. Simplified scheme with one undulator is shown on Fig.11.

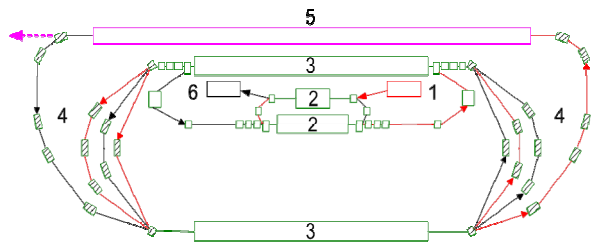

Figure 11. Recuperation groups of bunches: red – accelerating, blue – decelerating. 1-injector, 2 – two preinjection linacs, 3 – main linacs, 4 – bending arcs, 5 – undulator, 6 – beam dump.

Preliminary accelerating system consist of two linacs with energy gain 350 MeV and 40 MeV. Parameters of the linacs are: $Q_{in1} = Q_{in2} = 10^6$, $\rho_{in1} \cong 60\Omega$, $\rho_{in2} \cong 500\Omega$. On the Fig. 13 is shown the comparison of threshold currents calculated in the three cases: by stability condition (24), by numerical simulation without preliminary acceleration and with preliminary accelerating structure.

The examples of the stable and unstable operations are shown on the Fig. 12 and Fig. 13. The threshold current in the case of the maximum cavities detunings is shown on Fig. 14. The current if lower than it for two linacs system, but however satisfy the necessary condition for the accelerator (higher than 10 mA).

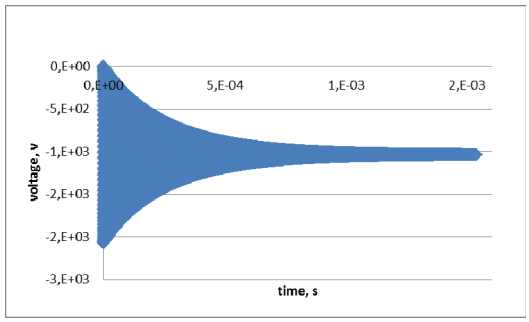

Figure 12. Example of the stable operation: the voltage deviations at the main linac

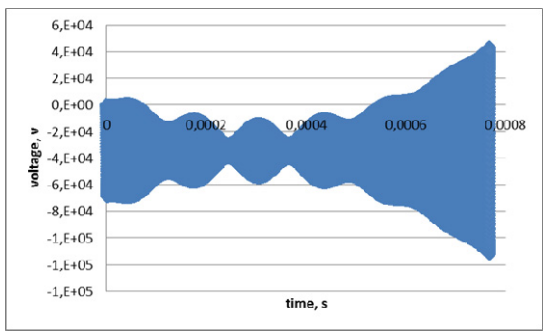

Figure 13. Example of the unstable operation: the voltage deviations at the preinjection linac

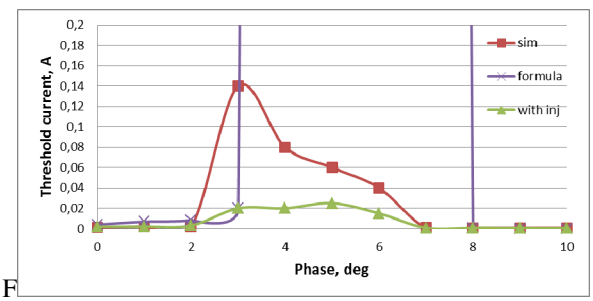

Figure 14: Threshold current: violet – formula (24), red – wakefields simulations, green – with preinjection linacs ($\xi_{1,2} = 1000$).

CONCLUSION

In this paper we derived the criterion of the longitudinal stability for the ERL with two accelerating structures. Numerical calculations specify stability phase region with high threshold current for the accelerating cavities of accelerator with two linacs.

Numerical simulations were made light source projects based on multiturn ERLs. The simulated threshold current is lower than the theoretical lower limit in the areas of the maximum current. To increase the threshold current, it is necessary to develop a proper feedback system.

REFERENCES

[1] L. Merminga et al., Annu. Rev. Nucl. Part. Sci. 53(2003) 387.
[2] N.A. Vinokurov et al., Proc. SPIE 2988 (1997) 221.
[3] D. Douglas, ICFA BD-Nl 26 (2001)40.
[4] N.A. Vinokurov et al., Proc. IPAC'10.
[5] Y. Petenev et al., Proc. IPAC'12 (2012) 604.
[6] F.R. Gantmacher [F.R. Gantmakher], The theory of matrices, 1, Chelsea, reprint (1977) (Translated from Russian).
[7] G.N. Kulipanov et al., J. of synchrotron radiation v. 5, pt 3 (1998). P. 176.
[8] G.N. Kulipanov et al., Nucl. Instr. and Meth. A467/468 (2001), P. 16.
[9] B. Zotter, S. Kheifets, Impedances and wakes in high-energy particle accelerators, World Scientific Publishing Co. Pte. Ltd., 1997.

NEW WAY TO ACCELERATING HIGH CURRENT BEAM IN ERL*

Z.C. Liu#, J. Gao, S. Jin, IHEP, Beijing, 100049, China
F. Wang, PKU, Beijing, 100871, China

Abstract

High beam current is available for the Energy Recovery Linac (ERL). Different methods are adopted to increase the BBU threshold of the cavity to deliver hundreds of milliampere beam current. The key is to absorbing HOMs more efficiently. The BBU threshold of the slotted cavity is much higher than other high current cavities. However, new tuning method is needed and multipacting should be checked. Here we will present a new way to accelerating the high current beam by a highly HOMs damped cavity, the slotted cavity including the tuning method.

INTRODUCTION

In the past 10 years, high current superconducting cavity is developed worldwide. It was designed for the use of ERL, eRHIC, ADS etc.. Various cavity shapes and various HOMs damping methods were developed. A 5-cell superconducting cavity with waveguide HOMs absorber was designed at JLab and several prototypes were fabricated. The cavity reached 22 MV/m and is able to deliver 100 mA beam current [1]. Cornell University has developed a high current cavity for the 5 GeV ERL [2, 3]. A 7-cell superconducting cavity was designed and tested. The cavity was designed in several types with slightly changed cell shapes which can obviously increase the cavity BBU threshold from 100 mA to 450 mA. BNL has developed several types of high current cavity. Now a 5-cell 50 mA superconducting cavity (BNL3) was designed and fabricated [4, 5]. It can deliver 50 mA beam for eRHIC and 300 mA beam for ERL. KEK has developed a 1.3 GHz 9-cell cavity with flute structure to deliver 100 mA beam current for ERL use [6]. The cavity reached 25 MV/m. ANL and PKU has developed a 1.3 GHz 5-cell superconducting cavity in collaboration [7]. The cavity is for the APS upgrade pre-research and can deliver 100 mA beam current.

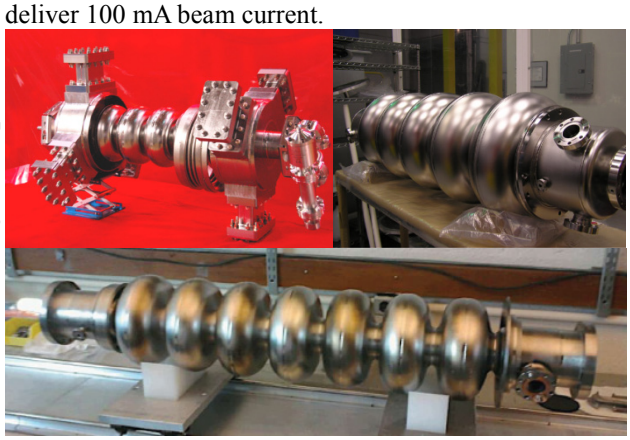

*Project 11275226 supported by NSFC
#zcliu@ihep.ac.cn

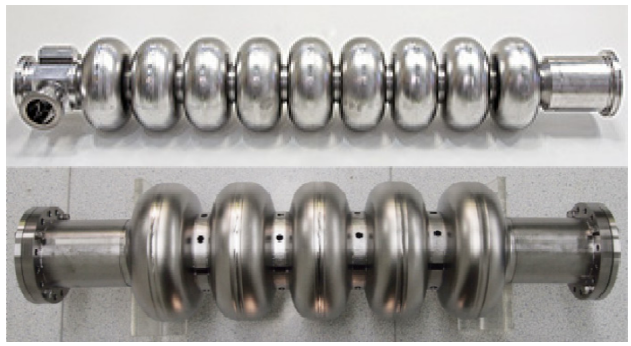

Figure 1: High current cavities around the world. From left to right and top to botom: Jlab, BNL, Cornell universiy, KEK, ANL&PKU [1-7].

To deliver high current beam, cavity is designed following such principles: low cell numbers, large iris and large beam pipe, optimized shape, efficient HOMs damping. Actually, the aim of all these designs is to increase the HOMs' damping.

HOMS DAMPING

The beam current that a cavity can deliver is limited by the BBU threshold of the cavity. For a single high-order mode, the BBU threshold is [8]

$$I_{th} = \frac{2c^2}{e\left(\frac{R}{Q}\right)_\lambda Q_\lambda \omega_\lambda} \frac{1}{T_{12}^* \sin \omega_\lambda t_r} \qquad (1)$$

and

$$T_{12}^* = T_{12}\cos^2\theta_\lambda + \frac{T_{14}+T_{32}}{2}\sin 2\theta_\lambda + T_{34}\sin^2\theta_\lambda \qquad (2)$$

Here, c is the speed of light, e is the elementary charge, λ is the mode number, $(R/Q)_\lambda$ is the shunt impedance (in units of Ω), Q_λ is the quality factor, ω_λ is the HOM frequency, θ_λ is the polarization angle from the x direction, t_r is the bunch return time, and the matrix T describes how a transverse momentum is transported to a transverse displacement after one turn.

Form equation (1), we know that the BBU threshold is inversely proportional to the cavity intrinsic parameter $(R/Q)_\lambda \cdot Q_\lambda$. The main focus to increase the BBU threshold is to decrease the impedance item $(R/Q)_\lambda \cdot Q_\lambda$.

In 1990, Y. Chen, D. Proch, and J. Sekutowicz experimentally investigated a broadband damping of monopole, dipole, and quadrupole modes by implementing small longitudinal slots near the equatorial region of a single-cell copper cavity [9]. And In 2010 Z. Liu and A. Nassiri proposed a novel rf structure for high current beam transportation [10] (Fig. 2). The structure

shows extremely high damping of dipole and quadrupole modes which can give an ampere class beam current.

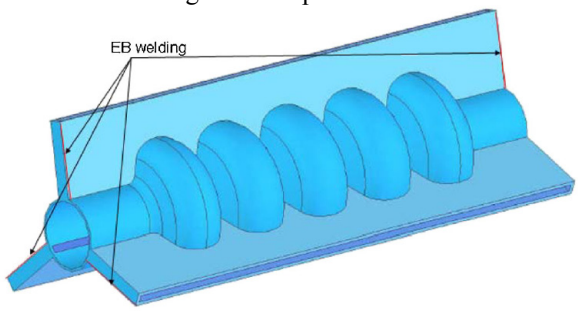

Figure 2: 5-cell slotted cavity [10].

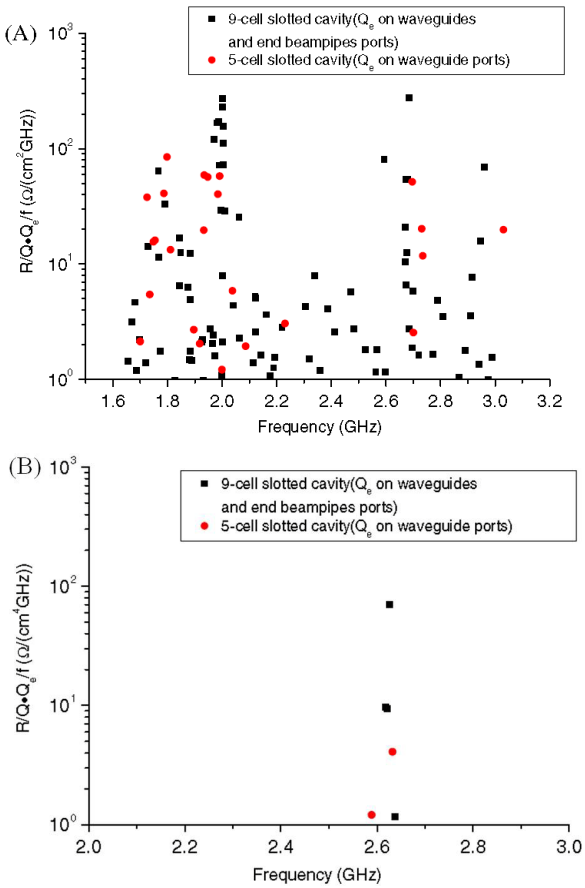

Figure 3: The impedance of dipole (A) and quadrupole (B) modes of 9-cell and 5-cell slotted cavity [10].

PROTOTYPE CAVITY DESIGN

To verify the physical design and develop related technology, we started the design of a 1.3 GHz 3-cell prototype cavity. The 1.3 GHz superconducting slotted cavity is used to accelerate electron bunches with a current above 100 mA. To accelerate 100 mA CW electron bunches, we need to follow these principles in the cavity design:

1) Proper cell numbers. For the test cavity, we chose a 3-cell cavity to simplify the fabrication and lower the cost.
2) Minimize E_{pk}/E_{acc} and B_{pk}/E_{acc}.
3) No hard multipacting barrier caused by cavity shape and the slotted structure.
4) Frequency can be easily tuned.
5) Easy to fabricate.

A 1.3 GHz slotted superconducting cavity prototype was studied and designed using CST-MWS [11]. The cavity parameters are shown in Table 1. And the cell shape parameters are shown in Table 2.

Table 1. The 1.3GHz slotted superconducting cavity parameters.

Type	Elliptical
Operating frequency (MHz)	1300
Working gradient(MV/m)	15
Q_0	1×10^{10}
Beta	1
No. of cell	3
Dia. of iris (mm)	41.152
R/Q (Ω)	268.9
E_{pk}/E_{acc}	3.57
B_{pk}/E_{acc} (mT/(MV/m))	5.72
Field flatness (%)	>97

Table 2. The 1.3GHz superconducting cavity cell shape parameters.

Parameters	Center cell	End cell
L (cm)	57.7	57.7
R_{iris} (cm)	41.152	48.733
Requator(cm)	103.899	103.899
A(cm)	37.904	35.434
B(cm)	23.825	23.55
a(cm)	10.83	16.786
b(cm)	16.244	16.244

TUNING METHOD

The cavity can not be tuned the same as conventional elliptical cavity. There are six niobium walls longitudinally around the cavity. It is difficult to pull and squeeze the cavity to change the frequency. However, as there are slots at the cavity wall, we can use perturbation method to tune the cavity frequency. One slot of the cavity should be used for perturbation and the others should be connected to HOMs damping waveguide. Sticks should be put in each cell at the equator part. The cavity frequency can be tuned by moving the stick in and out. Fig. 4 shows the slotted cavity with perturbation stick. As the stick was put into the cavity with high magnetic

field and electric field, the stick shape should be properly chosen to avoid E_{pk}/E_{acc} and B_{pk}/E_{acc} increasing and multipacting. And the stick size should be properly chosen to make enough tuning range.

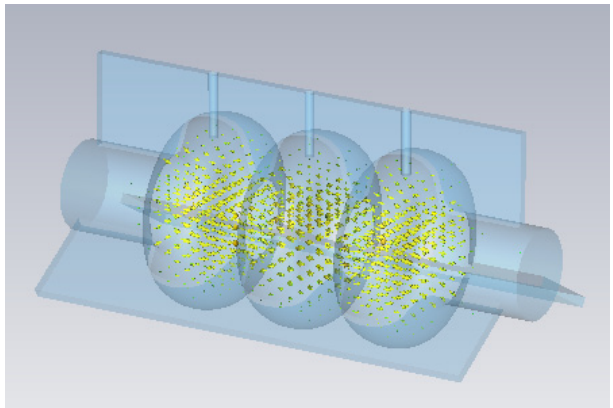

Figure 4: Cavity perturbation method.

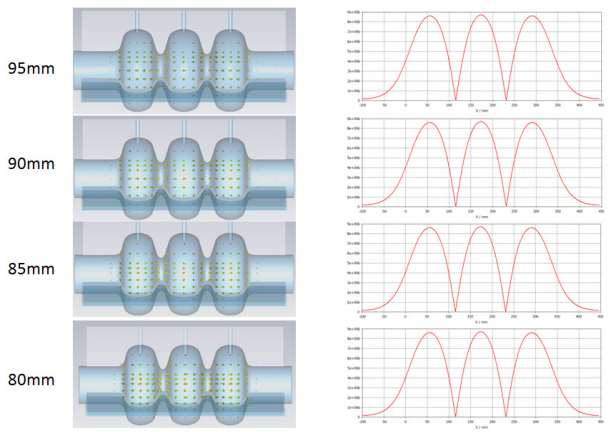

Figure 5: Field flatness of the cavity with different stick off axis distance (r=5mm stick).

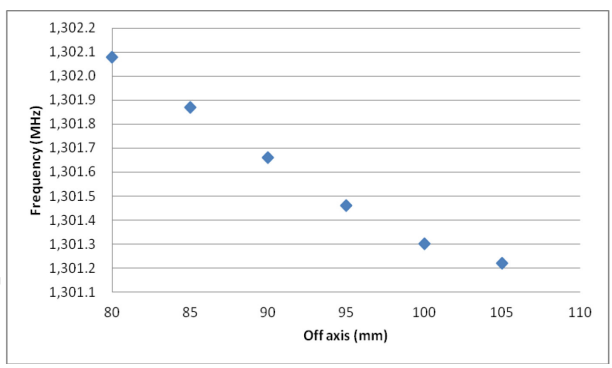

Figure 6: Frequency tuning range of the cavity (r=5mm stick).

The field flatness tuning is also a problem for this cavity. We need to find ways to pre-tune the cavity field to flat as the r=5mm stick can only tune about 7% field flatness. Otherwise, larger sticks should be used to tune the field flatness. Simulation shows that 50% field flatness can be tuned to about 100%.

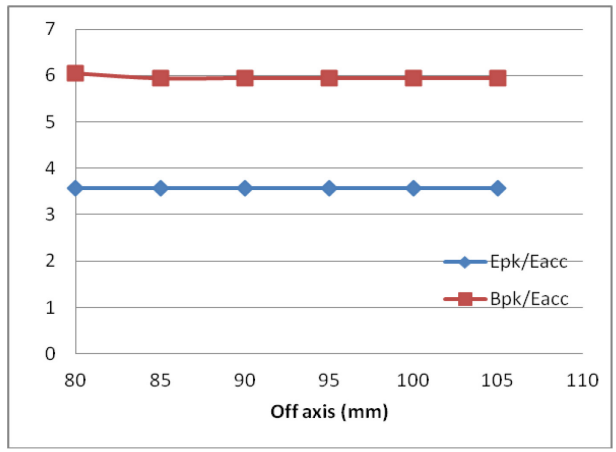

Figure 7: E_{pk}/E_{acc} and B_{pk}/E_{acc} versus sticks position.

MULTIPACTING

To achieve high accelerating gradient, one needs to eliminate the hard multipacting barrier in the cavity. Track3P [12] is used to simulate the multipacting phenomenon in cavity.

The criterion of multipacting event is that the particle resonant trajectories have successive impact energies within the right range for secondary emission yield (SEY) bigger than unity. Fig. 8 shows the SEY of normal niobium.

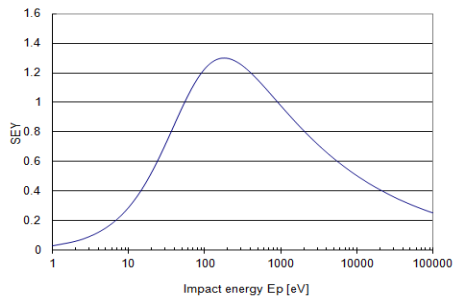

Figure 8: SEY of normal niobium.

We have simulated the multipacting phenomenon of the 1.3GHz slotted cavity without tuning parts from 1MV/m to 20MV/m with an interval of 1MV/m using the whole cavity. The simulation results show that there is no hard multipacting barrier in the cavity (see Fig.9). The multipacting of the slotted cavity with tuning sticks was simulated from 1MV/m to 40MV/m with an interval of 1MV/m using the whole cavity (see Fig. 10). The results show that the tuning parts will cause some resonant trajectories between the tuning sticks and the slot wall. Fig. 10 shows there will be no multipacting around 15MV/m.

FABRICATION

The deep drawing of the cell shape part is a difficult job. For the prototype cavity, we will deep draw each half-cell and then weld them together to form the cell shape part. We will fabricate the cavity sector as shown in Fig. 11. Firstly, weld the cell shape part and cut the slot wall; secondly, electron beam weld the cell shape part and the wall together to form a sector; then weld three sectors together to form a cavity.

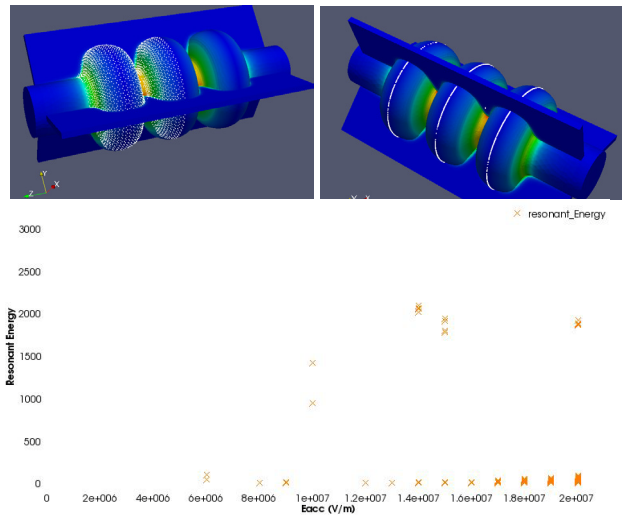

Figure 9: The initial emitting points in the cavity (up left) and the resonant points (up right). The impact energy versus E_{acc} of the 1.3GHz slotted cavity (down).

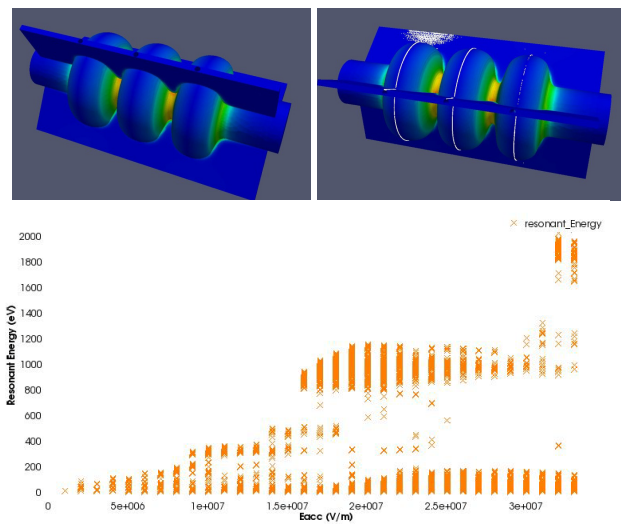

Figure 10: The cavity with one type of tuner (up left) and the resonant points (up right). The impact energy versus E_{acc} of the 1.3GHz slotted cavity (down).

SUMMARY

The benefit of ERL is delivering high average current beam for the use of beam cooling and high brightness free electron laser. Various high current cavities were designed for delivering 100 mA beam current for ERL. To deliver ampere class beam current, a new method was proposed. We are developing the slotted cavity which has extremely high damping of HOMs. The cavity fulfills the need of ERL. Now the 1.3 GHz prototype cavity has been designed. The cavity will be fabricated and tested in the future.

ACKNOWLEDGEMENT

We wish to thank the Advanced Computations Department of SLAC for providing the ACE3P code suite and related resources.

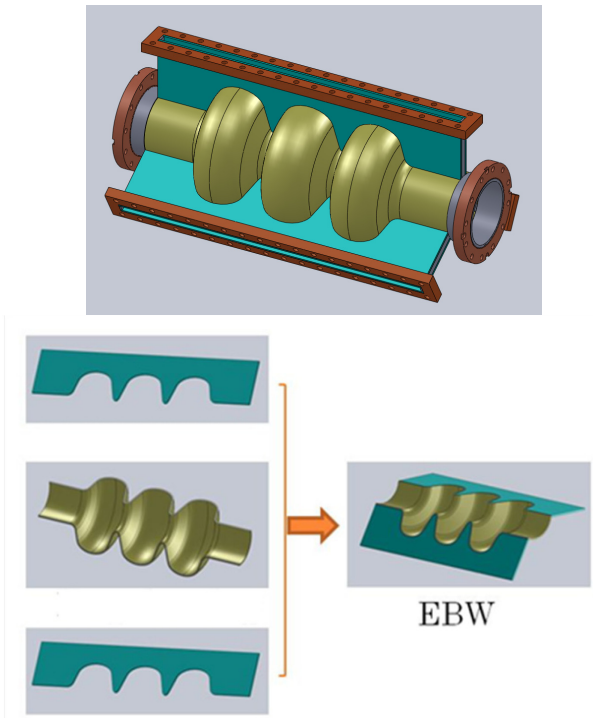

Figure 11: The mechanical structure of the slotted cavity (up) and the fabrication method (down).

REFERENCES

[1] R.A. Rimmer et al., In Proceedings of IPAC10, Kyoto, Japan, 2010, WEPEC076.
[2] N. Valles, Cornell ERL's Main Linac Cavities, In Proceedings of ERL11, Tsukuba, Japan, 2011.
[3] N. Valles and M. Liepe, In Proceedings of PAC11, New York, NY, USA, 2011, TUP064.
[4] W. Xu et al., In Proceedings of IPAC2012, New Orleans, Louisiana, USA, 2012, WEPPC113.
[5] I. Ben-Zvi, In Proceedings of LINAC2012, Tel-Aviv, Israel, 2012, TU2A04.
[6] K. Umemori et al., In Proceedings of IPAC10, Kyoto, Japan, 2010, WEPEC030.
[7] Y. Li et al., In Proceedings of IPAC11, San Sebastian, Spain, 2011, MOPC096.
[8] G. Hoffstaetter, I. Bazarov, and C. Song, Phys. Rev. ST Accel. Beams **10**, 044401 (2007)
[9] Y. Chen, D. Proch, and J. Sekutowicz, in Proceedings of the 14th International Conference on High Energy Accelerators, Tsukuba, Japan (Gordon and Breach, New York, 1989); Part. Accel. **29**, 741 (1990).
[10] Z. Liu and A. Nassiri, Novel Superconducting rf Structure for Ampere-Class Beam Current for Multi-GeV Energy Recovery Linacs, Phys. Rev. ST Accel. Beams **13**, 012001 (2010).
[11] http://www.cst.com.
[12] L. X. Ge et al., In Proceedings of PAC09, Vancouver, BC, Canada, 2009, WE5PFP020.

NOVEL ASTA USERS FACILITY AT FERMILAB : A TESTBED FOR SUPERCONDUCTING RF TECHNOLOGY AND ERL R&D *

V. Shiltsev# for ASTA team, FNAL, Batavia, IL 60510, USA

Abstract

The Advanced Superconducting Test Accelerator (ASTA) currently under commissioning at Fermilab will enable a broad range of beam-based experiments to study fundamental limitations to beam intensity and to develop transformative approaches to particle-beam generation, acceleration and manipulation. ASTA incorporates a superconducting radiofrequency (SRF) linac coupled to a photoinjector and small-circumference storage ring capable of storing electrons or protons. ASTA will establish a unique resource for R&D towards Energy Frontier facilities and a test-bed for SRF accelerators and high- brightness beam applications, including ERLs. The unique features of ASTA include: (1) a high repetition-rate, (2) one of the highest peak and average brightness within the U.S., (3) a GeV-scale beam energy, (4) an extremely stable beam, (5) the availability of SRF and high quality beams together, and (6) a storage ring capable of supporting a broad range of ring-based advanced beam dynamics experiments. These unique features will foster a broad program in advanced accelerator R&D which cannot be carried out elsewhere. Below we describe ASTA and its experimental program, with particular emphasis on the ERL-related accelerator R&D opportunities.

ACCELERATOR OVERVIEW

The backbone of the ASTA facility is a radio-frequency (RF) photoinjector coupled with 1.3-GHz superconducting accelerating cryomodules (CMs); see Fig. 1-(a) [1]. The electron source consists of a 1-1/2 cell 1.3-GHz cylindrical-symmetric RF gun comprising a Cs2Te photocathode illuminated by an ultraviolet (UV, 263 nm) laser pulse obtained from frequency quadrupling of an amplified infrared IR pulse The photocathode drive laser produces a train of bunches repeated at 3 MHz within a 1-ms-duration macropulse; see Fig. 1-(b). The 5-MeV electron bunches exiting the RF gun are then accelerated with two SRF TESLA-type cavities (CAV1 and CAV2) to approximately 50 MeV. Downstream of this accelerating section the beamline includes quadrupole and steering dipole magnets, along with a four-bend magnetic compression chicane (BC1) [2]. The beamline also incorporates a round-to-at-beam transformer former (RTFB) capable of manipulating the beam to generate a high transverse-emittance ratio. In the early stages of operation, the bunches will be compressed in BC1. In this scenario the longitudinal phase space is strongly distorted and the achievable peak current limited to less than 3 kA. Eventually, a third-harmonic cavity (CAV39) operating at 3.9 GHz will be added enabling the generation of bunches with ~10 kA peak currents by linearizing the longitudinal phase space. In addition CAV39 could also be used to shape the current profile of the electron bunch [4]. The photoinjector was extensively simulated and optimized [3]. The photoinjector also includes an off-axis experimental beamline branching at the second dipole of BC1 that will support beam physics experiments and diagnostics R&D.

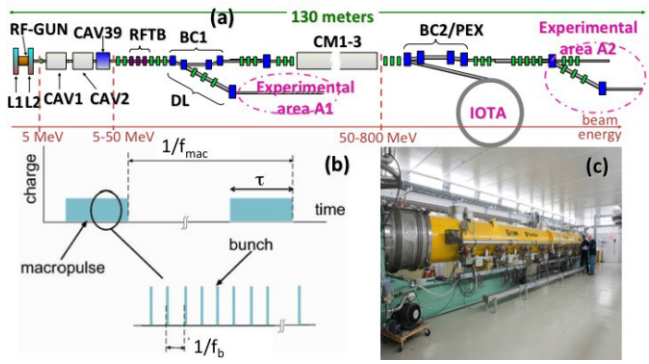

Fig.1: Overview of ASTA (a); "L1" and "L2" stand for solenoids,"CAV1", "CAV2", and "CAV39" correspond to accelerating cavities, "CM1-3" to an ILC cryomodule string, "BC1" and "BC2" to bunch compressors, and "DL" to a dogleg beamline. "EEX" represents a possible reconfiguration of "BC2" to act as a transverse-to-longitudinal phase space exchanger. Electron beam macropulse format (b) and photograph of CM1 module (c).

The 50-MeV beam is injected into the SRF linac, which will eventually consist of three, 12-m long, TESLA/ILC-type CMs. Each CM includes eight 1.3-GHz nine-cell cavities. The first two cryomodules (CM1 and CM2) are a TESLA Type-III+ design, whereas the third (CM3), will be an ILC-Type IV design [5]. Together, these three CM constitute a complete ILC RF Unit. The SRF linac will be capable of generating a beam energy gain of ~750 MeV. The installation of the cryomodules will be staged pending the completion of their construction. The 1st CM has already been tested in the ASTA Facility; see Fig. 1-(c). Downstream of the linac is the test beam line section, which consists of an array of multiple high-energy beam lines that transport the electron beam from the accelerating cryomodules to one of two beam dumps. In addition to testing the accelerator components, the intent of this facility is to also test the support systems required for a future SRF linac. The facility anticipated beam parameters appear in Table I.

*Work supported by DOE contract DE-AC02-07CH11359 to the Fermi Research Alliance LLC.
shiltsev@fnal.gov

TABLE I. Beam parameters expected at the ASTA facility; see Fig. 1-(b) for the definitions of the rf macropulse parameters.

parameter	nominal value	range	units
energy exp. A1	50	[5,50]	MeV
energy exp. A2	~ 300 (Stage 1)	[50,820]	MeV
bunch charge Q	3.2	[0.02,20]	nC
bunch frequency f_b	3	see [a]	MHz
macropulse duration τ	1	≤ 1	ms
macropulse frequency f_{mac}	5	[0.5, 1, 5]	Hz
num. bunch per macro. N_b	3000	[1,3000] [b]	–
trans. emittance [b]	$\varepsilon_\perp \simeq 2.11Q^{0.69}$	[0.1, 100]	μm
long. emittance [b]	$\varepsilon_\parallel \simeq 30.05Q^{0.84}$	[5, 500]	μm
peak current $\hat{I}$ [c]	~ 3	≤ 10	kA

(a) f_b and N_b are quoted for the nominal photocathode laser. Optical pulse stacking methods or field-emission sources could lead to smaller bunch separation within the rf macropulse.
(b) normalized rms values for an uncompressed beam. The scaling laws are obtained from Ref. [3] and correspond to an uncompressed case. Bunch compression results in larger horizontal emittances; see Ref. [2].
(c) the nominal value corresponds to a 3.2-nC compressed bunch without operation of CAV39. Higher values of I are possible with CAV39. For the uncompressed case, we have I[A] '=55Q[nC]$^{-0.87}$

During the 1st high energy beam operation and commissioning, only one CM will be installed allowing for the production of bunches with energies up to ~300 MeV. Eventually, the second and third cryomodules will be installed in Stage II. Together, the three cryomodules plus the RF power systems will make up one complete ILC RF unit. During Stage II operation the beam energy will reach approximately 800 MeV. Beyond that stage several options are under consideration, including the installation of a 4th cryomodule downstream of a phase-space-manipulation beamline (either a simple magnetic bunch compressor or a phase space exchanger) [6, 7].

ASTA was designed with the provision for incorporating a small storage ring to enable a ring-based AARD program in advanced beam dynamics of relevance to both Intensity and Energy Frontier accelerators. The Integrable Optics Test Accelerator (IOTA) ring is 39 meters in circumference capable of storing 50 to 150-MeV electrons to explore, e.g, optical stochastic cooling methods [8] and integrable optics [9]. It is planned to expand capabilities for AARD in ASTA by the installation of the 2.5-MeV proton/H- RFQ accelerator which was previously used for High Intensity Neutrino Source (HINS) research at Fermilab [10]. That accelerator starts with a 50-keV, 40-mA proton (or H-ion) source followed by a 2-solenoid low-energy beam transport line. The protons/ions are then accelerated by the pulsed 325-MHz RFQ to 2.5 MeV (with 1 ms pulse duration) prior to injection into IOTA.

Construction of ASTA (a.k.a. NML) began in 2006 as part of the ILC/SRF R&D Program and later American Recovery and Reinvestment Act (ARRA).The facility was motivated by the goal of building, testing and operating a complete ILC RF unit (3 cryomodules). To date, an investment of about $80M has been made, representing ~80% completion of the facility. First beam from ASTA photoinjector has been obtained on June 20, 2013. Pending on available resources, we plan: in FY2013 - to start commissioning of the 50 MeV photoinjector and to install the first user experiments and start the 1.3 GHz SRF cryomodule commissioning; in FY2014 – to carry out the first experiments at 50 MeV, to finish RF (no beam) commissioning of the SRF cryomodule, to install 300 MeV beamline to the beam dump and continue construction of the IOTA ring; in FY2015 – to perform more experiments with 50 MeV and 300 MeV beams and to finish IOTA construction and installation.

Detail description of the facility and proposed experimental program can be found at http://asta.fnal.gov

It was recognized early in the planning process that an e- beam meeting the ILC performance parameters was itself a power resource of interest to the wider Advanced Accelerator R&D community

USER OPPORTUNITIES

ASTA is intended to be operated 9 months a year as a scientific user facility for advanced accelerator research and development. All the characteristics of a national user facility will be in evidence in the operation of ASTA and its user program. The facility is open to all interested potential users and the facility resources will be determined by merit review of the proposed work. The user program will be proposal-driven and peer-reviewed in order to ensure that the facility focuses on the highest quality research. Proposals will be evaluated by an external Program Committee (the ASTA Program Advisory Committee), consisting of internationally recognized scientists. Proposal evaluation will be carried out according to established merit review guidelines. The 1st PAC and ASTA User's meetings had taken place at Fermilab in July 2013. We expect the first batch of some 30 proposals submitted as part of our proposal to DOE [11] will be reviewed in the Fall of 2013.

Three experimental areas [A1, A2, and IOTA in Fig. 1-(a)] will be available to users for installation of experiments. Area A1, situated in an off-axis beamline within the photoinjector, will provide electron bunches, possibly compressed, with energies up to 50 MeV. The current layout of the off-axis beamline includes a chicane-like transverse-to-longitudinal phase space exchanger, and provision for the installation of a short undulator for beam-laser interaction (e.g., to enable microbunching studies). The high-energy experimental area A2 consists of three parallel beamlines. Two of the beamlines are downstream of doglegs while one is in line with the ASTA linac. Experiments in the three user beamlines and IOTA could be ran simultaneously (switching the beam from one beamline to the other would only require minor optical-lattice adjustment). Finally, the eventual availability of an H- source would allow IOTA to be operated independently of the ASTA electron-beam users.

ANTICIPATED RESEARCH THRUSTS

Accelerator R&D for Particle Physics at the Intensity and Energy Frontiers. The combination of a state-of-the-art superconducting linear accelerator and a flexible storage ring enables a broad research program directed at the particle physics accelerators of the future. The proposed research program includes (1) the test of non-linear, integrable, accelerator lattices (using the IOTA ring) which have the potential to shift the paradigm of future circular accelerator design [12]; (2) the exploration of space-charge compensation schemes in high-intensity circular accelerators, (3) the test of optical stochastic cooling, (4) the investigation of advanced phase space manipulations for beam shaping and emittance repartitioning [13], (5) the exploration of at-beam-driven dielectric-wake_eld acceleration in slab structures [14], (6) the investigation of acceleration and cooling of carbon-based crystal structures for muon accelerators, (7) measurement of the electron wave function size in a storage ring, (8) high-power target studies for the LBNE experiment, (9) the generation of tagged photon beam for detector R&D, and (10) applications of X-rays produced via inverse Compton scattering to nuclear astrophysics.

Accelerator R&D for Future SRF Accelerators. High gradient, high power SRF systems are critical for many accelerator facilities under planning for the needs of high-energy physics, basic energy sciences and other applications. ASTA offers a unique opportunity to explore most critical issues related to the SRF technology and beam dynamics in SRF cryomodules, such as (1) the demonstration of high-power high-gradient operation of SRF CMs with intense beams, (2) the demonstration of technology and beam parameters for the Project X pulsed linac [15], (3) beam-based measurements of long-range wakefield in SRF CMs, (4) ultra-stable operation of SRF linacs using beam-based feedback systems.

Accelerator R&D for Novel Radiation Sources. High energy, high-peak and high-average brightness electron beams are crucial to the generation of high-brillance high-ux light sources with photo energies ranging from keVs to MeVs. The high average power and brightness of the ASTA electron beam has unmatched potential for development of several novel radiation-source concepts. Current proposals include (1) the production of high-spectral-brightness X-rays via channeling [16], (2) the generation and application of X-ray using inverse Compton scattering, (3) the generation of narrow-band X-rays [17], and feasibility studies for (4) an XUV free-electron-laser oscillator, (5) the production of attosecond vacuum UV pulses using space-charge-driven amplification of shot-noise density fluctuations, and (6) the investigation of laser-induced microbunching with high micropulse-repetition rate electron beams.

Accelerator R&D for Stewardship and Applications. With its high energy, high brightness, high repetition rate, and the capability of emittance manipulations built-in to the facility design, ASTA is an ideal platform for exploring novel accelerator techniques of interest for very broad scientific community beyond high energy physics. Examples of expressions of interest for such explorations include (1) the demonstration of techniques to generate and manipulate ultra-low emittance beams for future hard X-ray free-electron lasers [18], (2) the test of a beam-beam kicker [19] for the Medium-energy Electron-Ion Collider (MEIC) [20] (see also below), and (3) the development of advanced beam diagnostics.

ERL R&D OPPORTUNITIES AT ASTA

ASTA offers many opportunities for accelerator R&D towards modern ERLs. Among attractive features of the facility are its use of SC RF – the technique of choice for many next generation ERLs (see many contributions to these Proceedings) – and variety of options for beam diagnostics testing. Due to their high average power in CW beams, ERLs need non-intercepting diagnostics of all kinds. Beams of electrons in ASTA with energies of 300-800 MeV and significant charge in long macro-pulses could be a good start for a number of demonstrations, including:

1. CDR for bunch length and beam based feedback at 50 MeV and higher gamma;
2. ODR near field for beam size at 500 MeV and above;
3. OSR from dipoles for beam size and bunch length;
4. EOS based diagnostic;
5. undulator radiation diagnostics (an appropriate undulator is available in ASTA) should be very relevant to ERL) for bunch length, phase, energy, energy spread, beam position, beam size at micropulse level and sub-macropulse;
6. sub-ps source for VUV detector tests;
7. beam-based feedback;
8. beam arrival monitor development;
9. microbunching instability in compressed beams.

One specific experimental proposal for experimental studies at ASTA suggests a proof-of-principle test of the superfast beam-beam kicker, needed for the MEIC collider, currently under development at the Jefferson Lab [20]. The kicker utilizes a low- or medium energy sheet beam of high current density electrons for providing transverse deflection of higher energy electron beam in a ERL system of electron cooling – see Fig.2. This method was initially proposed for two round Gaussian beams [19], but can be significantly expanded to flat beams by using round-to-flat beam transformation beamline available at ASTA.

Experimental studies at ASTA are envisioned in several stages: first, proof-of-principle demonstration of sub-ns EM deflections by external short (round) electron bunches; then, exploration of the efficient and stable

deflection with flat bunches; and finally, attainment of the required repetition rate of several MHz, that will probably require energy recuperation of some kind.

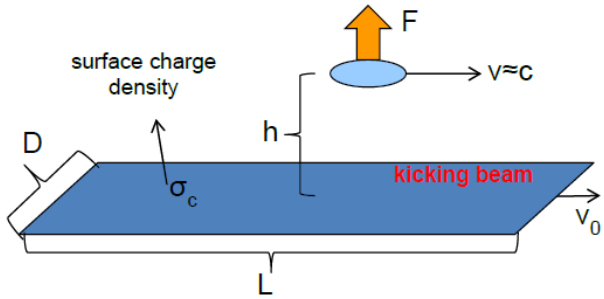

Fig.2: Schematic drawing of a fast beam-beam kicker.

SUMMARY

Advanced Superconducting Test Accelerator (ASTA) facility is being built and commissioned at Fermilab. It is intended to become a leading US DOE facility for accelerator R&D towards Energy Frontier and Intensity Frontier Accelerators, SC RF developments, novel radiation sources, accelerator stewardship and applications available for domestic and international users. ASTA will be a unique accelerator R&D user's facility because of:

- broad range in beam energies (50-800 MeV)
- high-repetition rate and the highest power beams available
- all the advantages of a modern, SRF-based accelerator
- high beam quality , beam stability, beam brightness
- arbitrary emittance partition with repartition of phase space
- flexible storage ring for novel studies with electrons and protons

ASTA will provide 3 experimental areas for multiple experiments:

- with 50 MeV electrons (Experimental Area 1);
- with 300-800 MeV electrons and SRF (EA2);
- with 50-150 MeV/c electron and protons in IOTA ring (EA3).

The facility offers a number of R&D opportunities for various accelerators, including Energy Recovery Linacs (ERLs), and the ASTA team welcomes new proposals.

REFERENCES

[1] M. Church (Editor), "Design of the ASTA facility", Fermilab report beams-doc 4212 (2011).
[2] C. R. Prokop, et al., ArXiV:1302.0726 (2013).
[3] P. Piot, et al., Proc. IPAC10, 4316 (2010).
[4] P. Piot, et al., PRL 108, 034801 (2012).
[5] T. Arkan, et al., Proc. LINAC10, 599 (2010).
[6] Y.-E. Sun, et al., PRL 105, 234801 (2010).
[7] J. Ruan, et al., PRL 106, 244801 (2011).
[8] V. A. Lebedev, et al., Proc. HB2012, Beijing, China, in press (2012).
[9] V. Danilov, et al., PRSTAB 13, 084002 (2010).
[10] J. Steimel, et al., Proc. IPAC12, 3877 (2012).
[11] see proposal at http://asta.fnal.gov/
[12] S. Nagaitsev, et al., arxiv:1301.7032 (2012).
[13] P. Piot, et al., PRSTAB 14, 022801 (2011).
[14] D. Mihalcea, et al., PRSTAB 15, 081304 (2012).
[15] for information see http://projectx.fnal.gov/.
[16] C. A. Brau, et al., Synchr. Rad. News, 25 (1), 2012.
[17] A. Afanasev, et al., Proc. IPAC10, 169 (2010).
[18] B Carlsten, et al., PRSTAB 14, 050706 (2011).
[19] V. Shiltsev, NIM A 374, 137 (1996).
[20] S. Ahmed, et al., Proc. IPAC12, 2014 (2012).

PERFORMANCE OF RF SYSTEM FOR COMPACT ERL INJECTOR IN KEK

Takako Miura# , Mitsuo Akemoto, Dai Arakawa, Hiroaki Katagiri, Tetsuo Shidara, Tateru Takenaka, Katsumi Nakao, Hiromitsu Nakajima, Shigeki Fukuda, Hiroyuki Honma, Hideki Matsushita, Toshihiro Matsumoto, Shinichiro Michizono, Yoshiharu Yano, Feng Qiu, Atuyoshi Akiyama, Takashi Obina, Shogo Sakanaka, Kenta Futatsukawa, Yosuke Honda, Tsukasa Miyajima,
KEK, Tsukuba, 305-0801, Japan

Abstract

The construction of the compact Energy Recovery Linac (cERL) injector in KEK was finished in April 2013, following which the beam commissioning has been performed for 2 months. The cERL injector consists of a normal conducting buncher cavity (BUN) and three superconducting (SC) 2-cell cavities with double couplers. The BUN and the first SC cavity (CAV1) are driven by individual Radio Frequency (RF) power source, respectively. The second and third SC cavities (CAV2 and CAV3) are driven by one klystron using vector-sum control. The low-level RF (LLRF) system is based on I/Q (in-phase, quadrature-phase) digital feedback. RF stabilities of amplitude and phase are, respectively, 0.05%rms and 0.06°rms for BUN and 0.01%rms and 0.02°rms for CAV1, CAV2 and CAV3. Finally, the RF stability was confirmed through the measurement of the beam momentum jitter using a small current and short beam. A momentum jitter of 0.006% was achieved.

INTRODUCTION

The construction of a compact Energy Recovery Linac (cERL) is ongoing as a test facility for the 3-GeV ERL planned for the future. The construction of the injector[1] was finished in April 2013. The construction of the entire cERL will be completed by mid-December 2013. The cERL injector consists of a normal conducting buncher cavity (BUN) and three superconducting (SC) 2-cell cavities with double couplers, as shown in Fig.1. Three RF power sources are used for driving 4 cavities. The phase of the first cavity (CAV1), where the Lorentz β is low, should be changed independently from the second and third cavities (CAV2 and CAV3) in order to suppress the beam dispersion due to the space charge effect. Hence, CAV1 is driven by an independent RF source. CAV2 and CAV3 are driven together by the vector-sum operation. A power distribution system was constructed while taking into consideration the phase matching of top and bottom couplers or phase adjustment between CAV2 and CAV3 for beam transit time. The low-level RF (LLRF) system is based on IQ digital feedback using the FPGA (field-programmable gate array). The requirements of the RF stability for cERL are 0.1% rms in amplitude and 0.1° rms in phase. The requirements for 3GeV ERL are 0.01%rms in amplitude and 0.01° rms in phase. The beam commissioning has been performed for 2 months from the end of April 2013. The beam is accelerated up to 5.5 MeV by the injector. The RF stabilities and the momentum jitter of the beam were measured during this commissioning.

#takako.miura@kek.jp

HIGH LEVEL RF SYSTEM

Figure 1 shows the configuration of the RF sources[2] of the injector. RF frequency is 1.3 GHz. The BUN is driven by a 20-kW inductive output tube (IOT), and CAV1 is driven by a 25-kW klystron. Both CAV2 and CAV3 are driven by a 300-kW klystron with vector-sum operation. In order to adjust the phase between CAV2 and CAV3 for the beam, a phase shifter is located in the line of CAV3 at the outside of the shield, as shown in Fig. 2. The circulators are placed for each cavity line. Each SC cavity has two input-couplers symmetrically equipped to the top and bottom. The RF power, therefore, should be fed at the same phase.

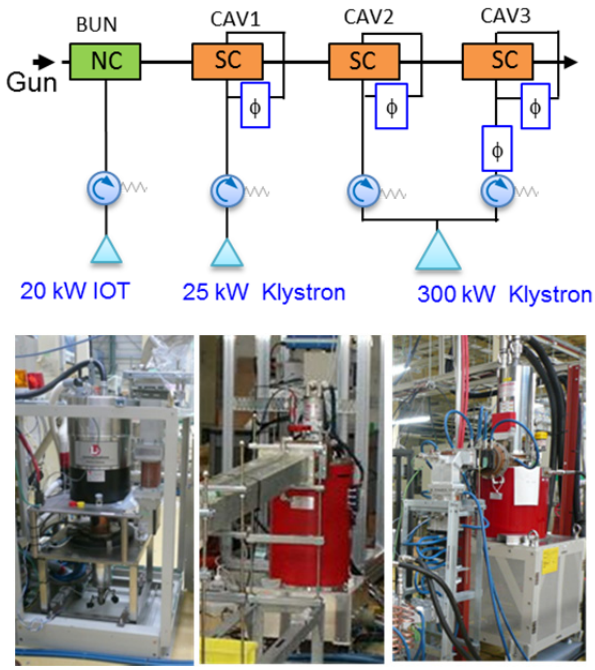

Figure 1: Configuration of RF sources of injector.

Figure 3 shows the power distribution layout feeding the injection cavity on the inside of the shielding-wall. The RF power from the RF-source is divided by the magic-T. The divided power distributed to each coupler. The length of waveguide is designed in advance. The phase shifter,

placed at the bottom line, is adjusted to maximize the cavity field using a network analyzer.

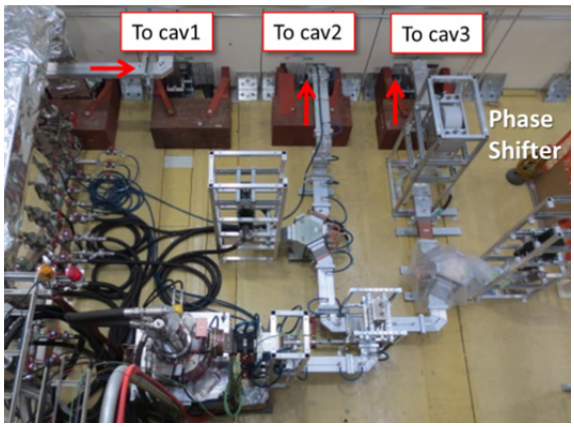

Figure 2: Power distribution system of 300-kW klystron on the outside of the shielding-wall.

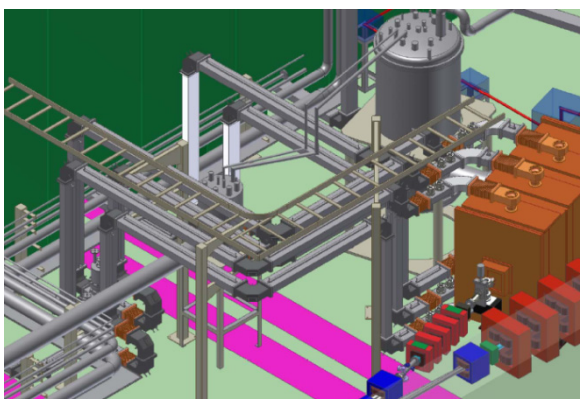

Figure 3: Power distribution layout to feed injection cavity on the inside of the shielding-wall.

LOW LEVEL RF SYSTEM

Figure 4: LLRF control racks.

Figure 4 shows a photograph of the LLRF control racks. The master oscillator (MO) and local oscillator (LO) generation system are installed inside the thermostatic chamber. The stability of the temperature inside the thermostatic chamber is 0.03°C.

Figure 5 shows a schematic of the low level RF (LLRF) digital feedback system[3]. The cavity pick-up signal of 1.3 GHz is down-converted to an intermediate frequency (IF) of 10 MHz. The IF is sampled at 80 MHz by a 16-bit ADC (LTC2208) using the µTCA digital feedback board[4,5]. The calculation in FPGA (Virtex 5 FXT) is performed by 160 MHz clock for short latency. The sampled data are separated into I/Q components. The vector-sum calculation is performed after the correction of the amplitude and the phase for the I/Q. After the I/Q data are passed through the IIR digital low-pass filter, the feedback calculation for PI control is performed. The baseband signals of I/Q from DACs (AD9783) are fed to the IQ modulator. Finally, the amplified 1.3-GHz RF signal is fed to the cavity. The feedback board is prepared for each RF source, and named FB0, FB1, and FB2 (BUN:FB0, CAV1:FB1, Vector-sum:FB2).

The digital board for tuner control[6] is prepared for each cavity. The hard-ware of the tuner board is the same as that for the feedback board, but the logic of FPGA is different from each other. The pulses for the control of the stepping motor are the outputs from the digital I/O. The signal for piezo control is the output from DAC. For the commissioning, the tuner was controlled by slow piezo-feedback through EPICS. Figure 6 shows a typical piezo control panel using CSS that displays information such as a DAC value, phase difference between input-RF and cavity-RF, and piezo voltage.

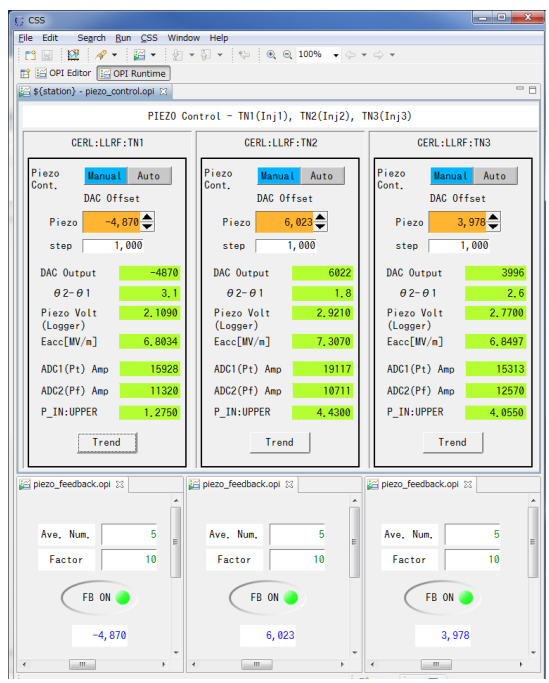

Figure 6: Piezo tuner control panel.

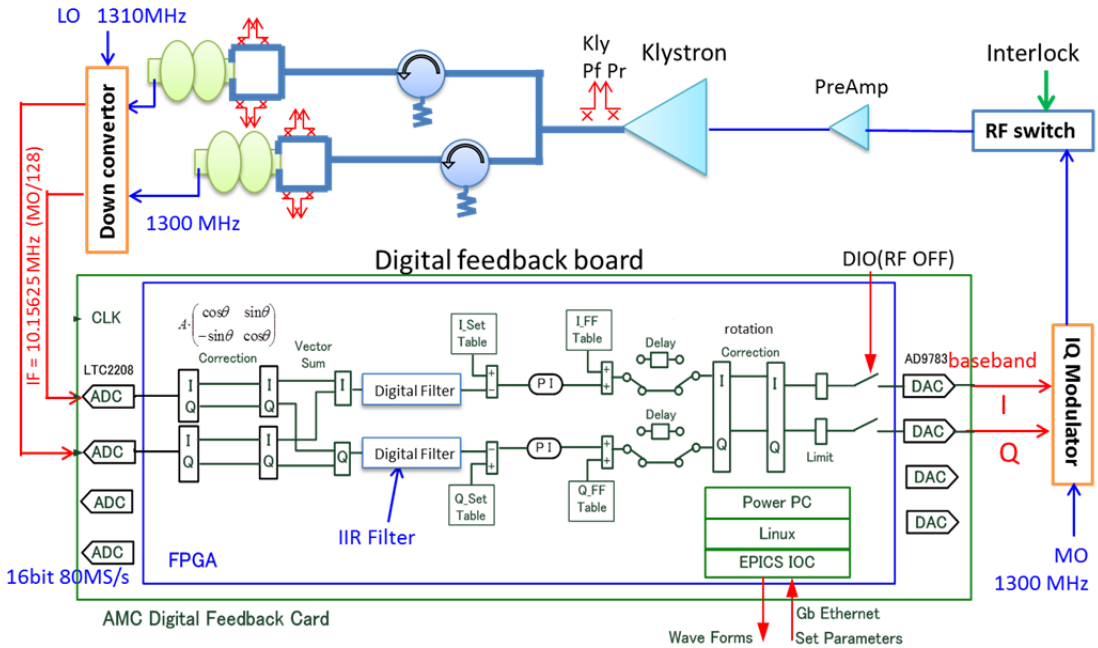

Figure 5: LLRF digital feedback system.

RF STABILITY

RF operational parameters in this commissioning are shown in Table 1. The field SC cavity field was limited to 7 MV/m because of the heating of the higher-order-mode couplers. The optimal gain was determined through a feedback gain scan[7]. Figure 7 shows I/Q data, and Fig. 8 shows the amplitude and phase data of vector-sum in FB2. A ripple of 300 Hz was observed in the data shown in Fig. 8. The ripple is caused by the DC power supply of the 300-kW klystron. However, the ripple was suppressed by FB, and RF stabilities of amplitude and phase are, respectively, 0.05% rms and 0.06° rms for BUN, 0.01% rms and 0.02° rms for CAV1, and vector-sum (CAV2 and CAV3). All systems satisfied the required stability criteria.

Table 1: Typical parameters for this commissioning

	BUN	CAV1	CAV2	CAV3
Type	NC	SC	SC	SC
Q_L	1.125×10^4	1.2×10^6	5.78×10^5	4.8×10^5
θ_b	–90°	0°	0°	0°
Ec		7 MV/m	7.4 MV/m	6.7 MV/m
Vc	114 kV	1.6 MV	1.7 MV	1.55 MV

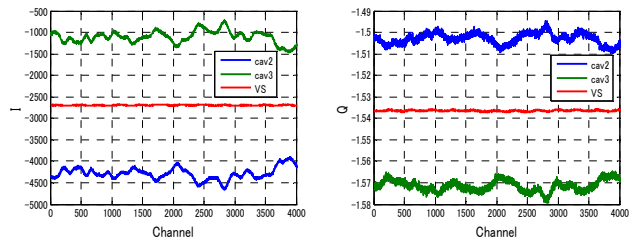

Figure 7: Waveforms for I (left) and Q (right) components in FB2 vector-sum control. Blue:CAV2, green:CAV3, red: vector-sum. (100 kS/s).

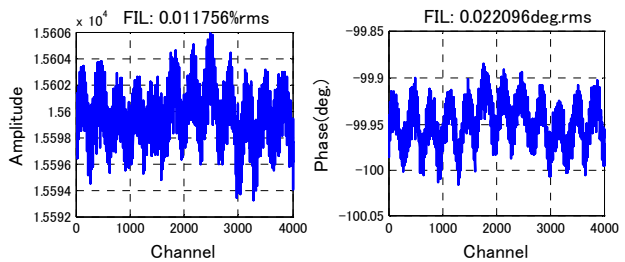

Figure 8: Amplitude and phase data in high-gain feedback for FB2 (vector-sum). (100 kS/s).

STABILITY OF BEAM MOMENTUM

The stability of beam momentum was measured using a screen monitor located downstream of the bending magnet where the dispersion is 0.82 m. The resolution is 53.4 μm/pixel. The beam conditions were very small current and short bunch (5 Hz, 0.77 pC/bunch, bunch

length = 3 ps rms, macro pulse = 1μs). Therefore, BUN was turned off in this measurement. The momentum jitter was determined by plotting the peak point of the projection of the screen. In the first result, even though RF feedback was working, the momentum jitter was large (0.3%rms), as shown on the left-side of Fig. 9. Then, the phase shifter between CAV2 and CAV3, and the feedback phase were adjusted to increase the beam energy. The beam phase was adjusted to be on the crest phase in all cavities. This phase optimization corresponds to the modification of the vector-sum calibration error. The right-side of Fig. 9 shows the result of this optimization. Beam jitter was improved to 0.006% rms. Good stability of beam momentum was achieved. Therefore, it was confirmed that the RF field for the beam is sufficiently stable.

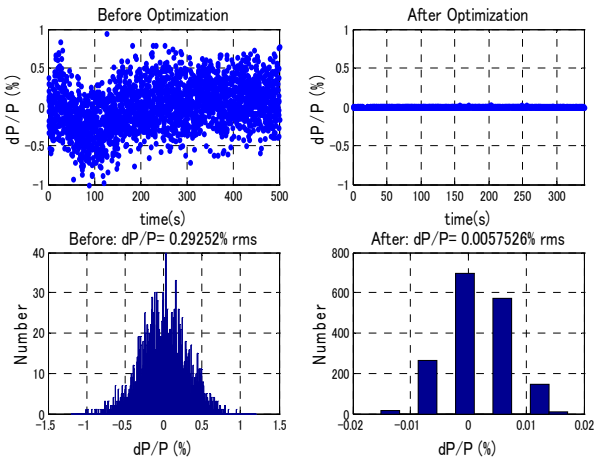

Figure 9: Beam momentum jitter. (Left: before optimization, right: after optimization).

SUMMARY

Construction of the RF system for cERL injector was completed and subsequently the commissioning has been performed for two months from the end of April 2013. RF stabilities of 0.05% rms in amplitude and 0.06° rms in phase for BUN and 0.01% rms in amplitude and 0.02° rms in phase for CAV1 and the vector-sum were achieved. RF fields satisfied the required stability. The beam momentum jitter was 0.006% rms. Good RF stability was confirmed by this result.

REFERENCES

[1] S. Sakanaka et al., "Construction and Commissioning of Compact-ERL Injector at KEK", these proceedings.
[2] S. Fukuda et al., "RF SOURCE OF COMPACT ERL IN KEK", Proc. of IPAC'10, Kyoto, pp.3981-3983 (2010).
[3] T. Miura et al., "LOW-LEVEL RF SYSTEM FOR CERL", Proc. of IPAC'10, Kyoto, pp.1440-1442 (2010).
[4] T.Miura et al., "PERFORMANCE OF THE μTCA DIGITAL FEEDBACK BOARD FOR DRFS TEST AT KEK-STF", Proc. of IPAC2011, 445 (2011).
[5] M.Ryoshi et al., "LLRF BOARD IN MICRO-TCA PLATFORM", Proceeding of Particle Accelerator Society Meeting of Japan, in Japanese, 667-669(2010).
[6] S. Michizono et al., "TUNER CONTROL FOR CERL CAVITIES BY DIGITAL FEEDBACK SYSTEM", Proceeding of Particle Accelerator Society Meeting of Japan, in Japanese, 749 (2011).
[7] F.Qiu et al., "Evaluation of the Superconducting LLRF System at cERL in KEK", Proc. of IPAC'13, Shanghai, 2956 (2013).

PROGRESS REPORT ON THE INTERNATIONAL CRYOMODULE AT DARESBURY

S. Pattalwar, R. Buckley, M. Cordwell, P. Corlett, P. Goudket, A. Goulden, T. Jones, L. Ma, A. May, A. Moss, P. A. McIntosh, J. Strachan, A.E. Wheelhouse, STFC, Daresbury, UK
S. Belomestnykh, BNL, US
R. Eichhorn, G. Hoffstaetter, M. Liepe, H. Padamsee, P. Quigley, J. Sears, V. Shemelin, CLASSE, Ithaca, US
D. Proch, J. Sekutowicz, DESY, Hamburg, Germany
A. Buechner, F. Gabriel, P. Michel, HZDR, Dresden, Germany
J. Corlett, D. Li, S.M. Lidia, LBNL, Berkeley, US
T. Kimura, T. Smith, Stanford University, Stanford, US
R. Laxdal, TRIUMF, Canada

Abstract

On successful completion of the assembly and preliminary testing of an optimised SRF cryomodule, being developed under international collaboration, for application on ERL accelerators, the cryomodule has now been installed on the 35 MeV ALICE (Accelerators and Lasers in Combined Experiments) Energy Recovery Linac (ERL) facility at STFC Daresbury Laboratory. Existing cryogenic infrastructure has a capacity to deliver approximately 120 W cooling power at 2 K, but the HOM (Higher Order Mode) absorbers, the thermal intercepts for the high power RF couplers and the radiation shields inside the cryomodule are designed to be cooled with gaseous helium instead of liquid nitrogen. As a result, the cryogenic infrastructure for ALICE has been modified to meet these additional requirements. This paper, presents our experience with the integration and cryogenic commissioning with some initial results.

INTRODUCTION

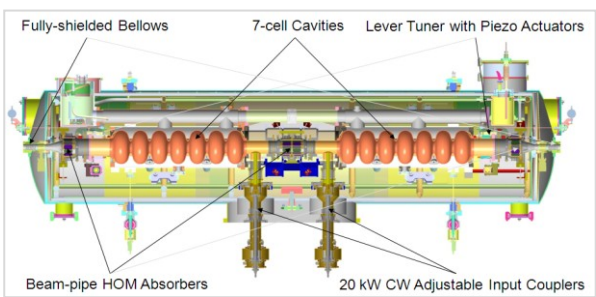

Figure 1: CW-ERL cryomodule under development.

On successful completion of the assembly of the optimised SRF cryomodule (Fig. 1) for CW ERL applications [1], extensive tests were conducted in 2012 to evaluate the cryogenic performance, first with liquid nitrogen and then with liquid helium at 4.2K with the assembled cryomodule (Fig. 2). The main purpose of these offline cold tests were to identify any unforeseen issues that may occur during the installation and commissioning on ALICE Several issues were identified and resolved during the tests, for example - large temperature gradient between the two cavities during cool-down and the lowest temperature reached was only ~8K. Most of these observations could be explained by considering the limitations on the non-ideal test conditions and attributed to the absence of the cooling power at intermediate temperatures for cooling the thermal intercepts on the RF couplers and the HOM absorbers.

Figure 2: Fully assembled cryomodule undergoing Qualification tests.

The cryomodule subsequently passed the offline acceptance tests [2] and was installed on ALICE as shown in Fig. 3 in February 2013. The existing cryogenic infrastructure [3] has a capacity to deliver approximately 120W cooling power at 2K and liquid nitrogen is used as a source for cooling to 80K.

However, for the new CW-ERL cryomodule the HOM absorbers, the thermal intercepts for the high power RF couplers and the radiation shields are designed to be cooled with gaseous helium instead of liquid nitrogen. This alternative solution was chosen to allow for investigation of microphonics susceptibility and so a

special system called COOL-IT [4] was developed to provide COOling power at Intermediate Temperatures and has been integrated with the main cryogenic system for ALICE (Fig. 4). Subsequent sections describe the first experience with the process of integration and cryogenics performance observed during the initial cool-down.

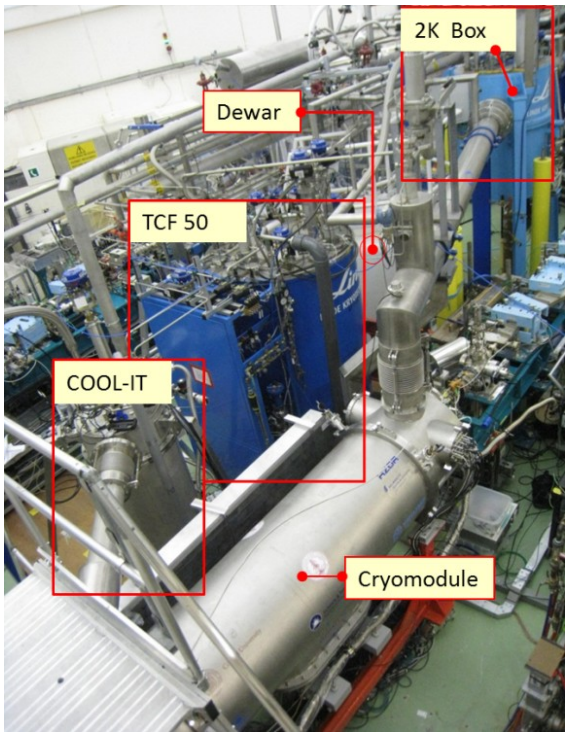

Figure 3: Cryomodule installed on ALICE- 25 MeV ERL facility at STFC Daresbury Laboratory.

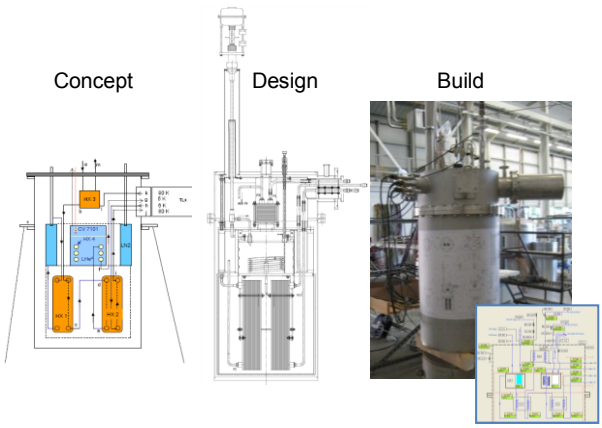

Figure 4: COOL-IT a system to provide cooling power at intermediate temperatures

CRYOGENIC PERFORMANCE

Cool-down to Base Temperature

The cryomodule was successfully cooled to 2K at the first instance and then thermally cycled between room temperature and 2K several times. Cool-down to 130K was very slow and was achieved only by radiation and conduction through the supports as shown in Fig. 5. A large temperature gradient between the two cavities below 100K can be attributed to the floating temperatures of various components, inside the cryomodule.

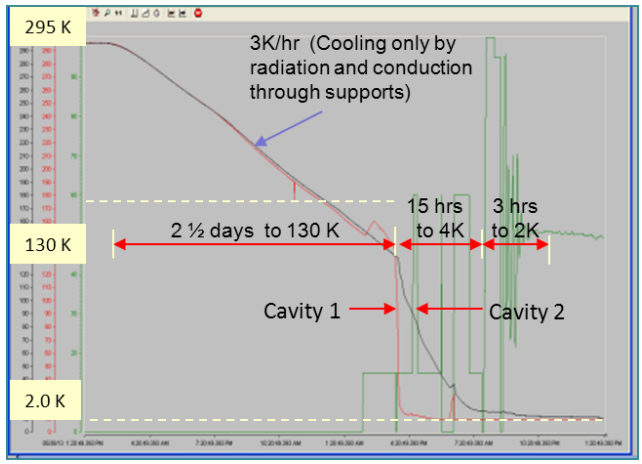

Figure 5: Cool-down to 2K. The red and black curves indicate the temperatures of the two cavities and the green curve shows position of the liquid helium feed valve.

Below 130K the cavities are cooled at a maximum possible rate by fully opening the liquid helium feed valves. Fig. 6 shows the control obtained over liquid helium levels and excellent pressure stability achieved of ±0.05 mbar around an absolute pressure of 30 mbar (Fig. 7) in the helium vessels surrounding the cavities after thermal equilibrium at 2K is attained.

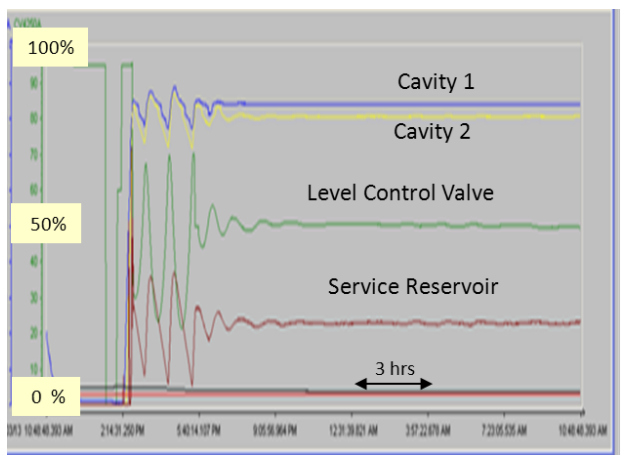

Figure 6: Liquid helium level control after reaching thermal equilibrium at 2K.

Temperature Measurements

In spite of achieving excellent temperature stability repeatedly, actual temperature readings of the cavities as measured using the Cernox temperature sensors appeared to be erroneous. This is likely to be due to the errors in the calibration curves while configuring the measuring instruments. Investigations are underway to confirm this reasoning.

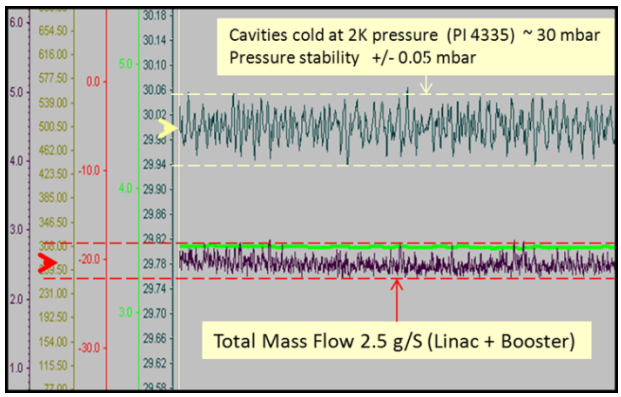

Figure 7: Excellent pressure stability of +/- 0.05 mbar around an absolute pressure of 30 mbar corresponding to a temperature of 2 K.

The thermal shield and the HOM absorbers were cooled to temperatures between 89K and 99K using cold helium gas provided by COOL-IT. The thermal intercepts could be cooled to temperatures between 13.5K and 15.5K instead of a target of 10K, but this is not anticipated to be a major issue, as the static heat load measurements at 2K have been found to be within specifications . The dynamic heat loads have not been measured but the cryo-system has sufficient overhead to handle additional heat leak in the presence of RF power, as along as power dissipation and Q_o for the cavities is within acceptable limits. The primary RF interlocks for the couplers have been set by the vacuum level (1.0E-07 mbar) and the secondary interlocks corresponding to temperatures will be set to 5K higher than those measured at thermal equilibrium.

Heat Load Measurements

Table 1: Cryogenic performance measurements under static conditions.

Parameter	Units	Value	Spec
Base Temperature	K	2.0	2.0
Static Heat Load	W	6.2	15
Absolute Pressure	mbar	30	30
Pressure Stability	mbar	+/- 0.05	+/- 1.0
Base Mass flow#	g/S	2.5	2.5
Dynamic Heat Load	*Not yet measured*		
Shield temperature	K	89 < T< 99	~ 90
Intercepts (80K)	K	89 < T < 99	~ 90
Intercepts (10K)	K	13.5 < T < 15.5	~10
Cavity Frequency	GHz	1.3	1.3
Tuning Range	MHz	+/- 350	+/- 350

This is a minimum mass flow equivalent to static heat leak for the entire cryogenic system for ALICE including a second (booster) cryomodule.

A summary of heat load measurements [5] is given in the Table 1, showing that all of the basic cooling parameters are within the specification and similar to the SRF LINAC previously operating with ALICE as reported in the reference 3. The temperatures of the thermal intercepts are higher than expected, but should not pose a major problem for the reasons mentioned in the previous section. This situation will certainly improve after optimising operation of COOL-IT. Currently the helium gas pressure is set to a fixed value of 2 barA, but in future it will be controlled automatically via a feedback loop based on the temperature of the thermal intercept on the HOM absorbers.

Initial RF Performance

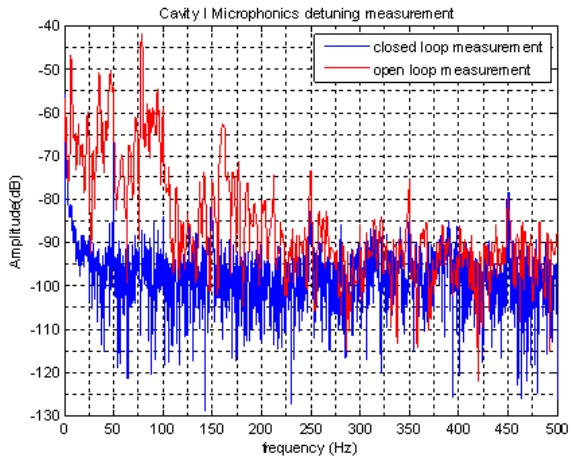

Figure 8: Microphonics tests on cavity 1

The operation of the modified Saclay II tuners was verified by tuning both the cavities to 1.3 GHz at 2K with a tuning range of ± 350 MHz. A digital low level RF (DLLRF) control system has been developed and initial testing with the cryomodule has been successfully carried out. Microphonic behaviour of both the cavities in the cryomodule was also studied, with various low frequency (mechanical) detuning peaks measured, and the DLLRF system has been demonstrated to overcome these disturbances [6]. These were adequately damped by use of a digital phase locked loop as shown in Fig. 8 for cavity 1, with Cavity 2 showing similar behaviour.

SUMMARY AND FUTURE PLANS

The CW-ERL cryomodule was successfully cooled to 2K after installation on ALICE. Initial cryogenic performance, particularly under static conditions is within the specifications. A newly developed digital low level RF system has been provisionally validated successfully by undertaking microphonic measurements. Evaluation of the cryomodule with high power RF initially through conditioning of the cavities and then in the presence the electron beams will resume after optimising the operation of the cryogenic system including COOL-IT over the next few weeks.

REFERENCES

[1] P. Goudket et al., “Assembly of the International ERL Cryomodule at Daresbury Laboratory,”SRF 2011, Chicago, p.385 (2011)
[2] S. Pattalwar, “Integration and cold testing of the CW-ERL cryomodule at Daresbury,”Tesla Technology Collaboration meeting, JLab, USA November 5-8 (2012)
[3] A. Goulden et al., “Installation and Commissioning of the Superconducting RF Linac cryomodules for the ERLP,”Advances in Cryogenic Engineering, 53 B, p.1573 (2008)
[4] S. Pattalwar and R. Bate, “COOL-IT, A heat exchanger system to provide gaseous helium at intermediate temperatures for SRF LINAC,”Advances in Cryogenic Engineering 55A, p.595 (2010)
[5] L.Ma, et al., “LLRF Characterisation of the Daresbury International Cryomodule,” IPAC’13, Shanghai, p.3046 (2013)
[6] A. Wheelhouse, “International ERL Cryomodule,” TTC topical workshop on CW-SRF, Cornell University, Cornell, June 12-14 (2013)

ELECTRON POLARIMETRY FOR ERLs*

K. Aulenbacher, Institut für Kernphysik, Universität Mainz, Germany

Abstract

Polarimetry at the planned ERL based linac-ring colliders can rely on similar techniques as have been developed for storage rings such as HERA. However, due to the low energy, operation of polarimetry at the prototype devices such as MESA is shown to be considerably more difficult. The usage of atomic traps which serve as a target of complete electron polarization is discussed for MESA.

INTRODUCTION

In collisions of spin-polarized particles, online analysis of the beam polarization is highly desirable. Usually, a high quality result will also call for a high absolute accuracy $\Delta P/P$ of the polarization measurement. Electron Polarimeters have been operated successfully in ring/ring ep-colliders for instance at HERA [1] and also at LINACs such as SLACs SLC [2]. If we consider the situation in an ERL based linac/ring collider such as eRHIC [3] or LHeC [4] we find that the high beam power at an ERL also requires minimally invasive techniques. In comparison with storage rings several advantages come into play. First, stronger interaction is possible between the beam and the analyzer, since any beam particle makes only a single passage through the interaction region at the experiment and/or the polarimeter. A further advantage lies in the fact that the beam can be analyzed invasively after deceleration in the ERL, i.e. before the beam dump, if the polarimeter can be made compatible with the still high beam power. Due to the rapid deceleration in an ERL the polarization loss between target will usually only lead to negligible depolarization, since depolarizing resonances are crossed very rapidly. Therefore, the information obtained from a dump-polarimeter may still be useful for the interpretation of the experimental data. In the following we will briefly address the issue of the high energy polarimeter for the planned ERL-ring colliders which may be realized in the next decade. In contrast to high energies, new techniques seem necessary for low energy projects like MESA which are going to be realized on a shorter timescale.

POLARIMETRY AT GEV LEPTON ENERGIES

In Laser-Compton polarimeters (LCP) circularly polarized optical photons with an energy $E_{\gamma,0}$ (typical a few eV) are backscattered off the extreme relativistic ($E_{beam} >> m_{lepton}$) lepton beam. The backscattered photons whose energy E_γ is in the many MeV region are concentrated in a small angular region ($\approx 2/\gamma = 2m_{lepton}/E_{beam}$, typically smaller 1 mrad) around the backscattering direction. A beam polarization dependent signal (asymmetry) $A = P_{lepton}P_{\gamma,0} * S_{long,trans}$ can be generated by switching the circular photon-polarization $P_{\gamma,0}$. The character of the analyzing power $S_{long,trans}$ depends on the transverse or longitudinal state of the electron beam polarization. For the transverse case a left/right asymmetry exists, causing a small shift of the center of intensity distribution, the detection of which causes some requirements towards the position resolution of the photon detector. In the longitudinal case an intensity asymmetry occurs, even if the scattered photon-spectrum is integrated over all angles. In this case energy resolution is necessary, since the quantity $S_{long}(E_\gamma)$ varies strongly with the energy of the scattered photon. In the following only the longitudinal case is considered. The largest asymmetry is carried by the photons with the highest energy, i.e. the backscattered photons. The Laser Compton has distinct advantages since the product $S_{eff} = D * P_{\gamma,0} * S(E_\gamma)$, the so-called effective analyzing power, can be determined very accurately. First, $P_{\gamma,0}$, the circular polarization of the photons, which can be considered as a target polarization, is comparatively easy to determine with an accuracy in the per mille range. Second the analyzing power $S_0(E_\gamma)$ can be calculated very accurately for this QED process. The factor D contains all experimental dilutions, like backgrounds or uncertain calibration of the detectors energy-scale. It has been shown that these can be controlled at the sub percent level too.

For electron beam energies of a few GeV or lower the energy of the backscattered photon is still much lower than the incoming beam energy. In this case the approximations in the following paragraph are valid. An exact calculation of the analyzing powers for arbitrary energies can be found in [5].

For 180 degree backscattering the energy of the photon is maximum and it is determined by the relativistic factor γ of the lepton beam: $E_{\gamma,max} \approx 4E_{\gamma,0}\gamma^2$. For a 1 GeV beam and incoming laser Photons of 2.5 eV (typical for frequency doubled high repetition rate laser systems) we obtain $E_{\gamma,max} = 40\,MeV$. On the other hand, the asymmetry is $E_{\gamma,max}/E_{beam}$ which is 0.04 for this example. The averaging over the photon spectrum leads to further reduction of this value in a real experiment.

Small asymmetries ($A < 0.01$) are difficult to measure accurately, not only because the measurement time for a given statistical accuracy increases $\propto 1/A^2$, but also because the contribution of systematic effects - e.g. background from residual gas scattering - becomes increasingly

*This work was supported by BMBF via project 05H12UM6 (Spin Optimierung) and by the European Union through EUCARD-II within FP7.

difficult to control. From this reasoning we conclude that some value of beam energy must be surpassed to make a LCP effective as a fast and accurate device. This limit is of the order of one GeV. In order to get an idea of the obtainable measurement speed we can compare with the Mainz LCP where 1% statistical accuracy was obtained within 12 hours at E_{beam}=1.5 GeV [6]. With 2.5 GHz c.w. beam at MAMI this experiment is similar to ERL conditions, but with a much lower beam current of 20 μA. Since the currents at ERLs are several magnitudes larger, it seems reasonable to assume that LCPs can be used effectively at ERLs whose energy considerably exceeds 1GeV. This is of course the case for the EIC and LHeC projects.

POLARIMETRY AT THE 100 MEV SCALE: THE HYDRO-MØLLER AT MESA

So far, MESA is foreseen to operate with spin-polarized beam only in external beam (EB-) mode. This is motivated by the fact that production of polarized beam at the 10 mA level is a demanding task which would add considerably to the already high complexity of the MESA-project. However, the usage of a polarized internal target in ERL-mode is already being discussed which would then operate with a polarized beam. Figure 1 shows the outline of MESA together with the location of polarimeters as if they would have been rearranged for ERL-operation. There are three EB-mode polarimeters [7]. Two of those are "'Mott"'-polarimeters, which are invasive. They only could be useful in ERL-operation if they are used as dump polarimeters.

MESA is foreseen to operate at a maximum energy of 200 MeV, where using the LCP is unattractive. Therefore another principle is foreseen to be used. This scheme - the so-called Hydro-Møller – was proposed by Chudakov and Luppov [8]. It uses the fact that hydrogen atoms can be trapped axially by a strong solenoid field. Radial trapping can be achieved by cooling the walls of the trap to 0.3 K and by covering these walls with a suprafluid ^{4}He-film. Though the feasibility of such a trap was demonstrated already a long time ago, we estimate several years of development time necessary, since the device is technologically demanding. The Hydro-Møller potentially carries similar advantages as the LCP, in particular the hydrogen atoms in the trap are polarized to a level of $P_{target} = 1 - \epsilon$, with $\epsilon \approx 10^{-5}$ in a magnetic field of B=8 T. Therefore, as in the LCP, the uncertainty in the knowledge of the target polarization is not a major issue. For 90 degree scattering in the CM-system the analyzing power is 7/9, so that with complete target polarization of the Hydro-Møller the observed asymmetry will become very large. Though the target density will be relatively small (of the order $10^{16} cm^{-2}$) a sufficiently high measurement speed can be obtained, even if operated at the 0.15 mA current level foreseen for the P2 extarnal beam experiment at MESA [9]. In addition, the low target density allows for on-line operation. Besides the technical issues, another challenge is of course to make the ERL lattice compatible with beam passage through the 8 T field. The length of the trap is about 0.5 m, but additional space must be foreseen for the detection system. It should be noted that the *nuclei* in the trap can also be polarized the device may therefore also serve as a polarized nuclear target.

POLARIMETRY AT RECOVERED ENERGIES

At the recovered energy one can think to install a polarization monitoring device which resides permanently in the beam. In the region of several MeV - corresponding to the recovered beam energy – Mott and Compton-transmission polarimeters have been tested at MAMI at power levels of several hundred Watts [10]. It is an open question if Mott polarimeters can handle the much higher beam power in ERL-mode, though one could think of rotating targets in order to reduce the thermal stress induced by the multi-kW beam. Compton transmission polarimeters, on the other hand, seem reasonably simple and robust to be used for this purpose [10].

REFERENCES

[1] D. P. Barber et al. et al. The HERA polarimter and the first observation of electron spin polarization at HERA, Nucl. Instrum. Meth. **A 329** 79 (1993)

[2] The ALEPH, DELPHI, L3 , OPAL, SLD Collaborations and The LEP Electroweak Working Group and The SLD Electroweak and Heavy Flavour Groups: Precision electroweak measurements on the Z resonance: Physics Reports **427** 257 454 (2006)

[3] V. Litvinenko: Future Electron-Hadron Colliders Proceedings IPAC 2010 p.2364 (2010)

[4] F. Zimmermann et al. Design for a Linac Ring LheC proceedings IPAC 2010 http://accelconf.web.cern.ch/ AccelConf/IPAC10/papers/tupeb039.pdf

[5] V. Gharibyan et al. The TESLA Compton polarimeter. DESY internal note LC-DET-2001-47 (2001)

[6] J. Diefenbach A4-Compton polarimetry Il nuovo chimento DOI 10.1007/s10751-0277-9 (2012)

[7] K. Aulenbacher, V. Tioukine and I. Alexander: The polarimetry chain for the P2 experiment. Il nuovo chimento **35,4**186-191 (2012)

[8] E. Chudakov and V. Luppov: Møller polarimetry with atomic hydrogen targets, IEEE Trans. Nucl. Sci. **51** 1533, (2004)

[9] D. Becker, S. Baunack and F.E. Maas: *Hyperfine Interact.* **213** 141-148 (2013)

[10] R. Barday et al. Compton transmission polarimeter for a very precise polarization measurement within a wide range of electron currents J. Phys.: Conf. Ser.**298** 012022 (2011)

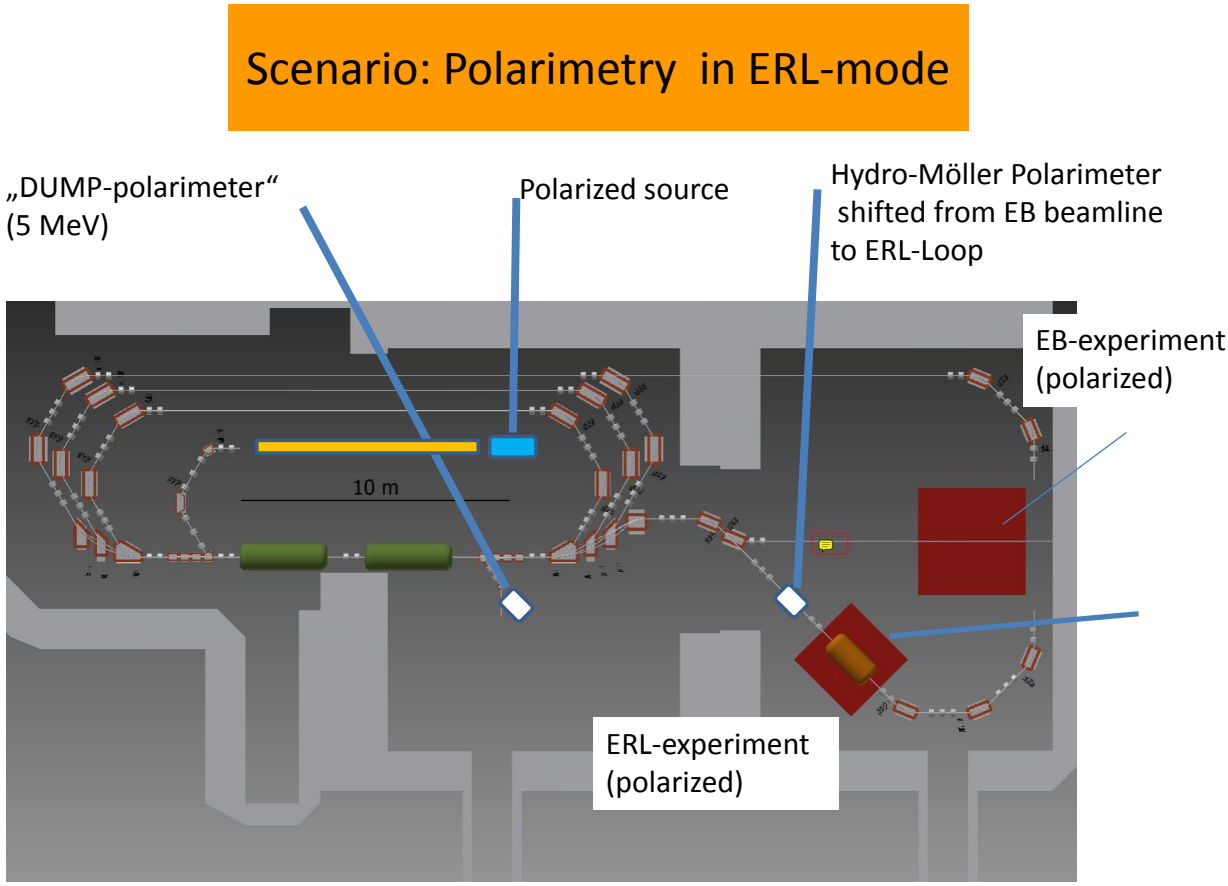

Figure 1: Outline of the MESA lattice with a scenario ”‘as if”’ the polarimeters foreseen for EB-mode would be used in ERL-mode.

MONITORING BEAM POSITION IN THE MULTIBEAM ACCELERATORS*

I. Pinayev#, BNL, Upton, NY 11973, USA

Abstract

In this paper we present the concept of a beam position monitors for the accelerating structures with multiple beams. Both cases with common and separated nominal orbits are considered. For the first case we utilize the phase information, when for the second case additional pick-up electrodes can be utilized.

INTRODUCTION

Most commonly used method for the beam position monitors (BPMs) is based on the evaluation of the signals induced on the pick-up electrodes (PUEs) by a circulating beam. Beam location is calculated from the signal amplitudes using delta over sum [1]. For the vertical plane BPM with two PUEs the equation can be written as

$$y = k\frac{U_{up}-U_{down}}{U_{up}+U_{down}} \quad (1)$$

where U_{up} and U_{down} are the amplitudes, k is a scaling factor, which is determined by the geometry of a vacuum vessel and the electrodes. For a symmetrical system and beam in the center both signals have equal amplitudes and the corresponding position readback is zero.

With two (or more) beams circulating inside the vacuum chamber we need to separate the signals and process them individually. For the colliders with beams moving in the opposite directions this task is solved by utilizing the striplines, which have directional properties. The signals from the different beams appear on the different ports and conventional processing units can be utilized.

This technique is not suitable for energy recovery linacs (ERL) and fixed-field alternating gradient accelerators (FFAG) where two or more beams co-propagate through a vacuum system in the same direction and each beam has its own trajectory.

PROPOSED METHOD

In the energy recovery linacs the beams pass either though an arc where only accelerated and decelerated beams of the same energy are present (on the last pass the only beam is present) or through an accelerating/decelerating section common for the all beams.

For ERL the time delay between accelerated and decelerated bunches is fixed by design and it is possible to employ the phase of the PUE signal to extract information on the position of each bunch. First we consider an arc where only two beams are present. If bunches, separated by a flyby time Δt_{12}, have different positions then each PUE sees different longitudinal "center of gravity" of the two bunches (see Fig. 1) and there is a phase shift between two signals. For a processing unit, utilizing signal processing at frequency ω, and small displacements of the first and the second bunches δ_1 and δ_2 ($S\delta_1, S\delta_2 \ll 1$, where $S=1/k$ is a sensitivity coefficient) we can write the linearized equations:

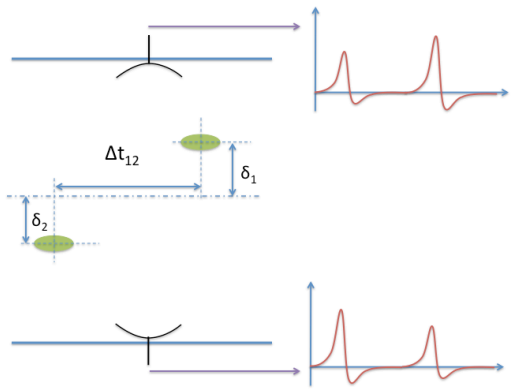

Figure 1: Signals induced on the pick-up electrodes by two bunches with different coordinates. Because of bunches' displacements the amplitudes of the induced voltages differ.

$$\begin{aligned} U_{up} &= U_1(1+S\delta_1)\sin\omega(t+\Delta t_{12}/2) + \\ &\quad U_2(1+S\delta_2)\sin\omega(t-\Delta t_{12}/2) \\ U_{down} &= U_1(1-S\delta_1)\sin\omega(t+\Delta t_{12}/2) + \\ &\quad U_2(1-S\delta_2)\sin\omega(t-\Delta t_{12}/2) \end{aligned} \quad (2)$$

When both bunches have equal charges (a valid assumption for ERL) then we re-write Eq. 2 as

$$\begin{aligned} U_{up} &= U_0\cos\tfrac{\omega\Delta t_{12}}{2}\left(2+S(\delta_1+\delta_2)\right)\sin\omega t + \\ &\quad U_0 S\sin\tfrac{\omega\Delta t_{12}}{2}(\delta_1-\delta_2)\cos\omega t \\ U_{down} &= U_0\cos\tfrac{\omega\Delta t_{12}}{2}\left(2-S(\delta_1+\delta_2)\right)\sin\omega t - \\ &\quad U_0 S\sin\tfrac{\omega\Delta t_{12}}{2}(\delta_1-\delta_2)\cos\omega t \end{aligned} \quad (3)$$

Neglecting second order terms we can estimate amplitudes ($A=\sqrt{U_{sin}^2+U_{cos}^2}$) of the signals induced on PUE

$$\begin{aligned} A_{up} &\approx 2U_0\left(1+S\tfrac{\delta_1+\delta_2}{2}\right)\cos\tfrac{\omega\Delta t_{12}}{2} \\ A_{down} &\approx 2U_0\left(1-S\tfrac{\delta_1+\delta_2}{2}\right)\cos\tfrac{\omega\Delta t_{12}}{2} \end{aligned} \quad (4)$$

*Work supported by Brookhaven Science Associates under Contract No. DE-AC02-98CH10886 with the U.S. DoE
#pinayev@bnl.gov

Substitution of the found amplitudes into the Eq. 1 gives

$$\hat{y} = k\frac{S(\delta_1+\delta_2)}{2} = \frac{(\delta_1+\delta_2)}{2} \quad (5)$$

That means that using information on the amplitude we measuring the average position of the beam. Now we will consider the phases of the signals. Using the same assumptions we will find

$$\begin{aligned} \varphi &\approx \frac{U_{cos}}{U_{sin}} \\ \varphi_{up} &\approx \frac{S(\delta_1-\delta_2)}{2}\tan\frac{\omega\Delta t_{12}}{2} \\ \varphi_{down} &\approx -\frac{S(\delta_1-\delta_2)}{2}\tan\frac{\omega\Delta t_{12}}{2} \end{aligned} \quad (6)$$

and difference of the two phases gives us the difference between two positions

$$\delta_1 - \delta_2 = k\frac{\varphi_{up}-\varphi_{down}}{\tan(\omega\Delta t_{12}/2)} \quad (7)$$

The processing frequency is usually equal to the RF frequency. Such a choice allows processing of any fill pattern because all bunches are separated by a multiple of the RF period. In the ERL distance between bunches can be different. It may be as small as half of the RF wavelength because the decelerated bunch should be in the opposite phase vs. accelerated one. Moreover, this distance can differ from the multiple of the half periods due to the shifts in the merge lines. Also, there is no revolution period in the ERL but only a round-trip time. Hence, choice of the processing frequency is somewhat arbitrary and can be used for optimization of the system. There are frequencies that should be avoided: if $\cos(\omega\Delta t_{12}) = 0$ then there is no signal for the average position calculation and with $\sin(\omega\Delta t_{12}) = 0$ phases will be constant and difference in orbits can not be found. Therefore, the processing frequency should be in between close to $\omega = \frac{\pi}{\Delta t_{12}}\left(\frac{1}{4}+N\right)$, where N is an integer.

SIGNAL-TO-NOISE RATIO

Modern digital beam position electronics have the required capability to process both amplitude and phase of the PUE signals [2].

To estimate the accuracy of the measurement let us consider vector diagram shown in Fig. 2. When the measurement error is not correlated with the signal the probable error will draw a circle around the end of the vector and r.m.s. phase error will be equal to the signal to noise ratio of the amplitude measurement

$$\sigma_\varphi = {}^{\sigma_A}/_{A} \quad (8)$$

That means that achievable error in the difference of position is the same as for the average position. For the system described in [2] r.m.s. position error is 3 microns for k=10 mm, which means that noise is 3×10^{-4} of the signal level and the ratio is close to the r.m.s. fluctuations of the phase measurements 0.01° (1.75×10^{-4} radians).

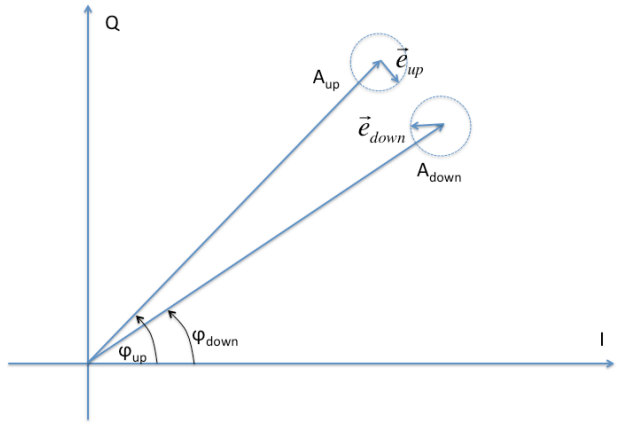

Figure 2: Vector diagram for the PUE signals. Two longer vectors indicate phases and amplitudes of the signal when two smaller ones show the noise amplitude.

So far we have neglected phase shifts in the system associated with propagation of the signals the cables and in the processing electronics. The system transfer function will not be identical for all channels and a phase shift corresponding to the identical beam positions should be established. Otherwise these phase shifts will include a systematic error in the measurement of the difference of the two positions. Similarly, the unequal gain and/or losses in the channels generate systematic offset in the average position readback.

Both phase and amplitudes can be calibrated using a RF generator with a splitter. In this case the whole chain from the cable to electronics can be characterized. For the phase calibration exclusively it is also possible to use exclusively the accelerated bunches (dumping the beam at high energy). In this case the BPM processing unit sees signal from a single bunch, and there are no ambiguities associated with the second bunch.

FOUR PUES SYSTEM

In the system with four pick-up electrodes, as shown in Fig. 3, the beam position is calculated with the modified equations.

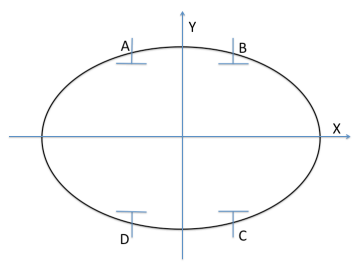

Figure 3: Geometry of the four PUE beam position monitor. Such configuration is used to avoid exposure of the PUEs to the synchrotron light.

$$\bar{x} = k_x \frac{U_B - U_A + U_C - U_D}{U_A + U_B + U_C + U_D}$$
$$\bar{y} = k_y \frac{U_B - U_C + U_A - U_D}{U_A + U_B + U_C + U_D} \quad (9)$$

As before, for the small beam displacements we can write

$$\begin{aligned} U_A &= U_0(1 - S_x\delta_{x1} + S_y\delta_{y1})\sin\omega(t + \Delta t_{12}/2) + \\ &\quad U_0(1 - S_x\delta_{x2} + S_y\delta_{y2})\sin\omega(t - \Delta t_{12}/2) \\ U_B &= U_0(1 + S_x\delta_{x1} + S_y\delta_{y1})\sin\omega(t + \Delta t_{12}/2) + \\ &\quad U_0(1 + S_x\delta_{x2} + S_y\delta_{y2})\sin\omega(t - \Delta t_{12}/2) \\ U_C &= U_0(1 + S_x\delta_{x1} - S_y\delta_{y1})\sin\omega(t + \Delta t_{12}/2) + \\ &\quad U_0(1 + S_x\delta_{x2} - S_y\delta_{y2})\sin\omega(t - \Delta t_{12}/2) \\ U_D &= U_0(1 - S_x\delta_{x1} - S_y\delta_{y1})\sin\omega(t + \Delta t_{12}/2) + \\ &\quad U_0(1 - S_x\delta_{x2} - S_y\delta_{y2})\sin\omega(t - \Delta t_{12}/2) \end{aligned} \quad (10)$$

With the similar to the above calculations we can find that Eq. 9 is applicable for the calculation of the average beam position when the difference can be found from

$$x_{diff} = \frac{k_x}{\tan(\omega\Delta t_{12}/2)}[(\varphi_B - \varphi_D) - (\varphi_A - \varphi_C)]$$
$$y_{diff} = \frac{k_x}{\tan(\omega\Delta t_{12}/2)}[(\varphi_B - \varphi_D) + (\varphi_A - \varphi_C)] \quad (11)$$

SUPPRESSION OF THE CABLE DRIFTS

The temperature changes and other slow processes can change physical length of the cable and/or phase velocity of the signal in the cable. To suppress the drifts one can lower the processing frequency to the range where the sensitivity to the variations of delays is less. Unfortunately, it also lowers the sensitivity to the position difference due to the $\tan(\omega\Delta t_{12}/2)$ term. To have both high sensitivity to the differential beam position (and low noise) and to suppress influence of drifts we can convert down the PUE signals. In this case the sensitivity is defined by sum of the local oscillator frequency and processing frequency, while drifts are defined by processing frequency only. Local oscillator signal should be brought to the PUE with a single cable and split to required number of mixers with shortest connection.

COMMON SECTION

In common section there more then two beams and we do not have sufficient data to resolve the position of each beam. To overcome this obstacle we can process at different frequencies. The set of the frequencies depends on the machine configuration and general rules are subject for development. For the system with all buckets filled (total number of independent bunches is equal to double of number of passes N_{pass}) all frequencies from the F_{rep} to $2xN_{pass}xF_{rep}$ can be utilized.

FFAG

In the FFAG the beams are separated in space as shown in Fig. 4. Nominal levels of the signals and linear coefficients can be easily found with numerical simulations (one need to account for the phase shifts for each bunch).

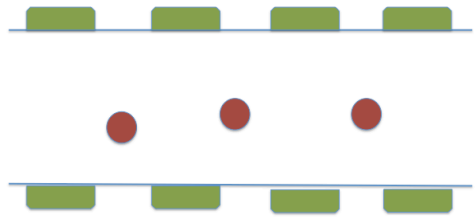

Figure 4: Arrangement of the circulating beams (red) and pick-up electrodes (green) for FFAG.

The difference with conventional accelerator will be that ratio will be not scalar but vector:

$$v_i = \frac{U_{upi} + U_{upi+1} - U_{downi} - U_{downi+1}}{U_{upi} + U_{upi+1} + U_{downi} + U_{downi+1}}$$
$$h_i = \frac{U_{upi} - U_{upi+1} + U_{downi} - U_{downi+1}}{U_{upi} + U_{upi+1} + U_{downi} + U_{downi+1}} \quad (12)$$

Matrices of the linear coefficients can be inverted and used for position calculations:

$$\vec{x} = M_H\vec{h}$$
$$\vec{y} = M_V\vec{v} \quad (13)$$

REFERENCES

[1] R.E. Shafer. “Beam Position Monitoring”, BIW’89, AIP Conf. Proc. 212 (NY, 1990), p. 26.

[2] M. Znidarcic et al., “Testing of New Hadron Beam Phase and Position Monitor at CIEMAT Laboratory,” DIPAC’11, Hamburg, May 2011, MOPD26, p. 104; http://www.JACoW.org

LONGITUDINAL BEAM HALO IN THE PHOTOEMISSION FROM GaAs-PHOTOCATHODES IN A 100 keV DC GUN

M.A. Dehn, K. Aulenbacher, E. Kirsch, F. Fichtner, V. Tioukine,
Johannes Gutenberg Universität Mainz, Germany

Abstract

At Johannes Gutenberg Universität Mainz measurements of the time response of photocathodes can be performed routinely at the "Testquellenlabor" (source testlab) using a deflector cavity. Short electron bunches are generated using a femtosecond tunable laser system operating at 800 nm for best polarisation/QE if GaAs is used. In our experiment the laser radiation is also frequency-doubled to 400 nm in order to compare the time response at different wavelengths. First measurements show an important modification of the longitudinal beam profile at 400 nm without the trailing electrons which are typically observed at 800 nm.

INTRODUCTION

In addition to a high beam current of 10−100 mA, a long cathode lifetime, low emittance and a low dark current, future accelerator projects (e.g. Mainz Energy-Recovering Superconducting Accelerator (MESA), Berlin Energy Recovery Linac Project (BERLinPro)) require extremely low levels of unwanted beam. To achieve these demands, an analysis of the emitted electron bunches is necessary to determine if the pulse response corresponds to the acceptance of the accelerator.

Emission of electrons which occurs after a certain time may be considered as 'unwanted beam'. In the present paper we extent our old results for GaAs [1] towards excitation with photons in the blue wavelength region. This is typical for an injector into an ERL based light source, where production of polarised electrons (which is only possible with infra-red excitation) is of no importance.

Our measurements indicate that using photons of higher energy leads to a considerable reduction of the unwanted longitudinal beam.

This project is part of joint German-Russian research program and is supported by the German Federal Ministry for Education and Research (Bundesministerium für Bildung und Forschung, BMBF [1]).

PHOTOCATHODES

For high average current machines only two out of the many possible types of photocathodes (see Figure 1) are of interest. Photocathodes of type Cs:GaAs belong to the group of semiconductors with a negative electron affinity (NEA) as opposed to semiconductors with positive electron affinity (PEA) such as K_2CsSb.

[1]FKZ: 05K12UM1 PCHB photocathodes

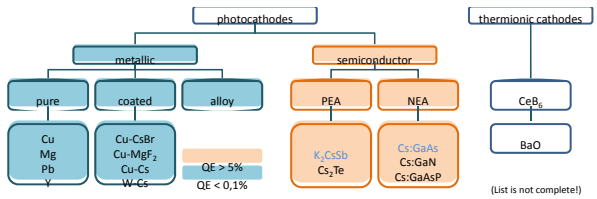

Figure 1: Overview of different cathode types [2]. The semiconducting photocathodes (highlighted) are the most interesting type for this analysis.

Until now, different types of GaAs photocathodes are used at both Mainzer Microtron (MAMI) and source testlab (PKAT) at Johannes Gutenberg University Mainz (JGU). At PKAT, there is the possibility of time response measurements. So, shape and length of electron bunches — generated by laser wavelength λ_{laser} of 800 nm — are well known [1].

Since early 2013 we have the possibility to study the pulse response also for photoexcitation with higher photon energies. Therefore, a direct comparison of the response of NEA-GaAs for excitation with sub-picosecond laser bunches with photon energies of $\approx$ 1.5 eV (800 nm) and $\approx$ 3 eV (400 nm) became possible.

EXPERIMENTAL SETUP

The time response of the emission process is encoded within the longitudinal beam profile. A TM_{110} deflector cavity operating at 2.45 GHz of the RF master of MAMI with a maximum input power of 340 W transforms the longitudinal beam profile into a transverse one. The beam spot is observable as an intensity distribution on a fluorescent screen (YAG-screen).

The design of the electron source at PKAT does not allow a bunch charge which is high enough for analysing a single electron bunch. Thus, the analysed image of a beam spot on a YAG-screen is a sample of more than 10^5 electron bunches. If the frequency of electron bunches is synchronised to the radio frequency (RF) of the defector cavity, every bunch is deflected at the same RF phase. Then the resulting intensity distribution represents the time dependency of electrons in one bunch.

Laser System

At PKAT the laser system consists of three components: A DC laser (P_{laser} = 10 W, λ_{laser} = 532 nm) is needed for pumping a modelocked Ti:Sapphire laser. The

Ti:Sapphire laser can be operated DC or pulsed with a pulse length as short as 150 fs. The repetition rate of 76 MHz equates to the 32nd subharmonic of the RF cavity. The synchronisation is provided by locking the laser to the cavity by a PLL circuit. With its tunable wavelength, modelocking of the Ti:Sapphire laser is possible in a range of $\lambda_{\text{laser}} = 755-800$ nm. This range can be extended to $\lambda_{\text{laser}} = 700-850$ nm by using optimised mirrors in the laser resonator. An external, single pass beta barium borate (BBO)-frequency doubler crystal is used in order to double the photon energy. By bypassing the doubler stage, it is possible to compare the time responses at the fundamental and the harmonic frequency. Changing from one type of excitation to the other typically requires 15 minutes.

PKAT Laboratory

The 100 keV DC photoemission electron source in PKAT is constructed in the same way as the polarised electron source of MAMI [3]. Besides the direction of the laser and the electron beam, the most important elements of the beamline for time response measurements are labeled in Figure 2: the deflector cavity, a fluorescence screen (YAG-screen), and the CCD-camera at the end of the beamline.

In 2013 the klystron [3] which was used to drive the cavity was replaced by a home build 2.45 GHz solid state amplifier.

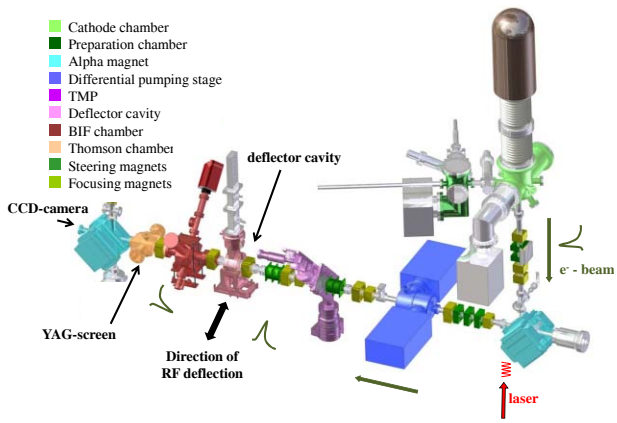

Figure 2: Test source laboratory PKAT at JGU. Direction of laser and longitudinal shape of electron bunches are shown schematically. [4]

TIME RESPONSE MEASUREMENT

The electron source at PKAT is not constructed for high bunch charges. So the observed image on the YAG-screen is no single shot but a sampling of many bunches depending on the exposure time of the CCD-camera. The contribution of timing jitter during the exposure time is estimated to be of the order of 1 ps or less.

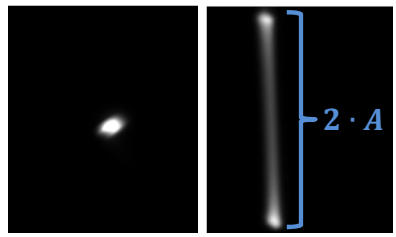

Figure 3: Transverse beam spot (RF off) on the left, and many electron bunches after RF-deflection on the right. RF and laser pulses are **not** synchronised. [5]

Calibration of the YAG-screen

A calibration of the YAG-screen is necessary to yield the correlation between time information and metric dimension of deflection as it is shown in Figure 3.

On the left a picture of transverse beam spot is shown. On the right RF is switched on but laser pulses are not synchronised to RF. The observed beam width corresponds to twice amplitude A of the RF.

The correlation between A and the power P_{RF} of RF is given by

$$A \propto \sqrt{P_{\text{RF}}} \tag{1}$$

The position on the screen is given by

$$x(t) = A \cdot \sin(\varphi_{\text{RF}}) = A \cdot \sin(\omega t) \tag{2}$$

where φ_{RF} is the RF phase. With the time derivation

$$\dot{x}(t) = A \cdot \omega \cdot \cos(\omega t) \tag{3}$$

the correlation between time and metric dimension can be done for $t = 0$.

Different calibrations with different P_{RF} (here at $\lambda_{\text{laser}} = 800$ nm) confirm this correlation. Increasing P_{RF} means a better time resolution:

$$P_{\text{RF}} = 45\,\text{W} \Rightarrow 1\,\text{mm} \mathrel{\hat{=}} 6.6\,\text{ps}$$

$$P_{\text{RF}} = 339\,\text{W} \Rightarrow 1\,\text{mm} \mathrel{\hat{=}} 2.4\,\text{ps}$$

Preliminary Results

Figure 4 shows a qualitative comparison of two beam spots, left original (transverse) beam spot, right longitudinal bunch profile when RF and laser pulses are synchronised. Sections of such CCD frames then serve for quantitative analysis.

Preliminary results at low beam current ($I_{\text{e-beam}} < 10$ nA $\mathrel{\hat{=}}$ 0.1 fC bunch charge) are shown in Figure 5. Exposure time of the CCD-camera is 4 ms — this corresponds almost to 3×10^5 bunches. Four measurements (normalised intensity over time [ps]) of transverse and longitudinal electron bunches at $\lambda_{\text{laser}} = 800$ nm (red) and 400 nm (black) are shown in comparison to each other.

While the transverse diameters d_{FWHM} from both laser wavelengths are in the same range ($d_{\text{FWHM}} \approx 260\,\mu$m) the

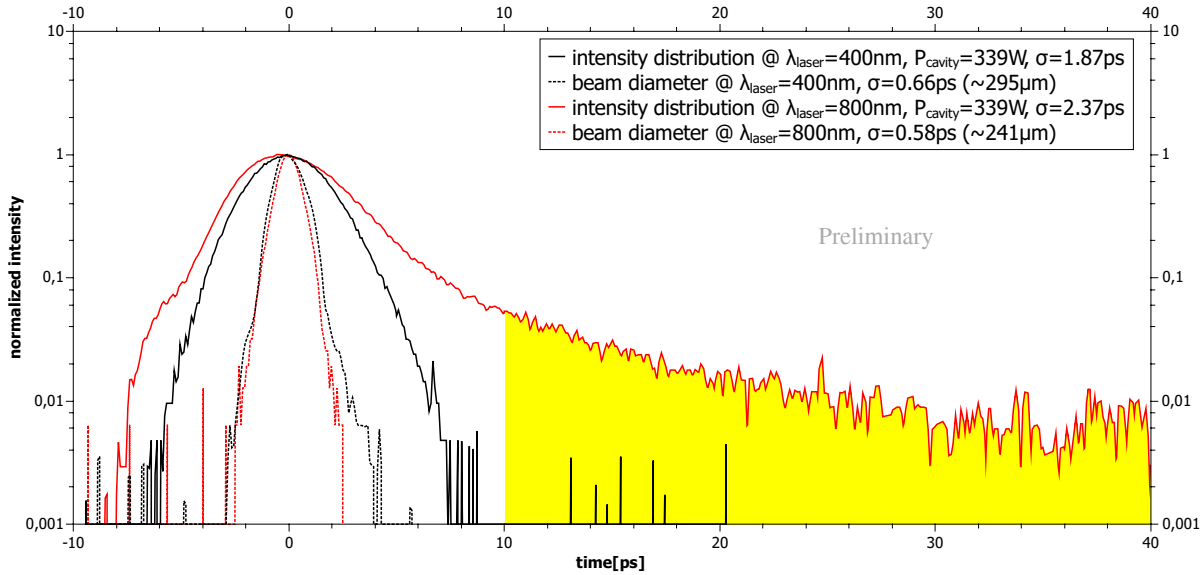

Figure 5: Longitudinal and transverse pulse profiles at $\lambda_{\text{laser}} = 800\,\text{nm}$ (red) and $\lambda_{\text{laser}} = 400\,\text{nm}$ (black) [5]. The yellow area shows the beam loss at the acceptance of an accelerator of $\sigma_{\text{pulse}} = 10\,\text{ps}$.

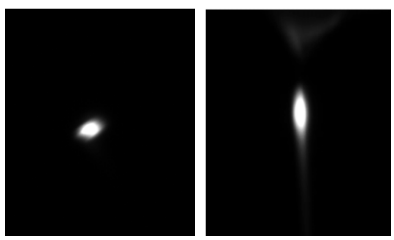

Figure 4: Original transverse beam (left), and longitudinal beam profile (right). RF and laser are synchronised. [5]

electron bunches have a different time structure. The response with deflection on is dominated by the longitudinal response for the bulk GaAs cathode used here, since the transverse extension of the beam is smaller by factor of 5. The tail of the bunches, which may be identified with the longitudinal halo, depends on λ_{laser} because of a higher absorption coefficient and smaller penetration depth at $\lambda_{\text{laser}} = 400\,\text{nm}$.

Assuming an acceptance of an accelerator of $\sigma_{\text{pulse}} = 10\,\text{ps}$, almost 10% of the beam intensity is lost at $\lambda_{\text{laser}} = 800\,\text{nm}$ (yellow area in Figure 5), e.g. for a beam current of $I_{\text{e-beam}} = 10\,\text{mA}$, 1 mA of current ("unwanted beam") will be lost.

Obviously, the contribution from unwanted beam for blue excitation is at least one order of magnitude smaller. A better estimation of the improvement will require a measurement of the beam profile with higher dynamic range.

OUTLOOK

To increase the dynamic range of time response measurements, implementation of an alternative method is planned. In addition to the YAG screen we will install a channeltron behind a $100\,\mu\text{m}$ slit. We expect an large increase of sensitivity since then the dynamic range of the device is controllable by the amplification of the channeltron. Bandwidth will be of the same order as with the CCD since a fast steering magnet will be used for scanning the bunch profile over the slit.

In a next step, time response measurements will be repeated with PCA photocathodes. These cathodes are known to exhibit higher beam current and a better lifetime [6].

REFERENCES

[1] K. Aulenbacher, J. Schuler, D. v. Harrach, E. Reichert, J. Röthgen et al.: "Pulse response of thin III/V semiconductor photocathodes", J. Appl. Phys. 92, 7536 (2002); doi: 10.1063/1.1521526

[2] D.H. Dowell, I. Bazarov, B. Dunham, K. Harkay et al.: "Cathode R&D for future light sources", Nuclear Instruments and Methods in Physics Research A 622 (2010) 685-697

[3] P. Hartmann: "Aufbau einer gepulsten Quelle polarisierter Elektronen", Dissertation 1997, JGU Mainz, Germany

[4] T. Weilbach, K. Aulenbacher, M. Bruker: "Beam profile measurement for high intensity electron beams", Proceedings of IPAC2013, Shanghai, China

[5] E. Kirsch: Diploma Thesis in preparation, JGU Mainz, Germany

[6] I. Bazarov, L. Cultrera, A. Bartnic, B. Dunham et al.: "Thermal emittace measurements of a cesium potassium antimonide photocathode", Appl. Phys. Lett. 98, 224101 (2011); doi: 10.1063/1.3596450

DARK CURRENT IN SUPERCONDUCTING RF PHOTOINJECTORS – MEASUREMENTS AND MITIGATION

J. Teichert#, A. Arnold, P. Murcek, G. Staats, R. Xiang, HZDR, Dresden, Germany
P. Lu, H. Vennekate, HZDR & Technische Universität, Dresden, Germany
R. Barday, T. Kamps, HZB, Berlin, Germany

Abstract

Unwanted beam can cause beam losses and may produce acute or chronic damages of the accelerator. Furthermore it can considerably disturb experiments or increase its back-ground. The operation of the superconducting RF photo gun at the ELBE accelerator has delivered the first experimental information on that topic for this gun type. It was found, that dark current is an important issue, similar to that of normal conducting RF photo injectors. In the presentation the measurement of dark current, its properties and analysis will be shown and we will discuss ways for mitigation, especially the construction of a dark current kicker.

INTRODUCTION

ELBE is a user facility with a superconducting electron linear accelerator based on TESLA-type RF cavities and operates in continuous wave (CW) mode with original design values of maximum beam energy of 40 MeV and average beam current of 1 mA. In 2012 an upgrade in beam current to 1.6 mA was realized. The facility serves for manifold applications of electromagnetic radiation and particle beams ranging from the operation of two free-electron lasers (FEL) for infrared light, the production of gamma rays for nuclear astrophysics, positrons for material science, neutrons for transmutation studies, and beams for oncological radiations. For high-current applications like FELs or gamma ray production, small fractions of beam loss of 0.1 % or less can damage accelerator components. For the other low-current applications like radiation treatment of cells, tests of new particle detectors, or Compton backscattering experiments unwanted beam produces irradiation dose errors or additional measurement background. A thermionic electron gun has served as injector since the commissioning of the accelerator in 2001. Unwanted beam derives from field emission in the acceleration cavities and beam halo due to jitter or other instabilities.

A new superconducting RF photo-injector (SRF gun) has been developed and installed at ELBE which produces beams of higher brightness and allows for higher bunch charges than the thermionic injector. The design of the SRF gun and its present status and properties are presented elsewhere [1, 2]. The SRF gun will replace step by step the thermionic injector.

Normal-conducting RF photo-injectors are known to produce a high amount of dark current due to field emission [3, 4]. Especially for RF photo-injectors with long bunch trains like at FLASH or the future European XFEL, dark current is a serious problem and requires counter measures as the installation of a dark current kicker [5]. Dark current might be also a problem for SRF guns, especially due to their CW operation. For the SRF gun at ELBE we therefore performed dark current measurements.

SRF GUN DESCRIPTION

The SRF gun at ELBE comprises a 3½-cell niobium cavity for 1.3 GHz with a 12 mm hole in the half-cell back wall for the insertion of the photo cathode as it is shown in Fig 1. The photo cathode is hold by the cathode cooler and its 10 mm diameter stem extends through the choke filter cell into the hole of the half-cell. There is a 1 mm circular gap between the cathode stem and cavity. Thus the cathode is electrically and thermally insolated off the cavity. The front part (plug) of the cathode stem consists of Mo whereas the other part is Cu. The Cs_2Te photo layer is deposited on the front surface of the Mo plug. Usually the cathode is about 2.5 mm retracted with respect to the half-cell wall resulting in a lower cathode surface field.

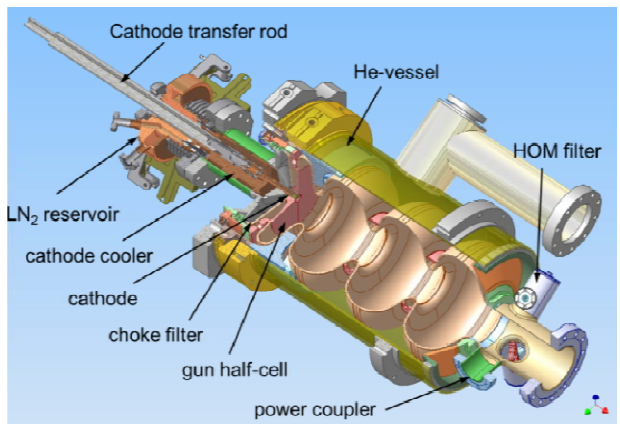

Figure 1: SRF gun cavity with liquid He vessel and cathode cooling system.

The on-axis acceleration field of the cavity is presented in Fig. 2a and the corresponding surface electric field is shown in Fig. 2b. The calculation was carried for the design value of 50 MV/m peak field but the relative field distributions are true also for the lower field values used in the measurements. Compared to the peak field in the three TESLA cells, the maximum on-axis field in the half-cell is 60 %, and at the cathode the value is 40 % caused by the retracted cathode. The details of the geometry near the cathode are shown in Fig. 3. For high-field areas, significant for field emission, the simulation delivers 80 % of the peak value at the cathode boring

edge and 110 % at the iris between half-cell and first TESLA cell.

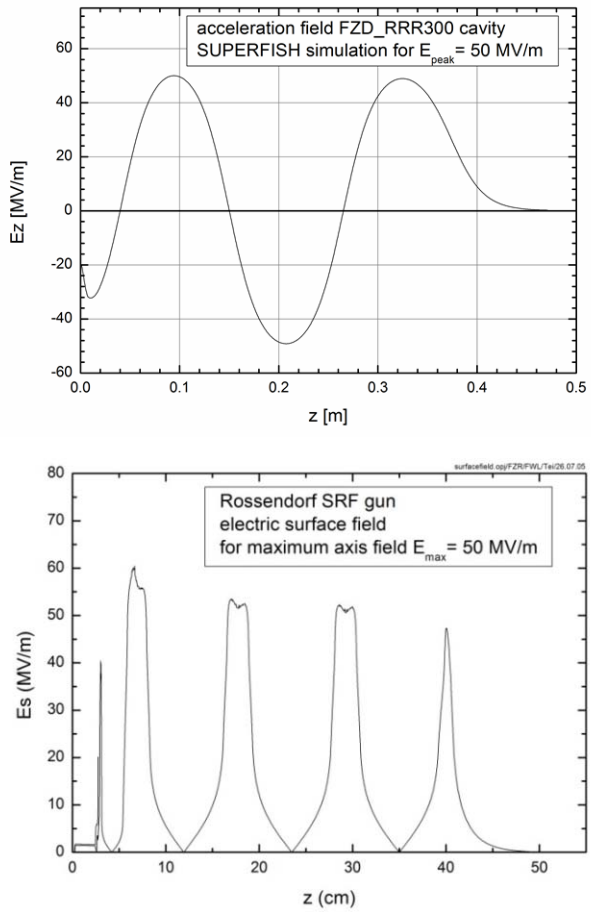

Figure 2: On-axis acceleration field (a), and electric surface field (b) versus cavity length coordinate.

Beam dynamic simulation showed that field-emitted electrons from the iris regions have wrong energy and do not leave the cavity. Thus, they do not contribute to the dark current. The dark current electrons must be emitted from the cathode or adjacent cavity areas. It is obvious that the simulation delivers probable field emission areas but the actual intensity depends on the local field enhancement and work function.

The standard operation of the SRF gun is CW mode. In this case the gun delivers an electron beam with a kinetic energy of 3 MeV and the acceleration gradient amounts to about 16.5 MV/m. Due to the lower field in the half-cell, the retracted photo cathode and the early launch phase, the field in front of the cathode which the electron bunch sees is rather low (see Table 1). In order to obtain higher gradients with the present cavity and simultaneously to keep the load to the liquid helium system low, the input RF power can be pulsed. The typical repetition rates are 1 to 10 Hz and the pulse length can be adjusted between 5 and 20 ms. In this case the peak field can be increased up to 21.5 MV/m and the corresponding final kinetic energy is 4 MeV. In both operation modes, CW or pulsed, a bias of -5 kV was usually applied to the cathode. This additional voltage increases the field at the cathode and improves slightly the beam quality.

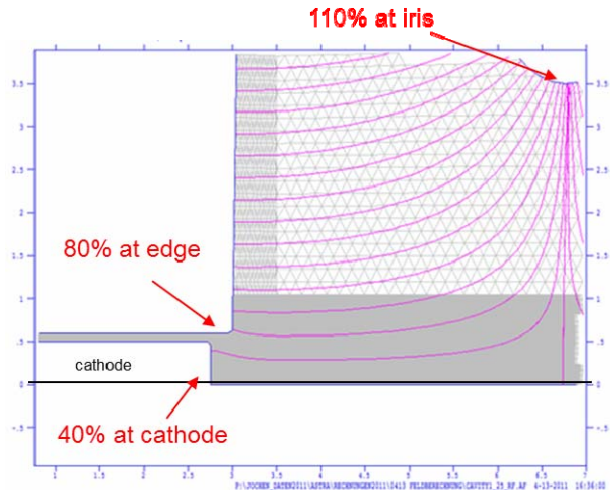

Figure 3: Electric field distribution in the cavity half-cell near the cathode (Superfish simulation).

In the SRF gun cavity the acceleration gradient is limited by the strong field emission in the half-cell, which has been in detail discussed in earlier papers [1, 2]. But it is important to note that the main reason for the field emission is a scratch near the cathode boring in the half-cell. As discussed above, the field emitted electrons originating from this near-cathode scratch contribute to the dark current leaving the gun.

DARK CURRENT MEASUREMENTS

Dark current has been measured with a removable Faraday cup located approximately 1460 mm downstream from the cathode. At the same position a YAG screen can be inserted for observing the beam spot. Together with a solenoid located in between, the cathode can be imaged with the dark current electrons onto this screen. The momentum distributions of the dark current electrons were measured with a 180° bending magnet and a following YAG screen in the diagnostic beamline.

First studies of the dark current emission of the gun were carried out in 2011. Figure 4 shows the dark current as function of the on-axis peak field for the measurements with two different Cs_2Te photo cathodes and for the gun without cathode. The curves show the typical Fowler-Nordheim dependence on the field strength. A comparison shows that the larger fraction comes from the cavity. Probably, the scratch in the cavity emits most of the electrons. The dark current contribution of one cathode (#250310Mo) is about 20 %. For the second cathode (#060410Mo) the dark current was, within the measurement accuracy, equal to that without cathode. But due to the long time between these two measurements a decrease of the cavity dark current contribution cannot be excluded.

Table 1: Typical values for gradients and fields in the HZDR SRF gun for CW and pulsed mode

gun operation mode	CW	pulsed RF
acceleration gradient	6.0 MV/m	8 MV/m
electron kinetic energy	3 MeV	4 MeV
peak field on axis	16.5 MV/m	21.5 MV/m
peak field at cathode (2.5 mm retracted)	6.5 MV/m	8.4 MV/m
cathode field at launch phase (10°)	1.1 MV/m	1.5 MV/m
cathode field at 10° and -5 kV bias	2.2 MV/m	2.6 MV/m

In a second series, four different cathodes were compared within one measurement shift. The first cathode (Nb/Pb cathode) had the standard design but a Nb plug and a Pb photo emission layer deposited by arc discharge at Soltan Institute, Swierk [6]. Further two cathodes had molybdenum plugs with modified head designs (HZB_cap_CsTe and HZB_plug_clean), and the forth cathode was a standard HZDR photo cathode with Mo plug (#300311Mo). For all the cathodes the plug front surfaces were polished to optical quality and cleaned at HZDR. Two of the photo cathodes had a Cs_2Te layer (HZB_cap_CsTe and #300311Mo) and one had a clean Mo surface (HZB_plug_clean).

The dark current results of the four photo cathodes and of a reference measurement without cathode are shown in Fig. 5. The dark current level is nearly the same as in the previous measurements (Fig. 4) and it is confirmed that the main dark current source is the cavity. The cathodes with Cs_2Te layer contribute with about 20 %, whereas the Nb/Pb and the pure Mo cathode do not significantly contribute to the dark current.

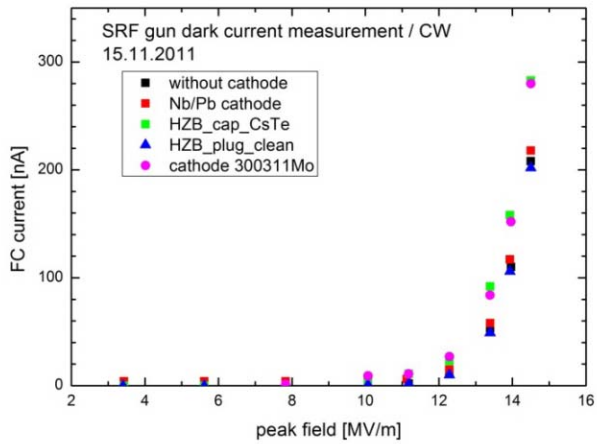

Figure 5: Dark current measurement results (Faraday cup current) for four photo cathodes of different shape or material tested in the SRF gun in fall 2011.

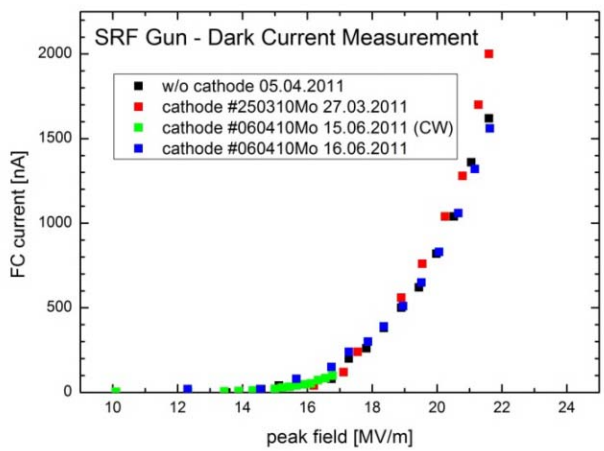

Figure 4: Dark current measurement results (Faraday cup current) for two photo cathode operated in the SRF gun in the 1st and 2nd run 2011.

The dark current measurements presented in Fig. 4 were analyzed using the field emission model for a time-dependent RF field [7]. The Fowler-Nordheim plot is shown in Fig. 6 with a fit curve delivers a field enhancement factor of 591 and an effective area of 0.63 nm^2.

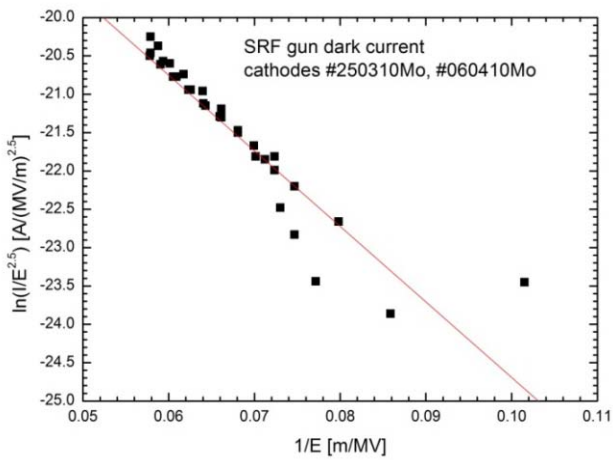

Figure 6: Fowler-Nordheim plot of the two photo cathodes operated in the SRF gun in 2011. (Data are shown in Fig. 4.)

For the SRF gun at ELBE two new cavities have been built in collaboration with Jlab. The first one (Compared to the used one, in the design slightly modified cavity made of fine grain Nb.) has been tested in the vertical cryostat until a peak field of 43 MV/m (E_{acc}=16 MV/m). During this test the measured field emission was very low. Since the beam quality requires a gradient as high as possible, the new cavity will be operated at its limits. It is therefore interesting to estimate the dark current for the

new cavity. The results are shown in Fig. 7. The green curve shows the extrapolation for the cavity in use. The blue curve is the estimation for the new cavity. Since this cavity reaches a two times higher acceleration gradient, the surface treatment is accordingly better and we assumed the same dark current contribution of about 1.5 µA when operating at the gradient of 16 MV/m. Concerning the photo cathodes, the 20% contribution measured in the existing gun has been extrapolated. Here no decrease is assumed. It yields about 40 µA at 16 MV/m acceleration gradient, which is obviously too high for future operation in CW accelerators. Thus further effort is needed to reduce the field emission of photo cathodes at high gradients.

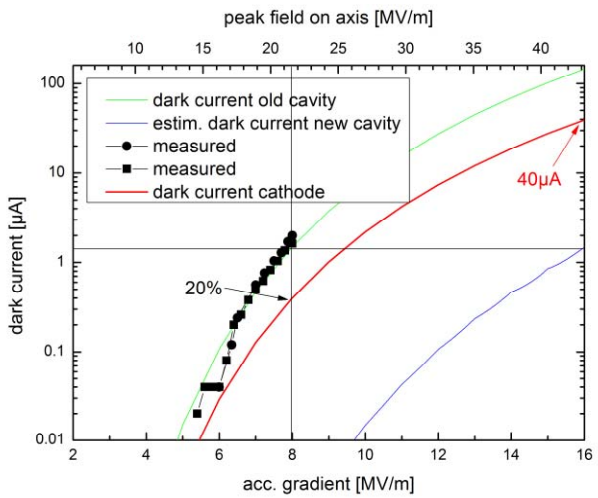

Figure 7: Estimation of dark current for higher gradients based on the Fowler-Nordheim data of the measurements; green curve: extrapolation of the existing cavity, blue curve: field emission assumption for the new cavity without surface damage and with lower field emission, red curve: extrapolation of photo cathode field emission.

Fig. 8 shows screen pictures in the dispersive part behind the 180° dipole magnet for a real beam with 30 pC bunch charge (1.5 µA @ 50 kHz) and an momentum of 3.3 MeV/c (E_{acc} = 6 MV/m) as well as for the accompanying dark current of 120 nA. The energy difference between electron beam and dark current was found to be less than 50 keV. This is nearly equal to the energy spread of the electron beam.

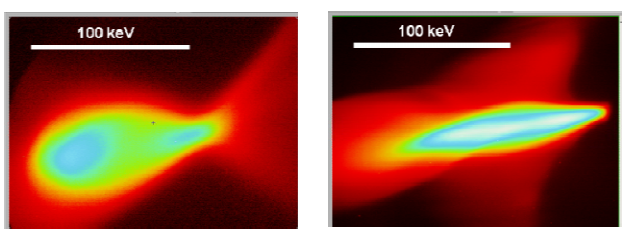

Figure 8: Dark current (left) and electron beam (right) images in the dispersive beamline behind the 180° dipole.

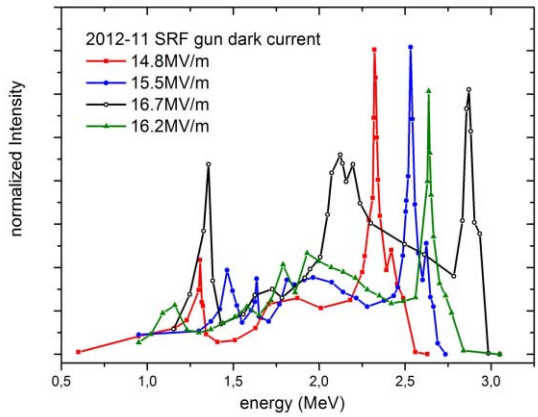

Figure 9: Dark current energy spectra for different acceleration gradients.

Detailed energy spectra of the dark current were measured as function of the cavity gradient and are shown in Fig. 9. The spectra are calibrated to each other by measuring the integral current with the Faraday cup at the same time. The high energy peak of each curve has nearly the beam energy as discussed earlier. The fraction of the high energy peak varies between 25 and 13 % depending on the gradient.

The high-energy fraction of the dark current can hardly be separated by dispersive methods. At ELBE the beam line acceptance is sufficient that this dark current is accelerated and transported to the user stations without further losses.

CONCLUSION

The dark current data measured up to now on several cathodes in the SRF gun at ELBE have been collected and analysed. Although the gradient is much lower than in normal-conducting RF guns, the data allow predictions to higher gradients. In the present measurements about 80% of the dark current emission comes from the cavity surface. The origin seems to be the damaged back wall surface near the cathode. For a new gun cavity which can reach about 40 MV/m peak field, the number of field emitters will be accordingly lower and the field emission level at its higher gradient nearly will be the same will or even lower. On the other side, the contribution from the photo cathodes will then increase to an estimated value of 40 µA. Experience at ELBE has shown that an unwanted beam level of 40 µA is too high for a CW accelerator. Thus an improvement of photo cathodes seems to be necessary. An alternative way is the installation of a dark current kicker. A schematic picture (Fig. 10) illustrates its function. The kicker should work with 13 MHz in CW mode with a sufficient amplitude to deflect the 1.3 GHz dark current pulses on a collimator. The kicker will be switched off for about 5 ps around the beam pulse. In this way the suppression is to 6.5 %.

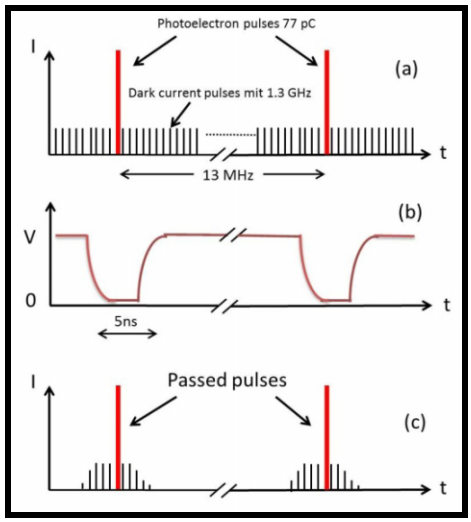

Figure 10: Dark current kicker functionality: (a) pulse distribution before the kicker, (b) kicker signal, (c) pulse distribution behind kicker and collimator.

ACKNOWLEDGMENT

The authors would like to thank Robert Nietubyc for preparing the Nb/Pb photo cathode and the whole ELBE team for their help and assistance. The work is supported by the European Community under the FP7 programme (EuCARD-2, contract number 312453, and LA3NET, contract number 289191), and by the German Federal Ministry of Education and Research grant 05K12CR1.

REFERENCES

[1] A. Arnold et al., Nucl. Instr. and Meth. A577 (2007) 440.
[2] J. Teichert et al.,"Pulsed Mode Operation and Longitudinal Parameter Measurement of the Rossendorf SRF Gun", IPAC 2011, San Sebastian, Spain, p. 262.
[3] W. Hartung et al., "Studies of Photo-Emission and Field Emission in an RF Photo-Injector with High Quantum Efficiency Photo-Cathode", PAC 2001, Chicago, USA, p. 2239.
[4] L. Monaco, et al., "Dark Current Investigation of FLASH and PITZ RF Guns", EPAC 2006, Edinburgh, Scotland, p 2493.
[5] F. Obier, et al. "Dark Current Kicker Studies at FLASH", FLASH Seminar, DESY, 2. Febr. 2010.
[6] P. Strzyzewski, et al., "Deposition of Lead Thin Films Used as Photo-Cathodes by means of Cathodic Arc under UHV Conditions", EPAC 2006, Edinburgh, p. 3209.
[7] J.W. Wang and G.A. Loew, "Field Emission and RF Breakdown in High-Gradient Room-Temperature Linac Structures", SLAC-PUB-7684 October 1997.

FEASIBILITY STUDY OF MULTI-TURN ERL-BASED SYNCHROTRON LIGHT FACILITY

A.N. Matveenko*, T. Atkinson, A.V. Bondarenko, Y. Petenev, Helmholtz-Zentrum Berlin, Germany

Abstract

Energy Recovery Linacs (ERL) have been discussed as drivers for synchrotron radiation facilities in X-ray region for over a decade. The first proposal for a multi-turn ERL as a next generation synchrotron light facility was in 1997 [1]. Since then great advances in ERL technology and high brightness electron source development were achieved [2], ERL-based high power free electron infrared laser at JLab (e.g. [3]) and the demonstration of multi-turn energy recovery at BINP [4]. The feasibility of an X-ray ERL-based light source seems more and more realistic.

An overview of the design of a multi-turn ERL under development at Helmholtz Zentrum Berlin (FSF – Femto-Science Factory) is given in this paper.

LAYOUT

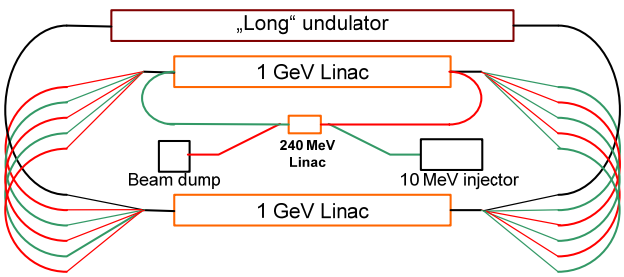

Figure 1: General layout of the FSF. Green lines – beam at acceleration, red – at deceleration, black – 6 GeV beam.

The accelerator layout is shown in the Fig. 1. It consists of a 10 MeV high brightness photo injector, medium energy (240 MeV in the picture) second stage injector, main linac, which is split into 2 1-GeV linacs (similar to CEBAF design). Each of the 1 GeV linacs is passed 3 times by the beam to gain 6 GeV, deceleration takes place in the reverse order. Undulators with user stations can be installed in (emittance optimized) arcs at all energies (see Fig. 4). Additionally, there is a possibility to have a long undulator at the maximal beam energy.

The beam and accelerator parameters are summarized in the following Table 1.

In following chapters we summarize specific features of this design.

*Work supported by grants of Helmholtz Association VH-NG-636 and HRJRG-214

#aleksandr.matveenko@helmholtz-berlin.de

Table 1: Main Parameters of the Multi-Turn ERL

Accelerator/beam parameters	High brilliance mode	Short pulse mode
E, GeV	6	6
$\langle I \rangle$, mA	20	5
Q, pC	15	4
$\varepsilon_{\perp n}$, mm	0.1	~0.5
$\varepsilon_{\parallel}$, keV·mm	~3	~3
τ, fs	200-1000	~10
$\langle B \rangle$, $\frac{Ph}{s \cdot mm^2 mrad^2 0.1\%}$	$8 \cdot 10^{22}$	$\sim 4 \cdot 10^{21}$
B_{peak}, $\frac{Ph}{s \cdot mm^2 mrad^2 0.1\%}$	10^{26}	$\sim 10^{26}$

Two-Stage Injection and Split Linac Geometry

The cascade injection drastically improves the low to high energy ratio in the first 1 GeV linac, which allows for reasonable focusing along the linac for all energies and improves TBBU stability of the installation. On the other hand, 250 MeV arcs can be used for the longitudinal bunch compression (additional compression stage) on acceleration, to reduce the energy spread during deceleration by decompression, and to compensate for the average energy loss of the beam due to radiation. Finally, if one has concerns of even higher energy spreads at deceleration (consider SASE FEL), beam scrapers (or an additional beam dump for a reasonable average current) at 250 MeV can be thought of.

Split linac geometry allows to separate beams in the arcs, (i.e. the beam on accelerating path have different energy compared to the beam on the decelerating path) so that they are transported in separate vacuum chambers. This way all the beams can be steered separately, and users see only one beam type in every undulator.

Operation Modes

As shown in the Table 1, two main operational modes of the accelerator are considered. The high brilliance mode is optimized for the maximum average brilliance. Low transverse emittance and high flux are important for this mode. A long bunch is preferable in this mode to maximize the flux keeping transversal emittance low. No bunch compression is necessary, the linacs operate at phase 90° (maximal acceleration) of the RF, longitudinal dispersion (R_{56}) of all arcs are zero.

The short pulse mode is designed to provide short pulses of X-ray radiation with high peak brilliance. The bunch length in undulators is limited by collective effects in this case and will vary depending on the bunch charge.

Bunch compression is distributed over 3 available compression stages: in the booster and merger; pre-injection linac and pre-injection arc; first turn in the main linacs, 1 and 2 GeV arcs. These arcs need to have adjustable longitudinal dispersion (R_{56}). The optimal distribution of the compression over the stages depends on the bunch charge and is subject to optimization.

Undulators

The parameters of the undulators investigated for the FSF are summarized in the Table 2. N is the number of periods, and N_{sec} is the number of undulator sections. Type 1 undulator is considered as "long undulator" for the 6 GeV return line. Type 2 undulators are considered for all arcs (5 undulator for each arc, up to 60 undulators in total).

Table 2: Undulator Parameters

Undulator parameters	Type 1	Type 2
N	3000	1000
N_{sec}	30	10
d, cm	4	4
K	0-2.5	0-2.5
Bmax, T	0.67	0.67

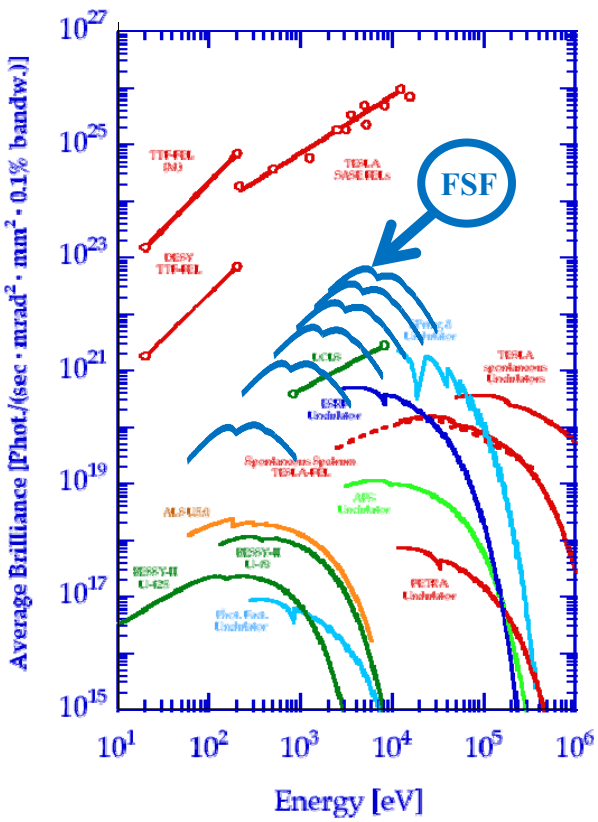

Figure 2: Brightness curves of the FSF arc undulators (Type 2 undulators of Table 2).

Coherent fraction of the radiation calculated according to [5] (see e.g. [6] for more detailed discussion)

$$\zeta = \frac{\lambda^2}{16\pi^2 \sigma_x \sigma_{x'} \sigma_y \sigma_{y'}}$$

is shown in Fig. 3. Transverse coherence approaching diffraction limit is achievable.

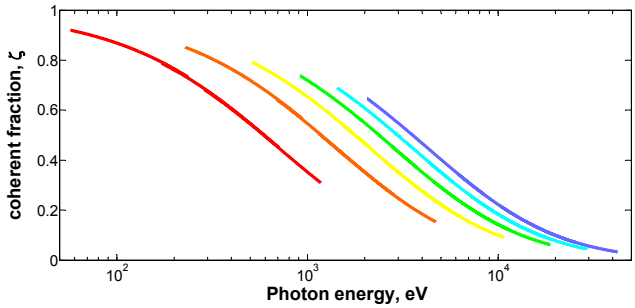

Figure 3: Coherent fraction of the FSF undulator radiation at 1 (red) through 6 (blue) GeV for the photon energies covered by the first to fifth harmonics.

Radiation Losses

The energy losses of the beam due to ISR, CSR, and other wakes are higher than the injection energy of the accelerator (see [11] for estimations in different operation modes). This energy must be compensated by booster linacs installed in the 6 GeV arc, or, alternatively, in the preinjector section with a separate high average power booster linac. Approximately 50 MeV and up to 500 kW losses should be compensated.

ACCELERATOR OPTIC ISSUES

Arcs

Each FSF arc consists of 6 30° bending sections and 5 undulators between them (Fig. 4).

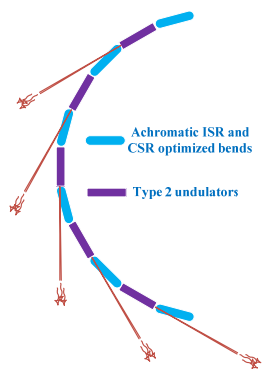

Figure 4: Layout of FSF arcs.

Each bending section of the 3 to 6 GeV arcs (detailed layout shown in Fig. 5) is optimized to minimize the emittance growth due to both incoherent (ISR) and coherent synchrotron radiation (CSR). Each section consists of 4 identical triple-bend cells with matching quadrupoles to the following undulator (or spreader). An important feature of the cell design is the negative middle bend to achieve zero R_{56} at a moderate strength of quads. Each cell has betatron phase advance Q_x=3/4 in order to cancel out the emittance growth due to CSR [7] in each 30°-section. Twiss parameters inside cells are optimized to minimize the radiation integral I_5.

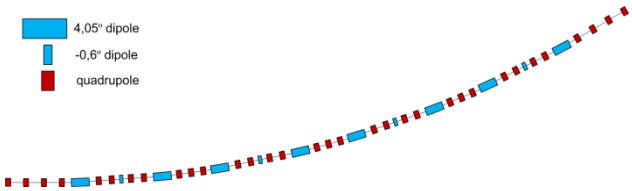

Figure 5: Layout of a 30°-section of the FSF arcs.

Bending sections of the 1 and 2 GeV arcs have a different design. Their contribution to the ISR emittance growth is small due to the low beam energy. On the other hand, they must have variable longitudinal dispersion for the beam compression in the short pulse mode. TBA cells are considered for these arcs.

Spreaders/Recombiners

The layout of the spreader at the entrance to linac 1 (which is identical to the recombiner at the exit of linac 1) is presented in the Fig. 7. The second pair of spreaders and recombiners is similar, but without the 6 GeV beam line, which goes to the long undulator section.

All spreader lines are isochronous.

One of the limiting factor for the spreader design is the contribution to the radiation integral I_5, which characterizes the transversal emittance growth due to incoherent synchrotron radiation (see e.g. [8]).

$$I_5 = \int \frac{\left(\gamma\eta^2 + 2\alpha\eta\eta' + \beta\eta'^2\right)}{|\rho|^3} ds$$

$$\Delta\varepsilon = \frac{2}{3} r_e C_q \gamma^5 I_5$$

Relatively high value of the horizontal β-function from the linac section limits the bending angle of the separating dipoles (which depicts η'). Quadrupoles are necessary to minimize the contributions of other dipoles to I_5, which in combination with isochronous and reasonable β-functions conditions demands large numbers of them. Also a compact design is of advantage for the installation footprint.

The difficulties (which grow with the number of the beam energies to be separated) originate from the conditions on the β-functions (low I_5 contradicts with „natural“ β-functions of linacs), and dispersion (low I_5 contradicts with the beam lines separation). A Lambertson septum-like separation magnet for 4, 5, and 6 GeV beam lines (green in the Fig. 7) helps to significantly reduce the distances necessary for the beam separation. The optic of the spreader is coupled in this case, which complicates the analysis and ongoing optimization.

Linacs

The focusing optic in linacs can be added quite naturally between cryomodules. The options include triplets, dublets, single quadrupoles, or no additional elements at all. It was argued [9], that the additional focusing does not change maximal β-functions in the linacs significantly. For a multi-turn ERL, however, we consider the transversal beam break-up (TBBU) to be a serious problem and hold the optic optimization in the linac for important. The option with triplets of quadrupoles between cryomodules seems most promising in our case, although the effect is of the order of 2-3 times larger in the TBBU threshold current.

β-functions in linacs are shown in Fig. 8. For the details of TBBU modeling and comparison of different injection schemes in this respect see [10].

Start-to-end Beam Dynamics Simulation

Comprehensive results of the FSF start-to-end beam dynamics modeling are presented in [11], here is a summary.

ASTRA simulations are used to track the space charge dominated beam from the photo-injector, through the Booster and Merger to the entrance of the 230 MeV pre-injector linac. Subtle beam transformation through the injection stage is used to produce a low emittance beam in all six dimensions. From here onwards, Elegant was used to optimize and track the beam during acceleration to 6 GeV and the deceleration recovery to the dump transfer line.

For the LEM the transverse emittance growth is kept to a minimum throughout the whole 7 km machine Fig. 6 to maximize user potential.

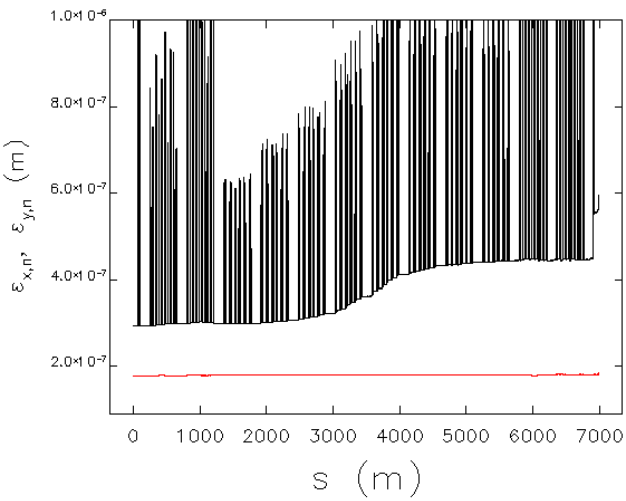

Figure 6: Normalized emittance plot for LEM.

The emittance growth is mainly due to incoherent radiation effects and can be estimated for the final energy arc as $\Delta(\gamma\varepsilon) = 4\cdot10^{-8}E^6I_5 \sim 0.04$ mm mrad.

Multipoles were implemented in the low energy arcs to recover the longitudinal emittance of the injector during bunch compression. Either side of off-crest acceleration in both linacs (ϕ_1=10°, ϕ_2=-20°,) combined with longitudinal dispersive optic (R_{56}=20 cm, R_{56}=5 cm) telescopic optic produces a 10 fs short bunch at the 6 GeV long undulator section. Fig. 9 shows the recovery of the normalized emittance (black) and the bunch length (red) throughout the machine. The slow emittance growth and the bunch (de)compression asymmetry are due to radiation effects.

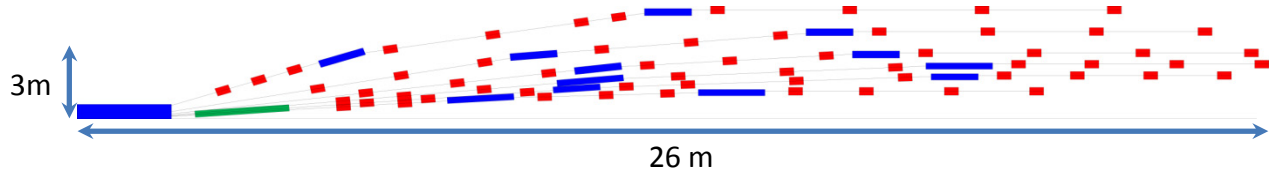

Figure 7: Layout of the spreader section behind the linac1.

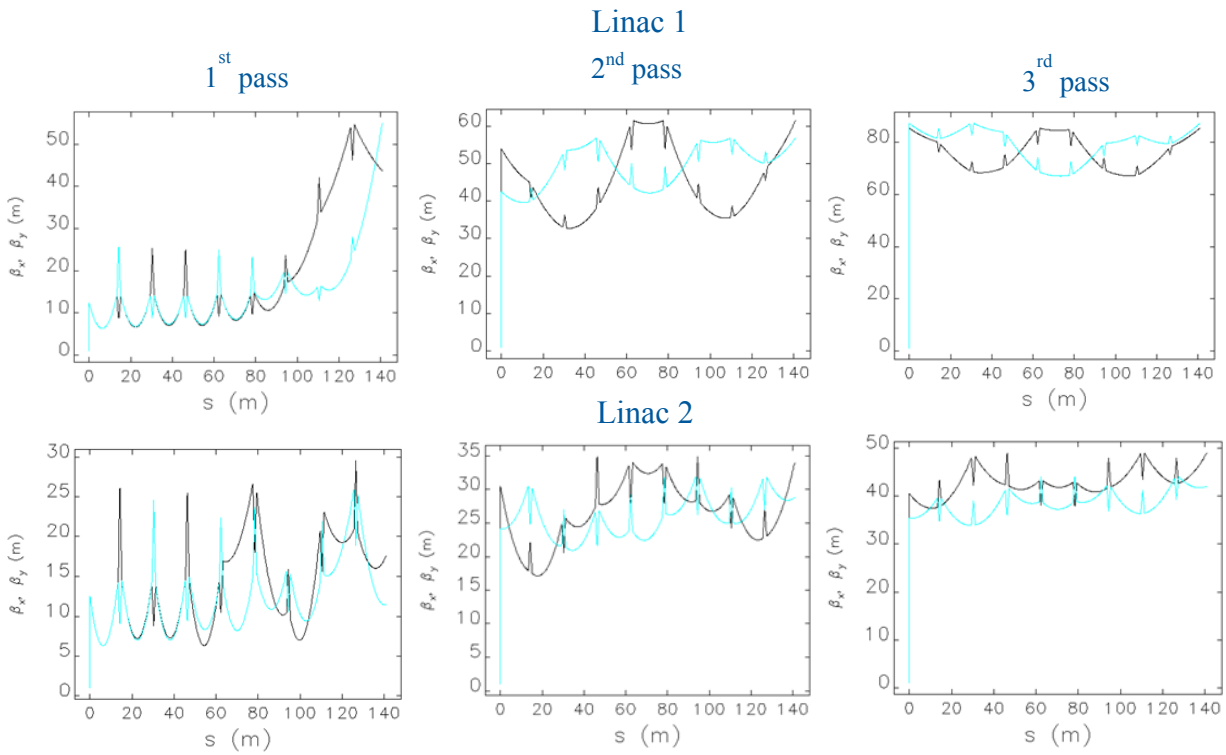

Figure 8: β-functions in linacs. Final energies in the first linac are 1, 3, and 5 GeV; in the second – 2, 4, and 6 GeV. Triplet-based optic common for all beams in each linac is optimized for minimal β-functions.

Simulation results of the recovered beam at the entry to the beam dump transfer line are given in Table 3. Although the energy spread of the beam in both modes at the entrance to the dump line is approximately 5%, the beam could be safely transported to the dump using a low dispersive optic.

CONCLUSION

An overview of the design of a multi-turn ERL (FSF – Femto-Science Factory) is given in this paper. Due to the availability of many (6) beam energies in the facility, a broad spectral region of synchrotron radiation (50 eV to 50 keV) is covered with ultimate photon beam brilliance reaching diffraction limit.

The facility will provide the possibility to generate very short (down to 10 fs) photon pulses with high peak brilliance and high pulse repetition rate (1.3 GHz).

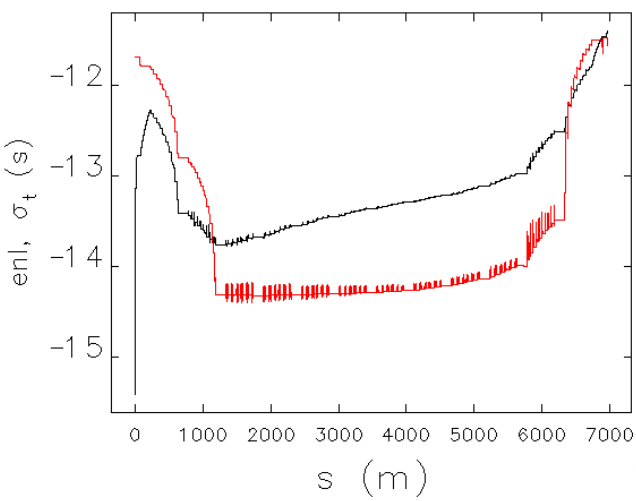

Figure 9: Log plot of the longitudinal bunch properties.

Table 3: Simulation Results at the Beam Dump Entrance

Type	ε_{nx} (mm mrad)	ε_{ny} (mm mrad)	St (ps)	DE/E (%)	Charge (pC)
SPM	0.48	0.20	2.24	3.76	1
LEM	0.36	0.18	4.02	7.60	15

REFERENCES

[1] D.A. Kayran, et. al., "MARS –A Project of the Diffraction Limited Fourth Generation X-ray Source", Proc. of 1998 Asian Particle Accelerator Conference.

[2] B. Dunham, et al., "Performance of the Cornell High-Brightness, High-Power Electron Injector", IPAC 2012, New Orleans, Louisiana (May 2012)

[3] S. Benson et al, High power lasing in the IR upgrade at Jefferson Lab, Proc. 2004 FEL Conf., 229-232.

[4] N.A. Vinokurov et al., Status and prospects of the Novosibirsk FEL facility, Proc. RuPAC'10, pp.133-135.

[5] X-ray data booklet, available online at http://xdb.lbl.gov/, section 2_1.

[6] I.V.Bazarov, PRST AB 15, 050703 (2012).

[7] J.Wu, at al., "Coherent Synchrotron Radiation Analysis for the Photoinjected ERL and UVFEL Projects at NSLS", Proc. of 2001 Pacticle Accelerator Conf., pp.2866-2868.

[8] M. Sands, "The physics of electron storage rings. An introduction", Proc. of the International School of Physics "Enrico Fermi", ed. B. Touschek, (Academic Press, 1971).

[9] V.Litvinenko, private communication.

[10] Y.Petenev, T. Atkinson, A.V. Bondarenko A.N. Matveenko, Analysis of Injection and Recovery Schemes for a Multi-turn ERL based Light Source, Proc. of 53th ICFA Advanced Beam Dynamics Workshop on Energy Recovery Linacs, Novosibirsk, 2013.

[11] T. Atkinson, A.V. Bondarenko, A.N. Matveenko, Y.Petenev, Start-to-end beam dynamics simulations for Femto-Science-Factory feasibility study, Proc. of 53th ICFA Advanced Beam Dynamics Workshop on Energy Recovery Linacs, Novosibirsk, 2013.

OVERVIEW OF THE LHEC DESIGN STUDY AT CERN

O. Brüning, CERN, Geneva, Switzerland

Abstract

The Large Hadron electron Collider (LHeC) offers the unique possibility of exploring lepton-proton collisions in the TeV Center of Mass (CM) range by further utilizing the existing LHC infrastructure. This paper summarizes the Linac-Ring option for the LHeC project and outlines the next developments for the study.

INTRODUCTION

Lepton-proton collisions in the TeV CM energy range provide a unique tool for studying new phenomena in the partonic structure of protons and nuclei, for precision Higgs physics and the search for physics beyond the Standard Model of particle physics [1,2]. The LHeC may become the first electron-ion collider ever built. The LHeC is designed to use one of the hadron beams of the LHC in a synchronous operation mode in parallel with the HL-LHC exploitation. It therefore represents an important opportunity for a further exploitation of the existing LHC infrastructure and its massive infrastructure investment already taken and to come. Achieving ep CM collision energies in the TeV range with a 7 TeV energy proton beam demands lepton beam energies above about 50 GeV. The LHeC Conceptual Design Report (CDR) [1] is based on a lepton beam energy of 60 GeV. But it also addresses the option of a much higher lepton energy (140 GeV) for exploring the high energy CM regime. The CDR was developed under the auspices of CERN, ECFA and NuPECC who sponsored around four dedicated LHeC workshops between 2008 and 2012.

The CDR explored two distinctly different design approaches for the LHeC collider: one design for a Ring-Ring option and one for a Linac-Ring option with Energy Recovery operation. Beam transfer aspects for both options are given in [3]. The last LHeC workshop in 2012 focused on the presentation of the CDR and concluded with a CERN mandate to develop the required technical R&D work over the next 4 years (2013 to 2016), focusing on the technologies required for the ERL option of the LHeC project, so that a decision on the project could be taken when the LHC starts its second run period at full energy.

LINAC-RING OPTION

The Linac-Ring [L-R] option requires a new linear accelerator for the electron beam that intersects in one location with the existing LHC machine. Several options have been considered for the linear accelerator (pulsed, re-circulating and Energy Recovery Linac configurations). These provide a range of energy and luminosity combinations. The baseline option for the LHeC CDR is a recirculating 60 GeV Energy Recovery Linac (ERL) which allows for high luminosity operation. A pulsed linac option provides still an interesting option for maximizing the energy reach of the LHeC (at the cost of a reduced peak luminosity performance) as could be demanded by findings at the LHC. Table 1 summarizes key parameters for both options. The 60 GeV ERL version is capable of reaching a luminosity as high as the Ring-Ring option (O(10^{33} $cm^{-2}s^{-1}$)). First considerations have been made as to further increase the luminosity reach of the LHeC Linac-Ring (L-R) option and to possibly reach a luminosity level of 10^{34} $cm^{-2}s^{-1}$, which would enhance the potential of the LHeC for precision Higgs measurements [2].

The 60 GeV ERL version features two 1km long superconducting RF sections and two return arcs that house magnets for three passages at different energies. Each linac section provides an energy gain of 10 GeV and the machine requires in total three recirculations through the two SC linacs to reach an energy of 60 GeV. The minimum acceptable bending radius of the return arcs is determined by the maximum acceptable energy loss through synchrotron radiation and the requirement of having a total circumference that is an integer fraction of the LHC circumference. For the 60 GeV ERL option these considerations lead to a radius of curvature of 1km for the two return arcs and a total machine circumference of ca. 9km (1/3 of the LHC circumference). Figure 1 shows a schematic layout of the 60 GeV ERL option and Figure 2 shows a schematic view of the resulting underground installation. The overall LHeC complex would have approximately the same size as the existing SPS machine.

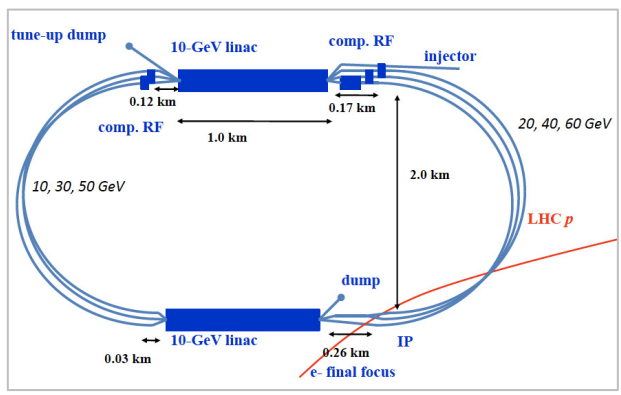

Figure 1: Schematic layout of the 60 GeV ERL option.

The L-R option has the advantage over the R-R option that all civil engineering and installation work can be done parallel to the LHC operation and thus independently of the LHC shutdown schedule. Furthermore, it is notable, as was recently pointed out [5],

that essentially the same machine in a 4-pass regime and going to 80 GeV has an interesting application as a cost effective photon-photon collider for the study of the newly observed boson at 125 GeV. Table 1 shows the baseline parameters for the 60 GeV ERL and 140 GeV pulsed linac options of the CDR. A pushed parameter set with luminosities well around L = 10^{34}cm^{-2}s^{-1} is given in [5].

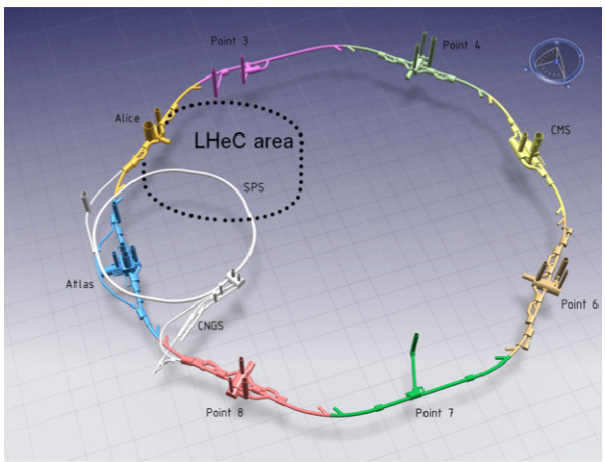

Figure 2: Civil engineering layout of the 60 GeV ERL option [4].

Table 1: LHeC baseline linac parameters for the 60 GeV ERL and 140 GeV pulsed option.

LINAC Parameters for the Linac-Ring Option		
Operation mode	**CW**	**Pulsed**
Beam Energy [GeV]	60	140
Peak Luminosity [cm^{-2}s^{-1}]	10^{33}	4 10^{31}
Cavity gradient [MV/m]	20	32
RF Power Loss [W/cavity]	13-37	11
W per W (1.8K to RT)	700	700
Cavity Q_0	2.5 10^{10}	2.5 10^{10}
Power loss/GeV	0.51-1.44	0.24
RF length [km]	2	7.9
Total length [km]	9	7.9
Beam current [mA]	6.4	0.27
Repetition rate	-	10 Hz
Pulse length	-	5ms

MAGNET DESIGN

A first magnet prototype development had been launched in collaboration with the Budker institute BINP in Russia and then further developed at CERN. Figure 3 shows first conceptual normal conducting magnet prototypes from BINP and Figure 4 a CERN prototype demonstrating that the required field quality and reproducibility (better than 10^{-4} relative field error and low magnetic field) can indeed be achieved.

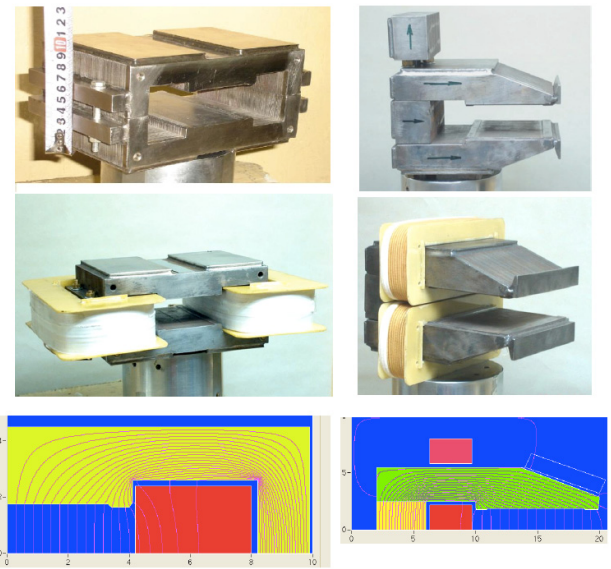

Figure 3: BINP prototype for a normal conducting LHeC dipole magnet.

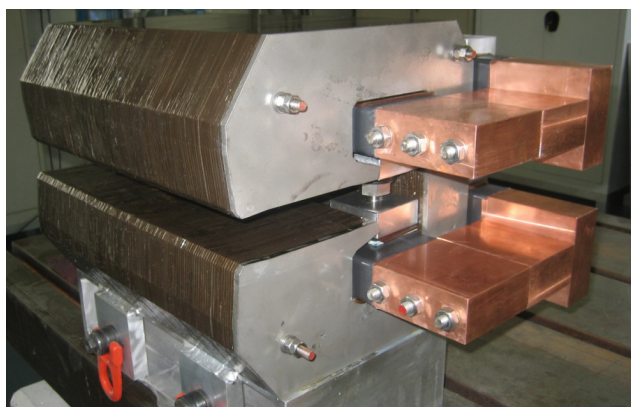

Figure 4: CERN prototype for a normal conducting LHeC dipole magnet.

Figure 5 shows a conceptual further development of the normal conducting dipole magnets for the ERL facility housing the coil windings of the three passages through the ERL return arcs within one common iron yoke. Figure 5 shows simulations for the mechanical stress within the 3-in-1 magnet cross-section.

IR DESIGN

The interaction region for the LHeC, running synchronously with the LHC, has the novel feature of accommodating three beams: the colliding proton and lepton beams and the non-colliding second proton beam of the LHC. Figure 6 shows a schematic view of the interaction region layout for the R-R option of the LHeC. The low-beta electron beam quadrupoles are placed close to the detector. They are followed by additional dipole separation magnets for the electron beam and then by low-beta quadrupole magnets for the proton beam.

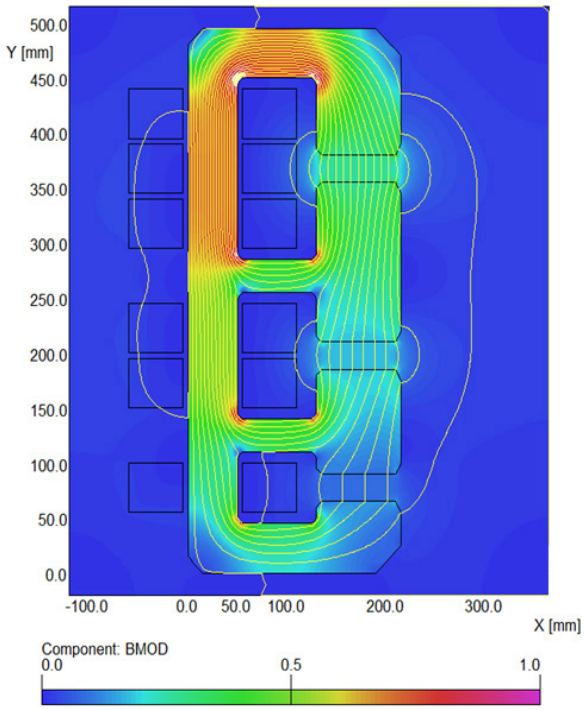

Figure 5: Conceptual design for a normal conducting 3-in-1 LHeC dipole magnet for the ERL return arcs showing simulations for the mechanical stress within the magnet cross section.

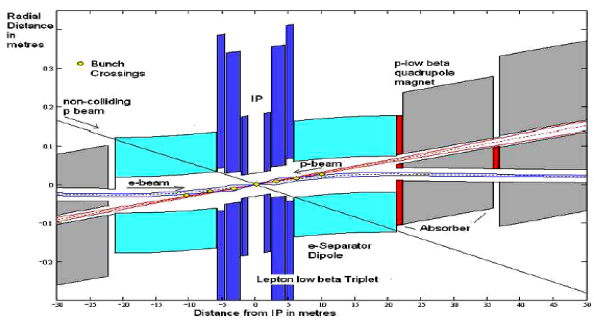

Figure 6: Schematic layout of the Interaction Region [example of the Ring-Ring option].

Figure 7 shows the conceptual design of a superconducting mirror quadrupole magnet featuring three beam apertures: two high field apertures for the two proton beams and one low field aperture for the lepton beam. Figure 8 shows the schematic IR layout together with the synchrotron radiation fan from the electron beam. The synchrotron radiation power reaches peak values of up to 30kW on the absorber blocks inside the LHeC detector. The total synchrotron radiation power inside the experimental area can be further optimized by a variation of the focusing element locations for the lepton beam (L^*) [13]. Figure 9 shows the expected total synchrotron radiation power as a function o the location of the first focusing element for the lepton beam next to the experiment (L^*).

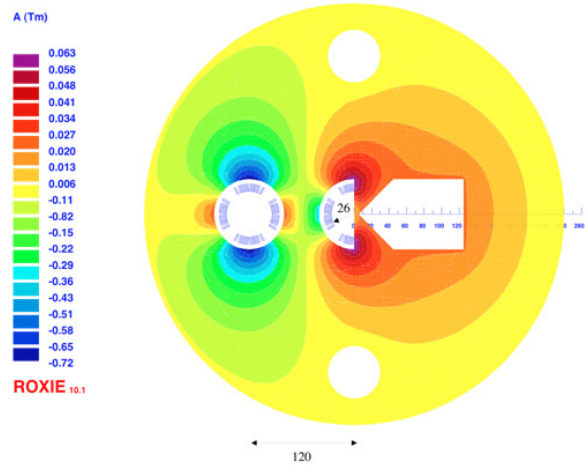

Figure 7: Conceptual design of a superconducting mirror quadrupole magnet with two high field apertures and one low field aperture for the lepton beam.

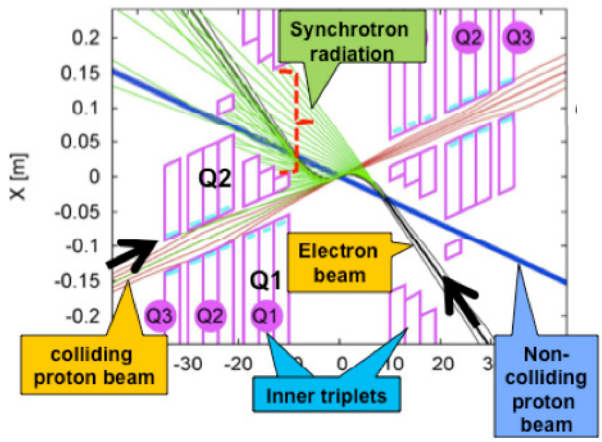

Figure 8: Schematic layout of the Interaction Region of the Linac-Ring option with the Synchrotron radiation fan.

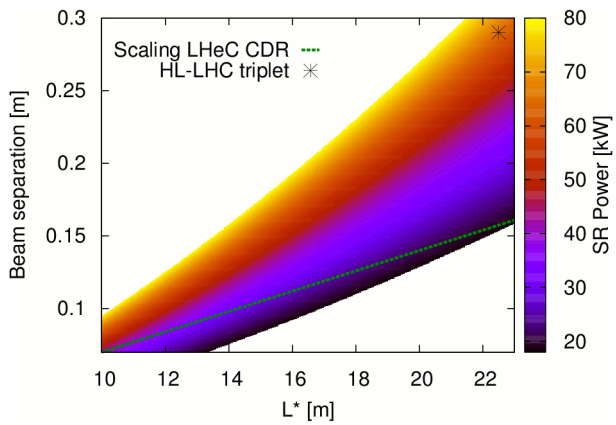

Figure 9: Expected total synchrotron radiation power as a function o the location of the first focusing element for the lepton beam next to the experiment (L^*).

BEAM DYNAMICS STUDIES

First beam dynamics studies focused on an evaluation of ion trapping in the electron beam of the ERL and the transverse beam stability with Wakefields and beam-beam encounters [14]. Figure 10 shows the simulation of the damping of transverse oscillations in the presence of cavity Wakefields and a linearized transverse kick from the beam-beam force at the collision point. The simulations are done for a bunch population of 3 10^9 ppb and two RF systems: one based on 720MHz cavities and one based on 1.3GHz cavities. One can clearly observe that the damping of the transverse oscillations is faster for the lower frequency RF system and that the oscillations are at the stability threshold for the 1.3 GHz system.

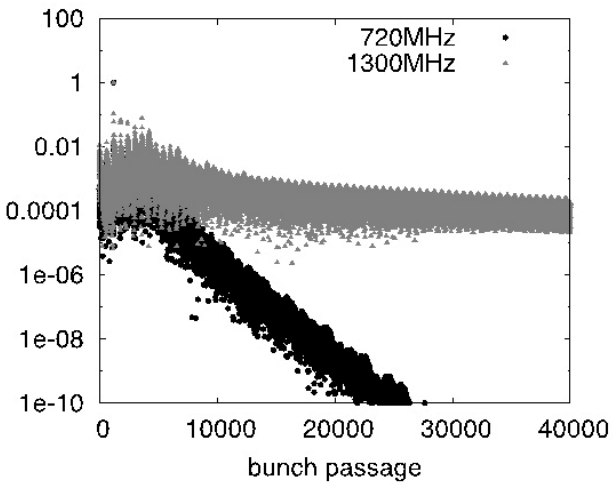

Figure 10: Simulation studies for the damping of transverse beam oscillations in the presence of cavity Wakefields and a linearized beam-beam force at the interaction point.

Further studies on RF power considerations from F. Marhauser showed that the optimum frequency choice for Nb cavities lies somewhere between 700MHz and 1GHz for small grain Nb cavities and 300MHz and 800Mhz for large grain Nb [7][8]. Observing further that the currently existing RF systems on the market (1.3 GHz for the ILC project and 704.42MHz for the SPL and ESS proton driver projects) are not really fitting the requirements for the LHeC (RF frequency is not an integer multiple of the LHC bunch spacing of 40.079MHz) led to the decision of adopting an entirely different RF frequency for the LHeC project. The choice of an RF frequency of 801.58MHz satisfies the harmonic criterion with the LHC bunch spacing (harmonic number of 20 wrt the LHC bunch spacing), satisfies the preference for lower RF frequencies from the stability point of view, lies in the overlap region of the optimum frequency intervals for small and large grain Nb cavities and provides a synergy with the HL-LHC upgrade project as the superconducting 801.58MHz cavities could also be used as a higher harmonic RF system for the HL-LHC.

Another focus of the beam dynamic studies is the evaluation of the electron beam disruption after the Interaction Point and the total beam-beam tune spread coming from the collisions with the disrupted electron beam. These studies are still in their early phases, but Figure 11 shows first simulation results [Ref Daniel 2] of the electron beam disruption indicating that careful attention has to be given to the matching of the spend beam into the return circulations of the ERL.

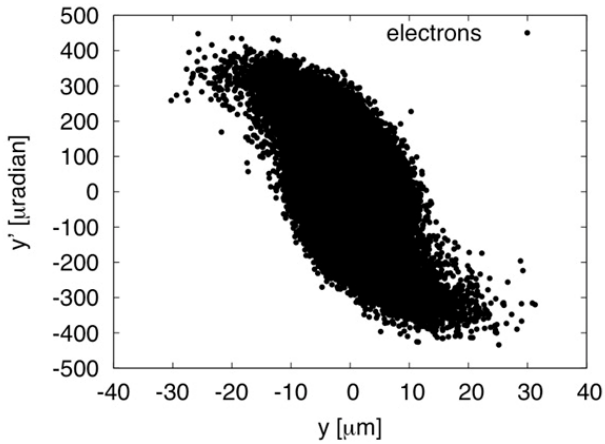

Figure 11: Simulation studies for the damping of transverse beam oscillations in the presence of cavity Wakefields and a linearized beam-beam force at the interaction point.

LHEC PLANNING AND TIMELINE

Figure 12 shows the tentative schedule for the LHeC project with the goal of a simultaneous operation start with the HL-LHC upgrade in mid 2020ies following the third long shutdown of the LHC complex.

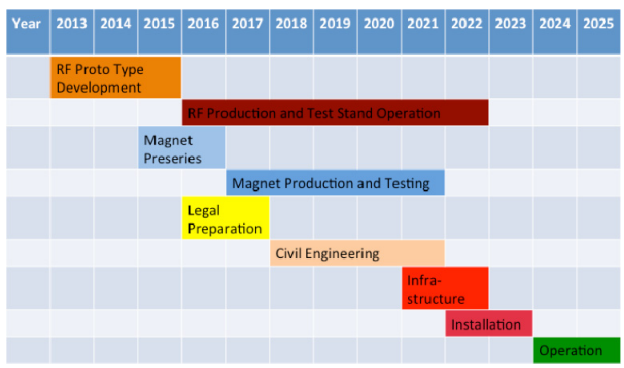

Figure 12: Tentative schedule for the LHeC project.

POST CDR STUDIES

Following the LHeC workshop in 2012 [6] it was decided to adopt the L-R option as baseline and to keep the R-R option as a backup for the LHeC project. The CERN management has given a mandate [6] to pursue the required R&D activities and studies for key components of the L-R LHeC option, e.g. SC RF, and to launch beam dynamics and design studies in the framework of international collaborations.

The first post CDR activities have been focused on:

- Choice of the LHeC RF frequency: a dedicated collaboration workshop identified in 2013 [7] 801.58MHz as the optimum choice for the LHeC based on RF power considerations [8] and offering synergies with the HL-LHC project [9].
- Beam dynamic studies in the ERL for different bunch filling patterns and including wake-fields and beam-beam interactions [10].
- Design studies for a dedicated LHeC test facility at CERN with ERL operation mode [11][12].
- Re-Optimization of the LHeC IR and it's integration into the HL-LHC lattice [13].
- Detailed civil engineering studies for the LHeC installation [4].
- Re-Optimization of the LHeC beam parameters based on the operations experience of the first LHC running period. The LHC operation in 2012 demonstrated the feasibility of beam brightness beyond 'ultimate' LHC parameters that open the door for a performance reach of up to L = 10^{34} $cm^{-2}s^{-1}$ [5].

The primary next goals of the LHeC study are the development of prototypes of the 801.58 MHz cavities together with their cryostats and the design of an LHeC Energy Recovery Linac Test Facility [LHeC-TF] at CERN. The development of the cavities provides a strong synergy with the HL-LHC upgrade program at CERN where these cavities could function as Higher Harmonic RF cavities for bunch lengthening and reduction of the IBS and geometric luminosity reduction factor. Figure 13 shows a schematic layout for an LHeC-TF at CERN as presented in [11][12].

SUMMARY

The LHeC offers the unique possibility for deep inelastic scattering physics in the TeV CM region and Higgs studies. Key technical R&D studies have been launched in 2013, in time for a project realization by 2025 and exploitation in parallel with the HL-LHC operation.

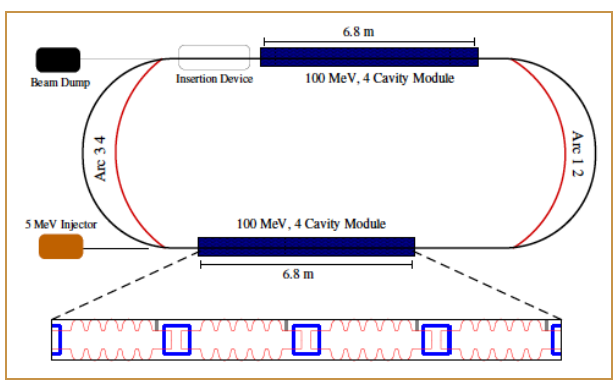

Figure 13: Schematic layout of an ERLTF at CERN [11].

REFERENCES

[1] LHeC Study Group, 'A Large Hadron Electron Collider at CERN', J.Phys.G: Nucl.Part.Phys 39(2012)075001 [arXiv:1206.2913(2012)].
[2] LHeC Study Group, 'On the Relation of the LHeC and LHC', [arXiv:1211.5102(2012)].
[3] C. Bracco and B. Goddard; 'Studies for the LHeC Beam Transfer System'; Conference Proceedings IPAC13.
[4] J. Osborne et al.; 'Civil Engineering Studies for Future Ring Colliders at CERN'; Conference Proceedings IPAC13.
[5] F. Zimmermann et al.; 'The LHeC as a Higgs Boson Factory'; Conference Proceedings IPAC13.
[6] 2012 LHeC Workshop, Chavannes de Bogies, Switzerland;
[7] https://eventbooking.stfc.ac.uk/news-events/lhec-meeting
[8] Frank Marhauser private communication.
[9] L. Rossi, O. Brüning; 'High Luminosity Large Hadron Collider A description for the European Strategy Preparatory Group'; CERN-ATS-2012-236
[10] D. Schulte, Conference proceedings, DIS2012; March 2012; University Bonn.
[11] R. Calaga et al.; 'A Proposal for an ERL Test Facility at CERN'; Conference Proceedings IPAC13.
[12] A. Valloni et al.; 'Strawman Optics Design for the LHeC ERL Test Facility'; Conference Proceedings IPAC13.
[13] M. Korostelev et al.; 'LHeC IR optics design with integration into the HL-LHC lattice', Conference Proceedings IPAC13.
[14] Daniel Schulte, EPS HEP conference 2013, Stockholm, Sweden; proceedings.

BEAM DYNAMICS STUDIES ON THE INJECTOR OF THE IHEP ERL TEST FACILITY*

Y. Jiao#, O.Z. Xiao, J.Q. Wang, S.H. Wang, IHEP, Beijing 100049, China

Abstract

In this paper we present the beam dynamics studies with the Impact-T program on the injector of the ERL test facility in the Institute of High Energy Physics, Beijing. Variable parameters, including driven-laser beam size, solenoid strengths and positions, RF cavity strengths, positions and phases, are varied to optimize the beam quality at the end of the injector.

INTRODUCTION

The energy recovery linac (ERL) and free electron laser (FEL) are considered to be candidates of the fourth generation light sources, and have received much attention worldwide. Since both of them are based on linac technologies, it is possible to combine FEL into an ERL facility, resulting in a compact two-purpose light source. A test facility, named energy recovery linac test facility (ERL-TF), was proposed at the Institute of High Energy Physics (IHEP), Beijing, to verify this principle [1]. Physical design of the ERL-TF started a few years ago and is well in progress [2-4]. It is worth mentioning that we thoroughly studied the beam breakup effect in such a two-purpose machine. It is found that two effects emerge as a result of the introduction of FEL beams: a reduction in the threshold current and a central orbit fluctuation for ERL current under threshold. Due to the fact that the repetition rate of FEL bunches is much smaller than that of ERL, the introduction of FEL beam does not have a fatal effect on the threshold current. As for the orbit fluctuation, we gave a simple model and found a resonance relation between the voltage spread and the ratio of HOM frequency to the FEL repetition rate. By choosing an appropriate FEL frequency, the amplitude of the orbit fluctuation can be kept small [4].

The layout of the facility is presented in Fig. 1. The nominal energy of the electron beam in the radiator is 35 MeV and beam current is 10 mA. Among the components of the facility, one extremely important device dominating the machine performance is the photo-injector. The injector, including a 500-kV photocathode direct-current (DC) gun equipped with a GaAs cathode, a 1.3 GHz normal conducting RF buncher, two solenoids, and two 2-cell superconducting RF cavities, was designed for the ERL-TF [2], with the layout shown in Fig. 2 and main parameters listed in Table 1. Preliminary optimization of the beam dynamics has been performed, and finally an electron beam with normalized emittance $\varepsilon_{n,x(y)}$ of 1.49 mm.mrad was obtained. In this paper, we optimize the beam dynamics of the injector in both the low-charge operation mode (bunch charge 7.7 pC, rep. rate 1.3 GHz) and the high-charge operation mode (bunch charge 77 pC, rep. rate 130 MHz) using the Impact-T program [5], a fully 3D program to track relativistic particles taking into account space charge force and short-range longitudinal and transverse wake-fields. Study shows that it is feasible to achieve a better beam quality at the end of the injector.

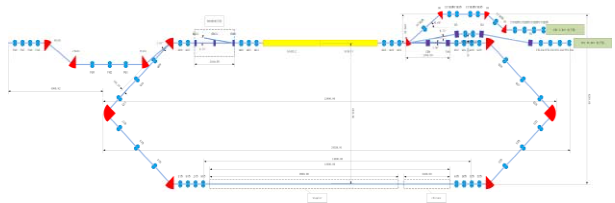

Figure 1: Layout of the ERL test facility.

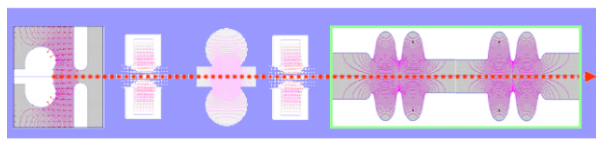

Figure 2: Layout of the ERL-TF injector.

Table 1: IHEP ERL-TF Injector Main Parameters

Parameter	Value	Unit
DC-gun voltage	300-500	kV
Laser power and wavelength	2.3/532	W/nm
Laser rep. rate	130 (or 1300)	MHz
Laser rms trans. size	0.3~1.2	Mm
Laser length	20	Ps
E- ave. kinetic energy	0.2	eV

OPTIMIZATION FOR THE LOW-CHARGE OPERATION MODE

For the low-charge operation mode, a parameter iterative scan program is developed with Matlab which starts several runs of tracking simultaneously. This code can finish the multi-variable scans, which usually contains a few hundred of runs, within an acceptable period of time (e.g. in 2 hours) on a desktop computer.

As the start of the simulation, initial beam distribution is generated according to initial laser parameters listed in Table 1. The normalized emittance $\varepsilon_{n,x(y)}$ is given by

$$\varepsilon_{n,x(y)} = \sigma_{x(y)} \sqrt{\frac{k_B T_\perp}{m_e c^2}}, \quad (1)$$

*Work supported by the special fund for the R&D of ERL in IHEP

#jiaoyi@ihep.ac.cn

where $\sigma_{x(y)}$ is the horizontal (vertical) rms beam size on the cathode, $m_e c^2$ is the electron rest energy, and $k_B T_\perp$ is the transverse beam thermal energy, which is found depending mainly on the incident laser wavelength [6],

$$k_B T_\perp (meV) = 309.2 - 0.3617\lambda(nm). \qquad (2)$$

For the incident 532 nm laser, $k_B T_\perp$ = 116.8 meV and $\varepsilon_{n,x(y)}$ = 0.57 mm.mrad.

With the generated initial beam distribution, twelve variables are iteratively scanned to search the optimal parameter setting that results in the lowest $\varepsilon_{n,x(y)}$, small energy spread σ_δ, bunch length σ_z of 2 ~ 4 ps, and kinetic energy E_k of 5 MeV. The optimization starts with the scan of the buncher parameters to realize a σ_z of 2 ~ 4 ps, then incudes the solenoid parameters in the scan to minimize the $\varepsilon_{n,x(y)}$ and the RF cavity parameters to optimize the E_k as well as the σ_δ and σ_z, and finally ends with a global scan of all variables. Finally, with a laser rms transverse size of 0.5 mm is made, an electron beam with E_k of 5 MeV, $\varepsilon_{n,x(y)}$ of 0.40 mm.mrad, σ_z of 0.74 mm and σ_δ of 0.33% is achieved at the end of the injector.

Recently significant progress was made in Cornell University on high-current operation from a photo-injector with a DC-gun [7]. One important technological improvement is to choose the active area off the cathode center, which helps avoiding the damage due to ion back-bombardment and hence providing good operational lifetime. To investigate the impact of the initial offset on the final beam quality, numbers of simulations with different initial offsets are performed. Since the beam distribution is no longer azimuthal symmetry with a nonzero offset, 3D space charge effects are turned on right at the beginning of the tracking. The result is shown in Fig. 3. It shows that a 5-mm offset from the cathode center does not lead to neither large difference between horizontal and vertical emittance nor large beam quality degradation. The emittance increases by about or more than 50%, but is still below 1 mm.mrad.

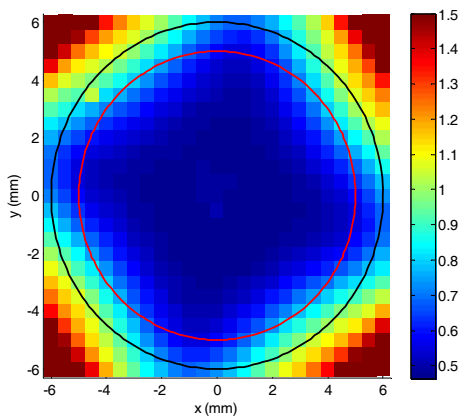

Figure 3: Simulation data of $(\varepsilon_{n,x}^2/2 + \varepsilon_{n,y}^2/2)^{1/2}$ with different initial offset at cathode. The red and black circles represent initial offset of 5 mm and 6 mm from the center, respectively.

To ensure the feasibility of the optimized beam quality in a realistic condition, error tolerance study is necessary and tolerable magnitude of the errors should be determined. For the ERL-TF, both the alignment and rotation errors of each element are considered in the analysis. We first set the amplitude of the alignment error the same as that of the rotation error. In the analysis 1000 random settings of the errors (truncated at 3σ) are added to each element, then tracking with 3D space charge forces is performed, and finally the beam parameters at the end of the injector are recorded. It is found that only the normalized emittance has evident increase due to errors. Therefore statistical analysis is performed only on emittance data. The variation of the average and the maximum emittance growth rates with error amplitude is shown in Fig. 4. Consequently the contributions of different element and different error to emittance growth are analysed. Study shows that only the alignment error of the solenoids (especially the first solenoid) is the main source of the emittance growth. To remain the emttance growth rate below 10%, the element alignment error of the solenoids must be smaller than 0.15 mm, while the other errors should be smaller than 0.3 mm or 0.3 mrad. .

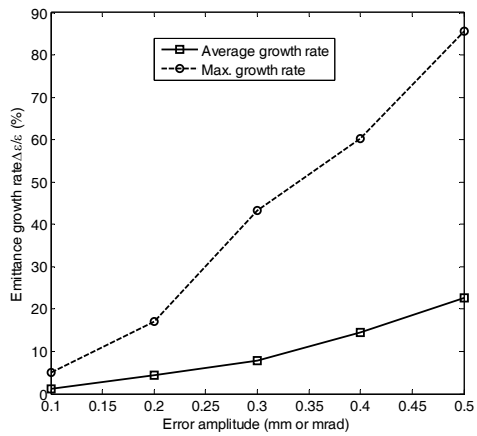

Figure 4: Variation of the emittance growth rate with the alignment and rotation error amplitude.

OPTIMIZATION FOR THE HIGH-CHARGE OPERATION MODE

For the high-charge operation mode, associated with the stronger space charge force compared to that in the low-charge operation mode, unfortunately the iterative scan loses it efficiency in achieving a promising beam qualify at the end of the injector. It is necessary to explore the available minimum emittance with more advanced method, for instance, the multi-objective genetic algorithm (MOGA). This method recently has been widely used in the accelerator designs to optimize the beam optics or the machine performance [e.g., 8]. Here we apply a genetic algorithm, NSGA-II [9] in the optimization.

Three objectives, such as the final emittance, bunch length (the closer to 3 ps, the better), and the beam kinetic

energy (the closer to 5 MeV, the better), are used in the optimization. The genetic optimization is rather time consuming. In our case it needs about one month to calculate 100 generations, with 350 random seeds in each generation. Figure 5 shows the pareto front of the objectives after 100th generation in the case that the initial laser beam rms transverse size of 0.5 mm. As expected, the available emittance decreases as the bunch length increases. If only considering the results with final bunch length below 4 ps, i.e., 1.2 mm, the available minimum emittance is about 2.7 mm.mrad.

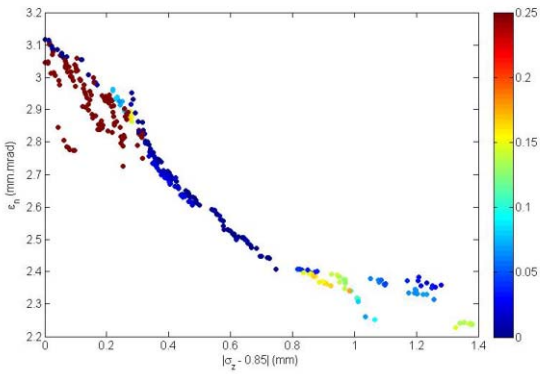

Figure 5: Pareto front of the objectives after 100th generation in the case that the initial laser rms transverse size of 0.5 mm. The colour indicates the difference of beam kinetic energy from 5 MeV.

Similarly, we perform the genetic optimizations for the cases with different initial laser beam rms size (up to 200 generations for each case), and record the result predicting the smallest emittance among those with final bunch length of 2 to 4 ps and kinetic energy of 5MeV. The variation of the minimum emittance with the initial laser beam rms size is presented in Fig. 6. It appears that a relatively large laser beam rms size (1 ~ 1.2 mm) is preferred for achieving a small-emittance electron beam in the high-charge operation mode. Too small or too large an initial laser beam size will lead to a large final emittance, because of the strong space charge effect or the large initial thermal emittance.

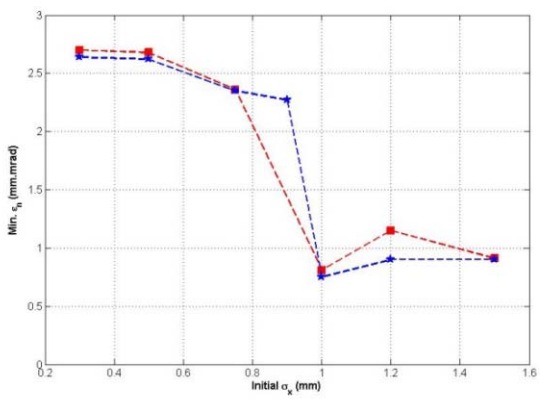

Figure 6: The available minimum emittances (σ_z – 2~4 ps, E_k ~ 5 MeV) with different initial laser beam rms size.

In addition, to demonstrate the efficiency of the iterative scan in the optimization for the low-charge operation mode, genetic optimization is also performed for the low-charge operation mode with initial laser beam rms size of 0.5 mm. The optimal results as well as the result obtained by the iterative scan (signified with a star) are shown in Fig. 7. It shows that the emittance obtained by the iterative scan is very close to the global minimum.

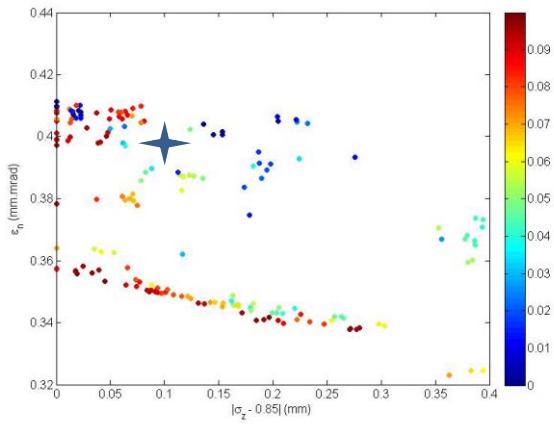

Figure 7: The available minimum emittances (σ_z – 2~4 ps, E_k ~ 5 MeV) with different initial laser beam size.

CONCLUSION

We show the beam dynamics optimization of the ERL-TF injector in both the low-charge and the high-charge operation mode at IHEP with iterative scans and multi-objective genetic algorithm based on simulations with the Impact-T program. The dependency analysis and the error tolerance study are also performed. It appears feasible to achieve a good beam quality at the end of the injector.

ACKNOWLEDGMENT

We thank the colleagues of the ERL-TF work group at IHEP for helpful discussions. Thanks also go to S.G. Liu for sharing the field data of the injector elements.

REFERENCES

[1] S.Y. Chen, S.H. Wang, X.W. Zhu, Chinese Physics C, 2010, 34: 112-114.
[2] S.G. Liu, J.Q. Xu, Chinese Physics C, 2011, 25(1): 88-91.
[3] S.H. Wang, et al. Chinese Physics C, 2012, 36(5): 469-474.
[4] X.H. Cui, Y. Jiao, J.Q. Wang, S.H. Wang, Chinese Physics C, 2013, 37(7): 077005.
[5] J. Qiang, et al., Phys. Rev. ST Accel. Beams **9**, 044204, 2006.
[6] I.V. Bazarov, et al., J. Appl. Phys. **103**: 054901, 2008.
[7] B. Dunham, et al., Appl. Phys. Lett. **102**: 034105, 2013.
[8] I. V. Bazarov, *et al.*, Phys. Rev. ST Accel. Beams **8**, 034202, 2005.
[9] K. Deb, IEEE Transactions on Evolutionary Computation **6** (2), 2002, p. 182-197.

PROGRESS ON THE CONSTRUCTION OF IHEP 500KV PHOTOCATHODE DC GUN SYSTEM

X.P. Li# , J.Q. Wang, S.Y. Chen, Y.L .Chi, S.H. Wang, G.W. Wang, J.S. Cao, J.Q. Xu, O.Z. Xiao, K. Lv，D.R. Sun, Z.S. Zhou, X.H. Peng, T. Zhang, J.R. Zhang
Institute of High Energy Physics, CAS, Beijing 100049, China

Abstract

As one of the most important key technologies for future advanced light source based on the Energy Recovery Linac (ERL), a 500kV photocathode DC gun was supported by IHEP in September of 2011. Up to now, the schematic design of all DC gun subsystems including drive laser, photocathode preparation system, electron gun body and ceramic insulator, high voltage power supply and beam diagnosis system has been finished. The detailed parameters of each subsystem are presented in this paper.

INTRODUCTION

The linac based Free Electron Laser (FEL), and the Energy Recovery Linac (ERL) based light source are the two major types of the 4th generation light source. FEL has higher brightness, shorter pulse length and higher coherent features, but with a minor number of photon beam lines. ERL combines the good beam performance of the linac and good operation efficiency of the storage ring machine, although its brightness and coherent degree not as higher as FEL, but with many photon beam lines. Hence, both FEL and ERL cannot be replaced each other, we really need both of them. Based on this point, IHEP has proposed the suggestion of "one machine two purposes", both FEL and ERL will share a same super-conducting (SC) linac for having a high efficiency [1].

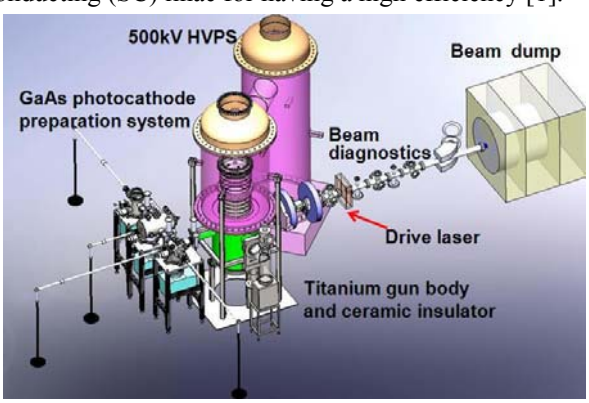

Figure 1: Overall design of the photocathode DC gun.

There are lots of technical challenges on ERL presently, especially on the electron sources which can deliver a high brightness electron beam with a low emittance and high current up to 100 mA are being developed for ERL worldwide [2]. The recent experimental results from JLab and Cornell demonstrated that a photocathode DC gun with a GaAs or multi alkali photocathode is one of the most promising candidate [3][4]. Since September of 2011, a 500kV photocathode DC gun has been supported by IHEP as an innovative project. The overall design of the photocathode DC gun is shown in Figure 1, which consists of the drive laser system, the cathode preparation system, titanium gun body and ceramic insulator, high voltage power supply system and beam diagnosis system. Table 1 shows the main parameters of the DC gun. Up to now, each subsystem has a smooth progress.

Table 1: Main parameters of the DC gun

Parameter	Design value
High voltage	350 ~ 500 kV
Cathode material	GaAs:Cs/O
Quantum efficiency	5-7% (initial), 1%
Live time	20 h
Drive laser	2.3W，530nm
Repetition rate	100MHz，1.3GHz*
Nor. emittance	(1~2)mm.mrad@77pC (0.1~0.2)mm.mrad@7.7pC
Bunch length	20ps
Beam current	(5~10) mA

* Two operation modes:
(1) 100MHz-7.7mA-77pC, (2) 1300MHz-10mA-7.7pC

DESIGN AND CONSTRUCTION PROGRESS

Drive Laser System

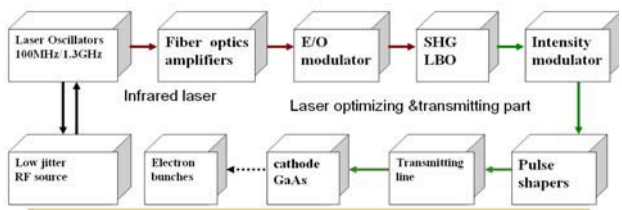

Figure 2: Schematic design of drive laser system.

Drive laser system, as shown in Figure 2, takes a fiber laser technology solution, which is among the most advanced drive laser system so far. Two laser oscillators, one is working at 1.3GHz (PriTel Inc) and the other is 100MHz (Menlosystems Inc) are used in this system,

#lxp@ihep.ac.cn

corresponding to two operation modes of DC gun. These two laser oscillators have been purchased and some preliminary tests including output power, pulse width and optical bandwidth have been completed. In addition, the independent development work on laser fiber amplifier has also been started.

GaAs Photocathode Preparation System

GaAs semiconductor photocathode which is able to generate a high-current electron beam with ultra small initial emittance due to its high quantum efficiency and low thermal emission from a negative electron affinity surface was used for electron emission in IHEP photocathode DC gun.

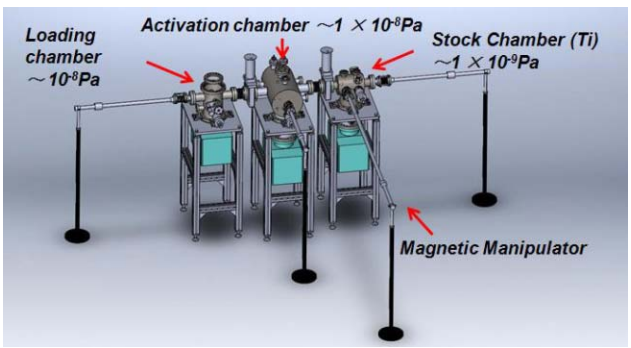

Figure 3: Structure of the photocathode preparation system.

Schematic design of a GaAs photocathode preparation system was shown in Figure 3. There are three load-lock vacuum chambers in the cathode preparation system including loading chamber, activation chamber and stock chamber. These three chambers are required to achieve a very high vacuum environment to preserve QE and lifetime of the GaAs photocathode during its activation process. The cathode puck will be transferred among the three chambers and electron gun body by the movement of magnetic manipulator.

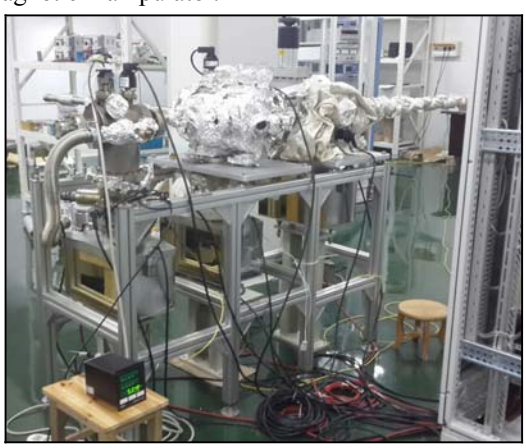

Figure 4: Baking and vacuum test of preparation system.

Up to now, the GaAs photocathode preparation system has finished its machining, assembling, baking and vacuum test. Table 2 shows the vacuum test results of these three chambers.

Table 2: Vacuum test results of these three chambers

	Material	Design vacuum	Measured vacuum
Loading chamber	SS 316L	$\leqslant 9\times10^{-8}$Pa	6×10^{-8}Pa
Activation chamber	SS 316L	$\leqslant 1\times10^{-8}$Pa	7×10^{-9}Pa
Stock chamber	Body: Ti(TA2) Flange: SS 316L	$\leqslant 1\times10^{-9}$Pa	5×10^{-10}Pa

Titanium Gun Body and Ceramic Insulator

The photoemission beam is accelerated by a static electric field applied between cathode and anode electrodes. Generally, the accelerate voltage should be as high as possible to suppress the emittance growth caused by space charge effect, but field emission electrons generated from the stem electrode and cathode will cause damage to the ceramic insulator and the surface of electrodes which is a strict limitation to the increase of accelerate voltage. A simulation about the E-field distribution was done by using CST (EM Studio) [5] to optimize the configuration of the gun body, as shown in Figure 5. And two cases with different gap distances between the cathode and anode (80mm and 100mm) were simulated under a 500kV high voltage direct current condition. From the simulation results, it can be found that the maximum electric field on the stem electrode is 8.17 MV/m and on the cathode electrode it is 10.0MV/m, meanwhile the accelerate field on the cathode surface is 6.8MV/m in case of 80mm. And in the case of 100mm, these three values are 8.17MV/m, 9.26MV/m and 6.0MV/m respectively. Considering the electrical breakdown field between the cathode and anode depends on the gap distance, electrodes material, and surface treatment of the electrodes, in our DC gun system, the stem electrode, cathode electrode and anode electrode are going to be fabricated by using titanium material which shows a higher breakdown field [6].

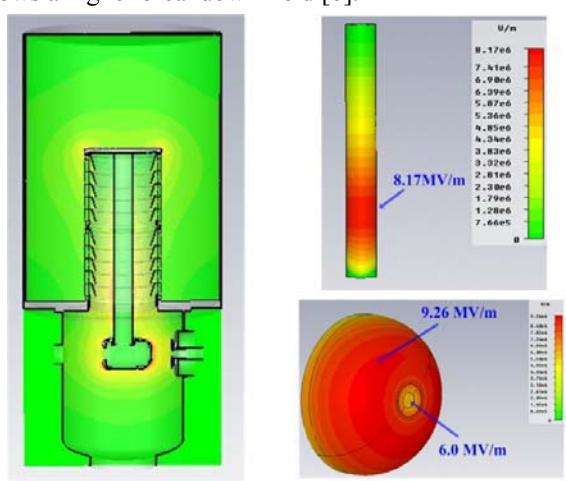

Figure 5: Simulation of E-field distribution by using CST.

The ceramic insulator is the most critical component in the development of a high-voltage DC gun. It needs to be well insulated and appropriately resistant to avoid any local concentration of the electron charge that can irreversibly damage the ceramic. In our design, the KEK/JAEA option is adopted [7], in which a segmented ceramic insulator structure with guard rings between every two adjacent segments is employed to effectively avoid the field emission electrons generated from the stem electrode toward the ceramic insulator and hence to protect ceramic insulator. Figure 6 shows the structure of one section ceramic insulator of our DC gun, in which two sections ceramics (totally ten segments) are going to be employed. Now, the procurement process of the ceramics is ongoing.

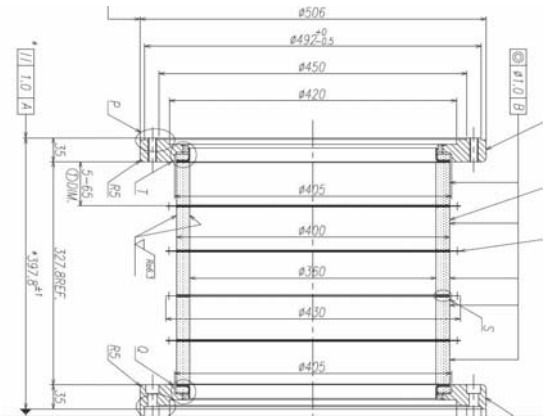

Figure 6: The structure of one section ceramic insulator.

For pumping system, considering the QE and lifetime of GaAs cathode largely depends on the vacuum environment, a kind of low out-gassing rate material titanium was selected for the fabrication of gun body to ensure the inside vacuum environment, which can reach an ultra high level of 5×10^{-10}Pa by employing a 500L/s ion pump and forty-eight 400L/s NEG pumps.

High-Voltage Power Supply System

Figure 7: HiTek HVPS.

Low-emittance is one of the most important parameters in the design of a photocathode DC gun, so the gun voltage must be 500 kV or higher to suppress the emittance growth by space charge effect [8][9]. As a 500 kV photocathode DC gun, the emittance of a 77pC bunch charge would be suppressed to less than 1mm.mrad. Another key parameter of the power supply system is the voltage ripple which is one of the major sources of bunch-to-bunch fluctuation such as jitters in emittance, bunch shape, and energy spread after the full acceleration [10]. According to these requirements of DC gun, a product made by a UK company HiTek [11], as shown in Figure 7, was chosen and its main parameters are listed in Table 3. Now, the construction of this power supply system has been finished and the test on its parameters is ongoing in company. Besides, the design on related HVPS tank and SF6 recycle system has also been completed.

Table 3: Main parameters of the HiTek HVPS

Parameter	Design value
High voltage	500 kV 550kV at HV conditioning
Current	10mA
Type	Cockcroft-Walton generator
Working style	DC
Voltage ripple	$5X10^{-4}$ (peak to peak)
Isolation medium	SF_6
Output resistor	100MΩ for HV conditioning, 50kΩ at beam operation

Beam Diagnosis System

The preliminary design of the components applied in beam diagnosis system has been completed, as shown in Figure 8. The beam line includes three pairs of solenoid and corrector, a laser box, a deflecting cavity, two YAG screens, a bending magnet and a beam dump. The beam emittance will be measured by solenoid scan and the bunch length will be measured with deflecting cavity.

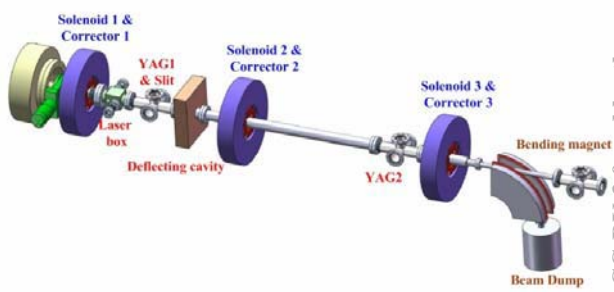

Figure 8: The preliminary design of the beam line.

SUMMARY

Since September of 2011, a 500kV photocathode DC gun has been supported by IHEP. In this paper we briefly described the major issues of the design studies and construction progress on each subsystem of the photocathode DC gun, including the drive laser system, the photocathode preparation system, the electron gun body and ceramic insulator, the high voltage power supply system and the beam diagnosis system. Up to now, each subsystem has a smooth progress.

ACKNOWLEDGMENT

We would like to thank Dr. M. Yamamoto, Dr. T. Miyajima, Dr. Y. Honda at KEK and Dr. R. Hajima, Dr. N. Nishimori at JAEA for their great help and useful discussion on the design of IHEP 500kV photocathode DC gun.

REFERENCES

[1] CHEN Senyu, ZHU Xiongwei and WANG Shuhong, Towards one machine two purposes: using a common SC linac for XFEL and ERL simultaneously, Chinese Physics C 34. 1, 2010, January.
[2] B. Dunham et al., “ERL2011 summary of workinggroup 1: Progress with DC photoemission electronsources”, ERL2011, Tsukuba, Oct. 2011.
[3] C. Hernandez-Garcia, et al., “A high average current DC GaAs photocathode gun for ERLs and FELs”,PAC’05, Knoxville, 2005, WPAP050, p. 3117(2005); http://www.JACoW.org.
[4] B. Dunham, et al., Appl. Phys. Lett. 102 (2013) 034105
[5] http://www.cst.com/
[6] F. Furuta et al., Nucl. Instrum. Methods Phys. Res. A 538, 33 (2005)
[7] R.Nagai, et al, “High-Voltage Test of a 500-kV Photocathode DC Gun for the ERL Light Sources in Japan”, Proceedings of IPAC’10, Kyoto, Japan.
[8] R. Hajima, R. Nagai, Nucl. Instrum. Methods Phys. Res. A 557, 103 (2006)
[9] V. Bazarov and C. K. Sinclair, Phys. Rev. ST Accel. Beams 8, 034202 (2005)
[10] R. Nagai et al., Proc. 4th annual meeting of Part. Acc. Soc. of Japan (2007) 676 (in Japanese).
[11] http://www.hitekpower.com/en-GB/Default.aspx

UPCOMING MEASUREMENTS OF TRANSVERSE BEAM BREAK UP AT THE SUPERCONDUCTING RECIRCULATING ELECTRON ACCELERATOR S-DALINAC*

F. Hug#, T. Kürzeder, N. Pietralla, TU Darmstadt, Darmstadt, Germany

Abstract

The superconducting accelerator S-DALINAC provides electron beams of up to 130 MeV for nuclear physics experiments at the university of Darmstadt since 1991. It consists of a 10 MeV injector and a 40 MeV main linac and reaches its final energy using up to two recirculation paths. The superconducting main linac houses eight 20-cell SRF cavities operated at 3 GHz and 2 K. Due to transverse beam break up the design beam current of 20 µA could not be reached in recirculating operation mode yet, the highest stable beam current obtained so far accounts for 5 µA, which is sufficient for the nuclear physics experiments carried out at Darmstadt [1].

On the other hand the very low threshold current for the occurance of beam break up in addition with the recirculating linac design gives a unique opportunity to the ERL community for testing different strategies of avoiding beam break up experimentally and to benchmark beam dynamics simulations concerning this topic. We will report on upcoming experiments which will be carried out at the S-DALINAC for that purpose.

INTRODUCTION

The Superconducting DArmstadt LINear Accelerator (S-DALINAC) is operating since 1987 as a source for nuclear- and astrophysical experiments at the university of Darmstadt [2]. It is designed for producing beams of either unpolarized or polarized electrons [3] up to energies of 1 up to 130 MeV with beam currents from several pA up to 60 µA in single pass mode or 20 µA in recirculating mode using two recirculations. The layout of the S-DALINAC is shown in Fig. 1.

For acceleration of the beam ten 20 cell superconducting elliptical cavities (see fig. 2) with a quality factor of $Q_0 \approx 10^9$ are used. The operation frequency of the cavities is 3 GHz while the maximum accelerating gradient of each cavity accounts for 5 MV/m. As the main linac consists of 8 standard 20-cell cavities it can provide an energy gain of 40 MeV. By recirculating

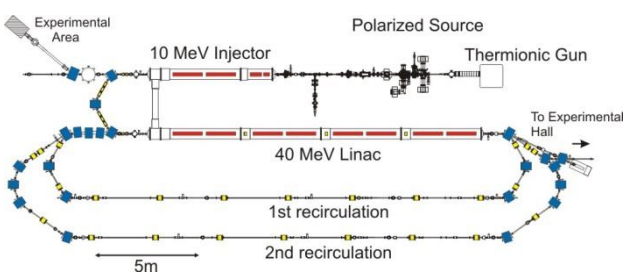

Figure 1: Floor plan of the S-DALINAC.

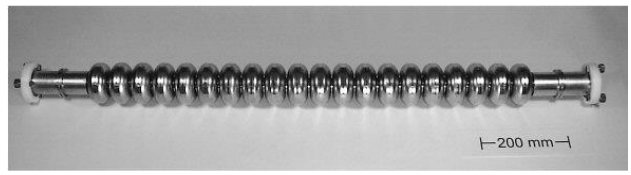

Figure 2: S-DALINAC 20 cell cavity.

the beam up to two times the maximum energy of 130 MeV can be achieved. In the adjacent experimental hall this beam can be used for different experiments such as electron scattering in two electron spectrometers or experiments with tagged photons. For these experiments an energy spread (rms) of $1 \cdot 10^{-4}$ as well as a very low γ-ray background are required.

OPERATIONAL EXPERIENCE

The S-DALINAC is the first superconducting and recirculating cw accelerator for electrons which has been put into operation in Europe [2]. After setting up the injector in 1987 the complete accelerator started operation in 1991 and has been used for experiments in nuclear, astro- and radiation physics since then. In 1996 a first infrared laser beam at the free electron laser (FEL) could be observed [4]. For the FEL operation the peak current of the electron beam was up to 2.7 A at a pulse length of some ps and an operation frequency of 600 MHz [4]. Originally it was planned to operate the S-DALINAC as an ERL as well when using the FEL but the challenges of operating this first European FEL had been big enough even without trying the ERL mode. One reason has been the occurance of instabilities due to the high peak current of the electron bunches – a first observation of transverse beam break up at the S-DALINAC which occurs at a relative low threshold current of some µA due to the design of the 20-cell accelerating cavities which haven't been optimized for suppressing any higher order modes (HOMs).

The beam break up also limits the maximum achievable beam current in recirculating operation of the S-DALINAC. Operational experience obtained during many years of beam time for nuclear physics showed that a stable operation in the twice recirculating mode is possible only up to some µA. The highest stable current achieved so far accounts for 5 µA [1], which is well below the design value of 20 µA but adequate for the experiments carried out. On the other hand this low threshold current gives an opportunity of investigating transverse beam break up experimentally.

*Work supported by BMBF through 05K13RDA
#hug@ikp.tu-darmstadt.de

PROPOSED EXPERIMENTS

Transverse beam break up (BBU) occurs when an accelerated beam with a high peak current excites higher order dipole modes in the accelerating cavities. These modes can disturb the following bunches or in a recirculating design as used in ERLs even the same bunch at its subsequent passes through the linac. Early observations of this phenomenon has been observed in the very first SRF linacs at threshold currents of a few µA [5,6]. Much effort has been made to raise the BBU threshold currents mainly by designing accelerating cavities with strong damping of HOMs but also by matching the transverse beam optics [7,8] or even using the chromaticity of the beam transport system [9]. The latter two have been investigated in simulations only so far. For that reason we propose experiments at the S-DALINAC for testing strategies of avoiding transverse beam break up taking advantage of the low threshold current of this recirculating linac mentioned above.

Variation of the transverse phase advance

Matching the transverse phase advance in a recirculating linac in a way that a negative feedback of the HOM excitation is provided can increase the threshold current significantly [8]. Figure 3 shows simulation results for the threshold current using different cavities and transverse phase advance in the recirculation for a once recirculating ERL [8]. It can be seen that the threshold current increases for certain amount of phase advance in the recirculation path.

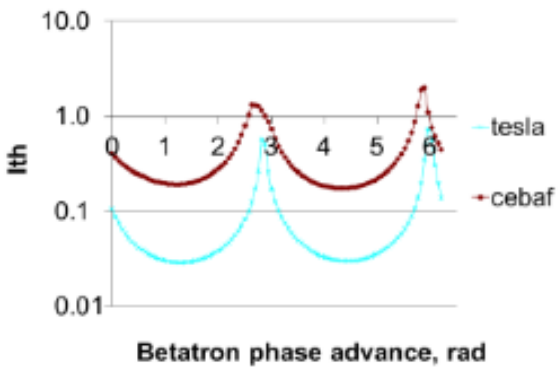

Figure 3: BBU threshold currents for two different types of accelerating cavities and different amount of betatron phase advance [8].

As the recirculation lattice of the S-DALINAC allows for an easy variation of transverse optics, such a relation should be measured as well when changing the transverse betatron phase advance of the recirculations. In order to make the results comparable with simulations the HOM spectrum of the S-DALINAC 20-cell cavities need to be derived first by carrying out simulations with CST microwave studio.

An opportunity to increase the threshold current even further can be a coupling of x and y planes of transverse motion as it has been presented in [8] as well. In such a scheme solenoids or skew quadrupoles are used to mix the horizontal and vertical plane of transverse motion.

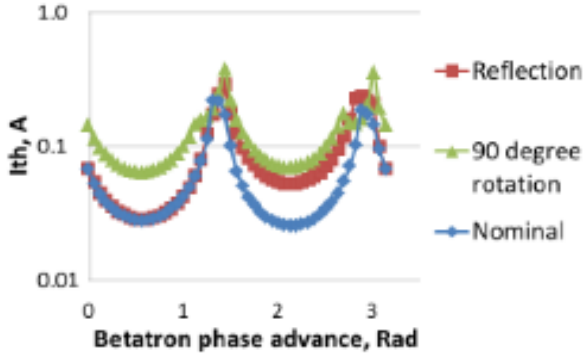

Figure 4: BBU threshold currents for different amount of betatron phase advance and coupled motion of x and y planes in tranverse phase space using reflectors (skew quadrupoles) or solenoids [8].

In order to test this topic at the S-DALINAC additional skew quadrupoles and solenoids need to be installed in the straight sections of the recirculation paths. These magnets are under design at the moment at will be installed within one of the next shutdown periods.

Variation of chromaticity

An interesting approach of avoiding transverse beam break up has been presented in [9]. The author proposes to keep natural chromaticity in a large scale recirculating linac (eRHIC at BNL) instead of correcting for it. If the product of chromaticity in the recirculation arcs and energy spread of the beam gets large enough

$$|\phi\sigma_\delta| >> 1 \qquad (1)$$

the electrons "forget" the kick of any dipole modes while passing the recirculations and each linac sees a fresh electron beam [9].

In order to test this hypothesis additional sextupoles for the S-DALINAC recirculation arcs are currently under design as the natural chromaticity of the S-DALINAC doesn't account for large enough values to satisfy the condition in formula (1). As soon as these sextupoles are installed first experiments on the influence of chromaticity on transverse beam break up will be carried out.

Variation of bunch length

As derived in [10] the strength of excitation of HOMs in cavities is dependent of the bunch length σ_b like:

$$P \propto e^{-\sigma b} \qquad (2)$$

This means that a bunch will excite HOMs stronger as it gets shorter, while longer bunches lead to weaker excitations. Usually in linacs acceleration is performed on

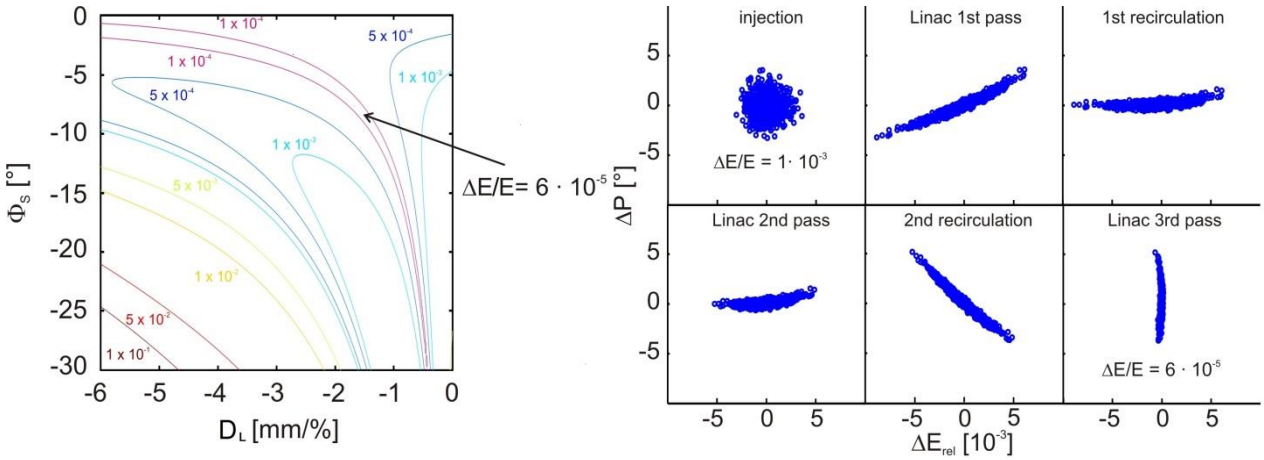

Figure 5: Hillplot of the resulting energy spread at extraction for different sets of longitudinal dispersion and synchrotron phase (left) in a twice recirculating linac [13]. Beside the isochronous point with acceleration on crest of the rf field exist areas of reduced energy spread. The minimum has been determined to D_L = -1.5 mm/% and Φ_S = -9.5° On the right side a bunch of 5000 particle has been tracked through the linac using the optimized parameters. The particles perform a half oscillation in longitudinal phase space ending up on a significant reduced energy spread. During acceleration the bunch length is enlarged which leads to weaker excitation of HOMs. This will be investigated within this project concerning its influence on BBU thresholds..

crest of the rf field using short bunches in order to achieve a low energy spread of the beam. In recirculating linacs like ERLs the recirculations have to be isochronous then in order to keep the bunch length short.

As an alternative one can use acceleration on edge of the rf field with non-isochronous recirculation paths like it is common in microtrons for stabilizing the beam against losses. But also for few turn accelerators the concept of non-isochronous recirculation can be of advantage like proposed in [11,12] and shown experimentally at the S-DALINAC in [13]. Using this acceleration scheme the longitudinal phase advance during the acceleration process has to add up to a half-integer number of synchrotron oscillations in order to get an optimized energy spread of the beam at extraction [11]. Figure 5 shows simulations performed for the S-DALINAC showing the optimized longitudinal working point and the propagation of longitudinal phase space during acceleration.

For suppressing beam break up this concept provides an opportunity to accelerate the beam on longer bunch lengths and hence weaker excitations of HOMs while the resulting energy spread keeps low. Within the planned experiments at the S-DALINAC it will be investigated if this leads to an increase of the BBU threshold current as it is expected.

Currently additional beam dynamics simulations in longitudinal phase space are in process in order to find settings with different bunch lengths during acceleration and similar energy spread at the end of acceleration process. In a next step systematic measurements will be performed using the accelerator settings achieved within these simulations.

SUMMARY AND OUTLOOK

The S-DALINAC is a superconducting, recirculating electron linac suffering from transverse beam break up at very low threshold currents of some µA. This provides a unique opportunity to the ERL community in testing different strategies of avoiding beam break up experimentally.

The proposed experiments at the S-DALINAC accelerator will be started as soon as possible. Currently different magnets like solenoids and sextupoles are under design and will be integrated into the beam line within one of the next shutdown periods.

In addition to the experiments with electron beam simulations of the HOM spectra of the used cavities as well as beam dynamics simulations will be carried out in order to refer the experimental results.

REFERENCES

[1] O. Yevetska et al., Nucl. Instr. Meth. A **618** (2010) 160.
[2] A. Richter., EPAC ’96, Sitges (1996) 110.
[3] Y. Poltoratska et al., J. Phys.: Conf. Ser. **298** (2011) 012002.
[4] M. Brunken et al., NIM A **429** (199) 21.
[5] C.M. Lyneis et al., Trans. Nucl. Sci. **B** (1979).
[6] P. Axel et al., Trans. Nucl. Sci. **26** (1979).
[7] G.H. Hoffstaetter et al., Phys. Rev. STAB **7** (2004) 054401.
[8] Y . Petenev et al., IPAC'11 San Sebastian, (2011) 718.
[9] V. Litvinenko, LINAC ’12, Tel Aviv (2012) 249.
[10] J-L. Biarrotte, Proc. PAC '01, Chicago (2001) 1098.
[11] H. Herminghaus, NIM A **305** (1991) 1.
[12] H. Herminghaus, NIM A **314** (1992) 209.
[13] F. Hug et al., LINAC ’12, Tel Aviv (2012) 531.

STATUS OF THE BNL ERL INSTRUMENTATION*

D. M. Gassner #, D. Kayran, V. Litvinenko, C. Liu, G. Mahler, R. Michnoff, T. Miller, M. Minty, M. Wilinski Collider-Accelerator Department, BNL, Upton, NY, 11973, USA

Abstract

The Energy Recovery Linac (ERL) project is currently under construction at the Brookhaven National Laboratory. Energy recovery operations are expected with high intensity beams that have current up to a few hundred milliamps, while preserving the emittance of bunches with a charge of a few nC produced by a high current SRF gun. To successfully accomplish this task the machine will include beam diagnostics that will be used for accurate characterization of the beam phase space at the injection and recirculation energies, transverse and longitudinal beam matching, orbit alignment, beam current measurement, and machine protection [1]. This paper describes the recent progress and present status of the systems that will be used to meet these goals.

INTRODUCTION

The diagnostics requirements have been described in several previously published papers [2,3,4]. There is a progression of ERL facility stages planned in order to advance towards achieving full energy recovery. The diagnostics system configurations vary for each stage. The initial stage for beam testing includes the 2MeV SCRF gun, a straight beam transport to an in-flange ICT, then to an isolated blank CF flange acting as a Faraday Cup. After gun testing with different cathodes we will extend the straight transport to include a pepper pot emittance station. When the beam parameters are acceptable we will connect the transport to the injection zig-zag [5] and deliver beam to a low power dump after the 5-cell Linac. The early commissioning stages are limited to 70W operation by the relatively small temporary beam dumps. The full complement of all of the ERL planned instrumentation subsystems, including devices in the energy recovery loop and high power beam dump, are shown in Figures 1 and 2.

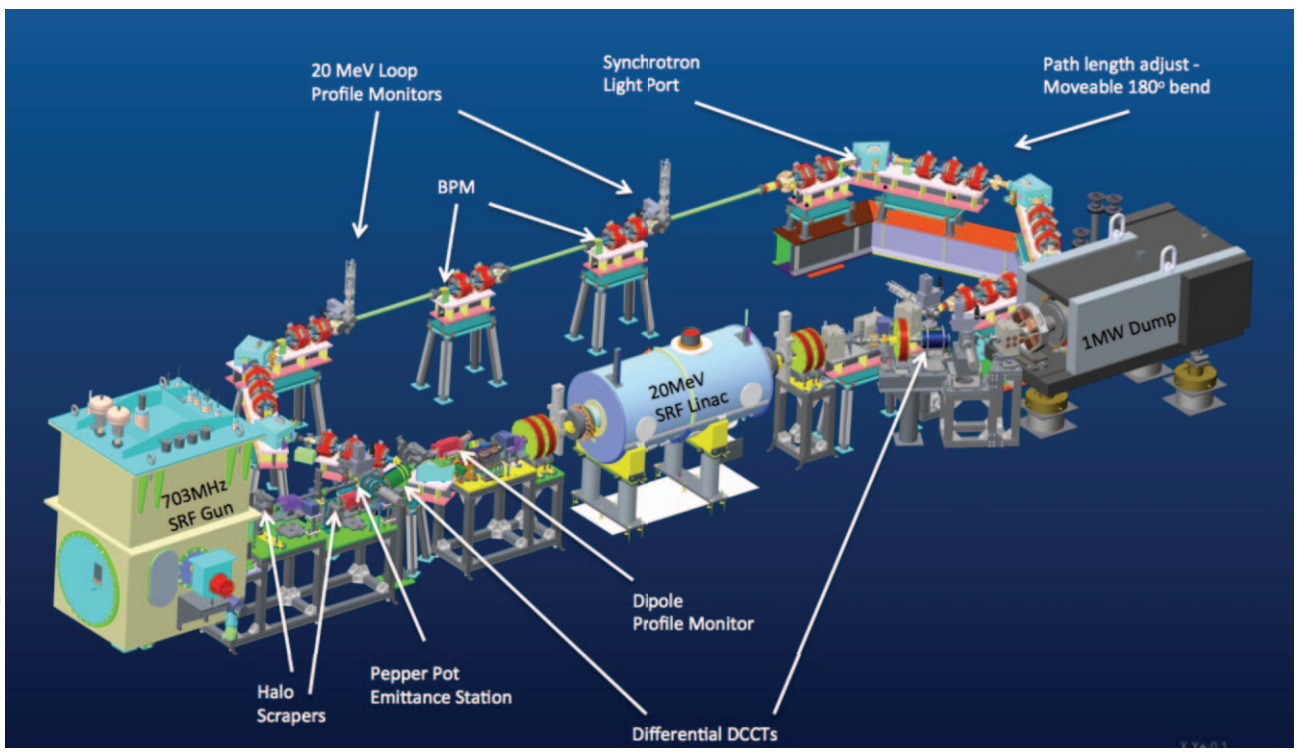

Figure 1: A 3D rendering of the ERL facility showing the SCRF Gun, zig-zag injection transport, 5-cell SCRF Linac, recovery loop, high power dump, and location details of some of the instrumentation detectors.

*Work supported by the auspices of the US Department of Energy
#gassner@bnl.gov

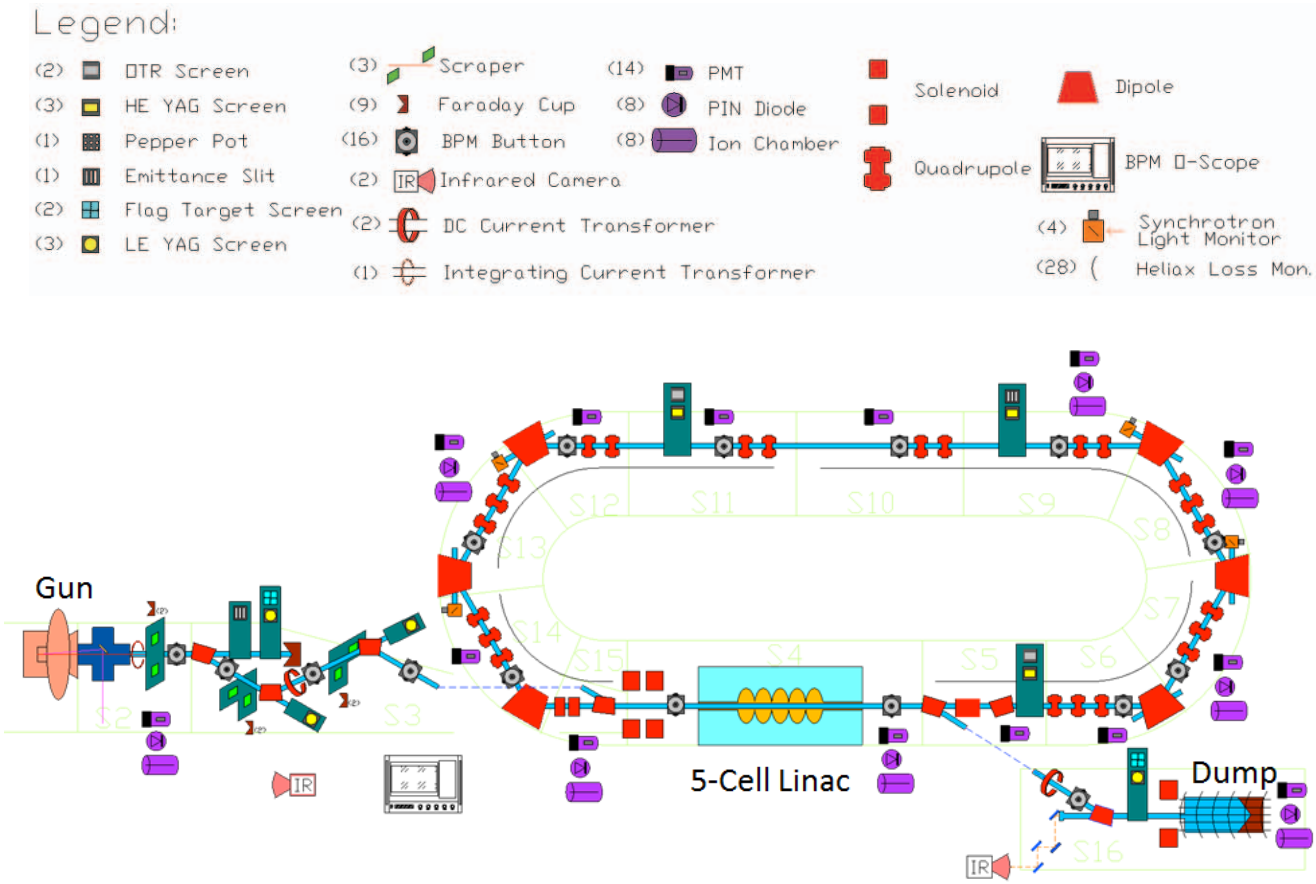

Figure 2: A schematic of the ERL facility showing the distribution of the instrumentation detectors.

Extraction Beam line – 2MeV

The design of the 2 MeV extraction beam line transport from the 5-cell Linac to the dump was detailed as shown in Figure 3. The instrumentation includes a BPM, DCCT and a plunging YAG profile monitor.

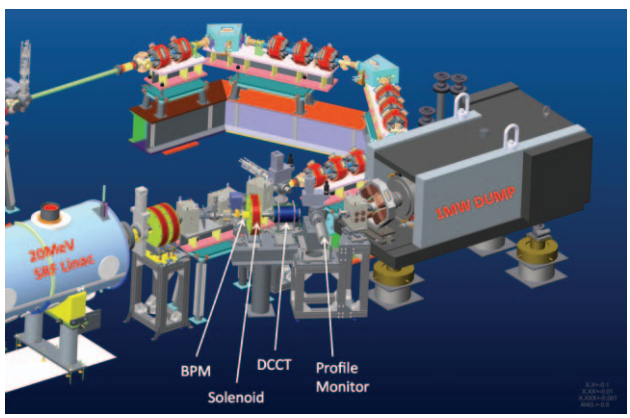

Figure 3: ERL 2MeV extraction line showing instrumentation locations.

DIAGNOSTICS SYSTEMS

Beam Position Monitors

There are 16 dual plane 10mm diameter button style Beam Position Monitors (BPMs), 4 in the injection transport, 11 in the recirculation loop, and 1 in the dump line. The buttons are Times Microwave Systems [6] model SK-59044; they are mounted on stainless cubes that are welded to the adjacent 6 cm diameter beam pipes. The orientations of the installed cubes are either at 45° or 90° depending on their location. A 45° orientation is used if there are space limitations and to avoid beam related energy deposition on a button downstream of bending magnets. The BPMs will be baked to 150C.

Libera Brilliance Single Pass electronics from Instrumentation Technologies [7] will process signals from the BPMs. These modules have been customized with a 700MHz SAW band pass filter that matches the fundamental frequency of the SCRF gun and Linac accelerating cavities. The Libera BPM electronic units have been integrated into the standard RHIC control system. ADO (accelerator device object) software has been written and executes directly on the Linux kernel that is resident in the Libera hardware. The ADO provides on-board communication to the Libera hardware through the CSPI (control system programming interface) library

provided by I-Tech, and communicates to higher level workstations via Ethernet using standard RHIC control system utilities.

Beam Profile Monitors

Transverse beam profiles will be measured at 7 locations by two methods, depending on the energy and the amount of beam charge in the bunch train. When in low charge operating mode with 1-100pC bunch charge trains, we will use 0.1 X 50mm YAG screens from Crytur [8] (40mm clear aperture). For higher energy and charge modes we will use OTR (optical transition radiation) screens that are comprised of a 250 micron thick silicon wafer coated with ~1000 angstroms of aluminum. The 2 low-energy, and 3 high-energy type profile monitor stations consists of a vacuum cross with a three-position pneumatic actuator allowing selection of a beam impedance matching "squirrel cage," a YAG crystal with its surface normal to the beam direction followed by a 45 degree turning mirror, or an OTR screen also followed by a 45 degree turning mirror. The profile monitor stations were specified by BNL then designed and fabricated by Radiabeam Technologies [9]. They have been delivered and are being tested and prepared for installation.

Optical resolution analysis can be done at any time using a resolution test pattern embedded in the virtual target (attached to the optics box) that is the same distance from the camera as the YAG and OTR screens. Initial test results show optical resolutions of better than 50um.

A pair of specially designed YAG dipole profile monitors will be provided due to space constraints in the zig-zag transport, they will plunge into the beam path inside of the two injection 30º vertical dipole chambers as shown in Figures 4 & 5.

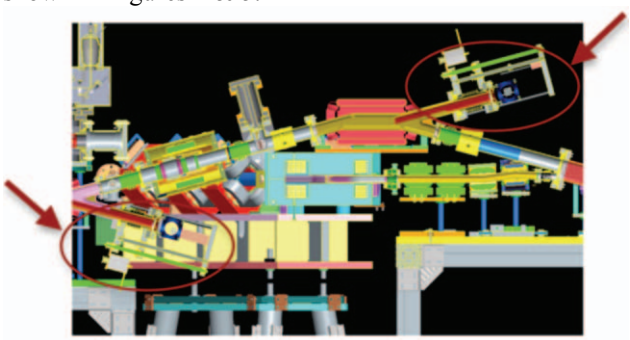

Figure 4: Cross section of injection Zig-Zag showing the locations of the Dipole Profile Monitors.

Precise positioning will be provided by a stepper motor actuated plunging mechanism, with a 4-inch stroke, that has a long YAG screen holder that extends into the dipole magnet chamber through an auxiliary port to intercept the electron beam. The beam can be imaged at different places on the crystal including the edge depending on the plunge depth. This can be useful for semi-destructive beam halo monitoring. A specification and statement of work has been prepared, we hope to receive these devices from a vendor next year. The dipole profile monitor ports will be blanked off during the initial commissioning of the injection zig-zag as the devices will likely not be delivered before first beams.

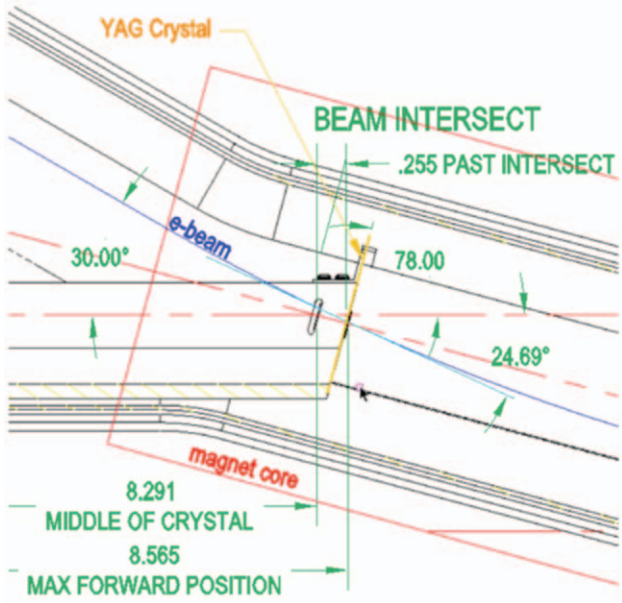

Figure 5: Injection Zig-Zag Dipole Profile monitor details, the electron beam trajectory in this view is right to left.

Images from the YAG or OTR screens are transported through a mirror labyrinth to a 3-motor lens and CCD camera in a local enclosed optics box. Communication cable length requirements and limited support for FireWire 1394 cameras in the WS5 and WS6 RedHat Linux kernels we currently use has prompted a migration to GigE camera technology for digital imaging tasks within our controls subsystems [10]. The Manta G-201B from Allied Vision Technologies [11] is the camera we plan to use for early operations. A software middleware layer is implemented using Aravis, an open-source glib/gobject based library which enables video acquisition from genicam based cameras, which makes the images available to various viewing and image processing applications. Users can control parameters such as image size, bit depth, resolution, exposure, gain, gamma, binning, triggering, etc. The images are used to characterize the beam and can be stored for later examination and calculation of projections, centroids, etc.

Synchrotron Light Monitors

Synchrotron light monitors will be used to measure transverse beam profiles while running with high power beams. Due to the resulting relatively long 14 micron IR synchrotron radiation wavelength (20MeV, 60° bend, 3.3kG dipole), using these monitors productively could be challenging. We plan to install optical transports and CCD cameras at a number of the ERL loop 60° dipole locations sometime after the full ERL has been commissioned and the beam current is high enough to produce enough synchrotron light for a good measurement. Five of the six

recirculation loop dipole chambers have dedicated synchrotron light output viewing ports.

Halo Scrapers

Halo scrapers fabricated by Radiabeam based on a BNL design will be installed in the low energy injection zig-zag beam line to explore the halo characteristics. A combination of horizontal and vertical stepper motor controlled 2mm thick copper jaws will be located at several locations in the injection transport. After the halo characteristics are determined by measurements with beam, a collimator station will be installed to scrape off the undesired halo at low energy to reduce higher power beam losses downstream.

Beam Current Monitors

High precision DC current measurements will be made using a matched set of Bergoz NPCT-S-115 DC current transformers (DCCT) and standard NPCT electronics [12]. There will be one of each installed in the injection and extraction transport beam lines. These DCCTs are configured in a nulling mode [13] where their calibration windings are joined in a single loop, and driven opposite the beam by a low-noise Khronhite model 523 current source. The output level of the dump DCCT is fed back as a reference to the current source to drive the dump DCCT output to zero. The output of the gun DCCT is then a measurement of the difference of beam current between the two DCCTs.

The DCCT signal processing will be done using a National Instruments PXI-1042 8 slot 3U chassis with a PXI-8115 Core i5-2510E 2.5GHz controller and a set of PXI-6289 625 kS/s, 18-bit digitizers for handling system tasks that include absolute and differential measurements. Drift (magnetic field, thermal, and gain) compensation will be automatically removed by periodic nulling without beam. The anticipated sub-micro-amp resolution may permit using this diagnostic as an additional layer of the machine protection system [14] in the case the beam loss monitors fail to thoroughly detect significant beam losses.

Bunch-by-bunch & bunch train charge will be measured by a Bergoz in-flange Integrating Current Transformer (ICT) part number ICT-CF6-60.4-070-05:1-H-UHV-THERMOE, located in the upstream injection line. This ICT assembly has an internal type E thermocouple for bake-out temperature monitoring; this feature was added by request. ICT signals will be processed by Bergoz BCM-IHR Integrate-Hold-Reset electronics that have the maximum 10 kHz repetition rate feature. A VMIC 3123 16-bit digitizer with a beam synched trigger will be configured using the double-channel digitizing method to increase the acquisition rate to 200 kS/s. The integrating window length range possible in the ICT electronics is from 100ns to 6.9us. The triggering frequency is independent of the integrating window size.

Beam Loss Monitors

Photomultiplier tube (PMT) based loss detectors will be installed at locations where beam loss is most likely. The design of this detector is based on ones developed at Jefferson Lab and used at CEBAF [15]. JLAB uses the Burle 931B PMT. At the BNL ERL we will use the Hamamatsu R11558 PMT that is very similar to the 931B except that it has lower dark current, higher gain, and improved anode and cathode responsivity. The PMT is installed in a light tight ABS plastic housing that includes a green LED for testing with 1uS light pulses, see Figure 6 below.

Figure 6: PMT based beam loss monitor detector, assembled at left, and disassembled.

Beam loss signals from the PMT detectors will be processed using the VME based eight-channel BLM module developed at JLAB. It provides linear, logarithmic, and integrating amplifiers that simultaneously provide the optimal signal processing for each application. Amplified signals are digitized and then further processed through a Field Programmable Gate Array (FPGA). Combining both the diagnostic and machine protection functions in each channel allows the operator to tune-up and monitor beam operations while the machine protection is integrating the same signal. Other features include extensive built-in self-test, fast shutdown interface (FSD), and 16-Mbit buffers for beam loss transient play-back. The new VME BLM board features high sensitivity, high resolution, and low cost per channel [16].

The actual PMT gain at each location will be field adjusted by setting the high voltage bias during beam commissioning. A CAEN HV multi-channel chassis with full remote control will bias the PMTs.

Eight standard RHIC Ion Chamber (IC) loss detectors will be employed at select locations at the ERL. The signals from each IC are transported on 75 ohm cables to the standard RHIC style BLM V119/V118 electronics processing modules. All V119 modules are supervised by a V118 module that monitors integrated signal level data compared to thresholds. The V118 module has a discrete loss output signal that will signal the machine protection system in the event of excessive losses.

Ion chamber type loss monitors based on gas filled heliax cables with ~10^4 dynamic range and sensitivity of >200nC/rad/m will also be employed at ERL [17]. The cable is 7/8 inch Heliax, Andrew type RG318, filled with Argon to 10 psig. A series of four long loss monitor cables will continuously run along the inside of the recirculation loop in order to have full beam loss monitor

coverage and a way to determine integrated losses in each loop quadrant as shown in Figure 2. The cable loss monitors are biased to ~150V by custom floating bias supplies (used in the AGS), mounted in NIM modules. The loss signal returns on the bias cable and is integrated by custom integrating amplifier modules (also used in the AGS) whose analog outputs are digitized by standard VME DAC modules.

In addition to amplitude proportional beam loss detection, as provided by the PMT, IC & Heliax detectors, event count based detectors will be employed. PIN Diode loss detector modules, Bergoz model BLM, will be installed at eight select locations in ERL. The TTL data output of each detector is counted by a Struck model SIS3808 scalar VME module [18].

It is important to ensure the hi-power dumped electron beam is distributed as designed inside the dump chamber. A variety of diagnostics are planned to help ensure dump performance and protection [19]. It is impractical with this dump design to install thermocouples to directly map temperature variations due to the two concentric layers of cooling water flow.

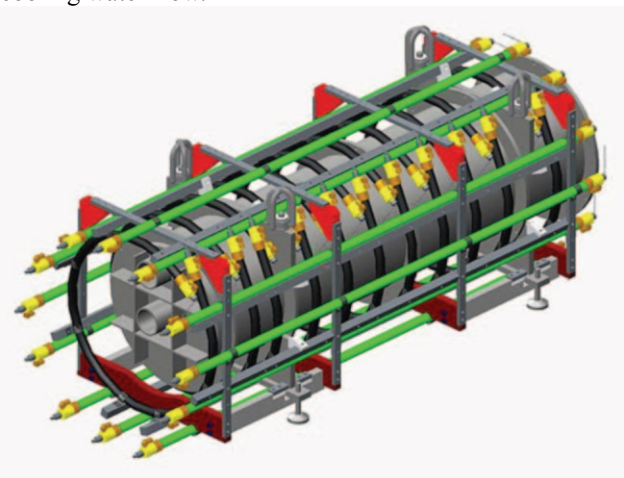

Figure 7: ERL Dump drawing showing the heliax cable type beam loss monitors shown in green and black.

A configuration of heliax loss monitor cables as shown in Figure 6 will be installed inside the outer shielding vessel of the beam dump to map losses at low power. An IR camera is planned to be used in an attempt to image the downstream portion of the inside of the dump while operating at reduced power using an optical labyrinth for camera protection, and a ZnSe viewport.

Thermal imagers will be used at several locations to measure beam pipe temperature gradients to ensure beam losses not seen by other loss detectors are monitored. We chose the FLIR A310 camera [20]. It offers image transfer and control via Ethernet, and configurable location specific temperature thresholds on the image can be programmed and used to provide a machine protection alarm or interlock signal from a digital output port on the camera assembly.

FUTURE INSTRUMENTATION

We plan to eventually add more instrumentation systems as the progress with the ERL facility moves forward. These systems include a streak camera, M_{56} measurement using a longitudinal BTF technique, and several techniques to measure high power transverse beam profiles. There is beam transport space available in the ERL loop far from the SCRF cavities. We are considering using conventional wire scanners, vibrating wire scanners, and laser wire scanner techniques. A combination laser wire with Compton photon counter can be used to measure all three dimensions of the electron bunches in the high power regime [21].

ACKNOWLEDGEMENTS

The authors acknowledge the contributions of I. Ben-Zvi and other members of the Accelerator R&D Division, Instrumentation Systems Group, Accelerator Components & Instrumentation Group, the Controls Group especially B. Olsen, J. Jamilkowski and L. Hoff, the Vacuum Group, and Jesse Fite and Sal Picataggio.

REFERENCES

[1] D. Gassner et al., "BNL Energy Recovery Linac Instrumentation", ERL 2011, WG4003.
[2] P. Cameron et al., "A First Look at Beam Diagnostics for the RHIC Electron Cooling Project", DIPAC 2005.
[3] P. Cameron et al., "Beam Diagnostics for the BNL Energy Recovery Linac Test Facility", BIW 2004, page 232.
[4] E. Pozdeyev et al., "Diagnostics of the BNL ERL", PAC07, page 4387, FRPMS116.
[5] D. Kayran et al., "A Method of Emittance Preservation in ERL Merging System", THPP071, FEL 2005, Stanford CA.
[6] http://www.timesmicrowave.com/
[7] http://www.i-tech.si/
[8] http://www.crytur.cz/pages/13/imaging-screens
[9] http://www.radiabeam.com/products/Diagnostics.html
[10] J. Jamilkowski et al., "Controls System Developments for the ERL Facility", ICALEPCS 2011, MOPMU027.
[11] http://www.alliedvisiontec.com/us/products/cameras/gigabit-ethernet/manta.html
[12] http://www.bergoz.com/
[13] P. Cameron et al., "Differential Current Measurement in the BNL ERL Facility", ERL2005 Workshop.
[14] Z. Altinbas et al., "The Machine Protection System for the R&D Energy Recovery Linac", MOP277, PAC 2011.
[15] J. Perry et al., "The CEBAF Beam Loss Sensors", PAC 1993, page 2184-2186.
[16] J. Yan, K. Mahoney et al., "New Beam Loss Monitor for 12 GeV Upgrade", WEP092, ICALEPCS 2009.
[17] K. Wittenburg, "Beam loss monitors" http://cds.cern.ch/record/1213279/files/p249.pdf

[18] http://www.struck.de/sis3808.htm
[19] T. Miller et al., "Instrumentation Designs for Beam Distribution Measurements in the ERL Beam Dump at BNL" these proceedings, ERL 2013, PS14.
[20] http://www.flir.com/
[21] A. Murokh et al., "A 10MHz Pulsed Laser Wire Scanner for Energy Recovery Linacs", MOPE095 IPAC10, Kyoto, Japan.

RADIATION MONITORING AT NOVOSIBIRSK FEL

T.V.Salikova, M.V.Petrichenkov, A.V.Repkov, O.A.Shevchenko, N.A.Vinokurov
Budker Institute of Nuclear Physics, Novosibirsk, Russia

Abstract

The radiation diagnostics system controls the levels of radiation in the accelerator hall and in the adjacent rooms where the FEL personnel works. The system provides radiation safety for the personnel. The software performs data visualization and records measurement results in the database. There are special ionization chambers installed in the accelerator hall. They track beam losses in the vacuum chamber; this information is used for beam orbit correction. These sensors detect induced radioactivity. Based on these data, we can trace the degradation of the material of the construction under the action of radiation.

FEL PARAMETERS

Novosibirsk high-power FEL is based on the multiturn energy recovery linac (ERL), see Fig. 1. The FEL parameters are listed in Table 1.

Table 1: Parameters of FEL

Number of orbits	1	2	4
Electron energy, MeV	12	22	42
Average beam current, mA	10	10	10
FEL wavelength, micron	120 - 240	40 - 120	5 - 40
Max output power, kW	1	10	10

The accelerator hall is shown in Fig 2; the thickness of its concrete walls is 3 meters. This thickness provides radiation protection for the 1 GeV accelerator.

Current losses:

Injector $\delta I/I < 5\%$

Microtron $\delta I/I < 0.5\%$

Higher dose rates are observed in the area of the RF resonators, bending magnets and dump, where radiation sensors are installed.

HARDWARE AND SOFTWARE OF THE RADIATION DOSIMETRY SYSTEM

Our institute has developed a radiation monitoring system using two types of radiation detectors based on ionization chambers. The first-type detectors register radiation at the natural background level of 0.01 – 0.02 μSv/h. They are located in the rooms where people work.

The second-type detectors register radiation of about 10 Sv/h. These twenty gas-filled detectors are located in the accelerator hall and control photon radiation there.

The spherical ionization chamber is filled with air at a pressure of 4 atm. The chamber is made of polyamide with a thin layer of colloidal graphite; its wall thickness is 1.1 mm (Fig. 3.).

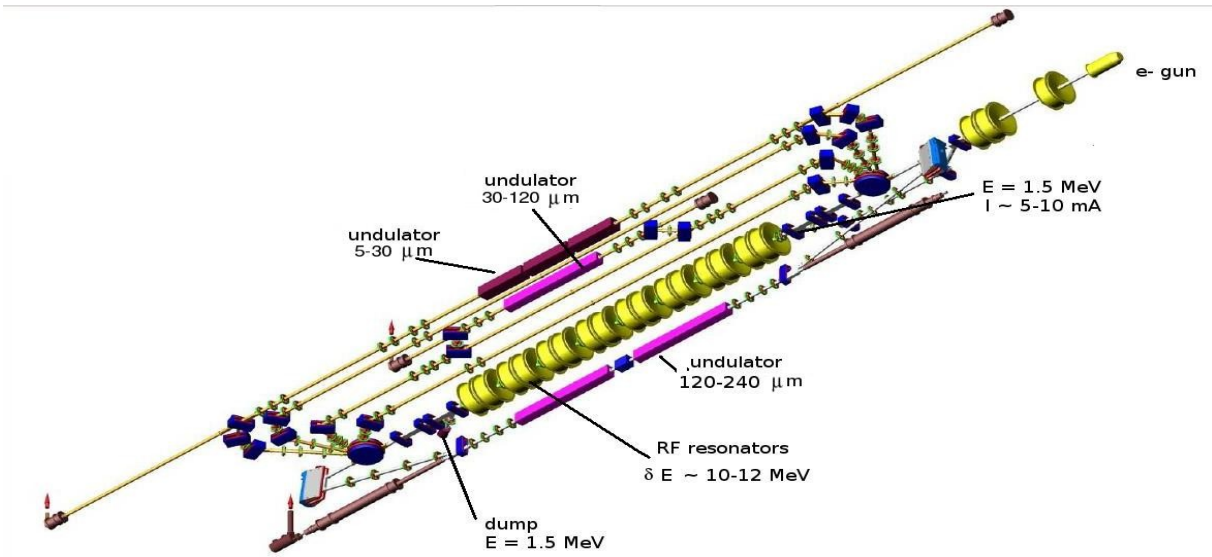

Figure 1: Novosibirsk ERL with the three FELs.

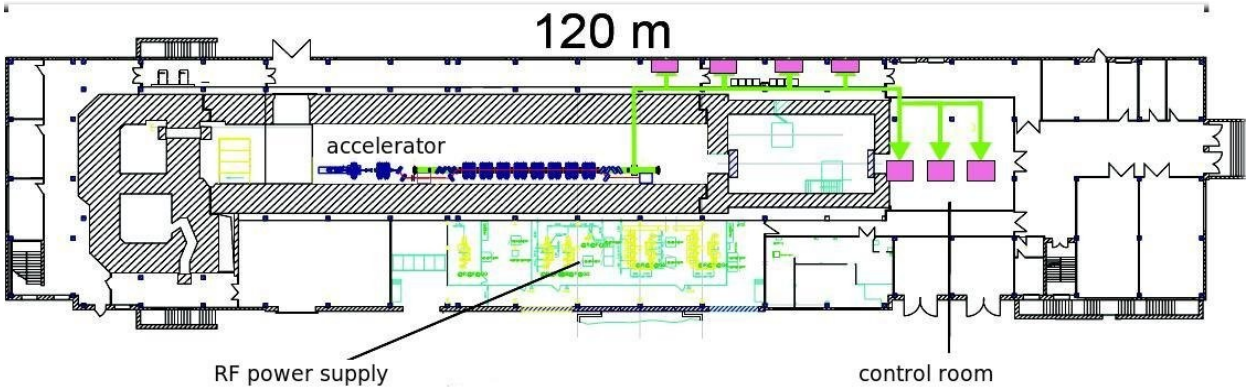

Figure 2: The layout of FEL systems

Figure 3: Ionization chamber.

The detectors that register small doses are connected to the microcontroller TINI with the Ethernet capability. The detectors that register large doses are connected to a module for preliminary processing of signals, which has the CANbus interface (Fig. 4).

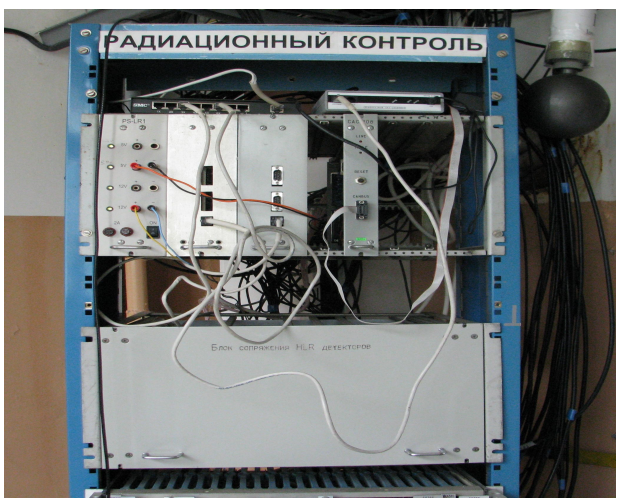

Figure 4: Hardware of the radiation safety system.

At FEL operation, the control system monitors dose rates and provides protection with the help of the user client “Xray”. The program “Xray” maintains a logbook; a record is created for each radiation transducer. Periodically, the program “Xray” records a timestamp and maximum and average values of dose rates for each transducer. The “Xray” program executes sampling from the transducers with a frequency of 1 Hz (Fig. 5). Besides, the "Xray" program allows watching the electron beam pass, since insignificant losses of electrons on the walls of the vacuum channel make the dose rate increase.

1. Radiation Monitoring in the accelerator hall. The program controls beam losses in the vacuum chamber. It enables the operator to adjust the orbit. Besides, it protects the vacuum chamber from heating (or burning). The information is input into the database, which helps us analyse the effects of radiation on materials and equipment and calculate the lifetime of the technological units.

2. Radiation Monitoring in the offices. The radiation levels do not exceed the federal limits and are mostly equal or less than the natural background radiation.

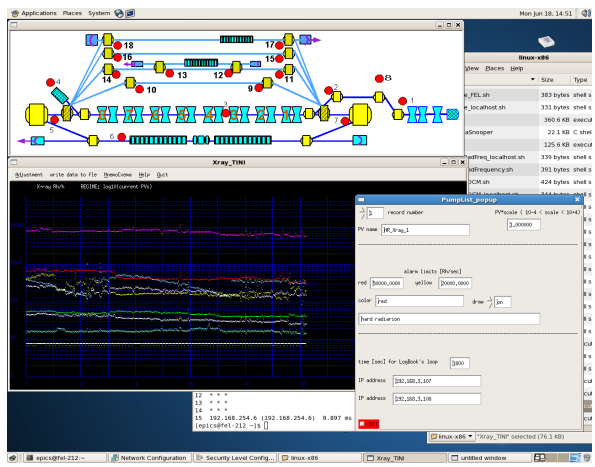

Figure 5: GUI client “Xray”.

REFERENCES

[1] Bolotin V.P., Vinokurov N.A., Kayran D.A., Knyazev B.A., Kolobanov E.I., Kotenkov V.V., Kubarev V.V., Kulipanov G.N., Matveenko A.N., Medvedev L.E., Miginsky S.V., Mironenko L.A., Oreshkov A.D., Ovchar V.K., Popik V.M., Salikova T.V., Serednyakov S.S., Skrinsky A.N., Shevchenko O.A., Scheglov M.A. “Status of the Novosibirsk terahertz FEL”. Nuclear instruments and methods in physics research. Sec. A. 2005. Vol. A543, No. 1. pp. 81-84.

INSTRUMENTATION DESIGNS FOR BEAM DISTRIBUTION MEASUREMENTS IN THE ERL BEAM DUMP AT BNL *

T. Miller #, S. Bellavia, I. Ben-Zvi, J. Fite, D. Gassner, D. Kayran
Brookhaven National Lab, Upton, NY, USA

Abstract

The R & D Energy Recover LINAC (ERL) at Brookhaven National Laboratory is undergoing continued development in parallel with piece-wise commissioning efforts as installation of each subsystem is completed. While the machine is planned to operate at low intensity with short, low frequency pulses during the commissioning phases, on going design efforts continue to provide a solution to measure the beam distribution inside the high power electron beam dump using several parallel methods. For low power measurements, this includes a new rad-hard version of long 7/8 in. Heliax ion chambers [1,2] that encage the dump both in circular and axial directions. For high power measurements, this includes both "pinhole" like multipoint imaging of the dump with ion chamber beam loss monitors [3] positioned over an array of holes drilled in the shielding around the beam dump as well as an infrared imaging system to peer through an upstream dipole chamber in the extraction line to monitor the temperature distribution on the target surface inside the dump. This paper presents the design details of these three systems that work to ensure the proper distribution of the high power electron beam on the target in an effort to avoid reaching the thermal limit of the water cooled beam dump [4].

INTRODUCTION

The ERL produces an electron beam of short bunches and is designed to operate over a wide range of pulse structures with the ultimate goal of 1MW CW operation. The machine parameters are summarized in Table 1.

Table 1: Machine Parameters

BEAM PARAMETERS	(low charge / high current)
Inj. Energy:	2.0 MeV
Max Energy:	20.0 MeV
Bunch Frequency:	9.383 MHz/ 351, 703 MHz
Bunch Charge:	0.050 – 1.4 nC / 1.4, 0.7 nC
Beam Current:	14 / 500 mA
Bunch Length (rms)	60 – 120 ps / 2 – 40 ps

The ERL has had a long history of R&D efforts at BNL. Its design includes a wide variety of instrumentation [5,6], markedly the three systems described here, to monitor the high power beam dump. Fig. 1 shows the layout and relative size of the machine.

*Work supported by U.S. DOE under contract No DE-AC02-98CH10886 with the U.S. DOE
#tmiller@bnl.gov

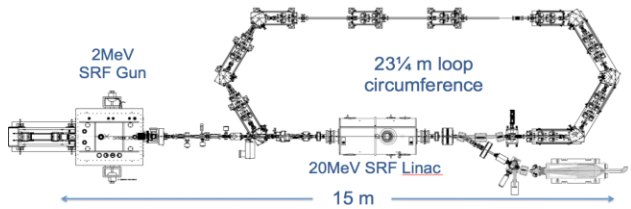

Figure 1: Layout of the ERL.

Electron Beam Distribution

In order to properly fit the beam dump with instrumentation, a simulation of the beam distribution inside the dump was made. Fig. 2 shows the simulated beam function in the X-Z plane. The distribution favors the rear of the dump where most of the energy is deposited on the cone. The predicted beam envelope is outlined in red.

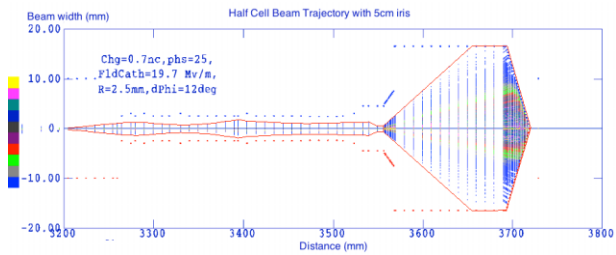

Figure 2: Simulated Beam Trajectory in the extraction line and beam dump.

Beam Dump Design

The design of this water-cooled beam dump is an adaptation of a design for a 1 MW klystron and was built to BNL specifications by CPI, a klystron manufacturer in Palo Alto, CA [7]. Figure 3 shows a drawing of the dump with the beam distribution from Fig. 2 scaled to fit. Before the beam enters the dump it is defocused by a quadrupole to have an opening angle of about 18° and drifts just over a meter before contacting the dump's internal surface. It is important to spread the beam over a large area to distribute the power. The goal of these instrumentation efforts is to continuously confirm an even distribution. When operating at full current, the dump will have to absorb nearly 1 MW of energy from the 2.0 MeV extracted decelerated beam. Simulations predict that when properly defocused, the power density of the absorbed beam will be 600 W/cm^2. However, if the defocusing were lost, a power density of 33 kW/cm^2 would destroy the beam dump. In order to take away the heat, a water jacket is formed around the inner copper dump material that channels cooling water at a flow rate

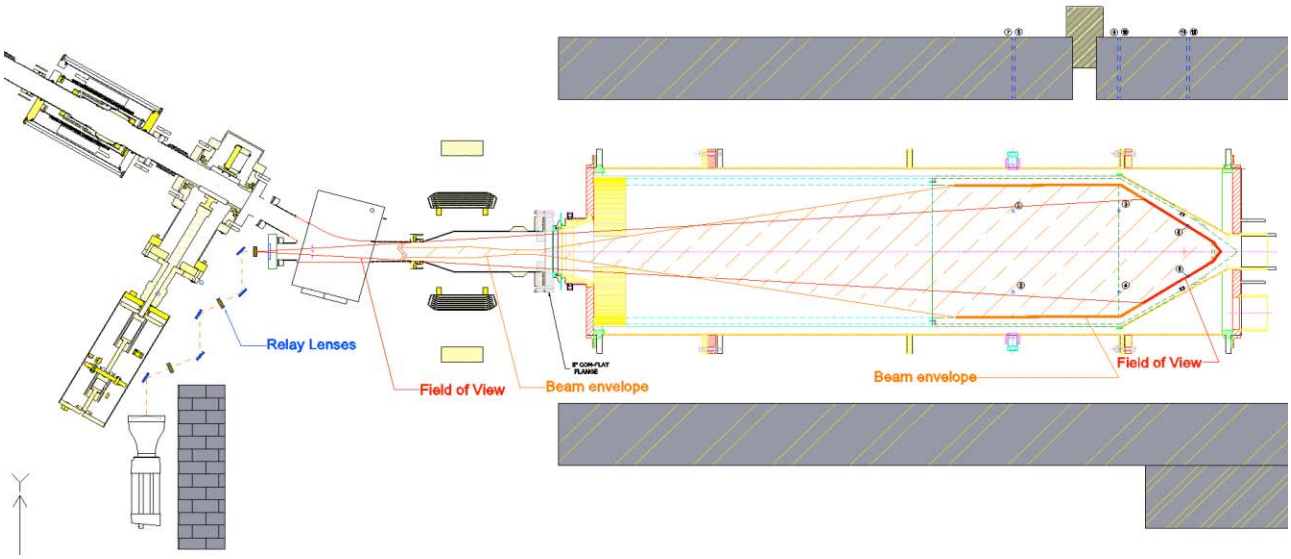

Figure 3: Beam Dump with beam distribution and IR camera field of view.

of 380 gal/min in order to keep the water below its boiling point. The radiation produced during this process is predicted to be 38 Mrad/hr. Although the ERL and beam dump are housed inside a 4 ft. thick concrete blockhouse; additional shielding is required to keep the radiation levels below 0.5 mrem/hr in the controlled area outside the blockhouse. A solid shield made of six inches of steel is placed over the dump like the lid of a butter dish.

LOW POWER BEAM LOSS MEASUREMENTS

As the ERL will be operated in low power for many months of its early commissioning and testing phases, a sensitive beam loss measurement system is installed around the dump under the steel shielding. For this, a matrix of long beam loss monitors (BLM) is created along and encircling the dump to give a cylindrical coordinate system (z,θ) of beam loss intensity. Fig. 4 shows a 3D model of the system layout. These long BLMs are composed of 7/8 in. Heliax cable with specially designed rad-hard fittings on the ends and act as long ion chambers to detect ionizing radiation.

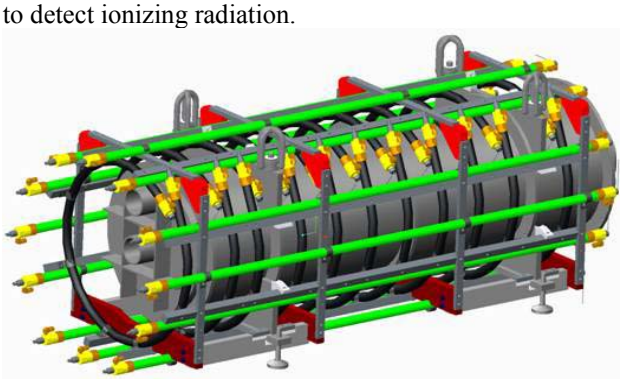

Figure 4: Beam Dump with Heliax BLM matrix.

Heliax BLM System

The Heliax BLM system was chosen for its long track record of beam loss detection in the AGS machine [1,2] at BNL, as well as in the Booster and Slow Extraction Beamlines. Made from 7/8 in. Heliax cable, Andrews [8] model HJ5-50, these BLMs are used as ion chambers to detect ionizing radiation. Argon gas is, either sealed inside, or trickled through the space between the center conductor and the shield in between the spirals of the helical insulating support. A bias voltage of -200V is applied between center conductor and shield and currents are measured in the loop by amplifiers in the bias electronics, located 30m away in the service building.

Here, two sets of 12 BLMs, one at 3.5 m long is installed along side the dump (shown in green in Fig. 4), and the other at 2 m long is bent in a circle and positioned at intervals along the z-axis (shown in black in Fig. 4). This type of BLM exhibits a dynamic range of up to 10^4 (with variable gain electronics) and a sensitivity of ~200 nC/rad/m [13] can be expected with 1 atm of argon. We typically operate near 10 psig of argon, giving a slightly elevated sensitivity.

Although these BLMs will not be used at the full ERL current due to expected saturation, they must withstand the high radiation of the full ERL current without being destroyed. The goal is to reduce the machine current and use these BLMs to map the beam distribution in the dump whenever the distribution comes into question while operating. This requires that all components of these BLMs be rad-hard. Although the center support helix, made of polyethylene (PE), is expected to harden and become inflexible under the effects of the radiation; the shape of the BLM cables is static and does not need to flex. Thus this poses little concern. On the contrary, the connectors that terminate the ends of the cables are typically Andrews model H5PNF, type-N female with a gas barrier to seal the flowing gas. It contains rubber O-

rings and Teflon insulators. An exploded view is shown in Fig. 5. Here the risk of a leak and HV breakdown are the concerns if the radiation destroys the connector insulators or seals. Table 2 summarizes the radiation sensitivity of the materials of interest [9,10].

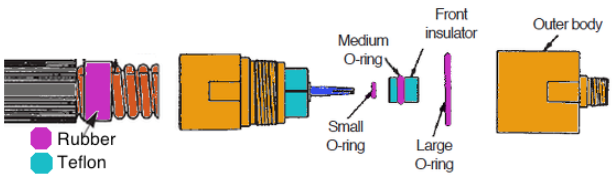

Figure 5: Andrews Heliax H5PNF connector for HJ5-50 Heliax cable.

Radiation Resistance

Efforts were made to develop a rad-hard alternative to the connector. The three rubber seals and the two Teflon insulators in the connector, shown in Fig. 5, had to be eliminated. To eliminate the seal to the corrugated solid shield, a copper body was machined to slip over the shield and joined by soldering. The other two seals that form the N connection to the center conductor were replaced by an off-the-shelf UHV feedthrough with a BNC connector that threads into the copper body and is sealed with Loctite 580 PST nuclear grade pipe sealant (without PTFE).

Table 2: Radiation Tolerance of Materials used

Material	Allowable Gamma Dose [10]
Teflon (PTFE)	0.001 Grad
Rubber (O-rings)	0.1 Grad
PEEK	1.0 Grad [9]
Kapton	>2 Grad

A threaded rod screws into an off-the-shelf banana plug that slides into the hollow center conductor of the Heliax cable. The threaded rod was bored and slit axially to create fingers to grab the electrode on the feedthrough opposite its BNC connector. Fig. 6 shows a cross-section view of the custom connector.

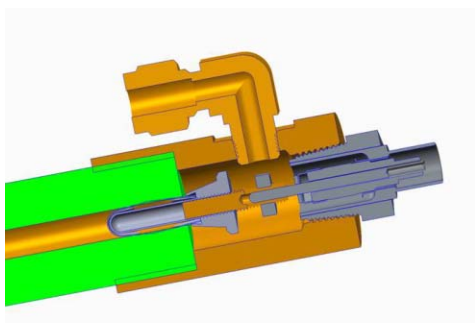

Figure 6: Rad-Hard BNC termination for 7/8 in. Heliax.

The Heliax BLM's are plumbed in series to create a single gas flow circuit. As only one side of the BLM requires electrical connection, the other end is terminated with a simple off-the-shelf copper 1 in. tube adapter & gas tube fitting that is likewise soldered to the copper shield of the Heliax cable.

Rad-hard BNC connectors, Accuglass [11] model 111023, for ultrahigh vacuum with PEEK insulators are used to connect to the Heliax BLMs. These connectors are designed to terminate Kapton coaxial cable, Accuglass model 100720. These cables will carry the signals out of the high radiation area to a patch panel outside of the steel shielding where standard RG58 cables with BNC connectors will make the long run back to the control room.

HIGH POWER BEAM LOSS MEASUREMENTS

Pin-hole Monitors

When operating the ERL at full current, the radiation levels will be their highest at 38 Mrad/hr inside the shielding. To provide a rough map of the beam distribution based on the radiation, ¼ inch "pin-holes" were drilled through the steel shielding for RHIC style BLMs [3] to take a sample of radiation over a small portion of the dump beneath the shield.

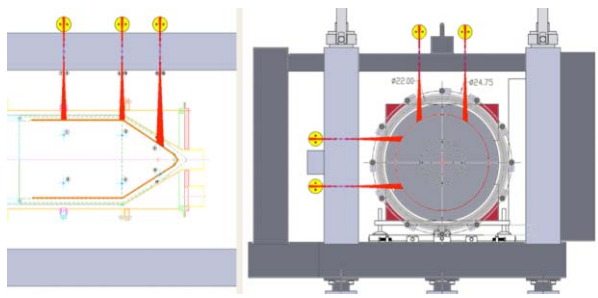

Figure 7: Pinhole radiation measurements: (left) top view, (right) axial view.

A pattern of 6 holes is drilled in the side and top of the "butter-dish" shield. Fig. 7 shows cross-sectional views depicting, in red, the measured areas of the dump.

The RHIC BLM is a "glass bottle" type sealed ionization chamber pressurized to ~1 atm of argon and accompanied by custom VME based amplifier electronics. These have separate connections and cables for their signal & bias voltage of +1400V. These are shown in Fig. 7 as the yellow circles. They benefit from a wider dynamic range than the Heliax BLMs, typically > 10^6, and a sensitivity of about 70 nC/rad [13].

Infrared Imaging of the Dump

Plans are underway to install an infrared camera to image the cone of the dump through an upstream auxiliary viewport in the chamber of the last dipole magnet in the extraction line. The camera is a Flir model A310, with an integrated 25° Germanium lens. It has an uncooled microbolometer sensor with 320 x 240 pixels (25 μm pitch) with a spectral sensitivity over the range of 7 – 13 μm. The viewport is made of ZnSe with a transmission

spectrum in the range of 0.6 – 16 μm (AR coated for 8 – 12 μm). It is model ZVP38ZNW, made by VG Scienta, with a 38 mm aperture. It is located just over 2m away from the end cone of the dump. The camera was purchased with an add-on 6° Germanium telephoto lens. With the camera located at the viewport, it could image nearly 80 % of the cone's surface. Its view is aperture limited by the downstream flange of the dipole vacuum chamber. This flange could not be enlarged as it would increase the aperture in the lead shield wall planned to limit the radiation to ~2.5 Mrad/hr exiting the dump, back streaming through the extraction line. Due to this high level of radiation, the camera must be moved out of the line of sight of the dump beam aperture and relayed with several mirrors to reduce the total radiation bounce off of the mirror(s). This lengthens the camera's optical path and requires relay lenses to compensate for the increased distance while maintaining the proper field of view. This is shown schematically in Fig. 3 with the "relay lenses" labeled in blue.

Although a location for the camera has been chosen with a place for four turning mirrors and the proper lead shielding, efforts continue to model a proper relay lens system to provide an acceptable limit of distortion. Fig. 8 shows the camera, vertical optics table and four mirrors. The relay lenses and lead shielding are not shown.

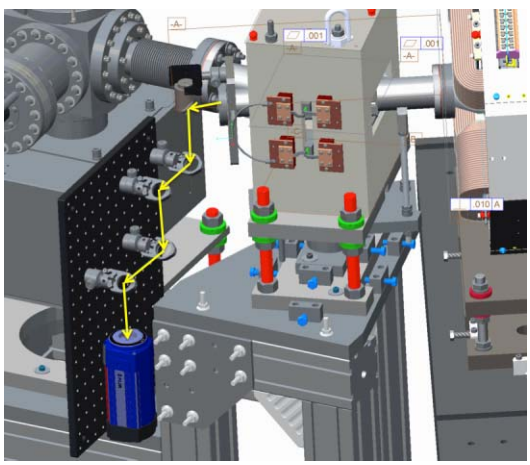

Figure 8: IR camera & turning mirrors (relay lenses not shown).

Optical components made of ZnSe are readily available; although in a diameter of only 1 inch. Preliminary models, with three lenses using the free software Oslo [12], have been made thus far with promising results. Once a satisfactory lens design is achieved, the lenses will located at their proper positions on the vertical optics board in between the four turning mirrors and the camera.

STATUS & FUTURE PLANS

With first beam tests planned for the ERL Gun next month, and low power beam around the loop to follow next year, the dump is expected to see high power beam near mid 2014. The dump is in house and is being assembled with the Heliax BLMs off of the ERL site. It will be lowered into the blockhouse by an overhead building crane and set on its steel support table while encaged by the Heliax BLM assembly. Once the cooling water is plumbed and the BLM signal & HV cables are routed, the steel "butter-dish" shield will be lowered onto the assembly. Then the ion chambers can be mounted over the "pin-holes" in the shield. In parallel to these efforts, the IR optics will be installed on the upstream beam line.

ACKNOWLEDGEMENTS

The authors would like to acknowledge the contributions of V. Litvinenko & G. Mc Intyre and thank members of the Beam & Experiment Services Group and recognize the support of the Accelerator Components & Instrumentation Group, especially, T. Curcio, D. Lehn & P. Ziminski.

REFERENCES

[1] E.R Beadle, et al, "The AGS Booster Beam Loss Monitor System", PAC 1991
[2] J. Balsamo, et al, "Long Radiation Detector system for Beam Loss Monitoring" IEEE Transactions on Nuclear Science, vol. NS-24, No. 3, June 1977
[3] R. Witkover, et al, "RHIC Beam Loss monitor System Design", PAC 1997, Vancouver, Canada
[4] A. Hershcovitch, "R&D ERL" Beam Dump", C-A/AP/#378, Upton, NY 2010
[5] D. Gassner, et al, "BNL Energy Recovery Linac Instrumentation", ERL 2011, Tsukuba, Japan
[6] D. Gassner, et al, "Status of the BNL ERL Instrumentation", ERL Workshop 2013, Novosibirsk
[7] Communication & Power Industries, 607 Hansen Way, Palo Alto, CA 94304, www.cpii.com
[8] CommScope, Inc., 1100 CommScope Place SE Hickory, NC 28602, http://www.commscope.com/catalog/ andrew/product_details.aspx?id=1458
[9] M. Tavlet, et al, "Radiation resistance and other safety aspects of high-performance plastics by ERTA", Workshop on Advanced Materials for High Precision Detectors, CERN 1994, Geneva
[10] M. H. Van de Voorde, "Effects of Radiation on Materials and Components", CERN 70-5, 1970, Geneva
[11] Accu-glass Products, 25047 Anza Drive, Valencia, CA 91355, www.accuglassproducts.com
[12] Optics Software for Layout and Optimization, Lambda Research Corp., 25 Porter Rd. Littleton, MA 01460, http://www.lambdares.com/additional-software/oslo
[13] K. Wittenburg, "Beam Loss Monitors", DESY, Hamburg, Germany, http://cds.cern.ch/record/1213279/ files/p249.pdf

THE DEVELOPMENT OF CRYOMODULE FOR C-ERL AT MHI

Hiroshi Hara, Haruki Hitomi, Fumiake Inoue, Katsuya Sennyu, Kohei Kanaoka, Takeshi Yanagisawa
Mitsubishi Heavy Industries, Ltd., Mihara, 729-0393, Japan

Abstract

Mitsubishi Heavy Industries, Ltd. (MHI) manufactured the Superconducting Accelerator Cavity Module of the Injector and the Main Linac of the c-ERL facility being constructed by the High Energy Accelerator Research Organization (KEK). This report provides status of the development.

INTRODUCTION

For the realization of nest generation synchrotron radiation light source ERL (Energy Recovery Linac), a small size ERL "Compact ERL" is under development at KEK (Fig. 1).

MHI manufactured Superconducting Cavities and Cryomodule for mounting Cavities as a high frequency acceleration device to accelerate electrons in the high electric field required as its nucleus technology, and completed installation and delivery of one (1) Injector Cryomodule and one (1) Main linac cryomodule [1].

At present, the beam acceleration test of the Injector Cryomodule is underway at KEK after having been through the High power test.

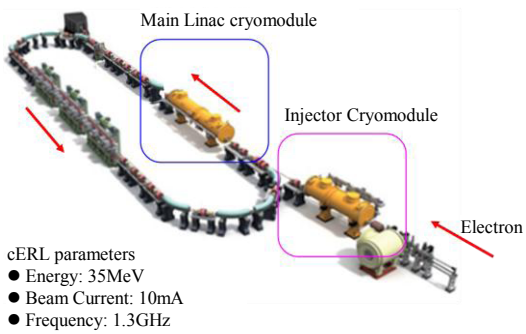

Fig. 1: Outline of the Compact ERL

INJECTOR CRYOMODULE

Configuration of the Cryomodule

The Container enclosing the whole assembly is made of stainless steel, inside of which Aluminum Shield cooled down to 80K is lined to shield radiant heat. Inside of the 80K Shield, the Helium Panels which can store helium of 5K are contained. The thermal anchor is led from the piping connecting two panels to the Input Coupler. Three (3) Cavities welded to the Jacket made of titanium are arranged in the middle of these components (See Fig. 2) [2]. Further, the Magnetic Shield is installed inside the Jacket to cover the Cell. Helium Panels and Piping to supply and recover liquid helium and liquid nitrogen are made of stainless steel, and they passed inspection of High Pressure Gas Safety Inst. of Japan.

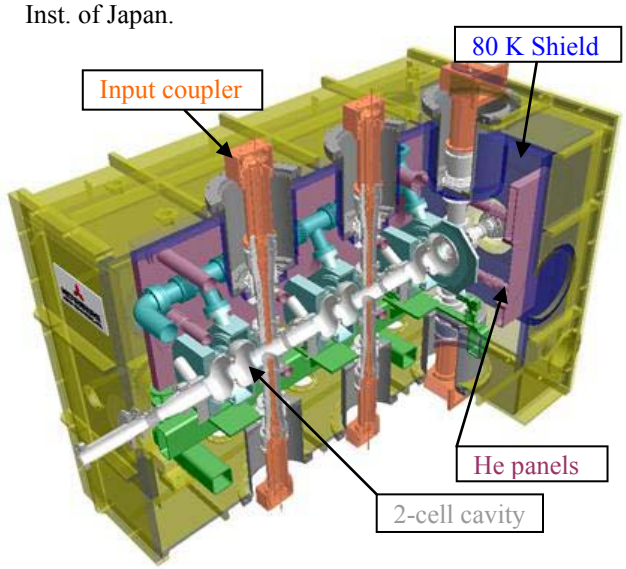

Fig. 2: Overall configuration of Injector Cryomodule

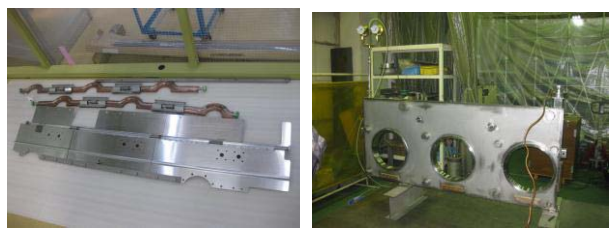

Fig. 3: Examples of component parts, (a) Thermal Shield and piping, (b) Helium Panel.

Superconducting Cavities

The construction is such that the Jacket made of titanium is installed outside of the 2 cells type Superconducting Cavities made of niobium so that the Cavities are held under the superconducting condition by storing liquid helium between the Jacket and the Cavities. The Jacket is designed to be compact so that the Slide Jack Tuner for frequency adjustment can be installed. The design specifications of the Cavities are as shown below, and they passed inspection of the High Pressure Gas Safety Inst. of Japan. The performance of subject three (3) Cavities are confirmed individually at KEK [3].

Table 1: High pressure gas design conditions of the Cavities

Design temp.	-271.4 to +30℃
Design press.	0.031+0.1013 MPa
Capacity	0.006 m^3
PV Value	0.0008 (<0.004) General rule

Fig. 4: Witness test by the High Pressure Gas Safety Institute of Japan

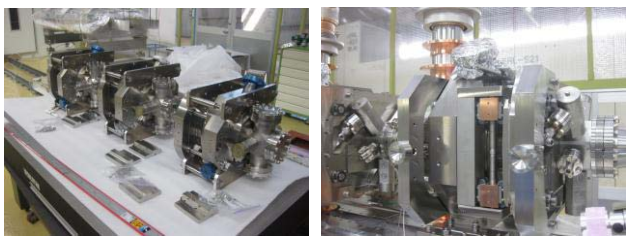

Fig. 5: Superconducting Cavities (left) and Frequency Tuner (right)

Assembly and installation of the Injector Cryomodule

In April of 2012, coupling of Cavities and Coupler installation work were performed in the clean room. Then, containing the Cavities in the Cryomodule was performed spending approximately a month and installation in the beam line was completed in June.

Fig. 6: Assembly and installation of the Injector Cryomodule (@ KEK-ERL Development Bldg.)

High power test of the Injector Cryomodule

In February of 2013, high power RF test was performed at KEK. Achievement of accelerating electric field of 8MV/m at CW operation and 15MV/m at pulse operation were confirmed.

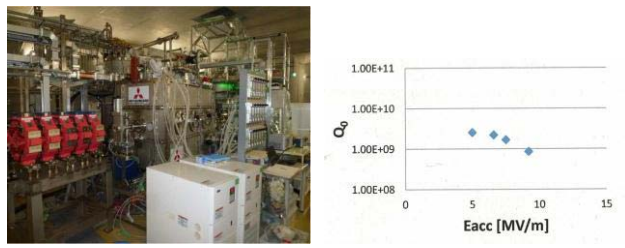

Fig. 7: High power test of the Injector Cryomodule

MAIN LINAC CRYOMODULE

Configuration of the Cryomodule

The Vacuum vessel enclosing the whole assembly is made of stainless steel, inside of which Aluminum Shield cooled down to 80K is lined to shield radiant heat. The main component called as Back Bone is contained in the vacuum vessel. The Cavities weld to the Jacket is fixed to the Frame cooled down to 5K and then covered by the Thermal Insulation and Magnetic Shield, and installed on the Back Bone (See Fig. 7) [4]. Piping to supply and recover liquid helium and liquid nitrogen are made of stainless steel, and they passed inspection of the High Pressure Gas Safety Inst. Japan.

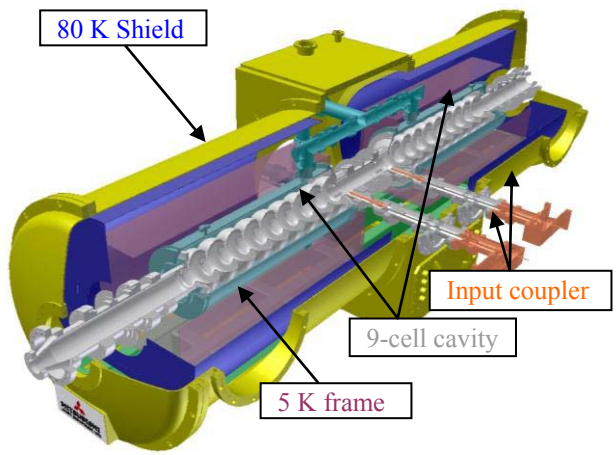

Fig. 8: Overall configuration of the Main Linac Cryomodule

Superconducting Cavities

The construction is such that the Jacket made of titanium is installed outside of the 9 cells type Superconducting Cavities made of niobium so that the Cavities are held under the superconducting condition by storing liquid helium between the Jacket and the Cavities. The design specifications of the Cavities are as shown below, and they passed the Designated Equipment Inspection. The performance of subject two (2) Cavities are confirmed individually at KEK [5].

Table 2: High pressure gas design conditions of the Cavities

Design temp.	-271.4 to +30℃	
Design Press.	0.031+0.1013 MPa	
Capacity	0.046 m^3	
PV Value	0.0061 (>0.004)	Particular rule

Fig. 9: Jacketing of the Cavities (Before jacketing of the 9 cells Superconducting Cavities and after jacketing of the Cavities)

Fig. 10: Witness test by the High Pressure Gas Safety Institute of Japan

Assembly and installation of the Main Linac Cryomodule

In August of 2012, coupling of Cavities and coupler installation work were performed in the clean room. Then, containing the Cavities in the Cryomodule was performed spending approximately a month and installation in the beam line was completed in October.

Fig.11: Assembly and installation of the Main Accelerator Module (@ KEK-ERL Development Bldg.)

High power test of the Main Linac Cryomodule

In February of 2013, high power RF test was performed at KEK. Achievement of acceleration electric field of 14MV/m at CW operation was confirmed.

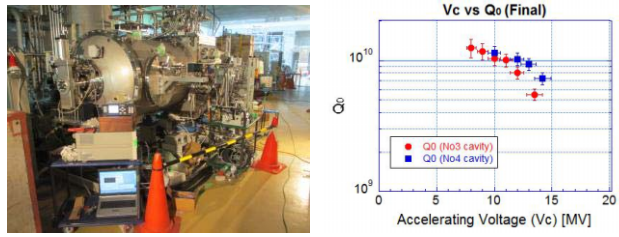

Fig. 12: Quenching test of the Main Accelerator Module

SUMMARY

MHI performed following for the construction of the cERL at KEK.

- Developed 2 cells type Superconducting Cavities for the Injector and manufactured three (3) real units conforming to the General High Pressure Gas Safety Act.
- Developed 9 cells type Superconducting Cavities for the Main Accelerator and manufactured 2 real units conforming to the High Pressure Gas safety Act.
- Manufactured one (1) Injector Module containing 3 units of the 2 cells type Superconducting Cavities for the Injector, and completed assembly, installation and delivery.
- Manufactured one (1) Main Accelerator Module containing 9 cells type Superconducting Cavities for the Main Accelerator, and completed assembly, installation and delivery.

REFERENCES

[1] H. Hitomi, et al., "Fabrication of Superconducting RF Cavity at MHI", ERL2011, Tsukuba, Japan, (2011), WG3002

[2] S. Noguchi, et al., "Injector Cryomodule for cERL at KEK", ERL2011, Tsukuba, Japan, (2011), WG3

[3] K. Watanabe, et al. "Progress of cERL injector cavities at KEK", ERL2011, Tsukuba, Japan, (2011), WG3005

[4] K. Umemori, et al. "Development of main linac cavity for cERL project", ERL2011, Tsukuba, Japan, (2011), WG3

[5] T. Furuya, et al., "Cryomodule of KEK-ML cavity", ERL2011, Tsukuba, Japan, (2011), WG3

List of Authors

Bold papercodes indicate primary authors

Institutes List

AIST
Tsukuba, Japan
- Yoshida, H.

Bergische Universität Wuppertal
Wuppertal, Germany
- Lagotzky, S.
- Müller, G.

BINP SB RAS
Novosibirsk, Russia
- Arbuzov, V.S.
- Dementyev, E.N.
- Dovzhenko, B.A.
- Getmanov, Ya.V.
- Gorniker, E.I.
- Knyazev, B.A.
- Kolobanov, E.I.
- Kondakov, A.A.
- Kozak, V.R.
- Kozyrev, E.V.
- Krutikhin, S.A.
- Kubarev, V.V.
- Kulipanov, G.N.
- Kuper, E.A.
- Kuptsov, I.V.
- Kurkin, G.Y.
- Medvedev, L.E.
- Mironenko, L.A.
- Osipov, V.N.
- Ovchar, V.K.
- Petrichenkov, M.
- Petrov, V.M.
- Pilan, A.M.
- Popik, V.M.
- Repkov, A.V.
- Repkov, V.V.
- Salikova, T.V.
- Scheglov, M.A.
- Sedlyarov, I.K.
- Serednyakov, S.S.
- Shevchenko, O.A.
- Skrinsky, A.N.
- Tararyshkin, S.V.
- Tcheskidov, V.G.
- Tribendis, A.G.
- Vinokurov, N.
- Vlasenko, M.G.
- Vobly, P.
- Volkov, V.

BNL
Upton, Long Island, New York, USA
- Altinbas, Z.
- Bellavia, S.
- Belomestnykh, S.A.
- Ben-Zvi, I.
- Bengtsson, J.
- Dai, J.
- Deonarine, S.
- Fite, J.M.
- Gassner, D.M.
- Hahn, H.
- Hao, Y.
- Jamilkowski, J.P.
- Jing, Y.C.
- Kankiya, P.
- Kayran, D.
- Laloudakis, N.
- Litvinenko, V.
- Liu, C.
- Masi, L.
- McIntyre, G.T.
- Michnoff, R.J.
- Miller, T.A.
- Minty, M.G.
- Pate, D.
- Phillips, D.
- Pinayev, I.
- Schubert, S.G.
- Seda, T.
- Smith, K.S.
- Steszyn, A.N.
- Tallerico, T.N.
- Than, R.
- Todd, R.J.
- Trbojevic, D.
- Weiss, D.
- Wilinski, M.
- Xu, W.
- Zaltsman, A.

CERN
Geneva, Switzerland
- Brüning, O.S.
- Calaga, R.
- Jensen, E.
- Valloni, A.

Cornell University (CLASSE), Cornell Laboratory for Accelerator-Based Sciences and Education
Ithaca, New York, USA
- Dunham, B.M.
- Mayes, C.E.

DELTA
Dortmund, Germany
- Ferrarotto, A.
- Weis, T.

Fermilab
Batavia, USA
- Shiltsev, V.D.

FZJ
Jülich, Germany
- Zaplatin, E.N.

HU/AdSM
Higashi-Hiroshima, Japan
- Iijima, H.
- Kuriki, M.

HZB
Berlin, Germany
- Anders, W.
- Atkinson, T.
- Barday, R.
- Bondarenko, A.V.
- Burrill, A.
- Jankowiak, A.
- Kamps, T.
- Klimm, C.
- Knobloch, J.
- Kugeler, O.
- Matveenko, A.N.
- Neumann, A.
- Panofski, E.
- Petenev, Y.
- Rudolph, J.
- Schmeißer, M.
- Siewert, F.
- Völker, J.

HZDR
Dresden, Germany
- Arnold, A.
- Büttig, H.
- Lehnert, U.
- Lu, P.N.
- Michel, P.
- Murcek, P.
- Schurig, R.
- Staats, G.S.
- Teichert, J.
- Vennekate, H.
- Xiang, R.

IHEP
Beijing, People's Republic of China
- Cao, J.S.
- Chen, S.Y.
- Chi, Y.L.
- Gao, J.
- Jiao, Y.
- Jin, S.
- Li, X.P.
- Liu, J.
- Liu, R.L.
- Liu, Z.C.
- Lv, K.
- Pei, S.
- Peng, X.H.
- Sun, D.R.
- Wang, G.W.
- Wang, J.Q.
- Wang, S.H.
- Xiao, O.
- Zhang, J.R.
- Zhang, T.
- Zhou, Z.S.

IKP
Mainz, Germany
- Aulenbacher, K.
- Dehn, M.A.
- Diefenbach, J.
- Fichtner, F.
- Heine, R.G.
- Kirsch, E.
- Schlander, F.
- Tioukine, V.

Insititute of High Energy Physics (IHEP)
People's Republic of China
- Xu, J.Q.

ISP
Novosibirsk, Russia
- Bakin, V.V.
- Gorshkov, D.V.
- Kosolobov, S.N.
- Scheibler, H.E.
- Terekhov, A.S.

ISSP/SRL
Chiba, Japan
- Takaki, H.

JAEA
Ibaraki-ken, Japan
- Hajima, R.
- Matsuba, S.M.
- Nagai, R.
- Nishimori, N.
- Sawamura, M.
- Shizuma, T.

JLAB
Newport News, Virginia, USA
- Evtushenko, P.E.
- Kneisel, P.
- Marchlik, M.
- Rimmer, R.A.

KAERI
Daejon, Republic of Korea
- Vinokurov, N.

KEK
Ibaraki, Japan
- Adachi, M.
- Adachi, S.
- Akemoto, M.
- Arakawa, D.A.
- Asaoka, S.
- Enami, K.
- Endo, K.
- Fukuda, S.
- Furuya, T.
- Haga, K.
- Hara, K.
- Harada, K.
- Honda, T.
- Honda, Y.
- Honma, H.
- Honma, T.
- Hosoyama, K.
- Hozumi, K.
- Ishii, A.
- Kako, E.
- Kamiya, Y.
- Katagiri, H.
- Kawata, H.
- Kobayashi, M.
- Kobayashi, Y.
- Kojima, Y.
- Kondou, Y.
- Konstantinova, O. A.
- Kume, T.
- Matsumoto, T.
- Matsumura, H.
- Matsushita, H.
- Michizono, S.
- Miura, T.
- Miyajima, T.
- Miyauchi, H.
- Nagahashi, S.
- Nakai, H.
- Nakajima, H.
- Nakamura, N.
- Nakanishi, K.
- Nakao, K.
- Nigorikawa, K.N.
- Nogami, T.
- Noguchi, S.
- Nozawa, S.
- Obina, T.
- Ozaki, T.
- Qiu, F.
- Sagehashi, H.
- Sakai, H.
- Sakanaka, S.
- Sasaki, S.
- Satoh, K.
- Satoh, M.
- Seimiya, Y.
- Shidara, T.
- Shimada, M.
- Shinoe, K.
- Shioya, T.
- Shishido, T.
- Tadano, M.
- Tahara, T.
- Takahashi, T.
- Takai, R.
- Takenaka, T.
- Tanimoto, Y.
- Tobiyama, M.
- Tsuchiya, K.
- Uchiyama, T.
- Ueda, A.
- Umemori, K.
- Watanabe, K.
- Yamamoto, M.
- Yamamoto, Y.
- Yano, Y.
- Yoshida, M.

KNU
Deagu, Republic of Korea
- Hwang, J.G.

MBI
Berlin, Germany
- Will, I.

MHI
Kobe, Japan
- Hara, H.
- Sennyu, K.

MSU
Moscow, Russia
- Shvedunov, V.I.

Nagoya University
Nagoya, Japan
- Kuwahara, M.

NSU
Novosibirsk, Russia
- Knyazev, B.A.

Osaka University
Osaka, Japan
- Kimura, S.I.

PKU
Beijing, People's Republic of China
- Chen, J.E.
- Chen, S.
- Feng, L.W.
- Huang, S.
- Lin, L.
- Liu, K.X.
- Quan, S.W.
- Wang, F.

- Wang, Zh.W.
- Xie, H.M.

Sokendai
Ibaraki, Japan
- Cenni, E.

STFC/DL/ASTeC
Daresbury, Warrington, Cheshire, United Kingdom
- Buckley, R.K.
- Cash, R.J.
- Corlett, P.A.
- Fell, B.D.
- Goudket, P.
- Goulden, A.R.
- Jones, L.B.
- Ma, L.
- McIntosh, P.A.
- Middleman, K.J.
- Militsyn, B.L.
- Moss, A.J.
- Noakes, T.C.Q.
- Pattalwar, S.M.
- Wheelhouse, A.E.

Stony Brook University
Stony Brook, USA
- Belomestnykh, S.A.
- Ben-Zvi, I.
- Dai, J.

TU Darmstadt
Darmstadt, Germany
- Hug, F.
- Kürzeder, T.
- Pietralla, N.

Yamaguchi University
Ube-Shi, Japan
- Kurisu, H.